HIGH FREQUENCY BANDWIDTH CUTTING FORCE MEASUREMENTS IN MILLING USING THE SPINDLE INTEGRATED FORCE SENSOR SYSTEM

By

Simon S. Park

B.Sc. (Mechanical Engineering) University of Toronto

Ma.Sc. (Mechanical Engineering) University of Toronto

A THESIS SUBMITTED IN PARTIAL FULFILLMENT OF
THE REQUIREMENTS FOR THE DEGREE OF
DOCTOR OF PHILOSOPHY

IN

THE FACULTY OF GRADUATE STUDIES
Department of
MECHANICAL ENGINEERING

We accept this thesis as conforming
To the required standard

THE UNIVERSITY OF BRITISH COLUMBIA

November 2003

ABSTRACT

The accurate measurement of forces at the tool tip is required for calibration of cutting force coefficients, adaptive control of maximum cutting forces, detection of tool failure, and monitoring of the force history applied to a workpiece during production. However, the majority of the present sensor systems are not effective due to low frequency bandwidths, limited workpiece size, wiring complexities, and susceptibility to harsh machining environments. To overcome the limitations, the Spindle Integrated Force Sensor (SIFS) system is developed, which can be used in production machines to measure cutting forces by integrating piezoelectric force sensors to the stationary spindle housing. Since the sensors are part of the spindle, the structural dynamics of the spindle assembly directly affect the accuracy and bandwidth of the force measurement. The thesis presents a systematic methodology to compensate the distortions caused by structural dynamic modes of the spindle and tool system.

The structural dynamic model between the cutting forces acting on the tool tip and the measured forces at the spindle housing is identified. A disturbance Kalman Filter is designed to remove the influence of structural modes on the force measurements. The frequency bandwidth is increased from 350 Hz to 1000 Hz by compensating the first three dominant structural modes of the spindle with the proposed sensing and the signal processing method. In addition, the mathematical coupling of Frequency Response Functions (FRFs) of the spindle and arbitrary cutting tool dynamics is proposed and verified using the Receptance

Coupling (RC) method with the identification of the joint dynamics to automate the dynamic compensation regardless of end mills. Based on the reconstructed cutting force measurements from the spindle integrated sensors, the adaptive control scheme is used to maximize productivity by optimizing the feed rate of the CNC machine, and the chatter and tool breakage detections are performed to monitor the milling processes.

TABLE OF CONTENTS

LIST OF FIGURES

LIST OF TABLES

NOMENCLATURE

k_p = *Static force sensor stiffness [N/m]*

k_b = *Static bolt stiffness[N/m]*

k_{eq} = *Equivalent static stiffness[N/m]*

ϕ = *Immersion angle*

U = *Mode shape matrix*

$M_{x,q}$ = *Mass matrix*

$C_{x,q}$ = *Damping matrix*

$K_{x,q}$ = *Stiffness matrix*

k_s = *Spring constant for the Receptance Coupling [N/m]*

k_p = *Static force sensor stiffness [N/m]*

k_b = *Static bolt stiffness[N/m]*

k_{eq} = *Equivalent static stiffness[N/m]*

H = *Receptance (x/F)*

F_a = *Applied force at the tool tip (N)*

F_m = *Measured force from the spindle integrated sensors (N)*

F_u = *Unbalanced force (N)*

Φ = *Transfer function between the tool tip and the spindle sensor (F_m/F_a)*

ω_n = *Natural frequencies of the spindle structure (Hz)*

ω_n = *Tooth passing frequencies (Hz)*

ζ = *Damping ratio of the spindle structure*

α = *Stiffness equivalent term of the spindle structure*

b = *Numerator of the transfer function*

a = *Denominator of the transfer function*

T = *Transformation matrix*

W = *Observability matrix*

w = *Process noise*

v = *Measurement noise*

K = *Kalman Filter gain*

t_d = *Discrete sampling time*

G = *Kalman Filter transfer function*

P = *Estimation error covariance matrix*

Q = *System noise covariance matrix*

R = *Measurement noise covariance matrix*

Γ = *System noise vector*

K_r = *Rear bearing stiffness [N/m]*

K_f = *Front bearing stiffness[N/m]*

F_s = *Reaction force at the SIFS[N]*

F_c = *Reaction force at the roller support [N]*

Ks = *Spring constant for the displacement sensor [N/m]*

δ_F = *Force measured from the displacement sensor [N]*

A = *System matrix*

A_e = *Expanded system matrix*

A_n = *Balanced system matrix*

B = *Input matrix*

B_n = *Balanced input matrix*

C = *Output matrix*

C_e = *Expanded output matrix*

C_n = *Balanced output matrix*

C_o = *Observer matrix*

D = *Feed forward matrix*

Ks = *Spring constant for the displacement sensor [N/m]*

δ_F = *Force measured from the displacement sensor*

A = *System matrix*

A_e = *Expanded system matrix*

A_n = *Balanced system matrix*

B = *Input matrix*

B_n = *Balanced input matrix*

h = *Chip thickness [mm]*

f_c = *Feed command [mm/sec]*

c = *Feed rate [mm/min]*

F_r = *Reference Force [N]*

G_m = *CNC and feed drive plant*

G_p = *Cutting process plant*

G_c = *Cascaded plant* ($G_m \times G_p$)

M = *Number of flutes*

n = *Spindle rotation [rev/min]*

ρ = *GPC weighting factor*

N_1 = *Minimum prediction horizon*

N_2 = *Maximum prediction horizon*

N_u = *Control horizon*

ε_i = *Residual index for tool breakage detection*

s = *Laplace operator*

z = *Discrete time Z operator*

ACKNOWLEDGEMENTS

I would like to sincerely thank Professor Altintas for his endless support, encouragement, and guidance. Without him, it is difficult to imagine myself studying at UBC. I am grateful for all past and present members of the Manufacturing Automation Laboratory (Kaan Erkorkmaz, Yuzhong Cao, Osamu Maeda, Fuat Atabey, Doruk Merdol, Jochem Roukema, Merhdad Nevis, Isabelle Belanger, Chi-Ho Yeung, Andrew, Dima Ostafiev, Martin Jun, Mathew Tse, and many others). Their assistance and presence made life at UBC very enjoyable. Especially, I wish to thank the former Ph.D student, Dr. Serafattin Engin at Pratt & Whitney Canada who helped me to get started in the laboratory and provided valuable feedback. Sebastian Fritz from ISW, University of Stuttgart supported me with the initial research on the disturbance observer for the compensation. Dr. Ismail Lazoglu gave me tremendous support during the first year of my study. Dr. Mohammad Movahhedy gave me invaluable input for the receptance coupling analysis. Dr. Andrea Kircheim from Kistler provided technical feedback regarding installation of the sensors into the spindle housing. Mr. Jeffrey Watts from Weiss Spindle provided the new instrumented spindle. I would also like to thank the German assistants, Ben Schröter and Andrea Albrecht, and the French assistant, Hellier Deportes, who helped me during their work terms. Finally, I would like to acknowledge that the research is supported by UBC Graduate Fellowship, Korean-Canadian Scholarship, NSERC Canada, Boeing US, Pratt & Whitney Canada, Weiss Spindle Germany, and Kistler Instrumente Switzerland.

Dedicated to Susie and My Family

CHAPTER 1.

INTRODUCTION

1.1 MOTIVATION

Modern manufacturing industries such as aerospace, automotive, and die and mold demand cost-effective and accurate machining processes to manufacture various shaped metallic and composite parts. To meet the demands, machine tool builders are trying to boost overall manufacturing productivity through High Speed Machining (HSM) equipment that can rotate at up to 40,000 revolutions per minute. Therefore, the monitoring and adaptive control of machine tools has become the essential part of the machining processes. The monitoring of milling processes such as tool wear, tool failure, breakage, chatter vibration, and cutting forces will result in flexibility, reliability, productivity, and quality in milling operations. Use of reliable sensing methods to monitor machine tools can save machining time from 10 to 65 percent [Tonshoff 88]. Furthermore, the adaptive control of milling processes will significantly boost the overall productivity. However, commercial sensors available today do not effectively provide the required performance for the monitoring and controlling of the high speed machining processes [Ulsoy 93].

According to several researchers [Tlusty 83, Bryne 95, Altintas 94], the measurement of cutting forces is the most effective method for monitoring machine tools as well as the adaptive control of machining processes. For example, the cutting force magnitudes at tooth passing periods change when one of the milling cutter teeth chips or breaks [Altintas 94, Tarng 93]. The thrust component of the cutting force increases as the

flank wear of the tool accelerates [Kline 82, Koren 86, Choudhury 00]. In addition, the spectrum of the cutting force at a chatter frequency increases when the machine tool experiences chatter vibrations [Tlusty 85].

To measure milling forces, table dynamometers are commonly used where a workpiece is mounted on top of the dynamometer, which is clamped to the machine tool table. A typical table dynamometer consists of four three-component piezoelectric force transducers fitted under high preloads between two plates [Gautschi 71]. Even though the table dynamometers provide effective measurements of cutting forces, they are limited to use in laboratory settings due to limited workpiece sizes and mounting constraints. Moreover, the inertial force caused by the movement of the machine tool table and the removal of the workpiece material would distort cutting force measurements. In order to overcome the limitations imposed on commercial sensors such as table dynamometers, the Spindle Integrated Force Sensor (SIFS) system is developed to be used in production machines.

1.2 SCOPE OF RESEARCH

This study presents measurements of cutting forces in milling using a reliable, high bandwidth, and cost effective sensing mechanism. Since the bandwidth of the integrated force sensing system is limited by the dynamics of the overall spindle structure, a dynamic compensation of cutting force measurements obtained from the Spindle Integrated Force Sensor system is performed. The cutting forces are measured from the piezoelectric sensors embedded into the spindle housing, which has three dominant structural modes influencing the measurements. Based on the obtained model of the

spindle structure, a disturbance Kalman Filter is designed to estimate the high frequency harmonics of actual cutting forces applied at the tool tip [Park 03[a]]. An alternative method to measure cutting forces using a capacitance displacement sensor is also investigated. However, when the tool is replaced by an end mill having a different length, the transfer function changes, and this then needs to be re-measured. To prevent these costly and time consuming impact hammer tests, the mathematical coupling of the spindle structure with an arbitrary end mill is proposed to acquire the necessary dynamics to compensate distorted cutting forces at high frequencies using the proposed Kalman Filter scheme. The proposed Receptance Coupling (RC) method with the novel joint dynamics identification algorithm is used to successfully couple the dynamics of the spindle and an arbitrary tool [Park 03[b]]. The compensated forces measured from the Spindle Integrated Force Sensors are then used to control and monitor milling processes.

1.3 THESIS OUTLINE

This thesis is organized as follows.

In Chapter 2, the background and the literature review of sensors and cutting force measurements are presented. Various compensation schemes are also presented in order to accurately measure cutting forces. The second part of the chapter reviews substructure coupling methods. The coupling of substructures such as a spindle and an arbitrary tool can significantly save unnecessary impact hammer tests in order to find chatter stability regions. One of the difficulties associated with the coupling method is the identification of joint dynamics. The joint dynamics extraction literatures are also reviewed.

In Chapter 3, the experimental setups of the Spindle Integrated Force Sensors (SIFS) and the capacitance displacement sensor are illustrated. The piezoelectric force sensors are embedded into the existing spindle housing to measure cutting forces at the tool tip. The displacement probe is mounted with the bracket at the spindle housing. The basic principles of piezoelectric materials, as well as the experimental modal analysis measurement procedures using an impact hammer, are also presented. Furthermore, thermal effects on the experimented spindle are briefly analyzed.

In Chapter 4, the static and dynamic analyses of the spindle structure are examined. The spindle structure consists of various components such as bearings, a tool holder, and the integrated force sensors. The analytical static force transmissions to the spindle integrated force sensors are investigated. The static calibration procedure is also presented in order to acquire sensitivity factors of the integrated sensors and cross talk effects are also investigated. The dynamics of the integrated sensor are identified through the experimental modal analysis because the spindle dynamics distort the cutting forces obtained from the spindle integrated sensors. The spindle structure is also mathematically modeled through simple three Degrees of Freedom (DOF) lumped masses and springs based on experimentally acquired mode shapes.

In Chapter 5, the receptance coupling analysis is performed to couple the spindle and an arbitrary tool to predict the overall dynamics. The mathematical derivation of the receptance coupling method is illustrated. Furthermore, the identification of a joint dynamics algorithm is presented in order to successfully couple the two substructures. The receptance coupling procedures are verified through the experiments, and the contributions are summarized.

In Chapter 6, a disturbance Kalman Filter compensation scheme is formulated to compensate unwanted structural dynamics based on the experimentally measured model. The method also extends to the three direction force compensations using the forces measured from the Spindle Integrated Force Sensors (SIFS). The compensation scheme is also used to reconstruct cutting forces using the displacement sensor. The milling experiments are performed to verify the compensation method from 1000 rev/min to 12,000 rev/min.

In Chapter 7, the applications of the Spindle Integrated Force Sensors are examined. The adaptive control scheme based on the Generalized Predictive Control (GPC) algorithm is experimented in real time with the open architecture system to regulate the feed rate of the Computer Numerical Control (CNC) machine. In addition, the chatter and the tool breakage detection algorithms are also tested using the forces measured from the spindle integrated sensors.

Chapter 8 presents the summary of this study and ideas about possible future research.

CHAPTER 2.

BACKGROUND AND LITERATURE REVIEW

The objective of the thesis is to develop a spindle integrated force sensor system with a wide dynamic bandwidth that can be used in production environments. The past research efforts and difficulties involved in sensing mechanisms are presented. Among several sensing measurement methods, cutting force measurements in milling operations provide the most accurate information about the states of machines and tool conditions. A milling operation is an intermittent metal removal process which is periodic at tooth and/or spindle periods. In order to capture milling forces accurately at high rotational speeds, the bandwidth of a sensor must be greater than at least the third harmonics of a tooth passing frequency. Several compensation techniques, such as an inverse filter and an accelerometric compensation, are examined to increase bandwidths of sensors. These compensation methods require accurate knowledge of machine tool dynamics. However, when a tool is changed with a different length or material, the overall dynamics are changed as well. This dynamics change can be predicted through substructuring methods by mathematically combining dynamics of a spindle and a tool. The biggest challenge associated with substructuring methods is the identification of joint dynamics and this is investigated in this thesis.

2.1 SENSORS FOR MACHINING OPERATIONS

Tool monitoring and adaptive controls are becoming essential for today's manufacturing environment. This trend is owing to machines processing small batch size

products at high speeds, factories becoming autonomous due to a shortage of skilled workers, and protection of machines and workers from damage. Despite significant research in this area, a reliable, versatile, and practical on-line sensor is not available yet [Ulsoy 84, Spiewak 91]. In order for sensors to function properly in hostile machining environments, a sensor should be robust and should meet the following requirements [Tonshof 88, Byrne 95]:

- Causes no reduction in the static and dynamic stiffness of the machine tool
- Leads to no restriction of working space and cutting parameters
- Be wear and maintenance free, easy to replace, and cost effective
- Be resistant to dirt, chips, and mechanical, electromagnetic and thermal influences
- Works independent of tool or workpiece
- Reliable transmissions of signals

2.1.1 SENSING METHODS

Several sensing methods, such as a spindle motor current and power [Matsushima 82, Constantinides 87], a feed drive measurement [Altintas 92, Kim 96] which is used to emulate force signals, and vibration signatures [El-Wardany 96] are used to monitor tool conditions. The problems associated with these sensing methods are that they have very narrow frequency bandwidths and are prone to small disturbances. Acoustic Emission (AE) sensor methods have been one of the common methods used to monitor tool conditions especially for turning operations [Sampath 87, Choi 99, Moriwaki 80]. The Acoustic Emission (AE) sensor detects high frequency oscillations generated by plastic deformation when large strain energy is released as the bonds between metal atoms are

disturbed. However, AE approach is not applicable for the monitoring of milling operations because its signals are more sensitive to variations in the cutting conditions and noise [Yan 95]. In addition, differentiations between tool chipping and change in cutting conditions are difficult to detect due to the nature of the sensor. Tlusty [Tlusty 83], Byrne [Byrne 95], and Dimla [Dimla 00] reviewed various sensors and their limitations for machine monitoring processes using dimensional, cutting force, feed force, spindle motor, and AE sensors. Among these sensors, the measurement of cutting forces has been the most effective method to monitor tool conditions [Altintas 00, Altintas 89, Tarn 89, Lister 93, Tlusty 83, Moriwaki 80, Dimla 99, Tarng 94, Dornfeld 90]. Force sensors have considerably higher signal to noise ratios at a chip thickness above 0.1 micrometers compared to other sensors [Dornfeld 98].

2.1.2 INTEGRATED SENSORS

There has been a strong interest in developing a force-sensing mechanism built into a machine tool structure that is independent of workpiece size and cutting conditions to overcome the limitations of table dynamometers. Promess placed strain gauges on the outer ring of the spindle bearings, which measured the dynamic component of the cutting forces transmitted to the housing [Tlusty 83]. Jeppsson also developed strain gauge based sensors, which were located on the outer spindle housing [Jeppsson 00]. The strain gauge sensors have several limitations such as susceptibility to temperature changes, and difficulties in installing and salvaging failed sensors [Tu 95]. Koenig et al. [Koenig 78] designed a force measurement plate that is located between the turret head and the base plate of the lathe. Stein and Tu [Stein 94] proposed a state space model of the bearing

system to predict forces at the spindle bearings caused by the thermally induced preloads using strain gauges and thermocouples. However, the complexity of the proposed thermal model may hinder the usage in production machines. Others used displacement gap sensors such as capacitance, inductive probes, optical fiber, or LVDT to monitor machining operations [Kang 01, Matsubara 00, Yang 98, Suh 96, Jin 95]. The majority of the gap sensors has been limited for tool deflection monitoring because the sensors have coarse resolutions and are prone to feed and spindle vibrations. Kistler [Kistler 99], Aoyama et al. [Aoyama 98], and Smith et al. [Smith 98] developed rotating force and torque dynamometers. They have limited frequency bandwidths that are dependent on each tool holder used because the rotating systems increase both the inertia and dynamic flexibility of the measurement system. In addition, the rotating and torque dynamometers require dedicated tool holder interfaces that are suitable to be used in research laboratories. Thus, the rotating sensors attached to the tool holder are still limited to laboratory use.

In cooperation with several research laboratories, Kistler proposed a spindle integrated piezoelectric 'force ring', which is the basis of the sensor system presented in this thesis [Scheer 99, Jun 02, Park 02]. Instead of adding a force ring to the spindle housing, arrays of sensors are embedded into the bolt connections between the spindle flange and housing. The proposed spindle integrated sensor system satisfies the ideal sensor requirements [Tonshof 88, Byrne 95] since the system is not limited by the size of workpiece, and does not interfere with machining operations.

2.2 CUTTING FORCE MEASUREMENTS IN MILLING

The elucidation of milling operations is imperative for cutting force measurements. The milling operation is a periodic process with functions of spindle speeds, number of flutes, and immersion angles to remove a workpiece with desired tolerances. Figure 2.1 depicts the top view of the milling operation where h is the chip thickness, and ϕ is the immersion angle. The cutting forces are correlated to the chip thickness and the cutting edge geometry, and they are periodic at tooth passing intervals or spindle passing intervals if an end mill has run out.

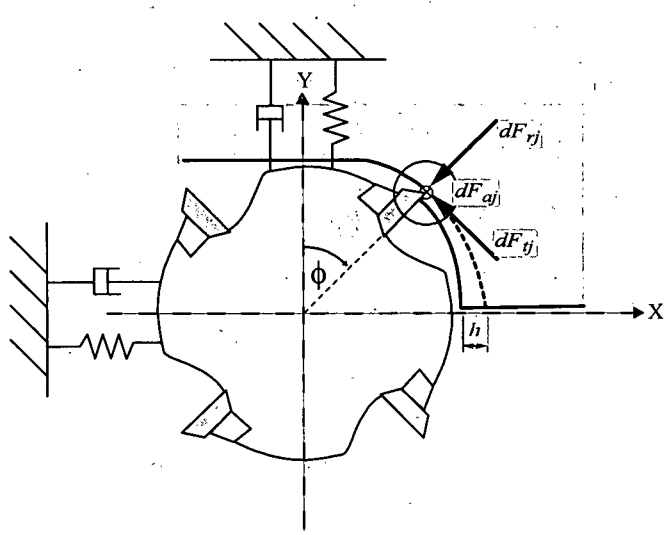

Figure 2.1 Milling Operation in X-Y plane

The tangential (dF_t), radial (dF_r), and axial (dF_a) forces with height (dz) can be expressed as [Altintas 00]:

$$\left.\begin{aligned} dF_t &= (K_{tc}bh + K_{te}b)dz \\ dF_r &= (K_{rc}bh + K_{re}b)dz \\ dF_a &= (K_{ac}bh + K_{ae}b)dz \end{aligned}\right\} \tag{2.1}$$

where b is the depth of cut, dz is the axial increment, K_{tc}, K_{rc}, K_{ac} are the cutting coefficients, and K_{te}, K_{re}, K_{ae} are the edge coefficients in the tangential, radial, and axial

directions, respectively. The chip thickness, h, changes with the immersion angle and the feed rate can be expressed as:

$$h(\phi, z) = c \sin \phi(z) \tag{2.2}$$

where c is the feed rate (mm/tooth). The cutting forces in the feed, normal, and axial directions are given as follows:

$$\left.\begin{aligned} dF_x(\phi) &= -dF_t \cos\phi - dF_r \sin\phi \\ dF_y(\phi) &= dF_t \sin\phi - dF_r \cos\phi \\ dF_z(\phi) &= dF_a \end{aligned}\right\} \tag{2.3}$$

Since the tangential, radial and axial cutting force directions are different for every immersion angle, the total feed, normal, and axial cutting forces can be formulated as;

$$\left.\begin{aligned} F_x &= \sum_{j=1}^{N} dF_{xj}(\phi_j) \\ F_y &= \sum_{j=1}^{N} dF_{yj}(\phi_j) \\ F_z &= \sum_{j=1}^{N} dF_{zj}(\phi_j) \end{aligned}\right\} \tag{2.4}$$

where N is the number of divisions in height. A typical cutting force is shown in Figure 2.2 with the three fluted cutter at 5000 revolutions per minute based on Eqs. 2.1-2.4. Consequently, the milling forces are periodic at a tooth passing frequency with up to three possible harmonics depending on the immersion angle. For example, for the cutting force measurements at 5000 rev/min, the tooth passing frequency of the corresponding speed would be $f_t = 5000\,rpm / 60\,s / \min \times 3\,teeth = 250\,Hz$. The accurate reconstruction of the forces would require three times of the tooth passing frequency which corresponds to 750 Hz. The frequency domain graph (see Fig. 2.2(b)) shows peaks at the tooth passing frequency, 250 Hz, and its harmonics. Thus, in order to capture the cutting

forces at 5000 rev/min with the three fluted cutter, the bandwidth of the sensors must be greater than the third harmonics (i.e., 750 Hz) of the tooth passing frequency.

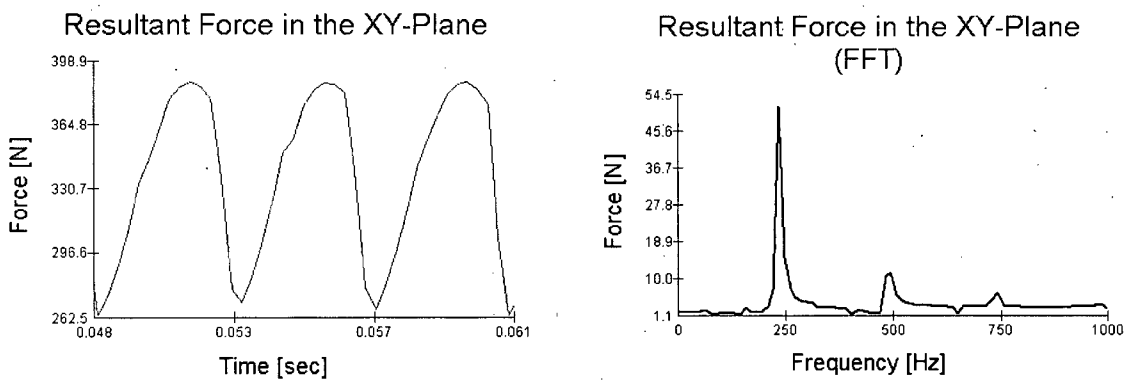

(a) Time Domain (b) Frequency Domain

Figure 2.2 Force measurements at 5000 rev/min in the time and frequency domains for the three fluted end mill

2.3 DYNAMIC COMPENSATION

Any force sensing system, which is away from the cutting point, has a limited bandwidth due to the structural dynamics of the mechanical elements located at a tool and a force measurement point. When the measured data is within the bandwidth of the force sensor, the cutting force data can be readily found by applying a calibration factor. However, when the frequency components of cutting force data, F_a (actual force), occur near the resonance, the force measurements from a spindle sensor, F_m (measured force), are distorted. The relationship between the measured and the applied forces is depicted as;

$$F_m = \Phi(s) \cdot F_a \tag{2.5}$$

where $\Phi(s)$ is the transfer function between the force applied at the tool tip and the force measured from the force sensor.

There have been several efforts to compensate the influences of structural dynamics to increase frequency bandwidths of sensors. The simplest method to compensate dynamics of the spindle to increase the bandwidth of the sensors is through the direct inversion of the transfer function (i.e., inverse filter). However, Patel, El-Wardany, and Chung [Patel 79, El-Wardany 96, Chung 94] reported that the inversion does not always exist, and the exact dynamics of the sensing system model have to be known to minimize the severe amplification of noise. The inverse filter of the force measured from the spindle integrated sensor is investigated to illustrate the arguments. The transfer function of the sensor system can be deduced to the following Linear Time Invariant (LTI) state space model;

$$\begin{aligned} \dot{x} &= A_s x + B_s u + w \\ z &= C_s x + D_s u + v \end{aligned} \tag{2.6}$$

where x is the state vector, $u = F_a$ is the input or the actual force applied to the tool, z = F_m is the measured cutting force from the spindle force sensor, A_s is the system matrix, B_s is the input vector, C_s is the output vector, D_s is the feed forward loop, w is the system disturbance, and v is the measurement noise. The output at time t can be shown by integrating the state space equation:

$$z(t) = C_s e^{At} x_0 + C_s \int_0^t e^{A(t-\tau)} B_s u(\tau) d\tau + C_s \int_0^t e^{A(t-\tau)} w(\tau) d\tau + D_s u(t) + v(t) \tag{2.7}$$

The following Single Input Single Output (SISO) transfer function can be obtained from the above equations;

$$z(s) = \Phi(s)u(s) + H(s)w(s) + v(s) \tag{2.8}$$

where

$$\begin{aligned} \Phi(s) &= C_s\left[sI - A_s\right]^{-1} B_s + D_s \\ H(s) &= C_s\left[sI - A_s\right]^{-1} \end{aligned} \tag{2.9}$$

The input (i.e., the actual force at the tool tip) can be expressed from Eq. 2.5 as:

$$u(s) = \Phi(s)^{-1}\left[z(s) - H(s)w(s) - v(s)\right] \tag{2.10}$$

In order to estimate the unknown input, the transfer function needs to be inverted then multiplied with the output as;

$$\hat{u} = \Phi(s)^{-1} z(s) \quad or \quad \hat{F}_a = \Phi^{-1}(s) \cdot F_m \tag{2.11}$$

where the noise (w, v) dynamics terms are neglected. The error can be derived from Eqs. 2.9 to 2.11 as;

$$\begin{aligned} e(s) &= \hat{u}(s) - u(s) \\ &= \Phi^{-1} z - (z - Hw - v)\Phi^{-1} \\ &= \Phi^{-1} Hw + \Phi^{-1} v \end{aligned} \tag{2.12}$$

where

$$\begin{aligned} \Phi(j\omega)^{-1} H(j\omega) &= \left[D_s^{-1} - D_s^{-1} C_s([j\omega I - A_s] + B_s D_s^{-1} C_s)^{-1} B_s D_s^{-1}\right] \\ &\quad \times \left[C_s[j\omega I - A_s]^{-1}\right]; \\ \Phi(j\omega)^{-1} &= D_s^{-1} - D_s^{-1} C_s([j\omega I - A_s] + B_s D_s^{-1} C_s)^{-1} B_s D_s^{-1} \end{aligned} \tag{2.13}$$

Eq. 2.13 can be obtained through using the matrix inversion lemma. To investigate the effects of the high frequency noise, frequency (ω) is assumed to be approaching infinity by making the Laplace operator s equal to $j\omega$ where j is the imaginary component. Typically, force sensing systems do not have feed forward loop D_s. As a result, the error becomes infinite as the frequency increases to infinity which is shown in Eq. 2.14:

$$
\begin{aligned}
e(j\omega) = & \left[D_s^{-1} - D_s^{-1}C_s([j\omega I - A_s] + B_s D_s^{-1} C_s)^{-1} B_s D_s^{-1}\right] \\
& \times \left[C_s[j\omega I - A_s]^{-1}\right] w \\
& + \left[D_s^{-1} - D_s^{-1}C_s([j\omega I - A_s] + B_s D_s^{-1} C_s)^{-1} B_s D_s^{-1}\right] v
\end{aligned}
$$

$$
\begin{aligned}
e(j\omega)\big|_{\omega\to\infty} = & \left[D_s^{-1} - D_s^{-1}C_s([j\infty I - A_s] + B_s D_s^{-1} C_s)^{-1} B_s D_s^{-1}\right] \\
& \times \left[C_s[j\infty I - A_s]^{-1}\right] w \\
& + \left[D_s^{-1} - D_s^{-1}C_s([j\infty I - A_s] + B_s D_s^{-1} C_s)^{-1} B_s D_s^{-1}\right] v = D_s^{-1} v
\end{aligned}
\tag{2.14}
$$

$$
e(j\omega)\big|_{\omega\to\infty} = \infty \quad \text{when } D_s = 0
$$

The errors between the estimated and the actual forces would be significantly influenced by the system and measurement noise (w, v). Therefore, the inverse filter may not be appropriate for a structure compensation scheme because the dynamics of the sensing system model have to be known exactly to minimize severe amplification of noises.

If a sensor mounted on a spindle or on a machine table moves at rapid acceleration, inertial forces are need to be compensated to acquire accurate cutting forces. Tlusty et al. [Tlusty 87], Tounsi et al. [Tounsi 00], and Knight et al. [Knight 71] have performed the accelerometric compensations of table dynamometers by compensating unwanted forces by estimating inertial and damping errors using accelerometers, as shown in Figure 2.3. In the figure, F_a is the applied cutting force, F_m is the measured force, k is the stiffness, c is the damping coefficient, and x_1 and x_2 are the displacements. The force sensors act as the spring between the top plate and the base plate. Therefore, the cutting forces are measured by the dynamometer, F_m, as the spring constant multiplied by the strains between the two plates as shown in Eq. 2.15. The aim is to measure the applied force, F_a, by adding the inertial and damping forces with the measured force from the table dynamometer. The shortfall of this technique is that the identification of mass and damping parameters is difficult, and the compensation is

geared toward to the single Degree of Freedom (DOF) system (i.e., table dynamometers), rather than multi DOF systems (i.e., Spindle Integrated Force Sensors).

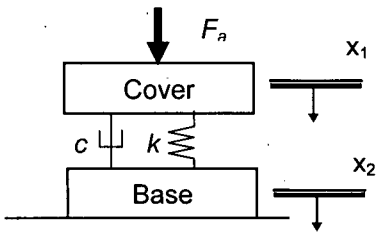

Figure 2.3 Schematics of a table dynamometer

$$m\ddot{x}_1 + c\dot{x}_1 + k(x_1 - x_2) = F_a$$
$$\left[m + \frac{c}{jw}\right]\ddot{x}_1 + F_m = F_a \tag{2.15}$$

Chung and Spiewak [Chung 94] adaptively compensated the workpiece attached to the table dynamometer using the inversion of the "equivalent system" approach. They obtained the dynamics of the dynamometer from the cutting force signals using the adaptive Infinite Impulse Response (IIR) filter based on the identification using the Box-Jenkins likelihood function. Stein et al. [Stein 88] investigated the problem by measuring the armature voltage and simultaneously observing states with unknown inputs through transformations based on the singular value decomposition. The biggest challenge with this approach is that accurate measurements of the derivatives of outputs are difficult. There has not been much work reported in compensating the force measurement system integrated to the spindle with multi-degrees of freedom dynamics. In this thesis, a disturbance Kalman Filter is used to compensate the dynamics of the spindle structure to reconstruct cutting forces at the tool tip. The disturbance Kalman Filter considers the system and measurement noise to offset the structure modes [Park 03[a]].

2.4 SUBSTRUCTURE COUPLING

When spindle integrated sensors are located away from the tool tip, the actual cutting force has to transmit through various masses, springs, and damping elements to the integrated sensors. These elements distort cutting forces measured from the spindle sensors. In order to accurately reconstruct the cutting forces from the sensors, the spindle dynamics are required. However, the transfer function of the force experienced at the end mill and measured at the spindle integrated force sensor varies depending on the stick out length and the material of the end mill. Therefore whenever a tool is changed, an experimental impact modal test needs to be repeated. Performing the impact modal tests require trained personnel and results in a loss of valuable machine time. Thus it is very desirable to model the stationary machine spindle with arbitrary cutters to minimize the costly impact tests. Furthermore, the coupling of substructures would significantly benefit chatter suppression methodologies where the dynamics at the tool tip are needed. Chatter is known as self-excited vibrations due to interactions between the tool and the machine. If the cutting conditions, namely the depth of cut and the spindle speed, are not selected properly, milling operations may become unstable with severe chatter or self-excited vibrations causing tool chipping, rough surface finish, and overload on a spindle drive and bearings. Regardless of varying approach, the dynamic compensation and chatter stability expressions require accurate measurements of Frequency Response Functions (FRFs) at the tip of the tool when it is attached to the tool holder-spindle assembly. Substructure coupling methods enable coupling of the spindle and arbitrary tool dynamics to predict the overall structure dynamics so that the compensation can be carried out without performing extensive experimental modal analysis.

2.4.1 SUBSTRUCTURING METHODS

The prediction of the response of the assembly by combining the responses of its components (i.e., substructures) has been an interest for a long time. The approaches taken to achieve this goal can be classified into two major categories: Component Mode Synthesis (CMS) and Receptance Coupling (RC). In the CMS technique, the dynamic responses of the components are projected from the physical space to the constrained space [Craig 81], in which usually dominant modes of the components are given importance to achieve computational efficiency. In the Receptance Coupling method, the Frequency Response Functions (FRFs) of the components, obtained analytically or experimentally, are used directly to obtain the response of the assembly. Clearly, the disadvantages of the CMS are the requirement of very accurate modal data, the introduction of errors due to curve fittings of the FRFs, and the residual effects of higher modes which degrade the outcome. On the other hand, the experimentally obtained FRF data are inevitably smeared with measurement noise for the RC method. The comparison of the two methods indicates that the Receptance Coupling method is more suitable to combine experimentally obtained dynamics to couple the spindle and an arbitrary end mill.

2.4.2 JOINT IDENTIFICATION

Even when all such data are available, the structure is assembled from the components by means of joints. These joints contribute to the dynamics of the system, sometimes substantially. Many researchers [Wang 90, Tsai 88, Ren 95, Liu 00, Jetmundensen 88] have addressed joint parameter identifications in the past two decades.

The starting step for this problem is to formulate the receptance coupling equations based on the inverse problem. Many formulations are presented for coupling receptances, but they all amount to different arrangements of the same set of equations. Tsai and Chou [Tsai 88] calculated joint properties for a single bolt joint by minimizing the squares of the errors through solving the sensitivity equations. They reported that using data from different frequency ranges yielded different results. To deal with the amplification of noise in matrix inversions, Wang and Liou [Wang 90] combined some elements of the receptance matrix in equations which have the advantage of not containing any matrix inversion. Ren and Beards [Ren 93] proposed a similar but more general formulation in which the joint impedance matrix can include a mass matrix as well as stiffness and damping matrices. They solved unknown joint parameters in the least square sense and applied various weighting methods to deal with the ill-conditioning of the coefficient matrices. Ren and Beards [Ren 95] solved this problem through the nonlinear optimization technique. Recently, Liu [Liu 00] used the neural network approach to solve the joint identification problem. It is noteworthy to mention that a considerable part of research about joint identification has been related to machine tools in one way or another. A recent study by Schmitz et al. [Schmitz 00, 02] is particularly related to the stability of machining operation using the coupling method to find the response of the assembled tool-spindle system. They, however, neglected the rotational degrees of freedom dynamics, and their joint parameters seem to have been obtained by trial and error rather than a systematic approach.

Even when a joint is assumed to be rigid, Rotational Degrees of Freedom (RDOF) dynamics are paramount for the coupling of substructures. The difficulty in obtaining

reliable RDOF responses has been a major obstacle in structural mechanics analysis over the years, and it has been the subject of numerous studies [Liu 00, Duarte 00, Avitabile 02]. There have been efforts to measure the angular response of the structure using angular transducers or laser vibrometers, but the high cost of such instruments has prohibited their extensive use in practice. As a result, attempts have been made to derive the rotational responses through a mathematical manipulation of the experimentally obtained translational FRFs. One of the mathematical methods used extensively in the literature is the finite difference method which finds the RDOF response functions from the translational FRFs of two or three closely spaced accelerometers. [Chen 85, Duarte 00]. However, noise present in the measurements and impractical placements of multiple accelerometers hinder the accuracy of these methods in acquiring RDOF FRFs.

To combine the dynamics of the spindle and an arbitrary end mill, an improved Receptance Coupling technique is developed in this study [Park 03[b]]. The end mill is modeled using a standard Finite Element (FE) model of a cylindrical beam, and the FRF of the spindle-tool holder system is identified using impact modal tests at the blank cylinder free end, which is mounted with a set length to the tool holder. The RDOF joint dynamics are indirectly identified using translational responses measured from a set of two blank cylinders.

CHAPTER 3.

SPINDLE INTEGRATED SENSOR SYSTEM SETUP

The experimental setup for the Spindle Integrated Force Sensor and the capacitance displacement system is described in this chapter. The proposed Spindle Integrated Force sensing system is installed between the spindle housing and the spindle flange at the bolt holes which can be easily retrofitted for existing machining centers. The system consists of three pairs of piezoelectric force sensors to measure forces in three directions. The piezoelectric force sensors have higher bandwidths and robustness compared with other sensing mechanisms such as strain gauges. Since the addition of the sensors may alter the overall dynamics of the structure, the experimental modal analyses are performed before and after the installation of the sensors. Similarly, the capacitance displacement probe is mounted on the outside of the spindle housing with a mounting bracket to measure displacements between the flange of the spindle and the probe. The displacement measurements can be interpreted as forces through the calibration factor. A brief Experimental Modal Analysis (EMA) procedure is also illustrated. Moreover, the thermal effect of the experimented spindle structure is examined.

3.1 DESIGN AND EXPERIMENTAL SETUP OF THE SPINDLE SENSORS

The Spindle Integrated Force Sensors and the capacitance displacement sensor are installed on a three-axis CNC vertical machining center (Fadal VMC40) where the power and torque of the motor are 11.2 kW and 217 Nm, respectively. The spindle housing of the machining centre is retrofitted by Electro Discharge Machine (EDM) to accommodate

three pairs of piezo-electric sensors as shown in Figure 3.1. The sensors are mounted on the bolt holes where the spindle flange is connected to the casted spindle housing by cap screws with 55 Nm of torque. The location of the sensors is ideal for force measurements because the cutting forces are transmitted to the stationary housing through the sensors from the rotary spindle shaft and the tool through bearings [Scheer 99]. Two pairs of shear sensors (Kistler 9145) are used to measure lateral forces in the feed (X-axis) and normal (Y-axis), and a pair of compression sensors (Kistler 9135) are used to measure the axial (Z-axis) forces in milling. The sensors are arranged to be opposite each other to compensate the unequal deformation and to improve the sensitivity of the force measurements, as shown in Figure 3.1 (b). The charge signals coming from each sensor are added and amplified by the charge amplifiers (Kistler 5010) to the voltage signals. In addition, accelerometers (PCB 353B31) are attached to the spindle housing in each direction where the force sensors are located in the housing to measure vibrations (see Figure 3.2 (b)).

A capacitance type displacement sensor is attached externally to the front of the spindle system using a bracket, which is clamped around the spindle housing (see Figure 3.1(a)). The cylindrical flange of the spindle shaft is used as a target surface for the sensor. The selected displacement sensor is a high-resolution capacitive sensor (Lion Precision type C1-A/B) for non-contact displacement measurement where the charge signal is converted by the amplifier (Lion Precision PM755D). The sensitivity factor of the sensor is 21.4 mV/μm, and the gap between the target and the sensor is 1.016 mm (see Figure 3.1 (c)). The displacement resolution and the measurement range of the sensor are 50 nm and 2250 nm, respectively.

The spindle encoder captures every spindle rotation by deflecting the photodiodes. The encoder is used to synchronize the spindle roundness errors. The signals from various sensors are first fed into an anti-aliasing filter (Krohn Hite 3905B) which is a low pass filter (i.e., fourth order Butterworth filter) with the cut off frequency at the Nyquist frequency (i.e., half of the sampling frequency). From the filter, the signals are fed into an in-house developed data acquisition system (MalDAQ^{TM}) with the data acquisition hardware (National Instrument DAQ). The pictorial view and schematics of the experimental setup is illustrated in Figure 3.2. A 7/24 taper (CAT 40) type hydraulic holder (Kenametal CV40HPHC) is used with 19.05 mm (3/4 inch) diameter helical end mills for the experimental cutting tests. A block of aluminum Al7050-T6 is used as a workpiece material during the experiments. The test workpiece is mounted on top of the table dynamometer (Kistler 6255B), which serves as the reference force sensor.

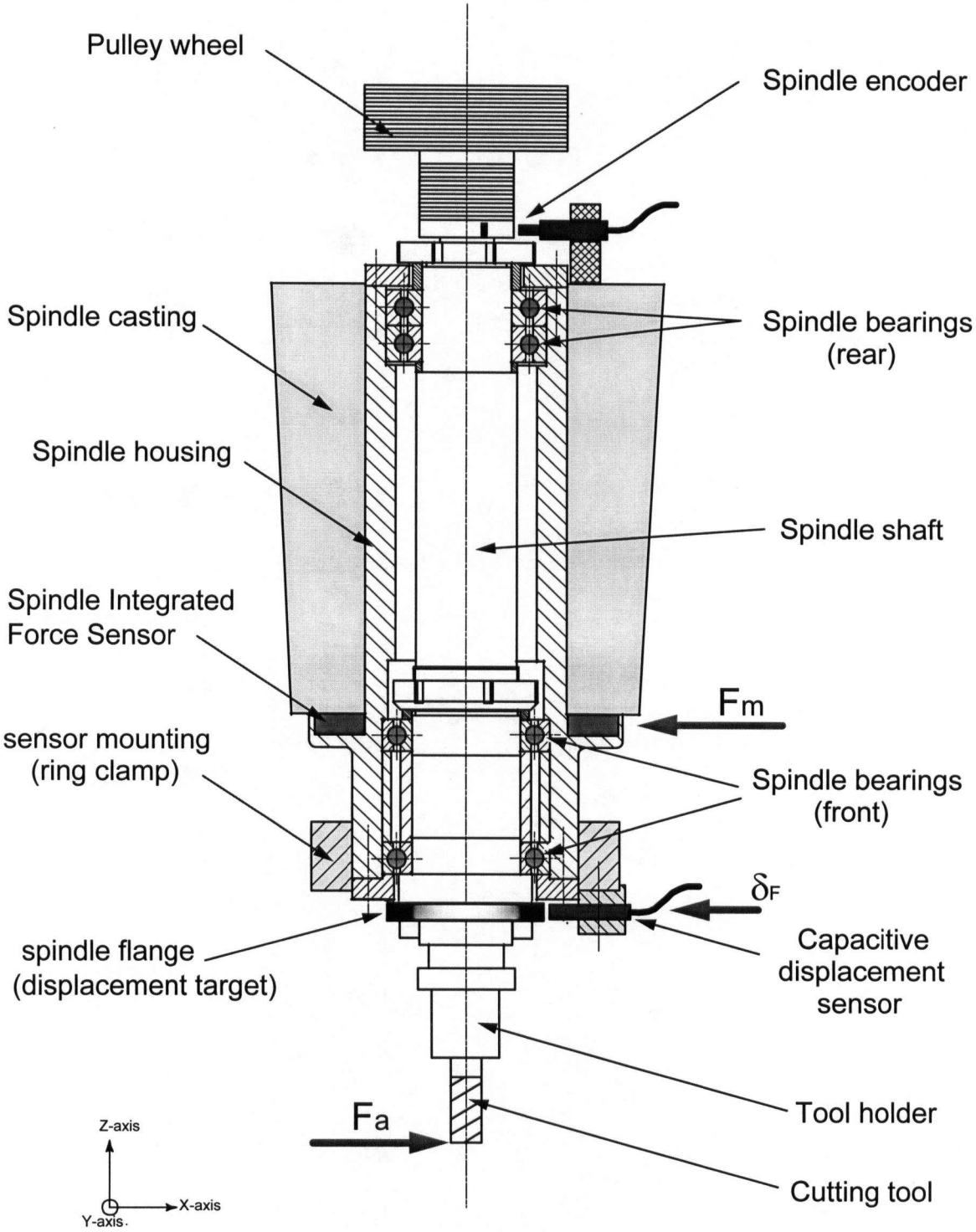

(a) Spindle Assembly of Spindle Integrated Force and Capacitance Displacement Sensors

(F_a = applied forces at the tool tip, F_m = measured forces from the Spindle Integrated Force Sensor, and δ_F = displacement from the capacitance sensor)

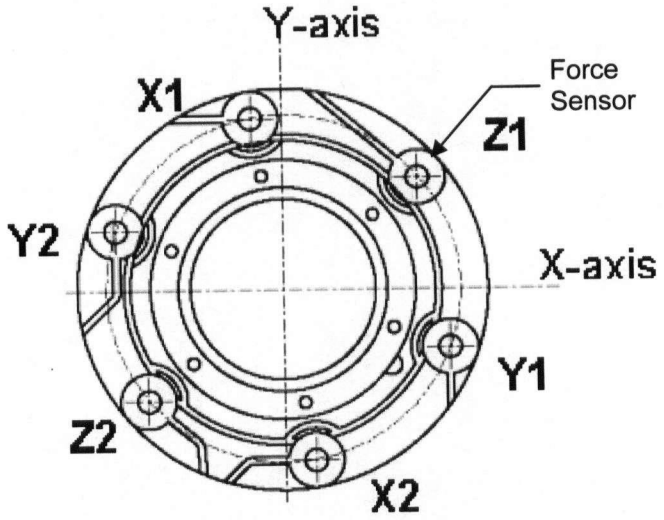

(b) Arrangement of the Spindle Integrated Force Sensors - Top View

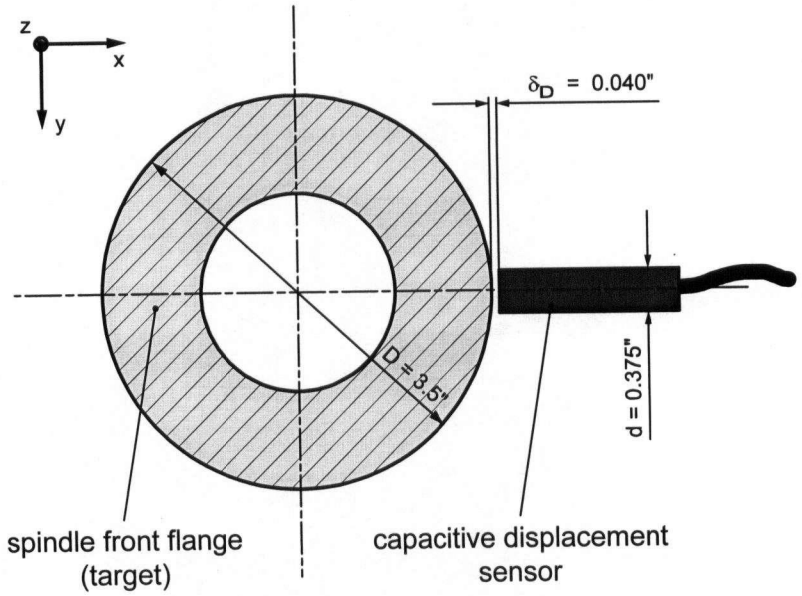

(c) Capacitance Sensor - Top View

Figure 3.1 Schematics of the Spindle Integrated Force Sensor and Capacitance Displacement Sensor Systems

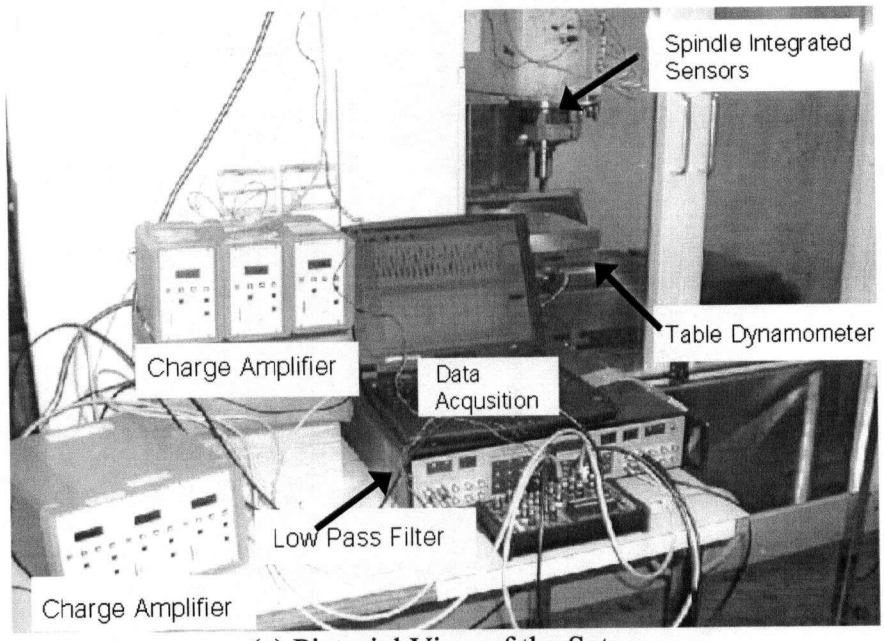

(a) Pictorial View of the Setup

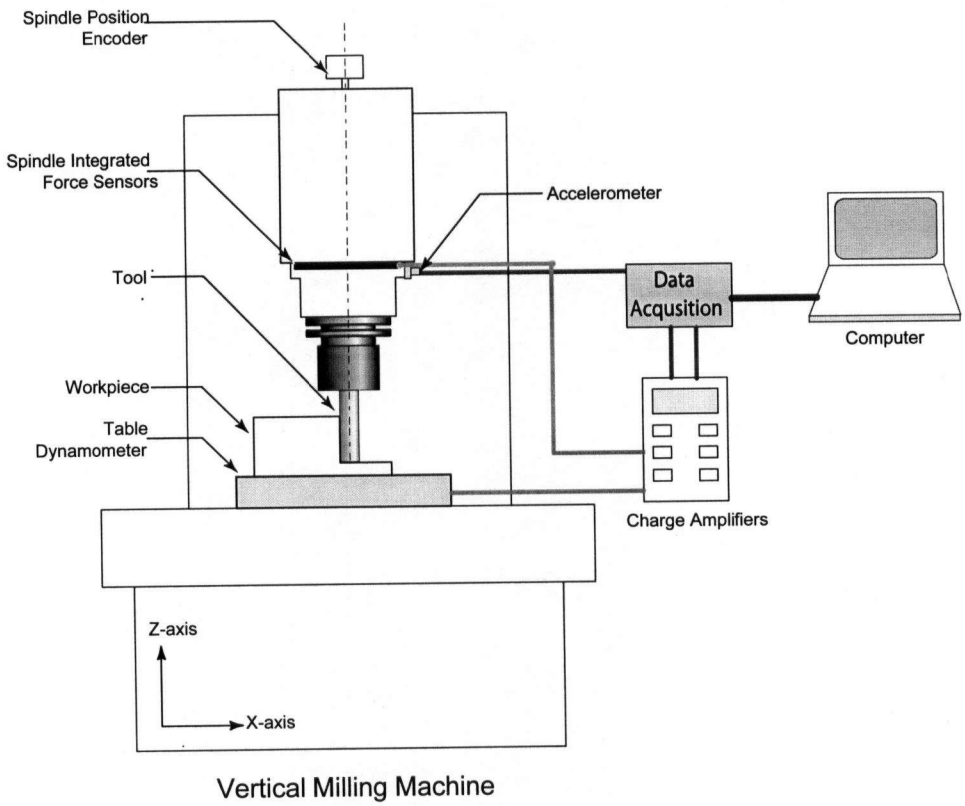

(b) Schematics of the Overall Setup

Figure 3.2 Experimental Setup

3.2 PIEZOELECTIRC TRANSDUCER

Since the piezoelectric force sensors are used in the proposed sensing system, principles of piezoelectric phenomenon are examined. The force sensors integrated to the spindle consist of both compression and shear elements. A typical material used for force sensors is quartz crystals. These crystals act as true precision springs depending on how the materials are stressed. Figure 3.3 shows electric behaviors of piezoelectric materials when stresses are applied through compression and shear.

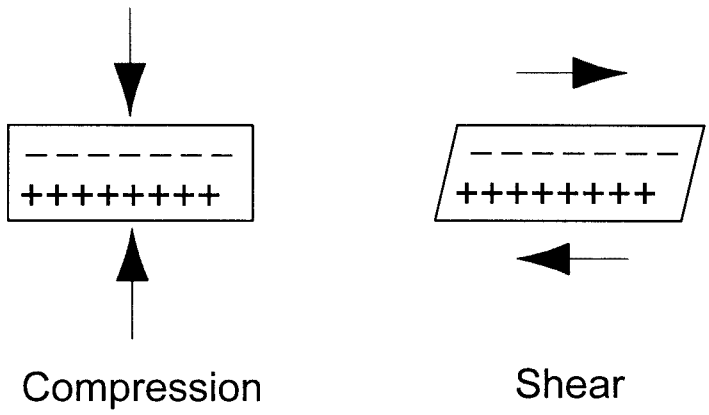

Figure 3.3. Piezoelectric material configuration

Piezoelectric force sensors undergo strain deformations when force is applied. When the strain deformation occurs, the quartz crystals generate charge signals proportional to strain or input force. These charge signals are then fed into external charge amplifiers through low noise cables. The charge amplifiers convert the charge signals to the usable voltage signals which can be fed into a data acquisition system. One thing to note about piezoelectric sensors is that they can only measure dynamic events because charge signals decay with some time periods (depending on the time constant set on the charge amplifiers). Therefore, the static measurements can be measured at a very short period of

time in quasi-static sense. The benefits of piezoelectric transducers over resistance based strain gauges are that they have wider frequency bandwidths due to very high stiffness and are resistant to thermal drifts. Further details on piezoelectric transducers can be found in the reference [Clark 98].

3.3 STIFFNESS CHANGES DUE TO THE INSTALLATION OF THE SPINDLE INTEGRATED FORCE SENSORS

One of the requirements for the ideal sensor system is that there must be minimum reduction in the static and dynamic stiffnesses of the machine tool due to the installation of the spindle integrated sensors. In order to examine the differences in static and dynamic stiffnesses, the impact modal tests are performed before and after the installation of the sensor system. This test is performed using a large instrumented impact hammer to investigate the stiffness change up to 1000 Hz. Figures 3.4 and 3.5 depict the transfer functions before and after the installation at the spindle housing location in X and Y directions, respectively. A new mode at 230 Hz appears after the installation of the sensor in X direction as shown in Figure 3.4. This additional mode may have emanated from the force sensors which act like springs between the flange of the housing and the spindle casting. Whereas for Y direction shown in Figure 3.5, the dynamic stiffness decreased at 230 Hz after the installation of the sensor. The reduction in the dynamic stiffness (i.e., $2 \times k \times \zeta$) may have resulted from a decrease in the contact surface between the housing flange and the spindle casting. In addition, the results show no change in the static stiffness (i.e., the zero frequency regions of the FRFs) but a slight change in the dynamic stiffness. The dynamics are unchanged after 500 Hz. Based on

the observations, the modification of the spindle housing to accommodate the spindle integrated sensors does not deteriorate the overall dynamics significantly.

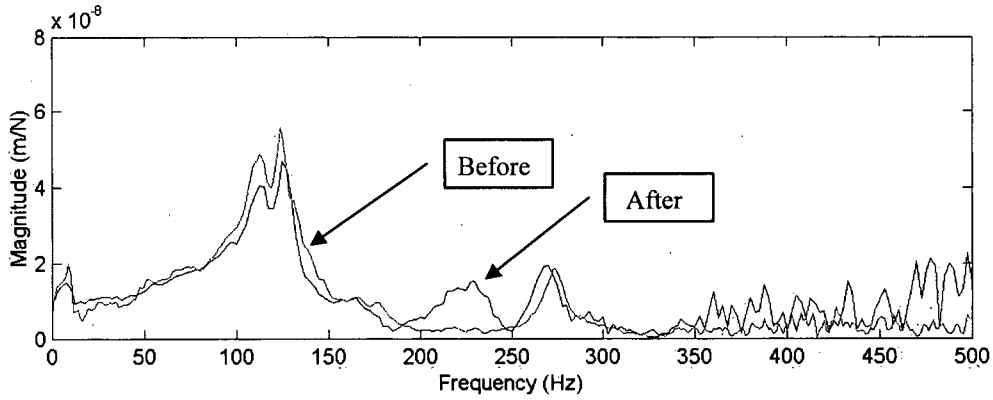

Figure 3.4 Comparison of the transfer functions before and after the installation of the SIFS in X direction

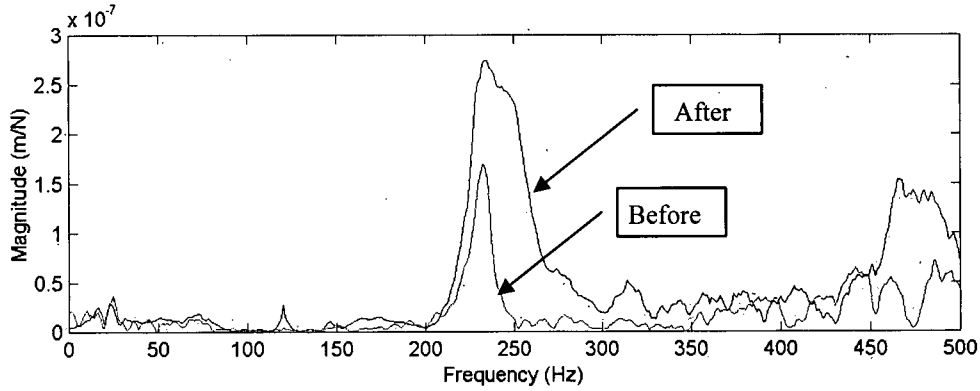

Figure 3.5 Comparison of the transfer functions before and after the installation of the SIFS in Y direction

3.4 EXPERIMENTAL MODAL ANALYSIS (EMA)

In order to acquire structure dynamics (i.e., frequency response functions), experimental modal analyses need to be carried out because the Frequency Response Functions (FRFs) implicitly contain the system characteristics by means of modal parameters, such as natural frequencies, stiffness, and damping coefficients. The impact modal test is performed by exciting the structure by an impulse of an instrumented force hammer with a wide frequency bandwidth and measuring vibrations through either an accelerometer or a laser displacement sensor, as shown in Figure 3.6.

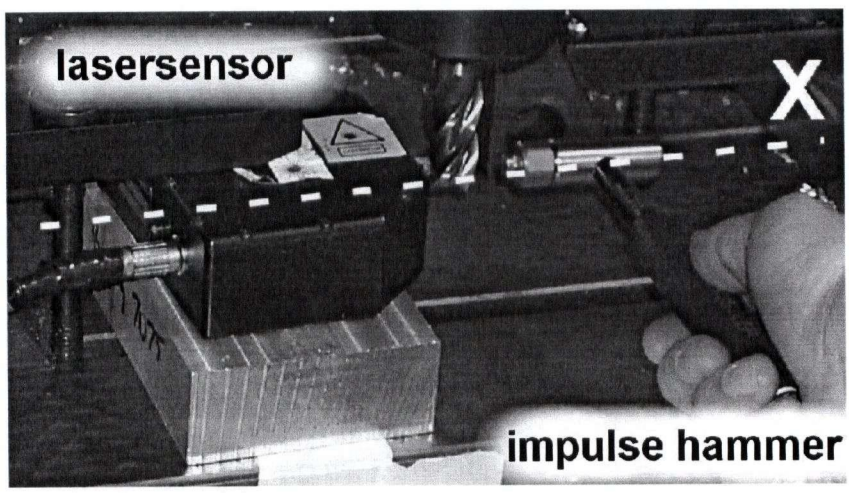

Figure 3.6. Impact hammer test diagram [CutPro Manual]

Once the measurements are simultaneously obtained, the time domain signals are transformed to frequency domain through discrete Fast Fourier Transformation (FFT);

$$F(j\omega) = \frac{1}{N}\sum_{n=0}^{N-1} f(nT)\left[\cos\frac{2k\pi}{N}n - j\sin\frac{2k\pi}{N}n\right],\ k = 0,1,\ldots,\frac{N}{2} \tag{3.1}$$

$$X(j\omega) = \frac{1}{N}\sum_{n=0}^{N-1} x(nT)\left[\cos\frac{2k\pi}{N}n - j\sin\frac{2k\pi}{N}n\right],\ k = 0,1,\ldots,\frac{N}{2}$$

where F is the force applied at the tool tip, X is the displacement measured from the vibration sensor, ω is the frequency in rad/sec, N is the number of samples, and T_s is the sampling time. In order to minimize noise, the power spectrum is evaluated by multiplying conjugates of the frequency domain signals, and the spectrum signals are then divided to acquire the transfer function (H);

$$H(j\omega) = \frac{X(j\omega)}{F(j\omega)} = \frac{S_{XF}(j\omega)}{S_{FF}(j\omega)} = \frac{X(j\omega)F^*(j\omega)}{F(j\omega)F^*(j\omega)} \tag{3.2}$$

where $*$ is the complex conjugate. The Frequency Response Functions (FRFs) can be obtained based on the signal processing procedures as shown in Figure 3.7. The detailed information on the spectral analysis can be found in [Harris 88, Ljung 94].

Similarly, the Experimental Modal Analysis (EMA) using the impact hammer is performed to acquire the transfer function ($\Phi(s)$), where the input is the impact force applied at the tool tip (F_a) and the output is the force from the Spindle Integrated Force Sensor system (F_m) derived by averaging the frequency response curves obtained from several successive impact tests to increase robustness of the measurements. The important things to look for during the experimental modal analysis are that the impact hammer hit or input has the sufficient energy contents at the desired frequency range and the coherence of the measurements should be close to one which indicates cleanliness of the output signal due to the input signal. The modal parameters such as natural frequencies, stiffness, and damping ratios can be identified using the least square method or the non-linear iteration method [Campomanes 98].

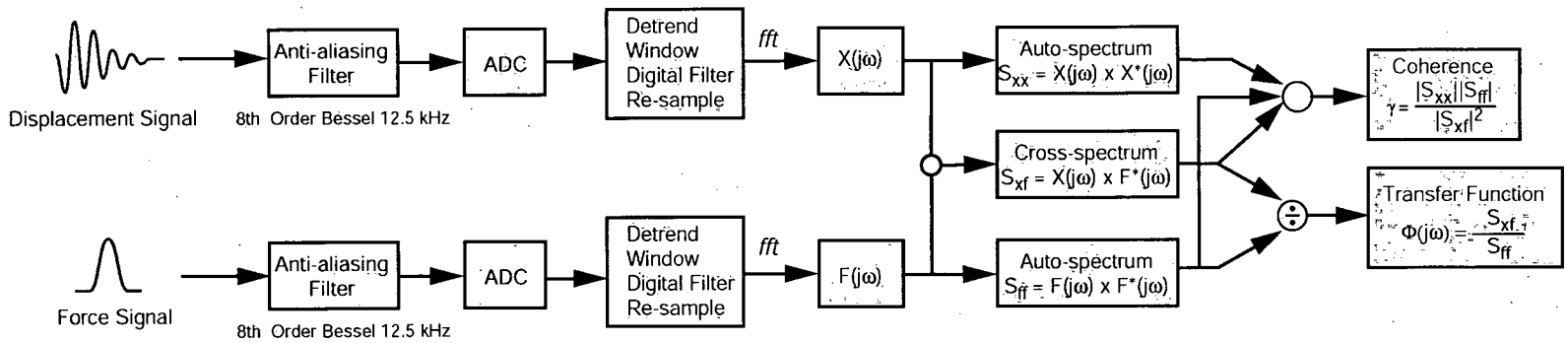

Figure 3.7. Frequency response function signal processing block diagram

3.5 THERMAL EFFECTS

Thermal effects of the spindle and the integrated sensors can be a concern if the temperature is not effectively controlled. Some spindles may experience severe thermal growth when they are not cooled effectively [Jun 02]. The thermal growth changes the preloads on the force sensors leading to drift, and increases the bearing preloads which shift the modal frequencies.

3.5.1 THERMAL EFFECTS ON THE SPINDLE INTEGRATED FORCE SENSORS

To investigate the thermal effects on the Spindle Integrated Force Sensors, the changes in the air cutting force magnitudes are examined from the time zero to one hour when the machine rotates at 1000 revolutions per minute. The spindle integrated sensors exhibit periodic oscillations due to spindle run-out at each rotation. Figure 3.8 shows the initial air cutting forces (i.e., $t = 0$ min.) from the spindle integrated sensor and the table mounted dynamometer. Figure 3.9 depicts the air cutting forces after a one hour period. By observing both figures, the cutting forces from the spindle sensors and the table dynamometer did not change after a long period of time (i.e., 1 hour), which verifies that the thermal growth of the spindle is negligible. This is particularly true for the experimented spindle because of the cooling mechanism where coolants are controlled through the outer jacket of the spindle housing to maintain the temperature. Furthermore, the dual sensors with 180 degree opposite locations (see, Figure 3.1 (b)) are able to cancel out the uniform thermal growth pressure on the spindle-housing interface.

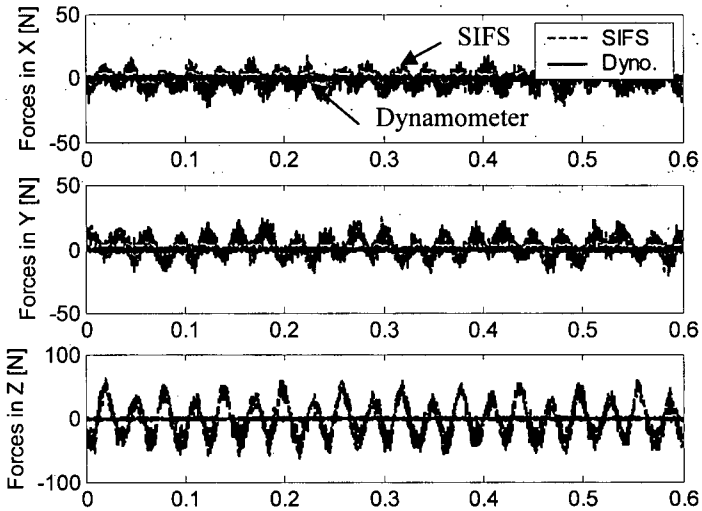

Figure 3.8. Initial air cutting force in X, Y, and Z directions using the spindle integrated sensors and the table dynamometer at 1000 rpm

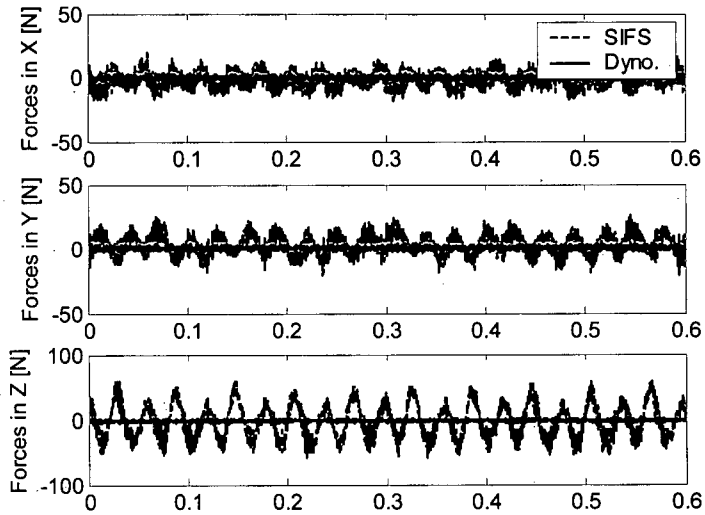

Figure 3.9 Air cutting force in X, Y, and Z directions using the spindle integrated sensors and the table dynamometer after 1 hour at 1000 rpm

3.5.2 THERMAL EFFECTS ON THE DISPLACEMENT SENSOR

Similar to the force sensors, the thermal effects of the capacitance displacement sensor are investigated by measuring the transfer functions through the impact hammer tests before and after the machine is warmed up. Figure 3.10 illustrates the transfer functions when the time is 0 minute (i.e., when the spindle is cool) and when the time is 60 minutes (i.e., when the spindle is warmed). Based on the figure, the transfer functions did not change after running the machine for more than an hour. This also indicates that the static stiffness of the displacement sensor remains the same even after the machine is warmed up. The air cutting displacements are also measured from time 0 minute to 60 minutes for every 10 minutes increment. The magnitudes of the air cutting displacements remained the same even after 60 minutes. The mean values and variances of the air cutting displacements are shown in Table 3.1. Therefore, the thermal growth of this particular spindle was not a big concern, since the air cutting measurements did not change even after running the machine for a period of more than an hour.

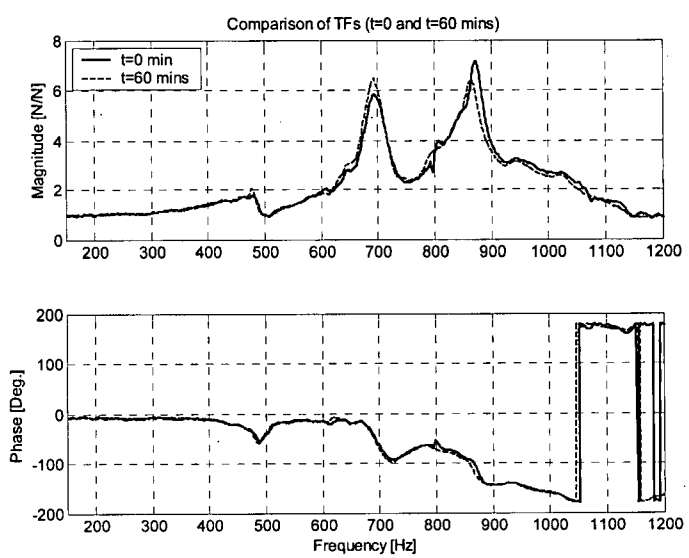

Figure 3.10 Comparison of the Transfer Functions before and after machining

Table 3.1 Mean Values and Variance of the Displacement Sensor during the Air Cutting from time 0 to 60 minutes

Time (min.)	0	10	20	30	40	50	60
Mean (1e-4 m)	-0.2600	-0.2580	-0.2607	-0.2588	-0.2587	-0.2613	-0.2611
Variance (1e-10 m)	0.1510	0.1500	0.1506	0.1501	0.1493	0.1490	0.1495

To further explore the thermal effects on the displacement sensors, a heater fan is used to stimulate additional heat at the spindle flange location (i.e., target location). When the temperature increases, the spindle flange expands which leads to an enlargement of the spindle flange diameter. The spindle is made out of steel with a thermal expansion coefficient, α_{Steel}, to be from 4.67e-6 to 8.33e-6 deg.C^{-1}. The thermal expansion length, L, of a metal object can be calculated as;

$$\Delta L = \alpha_{steel} \cdot \mathrm{L} \cdot \Delta T \tag{3.3}$$

where ΔT is the temperature difference. For the example of the spindle flange, an increase in temperature of 1 degree Celsius expands the spindle flange diameter (i.e., 88.9 mm) from 0.42 μm to 0.74 μm, which translates to approximately 21 N to 37 N of additional forces. Figure 3.11 illustrates the temperature influences of the spindle flange by heating the spindle with the heater fan while measuring variations in the displacement signal and flange temperature. Based on the graph, an increase in the temperature by 10 degrees Celsius would result in an increase up to 8 microns. The temperature compensation may be required when the temperature of the spindle flange significantly increases (i.e., 10 deg.C. changes). The thermal influence on the displacement sensor is elevated because only one sensor is used to measure instead of dual sensors in the SIFS case. If two

identical sensors located 180 degrees opposite of each other measure the displacement, the thermal effects will be minimal.

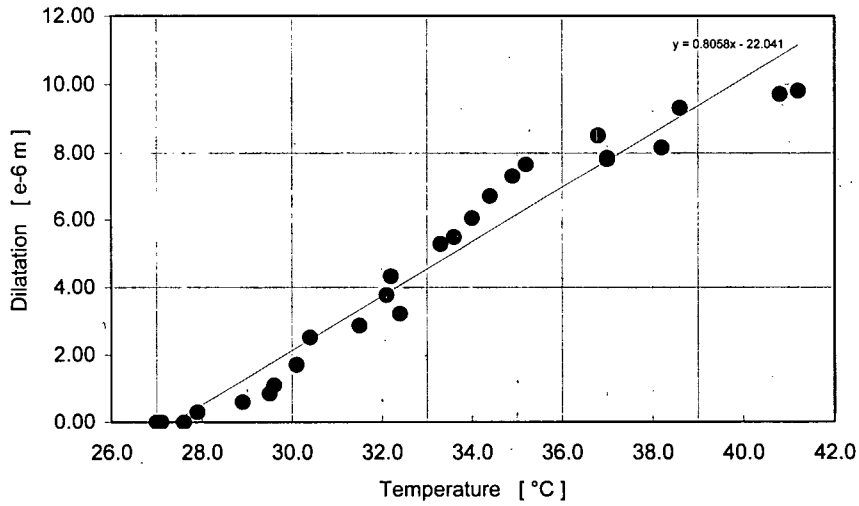

Figure 3.11 Variations in the gap between the displacement sensor and the spindle flange due to induced heat

3.6 CONCLUSION

The design and installation of the Spindle Integrated Force Sensor and the capacitance displacement sensor systems are presented in this chapter. The spindle integrated sensors are embedded between the spindle flange and the housing with preloads. The piezoelectric based sensors generate charge signals relative to the strains generated due to forces at the tool tip. The charge signals are then converted to voltage signals through the charge amplifiers. The proposed sensing mechanism can be implemented on existing machines without significantly affecting the dynamics of the overall machine. Likewise, the capacitance displacement probe can be used to interpret displacements to forces and it can be easily mounted on the outside of the spindle

housing using the mounting bracket. Experimental Modal Analysis (i.e., impact modal test) is also examined because it is important to understand the machine tool by representing the complex system through mass, stiffness, and damping elements so that behaviour can be predicted. In addition, thermal effects of the experimented spindle are found to be negligible mainly as a result of the cooling system which runs in the outer layer of the spindle. However, the displacement sensor may be more susceptible to temperature fluctuations if not cooled effectively.

CHAPTER 4.

STATIC AND DYNAMIC ANALYSIS OF THE SPINDLE INTEGRATED FORCE SENSOR SYSTEM

The cutting forces applied at the tool tip are transmitted to the spindle integrated sensors through various mass, spring, and damping elements. Consequently, the static and dynamic structural analysis is paramount in understanding behaviour of the spindle structure to accurately measure cutting forces from the spindle integrated sensors. The static analysis is carried out to approximate the cutting forces measured from the force sensors using the Finite Element Analysis based on a commercial software package, Ansys™. The dynamic analysis is performed through the impact modal tests. Three distinctive modes in X direction are identified and the complex structure dynamics are discretized to lump mass, stiffness, and damping elements to the three Degrees of Freedom structure based on the experimentally obtained mode shapes.

4.1 STATIC ANALYSIS

4.1.1 SPINDLE ANALYSIS

Static deformations of various spindle components and their connections under loads are essential for understanding the roles of various components. The spindle structure can be simplified as the spindle shaft, bearings, and the spindle housing. The shaft is supported by the front and rear bearings which consist of hybrid ceramic ball bearings with a contact angle of 25 degrees. The simplified schematic of the spindle and

bearing system is shown in Figure 4.1, where K_r and K_f denote the rear and front bearing stiffnesses, respectively, and F_a represents the actual force acting at the tool tip. The spindle structure consists of the spindle housing which is supported by the clamped mechanism at the force sensor location and the roller mechanism at the rear end of the spindle. F_s denotes the reaction force at the force sensor location which is assumed to be analogous to the measured force (i.e., F_m) from the force sensor, and F_c is the reaction force at the roller support. The tool and the tool holder are connected using the taper 7/24 (Cat 40) interface. The interface acts as a torsional spring. The reaction force caused by the force at the tool tip can be calculated based on the Finite Element model as shown in Figure 4.1, where K_r and K_f are found to be approximately 11.6e8 N/m and 12.2e8 N/m, respectively [NSK bearing catalog] and the torsional spring is assumed to be rigid. The Finite Element analysis is performed by applying 1 N of translational force at the tool tip and the reaction force (F_s) at the force sensor location is predicted to be approximately 1.31 N. This value is similar to the experimental result which is obtained by comparing the static calibration factors between the tool tip and the force sensor locations where the ratio between the two static calibration factors is found to be 1.6. The discrepancy between the FE and the experimental analyses is approximately 18 %. This discrepancy may have originated from the tool holder interface which is quite flexible. Furthermore, the accurate knowledge of the stiffness values for individual elements is not readily available especially at the bearings and the tool holder locations.

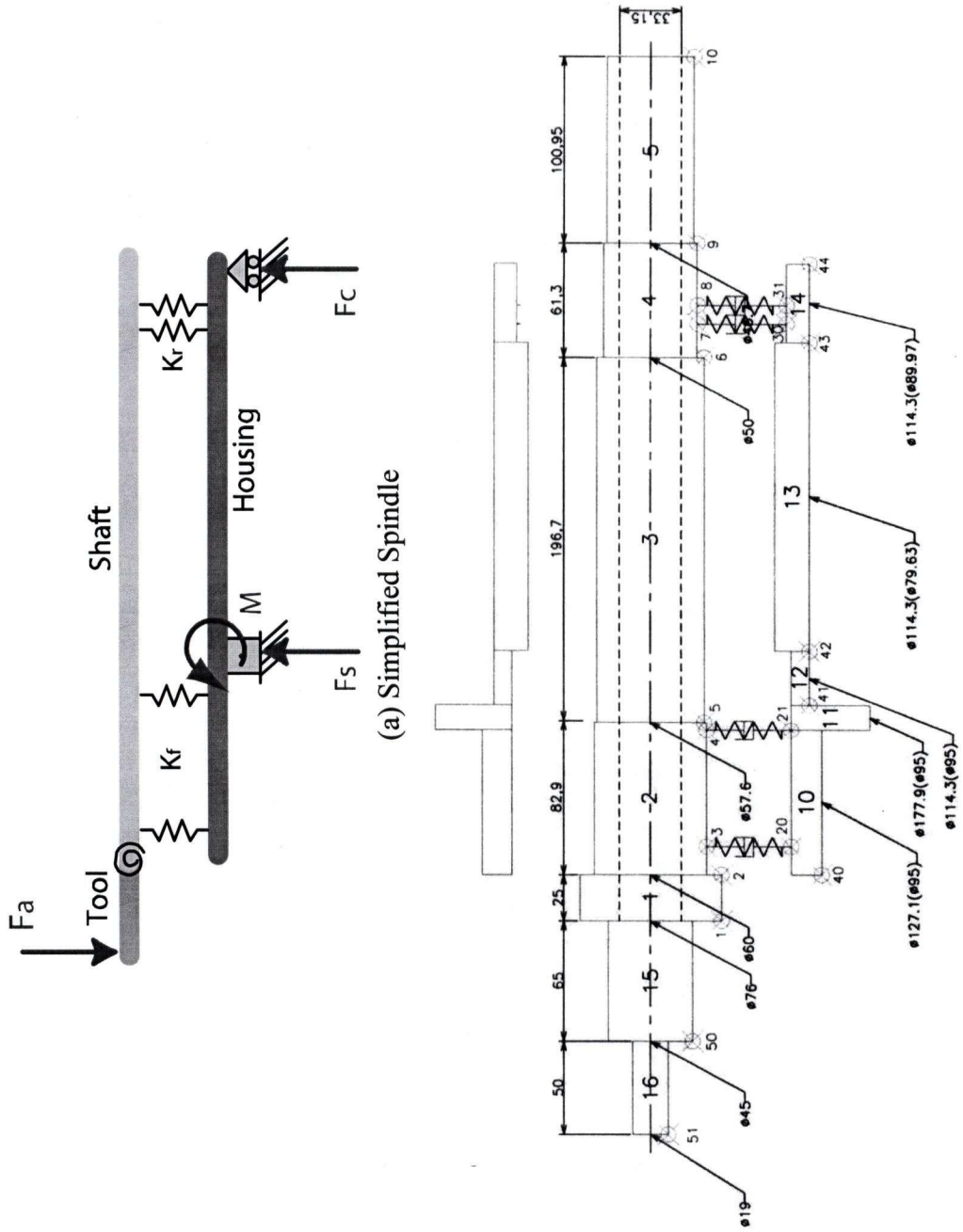

Figure 4.1 The Schematics of the Simplified Spindle Structure

The determination of a joint or contact stiffness and damping has been quite difficult due to the complex nature of the problem. Damping in mechanical systems usually occurs due to the loss of energy in material of the component and contact areas between fitting parts – micro asperities on the contacting surfaces. The tool holder interface can be considered as the joint where the joint stiffness and damping is vital in understanding the overall characteristics of the structure. The tool holder is clamped to the spindle shaft by the clamping mechanism. If the clamping force is increased, the stiffness would increase as well. Typically, the analysis of contact deformations between point contact or line contact areas are formulated using Hertz formula which assumes that the contact areas are small relative to dimensions of the contact bodies [Harrison 91]. However, the contact stiffness at the tool holder interface cannot be formulated using Hertz formula because the contact area is relatively large. Some attempts were made to experimentally obtain the joint dynamics through the receptance coupling method [Wang 94] but inaccessibility of the joint (or the tool holder interface) limits its usage. According to Jacobs [Jacobs 99], the joint linear spring constant is determined to be 1.375e9 N/m and the torsional spring constant to be 8.108 N/m/rad for CAT 40 (7/24) style tool holder interface. Also, the bending stiffness for the CAT 40 tool holder identified by Jacobs was approximately 9.3e7 N/m. Hazem et al. [Hazem 87] have also conducted a series of static bending stiffness tests using various tool holder interfaces. Figure 4.2 depicts the results where the stiffness of CAT 40 (7/24) taper tool holder yields approximately 12e6 N/m. This value is considerably lower than the measurements done by Jacobs. This concludes that the identification of the joint stiffness is extremely

difficult and further study is needed to accurately predict both static and dynamic components of the tool holder interface stiffness.

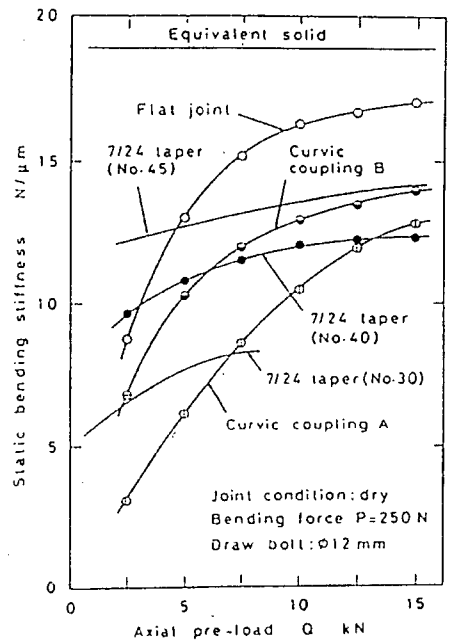

Figure 4.2 Effects of axial preloads on static bending stiffness of various interface systems [Hasem 87]

4.1.2 SPINDLE INTEGRATED STATIC FORCE SENSOR STIFFNESS ANALYSIS

The static behaviour of the spindle integrated sensors is determined by the static stiffness of the sensor. The piezoelectric force sensor measures the strain deformation by shearing between two plates. The Spindle Integrated Force Sensors (SIFSs) are sandwiched between the spindle casting and the spindle housing flange. These force sensors comprise of piezoelectric crystals that undergo strain deformation when force is applied. When the strain deformation occurs, the sensors generate charge signals proportional to strain. The sensors are preloaded by the cap screws. The comprehensive analysis of force transmission is required to determine the equivalent stiffness of the

spindle integrated sensors. The bottom face of the cap screw is touching the spindle housing flange. The spindle housing flange and the cap screws are assumed to be rigid contact (i.e., no slippage) because the high torque (i.e., 55 Nm) is applied to the cap screw. Figure 4.3 illustrates the side view of the spindle sensor mounting located between the fixed spindle casting and the spindle housing flange which is secured by the cap screw.

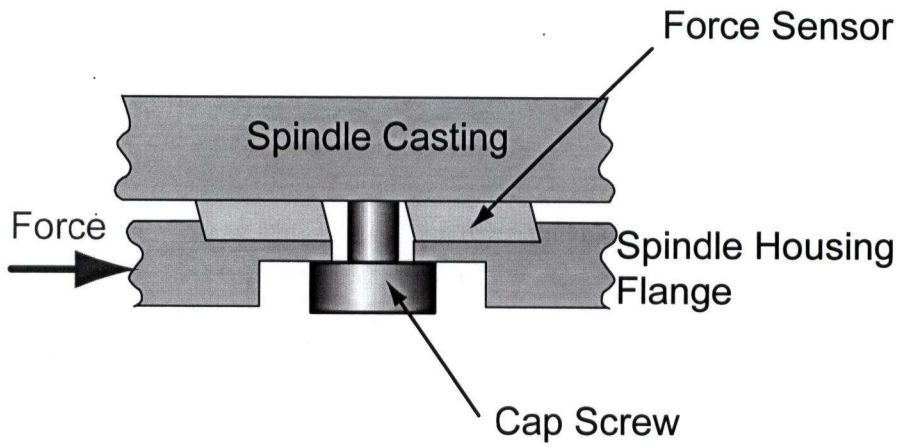

Figure 4.3 The Expanded view of the Force Sensor, Spindle Casting, and Housing

The cutting forces at the tool tip would shear the spindle housing which in effect shears the force sensors because the spindle casting is fixed. Therefore, the force from the tool tip is transmitted through both the cap screw and the force sensor. The simplified view of the shear force sensor is shown in Figure 4.4 where the integrated force sensor system and the cap screw are assumed to be attached in parallel. k_p and k_b are the force sensor and bolt stiffnesses, respectively, and δ is the displacement caused by the force.

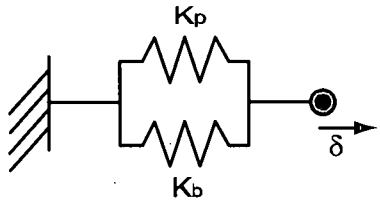

Figure 4.4. Simplified Stiffness for the Force Sensor (K_p) and the Bolt (K_b)

By neglecting contact surface stiffness, the cap screw can be approximated using the cantilever beam analysis by a simple evaluation of force transmission mechanism. According to Chung [Chung 93], the stiffness of a similar sensor is found to be approximately 0.249e9 N/m (i.e., k_p). Since the contact area between the cap screw and the spindle housing is only at the head, the length of the beam can be assumed to be the length from the spindle casting to the head. The simplified stiffness of the bolt is derived based on the cantilever beam analysis as:

$$k_b = \frac{3EI}{l^3} \tag{4.1}$$

where E is Young's modulus, I is the second moment of area of the section, and the l is the length of the cap screw. The diameter and length of the screw is 8.92 mm and 9.66 mm, respectively, and the modulus of steel is approximately 2.1e11 Pa. Based on Eq. 4.1, the bolt stiffness is found to be approximately 0.207e9 N/m (i.e., k_b). The equivalent stiffness between the cap screw and the force sensor is sum of the two stiffnesses:

$$k_{eq} = k_p + k_b = 0.456e9 \ N/m \tag{4.2}$$

Therefore, applying 1 N of force at the sensor location of the housing would transmit approximately 0.55 N to the piezoelectric sensor and 0.45 N to the cap screw. The analysis is based on the rough estimate of the sensor sensitivity.

Whereas the measured cutting force from the spindle integrated sensors can be represented by:

$$F_m = k_p \times \delta \tag{4.3}$$

where δ is the displacement caused by the force.

4.1.3 STATIC CALIBRATION OF FORCE SENSORS

The sensor system is statically calibrated by applying a gradually increasing load at the tool tip and simultaneously measuring the corresponding voltage signals generated by the spindle force sensors (see Figure 4.5) so that one Newton of force at the tool tip (F_a) corresponds to one Newton of force at the SIFS (F_m). The static response is linear with sensitivity factors of 3.2 mV/N, 3.5 mV/N, and 0.59 mV/N in X, Y, and Z directions, respectively as shown in Figure 4.6. The cross talks are also measured in all three directions, and the following static calibration matrix has been identified:

$$\begin{Bmatrix} F_{xa} \\ F_{ya} \\ F_{za} \end{Bmatrix} = \begin{bmatrix} 1 & 0.07 & 0.05 \\ 0.09 & 1 & 0.02 \\ 0.19 & 0.12 & 1 \end{bmatrix} \begin{Bmatrix} F_{xm} \\ F_{ym} \\ F_{zm} \end{Bmatrix} \tag{4.4}$$

The cross talks in major cutting force directions (X and Y) are under 10 % and similar to dynamometers with a workpiece attachment, which is acceptable. However, the axial force (Z) is influenced by the cross talk with X and Y directions of the table by 19 % and 12 %, respectively. The cross talk amplitude, especially in the axial direction, is dependent on applying equal preload on opposing sensors during installation, which in turn depends on the precision of parallelism between the flange and housing surfaces. It was not possible to grind the contact surfaces on the instrumented machine; hence the parallel contact surfaces were not fully achieved. In milling, the major cutting force

components are in the feed (X) and normal (Y) directions where the axial forces have negligible cross talk influence (5 %, 2 %).

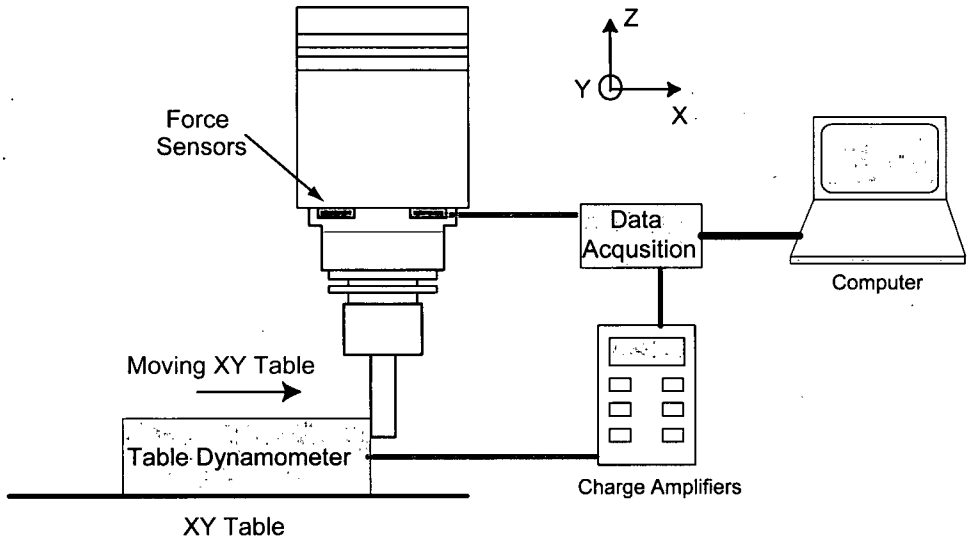

Figure 4.5. Static Calibration Setup Using the Table Dynamometer

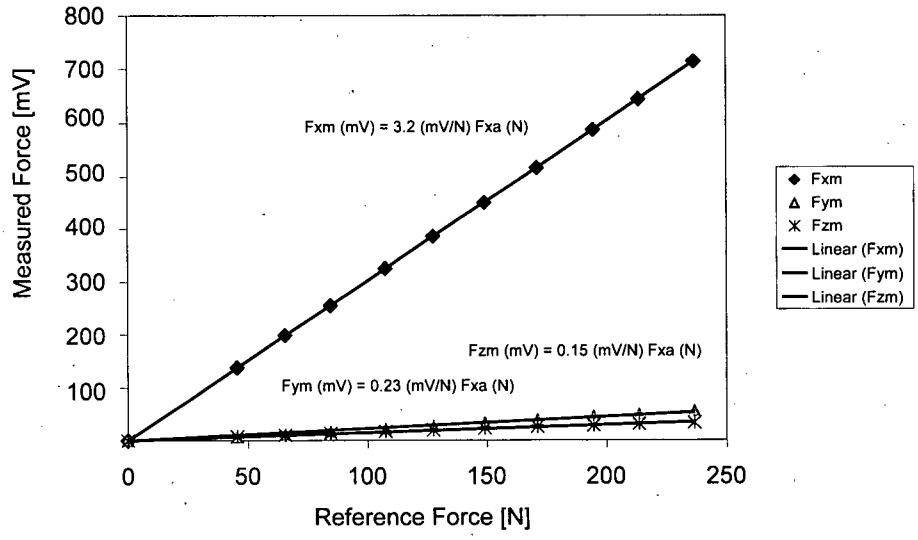
Measured Force [mV]
800
700
600
500
400
300
200
100
0
50
100
150
200
250
Reference Force [N]
Fxm (mV) = 3.2 (mV/N) Fxa (N)
Fzm (mV) = 0.15 (mV/N) Fxa (N)
Fym (mV) = 0.23 (mV/N) Fxa (N)
Fxm
Fym
Fzm
Linear (Fxm)
Linear (Fym)
Linear (Fzm)

(a)

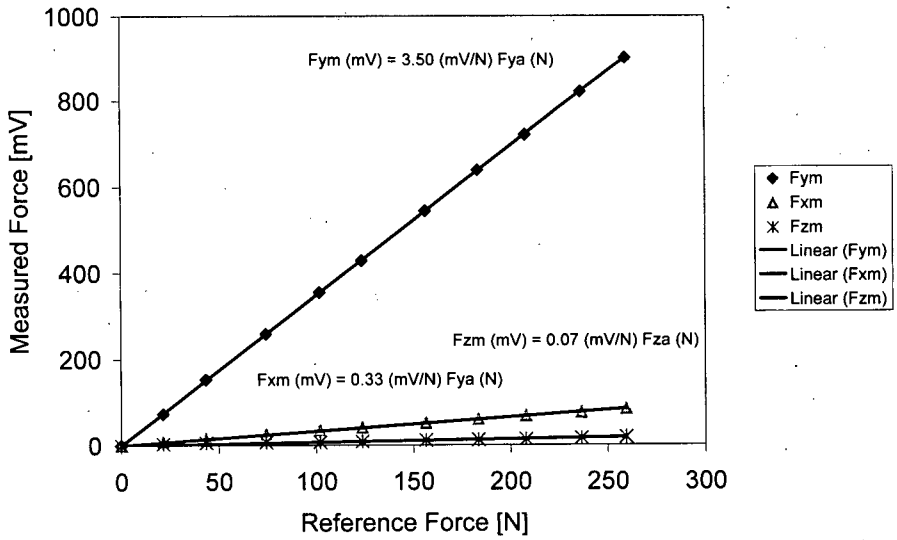
Measured Force [mV]
1000
800
600
400
200
0
0
50
100
150
200
250
300
Reference Force [N]
Fym (mV) = 3.50 (mV/N) Fya (N)
Fzm (mV) = 0.07 (mV/N) Fza (N)
Fxm (mV) = 0.33 (mV/N) Fya (N)
Fym
Fxm
Fzm
Linear (Fym)
Linear (Fxm)
Linear (Fzm)

(b)

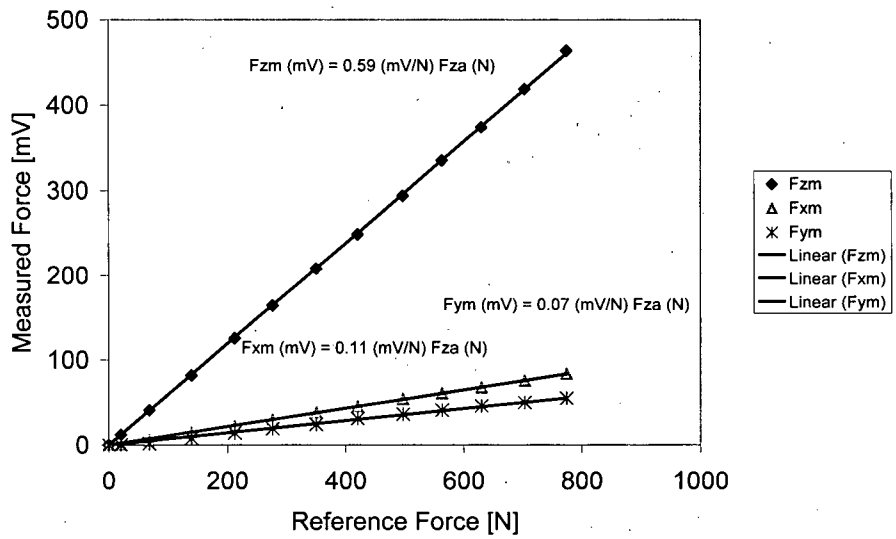

(c)

Figure 4.6 (a) Static sensitivity calibration in X direction, (b) Static sensitivity calibration in Y direction, (c) Static sensitivity calibration in Z direction *(Reference Force is measured from the table dynamometer and Measured Force is measured from the SIFS).*

Based on the obtained calibration factors, the cutting forces measured from the dynamometer are compared with the forces obtained from the spindle integrated sensors (without considering the cross talks) as shown in Figure 4.7 with small incremental displacements. The figures show stair stepping profiles and the comparisons between the forces measured from the dynamometer and the Spindle Integrated Force Sensor system are almost identical using the direct calibration factors. The cross talks are neglected in Figure 4.7.

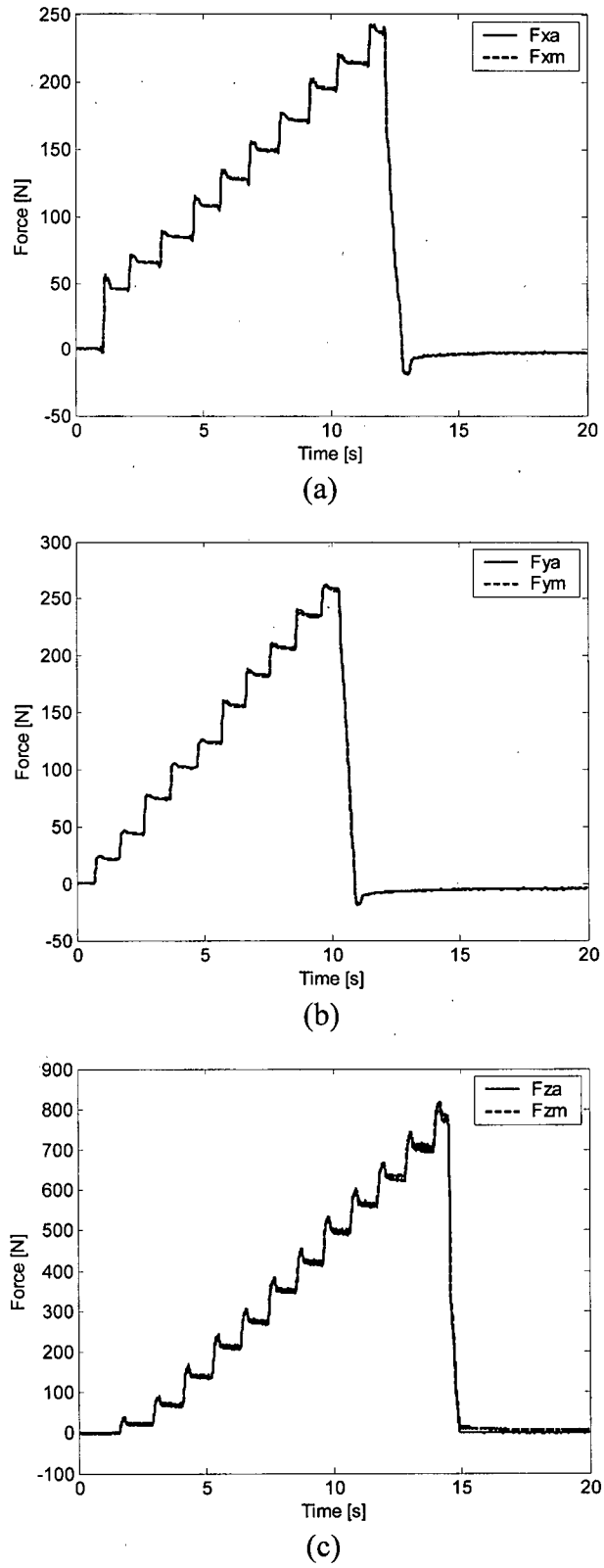

Figure 4.7. Comparison of Static Cutting forces in (a) X, (b) Y, and (c) Z directions.

4.2 DYNAMIC ANALYSIS

Experimental modal impact hammer tests are performed on the proposed Spindle Integrated Force Sensor system to acquire the transfer functions between the tool tip and the sensor in X direction as an exemplar case. The physical modeling of the spindle is carried out based on the experimentally obtained modal parameters and mode shapes.

4.2.1 SPINDLE AND SENSOR DYNAMICS

The Experimental Modal Analysis (EMA) using the instrumented impact hammer is performed to acquire the transfer function ($\Phi(s)$) between the impact force applied at the tool tip (F_a) and the Spindle Integrated Force Sensor system (F_m) by averaging the frequency response curves obtained from several successive impact tests. As shown in the previous section, the Spindle Integrated Force Sensor system is statically calibrated (3.2 mV/N) in X direction by applying a gradually increasing load at the tool tip and measuring the corresponding voltage signals generated by the spindle force sensors. The input is given by the impact force hammer at the tool tip to mimic the actual cutting force, F_a, and the output is measured by the Spindle Integrated Force Sensors (SIFS), F_m. Figure 4.8 illustrates the relationship between the applied force and the measured force where the force transmits through the tool, the tool holder, the spindle, and the spindle integrated sensors. The measured and modeled transfer function of the force and the acceleration sensing systems are shown in Figure 4.9 (a) and (b).

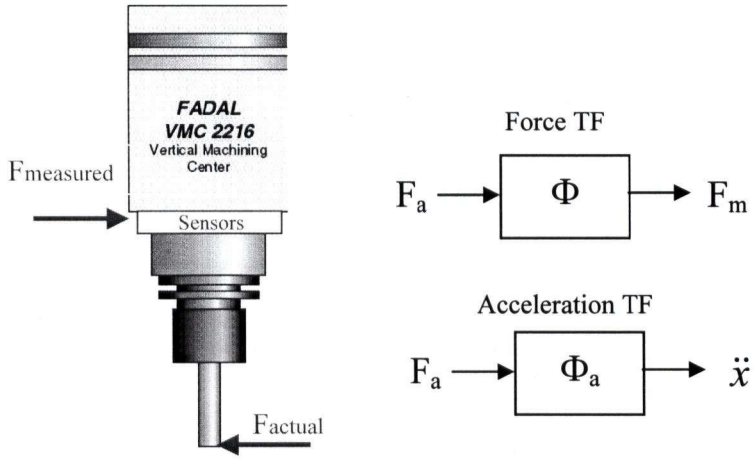

Figure 4.8 Force Diagram

The system exhibits three dominant modes at 500, 719, and 990 Hz. The tool holder causes the modes at the spindle taper joint, and bending of the spindle. The transfer function measurement indicates that the spindle sensor system can reliably measure milling forces that have harmonics less than 350 Hz. The experimentally measured transfer function in the Laplace domain is identified by a modal curve fitting technique [Altintas 00], which leads to the following:

$$\Phi(s) = \frac{F_m(s)}{F_a(s)} = \sum_{k=1}^{3} \frac{\alpha_k^{-1}\omega_{n,k}^{2}}{s^2 + 2\zeta_k\omega_{n,k}s + \omega_{n,k}^{2}} \tag{4.5}$$

where k is the number of modes, F_m is the measured force from the Spindle Integrated Force Sensor, and the F_a is the applied force at the tool tip. The modal parameters of the transfer function in X direction are identified as:

ω_{n1}	*500 Hz*	ζ_1	*0.042*	α_1	*2.289*
ω_{n2}	*719 Hz*	ζ_2	*0.0196*	α_2	*5.094*
ω_{n3}	*990 Hz*	ζ_3	*0.025*	α_3	*2.7763*

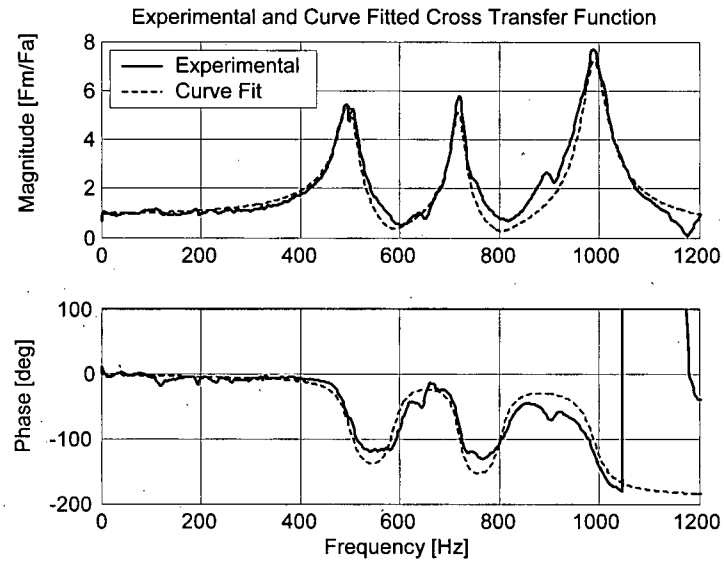

(a)

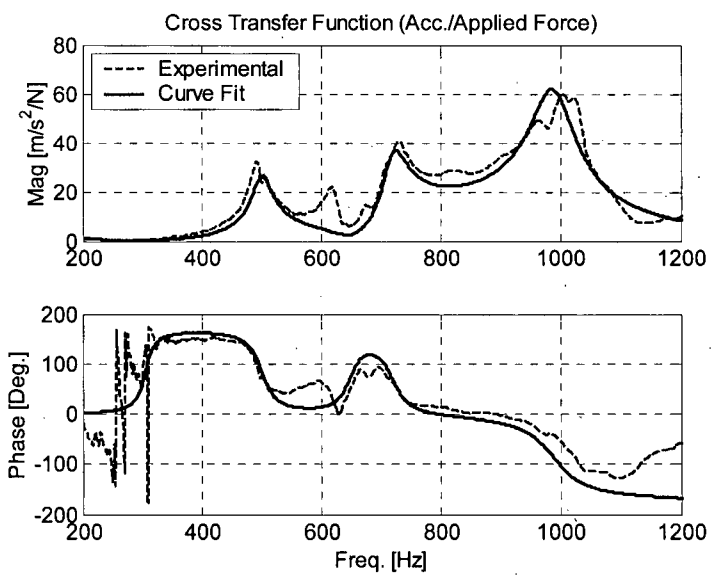

(b)

Figure 4.9 (a) Transfer Function $\Phi(\omega) = F_m(\omega)/F_a(\omega)$ and (b) Transfer Function $\Phi_a(\omega) = \ddot{x}(\omega)/F_a(\omega)$ (the curve fit is performed using CutPro™ Modal Analysis™).

Eq. 4.5 can be expanded to pole-zero and polynomial forms as:

$$\Phi(s)=\frac{F_m(s)}{F_a(s)}=\frac{(s-z_1)(s-z_1^*)(s-z_2)(s-z_2^*)}{(s-p_1)(s-p_1^*)(s-p_2)(s-p_2^*)(s-p_3)(s-p_3^*)}$$
$$=\frac{b_0s^5+b_1s^4+b_2s^3+b_3s^2+b_4s+b_5}{s^6+a_1s^5+a_2s^4+a_3s^3+a_4s^2+a_5s+a_6} \tag{4.6}$$

where the parameters are shown as:

z_1	-113+5050i	b_0	0	a_1	752
z_2	-124+3690i	b_1	2.23e7	a_2	6.92e7
p_1	-155+6218i	b_2	1.05e10	a_3	3.36e10
p_2	-89+4517i	b_3	8.726e14	a_4	1.37e15
p_3	-132+3138i	b_4	2.09e17	a_5	3.39e17
		b_5	7.794e21	a_6	7.794e21

The measured and curve fitted transfer functions are in good agreement as can be seen in Figure 4.9 (a).

Similarly, the transfer function between the impact force at the cutting tool tip and acceleration at the spindle sensor location is measured and identified as:

$$\Phi_a(s)=\frac{\ddot{x}(s)}{F_a(s)}=\frac{(s-z_{a1})(s-z_{a1}^*)(s-z_{a2})(s-z_{a2}^*)}{(s-p_1)(s-p_1^*)(s-p_2)(s-p_2^*)(s-p_3)(s-p_3^*)}$$
$$=\frac{c_0s^5+c_1s^4+c_2s^3+c_3s^2+c_4s+c_5}{s^6+a_1s^5+a_2s^4+a_3s^3+a_4s^2+a_5s+a_6} \tag{4.7}$$

where the parameters are shown as:

z_{a1}	-103±4901i	c_0	0	a_1	752
z_{a1}	-130±3375i	c_1	2.97e6	a_2	6.92e7

p_1	*-155+6218i*	c_2	*1.39e9*	a_3	*3.36e10*
p_2	*-89+4517i*	c_3	*1.05e14*	a_4	*1.37e15*
p_3	*-132+3138i*	c_4	*2.56e16*	a_5	*3.39e17*
		c_5	*8.15e20*	a_6	*7.794e21*

The acceleration transfer function has the same characteristic equation with exactly the same poles as the force transfer function because the natural frequencies and the damping ratios of both the transfer functions are the same, see Figure 4.9 (b). The additional mode appearing at 620 Hz may be due to the location of the accelerometer which is slightly different than the spindle integrated sensor and did not considered in the model.

The experimentally obtained model (Eqs. 4.5 – 4.7) is utilized for the dynamic compensation using the disturbance Kalman Filter in Chapter 6.

4.2.2 PHYSICAL MODELING

In this subsection, the physical model is analytically derived from the mode shapes and modal parameters in the feed (i.e., X) direction. Attempt is made to employ the physical model to acquire the applied force, F_a, using the Unknown Input Analysis (UIA) by predicting the input through the state reduction transformation. However, the accuracy of the estimated applied force is not as good as the dynamic compensation using the disturbance Kalman Filter.

<u>MODELING</u>

Simplifying (i.e., discretization) the complex structure is vital to understand the physical behaviours of the spindle and the sensors. For example, the weak joints can be

identified by observing large displacements of mode shapes at specific natural frequencies. The experimental modal analysis is carried out based on the reference [Altintas 00] where the spindle structure is excited at various heights while fixing the displacement sensor at specified locations as shown in Figure 4.10 (a). The mode shapes acquired from the experimental modal analysis are shown at their natural frequencies in Figure 4.11. By observing the mode shapes, the weakest link of the spindle structure is identified as the tool holder interface since the tool holder is connected to the spindle by the clamping force. The black circular dots shown in Figure 4.11 indicate ideal spring locations and the location '*VII*' in the figure is assumed to be fixed and corresponds to a location just above the front bearings. From the mode shapes, the mass normalized modal matrix, U, can be represented as:

$$U = \begin{bmatrix} 0.198 & 0.334 & 1.045 \\ 0.101 & 0.061 & -0.013 \\ 0.0042 & 0.006 & -0.023 \end{bmatrix} \tag{4.8}$$

Since only three modes are considered, the system would be simplified to the three-DOF system based on the analysis of the mode shapes. The first mass is presumed to be the tool and the tool holder. The second mass is the mass between the tool holder and the Spindle Integrated Force Sensors and the third mass is "everything behind". The Spindle Integrated Force Sensors are assumed to be located between Mass 3 and Mass 2 and they are modeled to be the second spring, k_2. The acceleration is measured at the second mass, before the force ring. The actual cutting force is applied at Mass 1.

The simplified three DOF system can be formulated in the local coordinate as:

$$M_x\ddot{X} + C_x\dot{X} + K_xX = F_a \tag{4.9}$$

$$\begin{bmatrix} m_1 & 0 & 0 \\ 0 & m_2 & 0 \\ 0 & 0 & m_3 \end{bmatrix}\begin{bmatrix} \ddot{x}_1 \\ \ddot{x}_2 \\ \ddot{x}_3 \end{bmatrix}+\begin{bmatrix} c_1 & -c_2 & 0 \\ -c_2 & c_2+c_3 & -c_3 \\ 0 & -c_3 & c_2+c_3 \end{bmatrix}\begin{bmatrix} \dot{x}_1 \\ \dot{x}_2 \\ \dot{x}_3 \end{bmatrix}+\begin{bmatrix} k_1 & -k_2 & 0 \\ -k_2 & k_2+k_3 & -k_3 \\ 0 & -k_3 & k_2+k_3 \end{bmatrix}\begin{bmatrix} x_1 \\ x_2 \\ x_3 \end{bmatrix}=\begin{bmatrix} F_a \\ 0 \\ 0 \end{bmatrix}$$

where the solution of the eigenvalue problem yields the normalized modal matrix, U, i.e., modal masses are unity. The above equation can be transformed into the modal coordinates by multiplying the normalized modal matrix, U, and transforming the local displacement vector, X, into the modal coordinate vector, Q:

$$X = UQ \tag{4.10}$$

when Eq. 4.10 is inserted into Eq. 4.9 and then pre-multiplied by U^T lead to the equation of motion in the modal coordinate;

$$\begin{aligned} &U^T M_x U\ddot{Q}+U^T C_x U\dot{Q}+U^T K_x U Q = U^T F_a \\ &M_q\ddot{Q}+C_q\dot{Q}+K_q Q = U^T F_a \end{aligned} \tag{4.11}$$

where M_q, C_q, and K_q are the diagonal mass, damping, and stiffness matrices in the modal coordinate, respectively. Proportional damping is assumed to dominate the structural damping. Eq. 4.11 can be rearranged to form the following equation:

$$\begin{bmatrix} 1 & 0 & 0 \\ 0 & 1 & 0 \\ 0 & 0 & 1 \end{bmatrix}\begin{bmatrix} \ddot{q}_1 \\ \ddot{q}_2 \\ \ddot{q}_3 \end{bmatrix}+\begin{bmatrix} 2\xi_1\omega_{n1} & 0 & 0 \\ 0 & 2\xi_2\omega_{n2} & 0 \\ 0 & 0 & 2\xi_3\omega_{n3} \end{bmatrix}\begin{bmatrix} \dot{q}_1 \\ \dot{q}_2 \\ \dot{q}_3 \end{bmatrix}+\begin{bmatrix} \omega_{n1}^2 & 0 & 0 \\ 0 & \omega_{n2}^2 & 0 \\ 0 & 0 & \omega_{n3}^2 \end{bmatrix}\begin{bmatrix} q_1 \\ q_2 \\ q_3 \end{bmatrix}=U^T\begin{bmatrix} F_a \\ 0 \\ 0 \end{bmatrix} \tag{4.12}$$

The modal damping matrix and natural frequencies in Eq. 4.12 are identified from Eq. 4.5 which would represent the corresponding modal mass, damping, and stiffness matrices as:

$$M_q=\begin{bmatrix} 1 & 0 & 0 \\ 0 & 1 & 0 \\ 0 & 0 & 1 \end{bmatrix},\ C_q=\begin{bmatrix} 263.89 & 0 & 0 \\ 0 & 177.09 & 0 \\ 0 & 0 & 311.02 \end{bmatrix}\text{N/m/s},\ K_q=\begin{bmatrix} 0.9870 & 0 & 0 \\ 0 & 2.041 & 0 \\ 0 & 0 & 3.869 \end{bmatrix}\times 1e7\,\text{N/m}$$

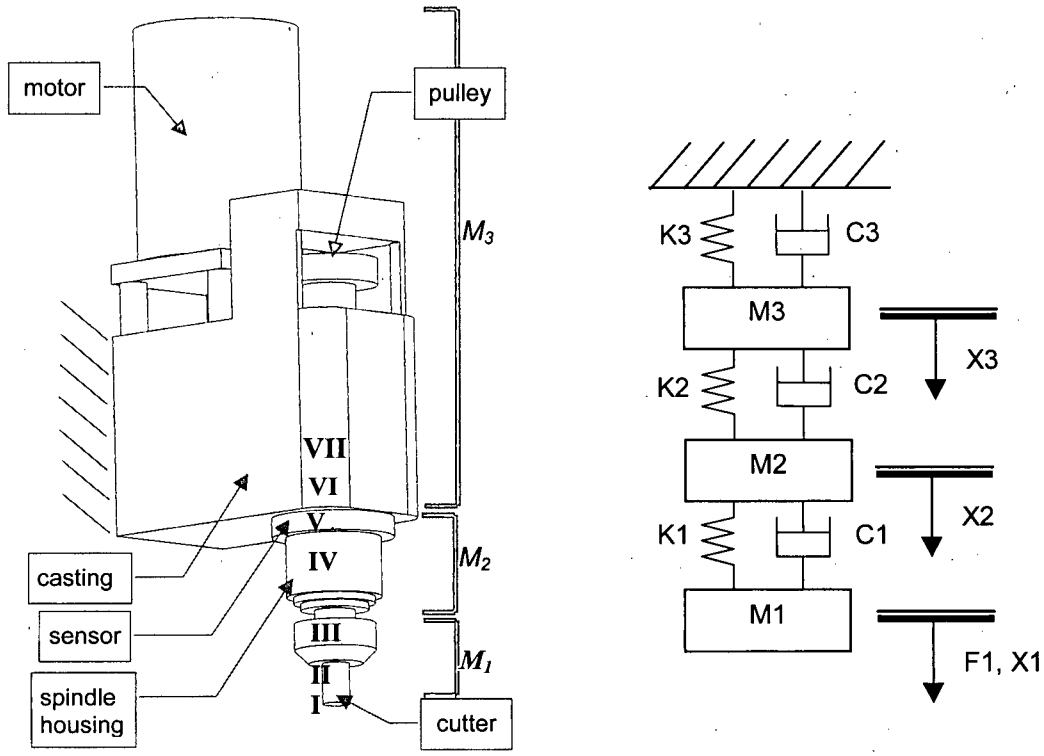

(a) Spindle Structure (b) Equivalent Mass-Spring-Damper

Figure 4.10 The spindle structure and its equivalent mass-spring-damper model.

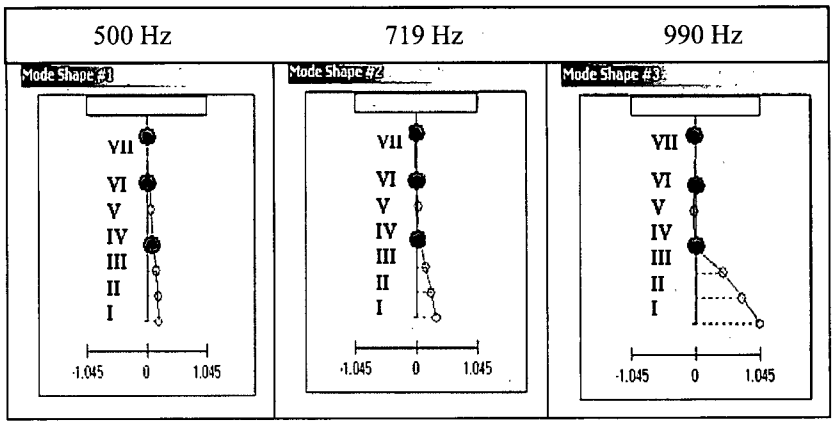

Figure 4.11 Mode Shapes of the Spindle in X direction at the natural frequencies.

The measured force, F_m, from the Spindle Integrated Force Sensor, which is mounted between the column and the spindle housing, can be equated as functions of spring constant, k_2, and deflections $x_2 - x_3$ (see Eq. 4.3):

$$k_2 x_2 - k_2 x_3 \equiv F_m \tag{4.13}$$

The damping is assumed to be negligible for the cutting force measurements from the SIFS. The above equation has to be transformed into the modal coordinate by performing the modal transformation via substituting $X = UQ$. Then Eq. 4.13 becomes:

$$\begin{bmatrix} 0 & k_2 & -k_2 \end{bmatrix} \cdot U \cdot \begin{bmatrix} q_1 \\ q_2 \\ q_3 \end{bmatrix} \approx F_m \tag{4.14}$$

At this point, the unknown parameter is the spring stiffness at the location 2, k_2. The calculation of the stiffness through the modal transformations is:

$$K_x = (U^T)^{-1} \cdot K_q \cdot (U)^{-1} \text{ [m/N]} \tag{4.15}$$

However, Eq. 4.15 is found to be inappropriate. According to Baruch [Baruch 97], the direct identification using the modal data is insufficient for the identification of both mass and stiffness matrices. The major problem of the direct identification is that the mode shape is not uniquely defined. Rather, it is relative to each other, which means that the mode shape can be multiplied by any non-zero constant. If we let $\phi = U\varepsilon$ where ε is any arbitrary non-zero constant;

$$\phi^T \overline{M}_q \phi = I \qquad \phi^T \overline{K}_q \phi = \omega_n^{\ 2} \tag{4.16}$$

where

$$\overline{M}_q = (\phi\phi^T)^{-1} = (U\varepsilon^2 U^T)^{-1}$$
$$\overline{K}_q = (\phi\omega_n^{\ 2}\phi^T)^{-1} = (\varepsilon U^T)^{-1}\omega_n^{\ 2}(U\varepsilon)^{-1} \tag{4.17}$$

Therefore, there are an infinite number of solutions for mass and stiffness matrices depending on the value of ε. In order to identify or update the mass and stiffness matrices, either the mass or stiffness matrix must be known. In this study, we approximate the mass matrix from the design dimensions to calculate the stiffness matrix.

IDENTIFICATION OF STIFFNESS USING PSUEDO INVERSE APPROACH

To overcome some of the difficulties associated with the modal transformation to identify the stiffness, the pseudo-inverse method used by Ismail [Ismail 80] is utilized to estimate the stiffness matrix. Various coordinate transformations are applied based on the references [Tlusty 76, Altintas 00]. This method maximizes the correlation between the experimental and the analytical parameters (i.e., mass). The pseudo inverse method forms the equation:

$$[D_i]\{K_d\} = \{g_i\} \tag{4.18}$$

where K_d is the unknown stiffness vector and D_i and g_i are the known parameters. This method utilizes the known mass and natural frequencies to obtain the stiffness parameters. Based on Figure 4.10, the first mass is found to be 1.8 kg by weighing the tool holder and the tool. The second mass and the third mass are obtained from the drawings to be approximately 14 kg and 125 kg, respectively. The simplified equation of motion is:

$$M_x\ddot{U} + K_x U = 0 \tag{4.19}$$

The damping matrix is assumed to be negligible for simplicity. The above equation can be rearranged to be;

$$\begin{aligned} &[[K_x]-\omega_{ni}^2[M_x]]\{U_i\}=0 \\ &[K_x]\{U_i\}=\omega_{ni}^2[M_x]\{U_i\} \end{aligned} \text{ or} \tag{4.20}$$

where i is degrees of freedom. The transformation matrix, T, from the local coordinate to the design coordinate, is obtained by examining Figure 4.10 (b) where the simple lumped masses, linear springs, and linear dampers are illustrated. The mode shape is shown in Eq. 4.8. The transformation matrix and the known mass matrix are:

$$T=\begin{bmatrix} 1 & -1 & 0 \\ 0 & 1 & -1 \\ 0 & 0 & 1 \end{bmatrix}; \text{ and}$$

$$M_x = T^T M_d T = \begin{bmatrix} 1 & -1 & 0 \\ 0 & 1 & -1 \\ 0 & 0 & 1 \end{bmatrix}^T \begin{bmatrix} 1.8 & 0 & 0 \\ 0 & 14 & 0 \\ 0 & 0 & 125 \end{bmatrix} \begin{bmatrix} 1 & -1 & 0 \\ 0 & 1 & -1 \\ 0 & 0 & 1 \end{bmatrix} = \begin{bmatrix} 1.8 & -1.8 & 0 \\ -1.8 & 15.8 & -14 \\ 0 & -14 & 139 \end{bmatrix} kg$$

The stiffness in the local coordinate can be transformed to the design coordinate (denoted as subscript 'd') through the transformation matrix as:

$$K_x = T^T K_d T \tag{4.21}$$

The above equation can be substituted into Eq. 4.20 to form:

$$[T]^T\ [K_d][T]\{U_i\} = \omega_{ni}^2[M_x]\{U_i\} \tag{4.22}$$

$$[T]^T\ [K_d]\ \{\Delta_i\} = \omega_{ni}^2[M_x]\{U_i\} \tag{4.23}$$

where $[T]\{U_i\} = \{\Delta_i\}$. Since the stiffness matrix in the design coordinate, K_d, is a diagonal matrix; the matrix can be rearranged as a vector. Also, the vector Δ_i is converted to a diagonal matrix as $\Theta = diag[\Delta]$. Let $[D_i]=[T]^T[\Theta_i]$ and $\{g_i\} = \omega_{ni}{}^2[M_x]\{U_i\}$, Eq. 4.23 can be rewritten as follows:

$$\underbrace{[T]^T[\Theta_i]}_{[D_i]}\underbrace{\{K_d\}}_{\{K_d\}} = \underbrace{\omega_{ni}{}^2[M_x]\{U_i\}}_{\{g_i\}} \tag{4.24}$$

Thus, the vector K_d can be obtained using the pseudo-inverse approach as:

$$\{K_d\} = \left[[D_i]^T[D_i]\right]^{-1}[D_i]^T\{g_i\} \tag{4.25}$$

D_i matrices of each degree of freedom are obtained as:

$$D_1 = \begin{bmatrix} 197.899 & 0 & 0 \\ -197.899 & 0.0968 & 0 \\ 0 & -0.0968 & 0.0042 \end{bmatrix}; D_2 = \begin{bmatrix} 0.2730 & 0 & 0 \\ -0.2730 & 0.055 & 0 \\ 0 & -0.055 & 0.0060 \end{bmatrix}; D_3 = \begin{bmatrix} 1.032 & 0 & 0 \\ -1.032 & 0.036 & 0 \\ 0 & -0.036 & -0.023 \end{bmatrix}$$

In addition, g_i vectors of each degree of freedom are obtained as:

$$g_1 = 1e9 \times [3.5157 \quad -3.5024 \quad -0.0082]^T;\ g_2 = 1e7 \times [1.003 \quad 0.5686 \quad -0.0408]^T;$$

$$g_3 = 1e8 \times [0.7188 \quad -0.5237 \quad -1.3074]^T$$

The average of the stiffness for each column of the mode shape is identified as:

$$K_d = \begin{bmatrix} 4.14e7 \\ 3.21e8 \\ 2.87e9 \end{bmatrix} N/m$$

Therefore, the stiffness of the sensor, k_2, is obtained as 3.21e8 N/m. The predicted value of k_2 is similar to the value obtained from Chung [Chung 93] which is approximately 2.49e8 *N/m*.

The analysis is performed in modal coordinates so that the experimentally obtained modal parameters can be readily used. Only a few parameters in the local coordinate are needed to formulate the forces obtained from the integrated force sensor system. The equation of motion in modal coordinates (Eq. 4.12) is transformed into the state space form as;

$$\begin{aligned} \dot{x}_q &= A_q x_q + B_q u \\ z &= C_q x_q \end{aligned} \tag{4.26}$$

where x_q is the state vector, $u = F_a$ is the input or the actual force applied to the tool, and $z = F_m$ is the measured cutting force from the spindle force sensor. The corresponding system matrix and the input vector are shown as;

$$A_q = \begin{bmatrix} [0]_{(3\times3)} & [I]_{(3\times3)} \\ -K_{q(3\times3)} & -C_{q(3\times3)} \end{bmatrix}; \; B_s = \begin{bmatrix} [0]_{(3\times1)} \\ [U_1]_{(3\times1)} \end{bmatrix} \tag{4.27}$$

where $U_1 = U^T[1 \quad 0 \quad 0]^T$ and U is the mode shape. Eq. 4.26 can be rewritten as;

$$\begin{bmatrix} \dot{q}_1 \\ \dot{q}_2 \\ \dot{q}_3 \\ \ddot{q}_1 \\ \ddot{q}_2 \\ \ddot{q}_3 \end{bmatrix} = \begin{bmatrix} 0 & 0 & 0 & 1 & 0 & 0 \\ 0 & 0 & 0 & 0 & 1 & 0 \\ 0 & 0 & 0 & 0 & 0 & 1 \\ -0.987e7 & 0 & 0 & -263.9 & 0 & 0 \\ 0 & -2.041e7 & 0 & 0 & -177.1 & 0 \\ 0 & 0 & -3.869e7 & 0 & 0 & -311.02 \end{bmatrix} \begin{bmatrix} q_1 \\ q_2 \\ q_3 \\ \dot{q}_1 \\ \dot{q}_2 \\ \dot{q}_3 \end{bmatrix} + \begin{bmatrix} 0 \\ 0 \\ 0 \\ u_{11} \\ u_{12} \\ u_{13} \end{bmatrix} F_a$$

$$[F_m] = [ku_1 \quad ku_2 \quad ku_3 \quad 0 \quad 0 \quad 0] \begin{bmatrix} q_1 \\ q_2 \\ q_3 \\ q_4 \\ q_5 \\ q_6 \end{bmatrix} \tag{4.28}$$

where

$$\begin{aligned} [ku_1 \quad ku_2 \quad ku_3] &= [0 \quad k_2 \quad -k_2] \begin{bmatrix} u_{11} & u_{12} & u_{13} \\ u_{21} & u_{22} & u_{23} \\ u_{31} & u_{32} & u_{33} \end{bmatrix} \\ &= [k_2 u_{21} - k_2 u_{31} \quad k_2 u_{22} - k_2 u_{32} \quad k_2 u_{23} - k_2 u_{33}] \\ &= [3.11 \quad 1.76 \quad 1.16] \times 1e7 \end{aligned} \tag{4.29}$$

Based on the obtained stiffness, k_2 (i.e., 3.21e8 N/m), the physical model transfer function is attained from Eq. 4.26 by:

$$\Phi_{physical}(s) = \frac{F_m(s)}{F_a(s)} = \frac{z(s)}{u(s)} = C_q(sI - A_q)^{-1}B_q \tag{4.30}$$

The physical model transfer function is shown in Figure 4.12. Some deviations between the experimental model and physically derived model FRFs can be seen especially at the third mode in the figure. These deviations may have been caused by several factors which include measurement errors, neglecting of the damping elements during the stiffness identification, unmeasurable internal nodes, non-linearity, etc. The obtained physical model is used to estimate the applied force at the tool, F_a, using the Unknown Input Analysis (UIA) as shown in Appendix A. Unfortunately, the force compensation using the UIA approach is found to be not as accurate as the disturbance Kalman Filter approach due to the difficulties associated with the discrete UIA method. Furthermore, the arbitrary selection of the transformation matrix, which would satisfy full rank properties of certain matrices, posed a big challenge. Therefore, the detailed description of the UIA is added as part of the appendix rather than a regular section in the thesis.

Several model updating methods [Mottershead 93] were tried to identify the unknown parameter. However, the model updating methods did not produce desirable results. The biggest problem associated with the model updating methods is that the mode shape needs to be very accurate in order to acquire the desirable results. Miniscule deviations in the experimentally obtained mode shapes can cause large discrepancies. Therefore, the obtained mode shape using the experimental modal analysis may not be sufficient to describe the entire phenomenon occurring in the spindle.

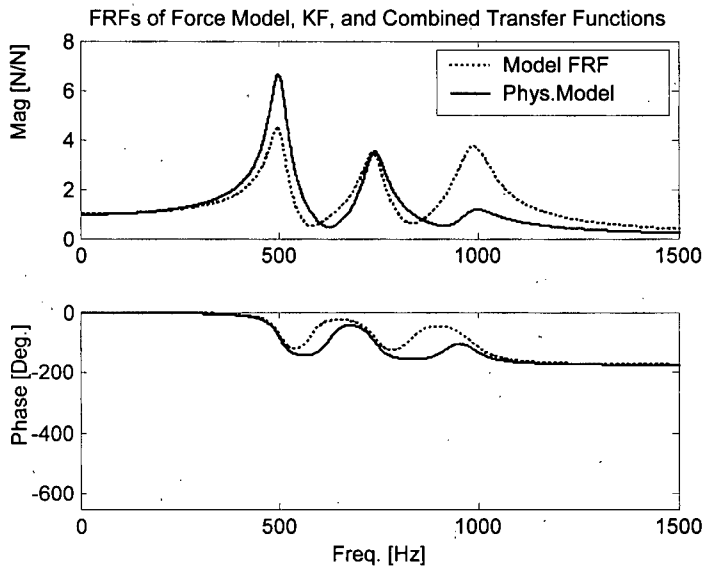

Figure 4.12 FRFs of Force Model using the impact force hammer and the Physical model.

4.3 CONCLUSION

The static analysis of the spindle system is examined to understand how the cutting forces are transferred from the tool tip to the force sensor. The static stiffness of the force sensors is approximately 2.49e8 N/m and the static calibration tests are performed to acquire the static calibration factors. They are found to be 3.2 mV/N, 3.5 mV/N, and 0.59 mV/N in X, Y, and Z directions, respectively. The experimental modal analyses are performed to elucidate the dynamics of the spindle system. The FRFs of the transfer function in X direction are examined with three distinctive modes. The mode shapes are experimentally acquired through the impact modal tests. The pseudo-inverse method is utilized to identify the stiffness of the force sensor. With the identified stiffness, the physical model is formulated and compared with the experimentally obtained FRFs. Some deviations can be found due to unmeasurable springs and damping elements. The elucidation of the spindle structure through static and dynamic analysis is

invaluable for the overall analysis of the system. However, the accuracy of the simple lumped physical model may be insufficient to accurately compensate the dynamics of the spindle structure to acquire the cutting forces from the spindle integrated force sensors.

CHAPTER 5.

RECEPTANCE COUPLING OF THE SPINDLE AND ARBITRARY TOOL DYNAMICS

Frequency Response Functions (FRFs) of the machine structure are important for the accurate reconstruction of the cutting forces at the tool tip and chatter suppressions. In this study, a classical receptance coupling technique is enhanced by proposing a method of identifying the end mill – spindle / tool holder joint dynamics. Since the tool bends inside the tool holder, which acts as a torsional spring, the rotational displacement of the tool at the joint cannot be neglected for the accurate construction of the FRF at the tool tip. On the other hand, it is rather difficult to experimentally measure the dynamics of angular displacements by applying a moment and force. Therefore, an algorithm that allows analytical extraction of rotational dynamics at the joints from linear displacements and impact force tests is proposed. The rotational dynamic response of the spindle-holder is identified analytically by substituting the direct and cross FRF measurements taken at the free end of the assembly and the joint of the blank cylinder to the receptance coupling expressions. Based on the obtained joint dynamics, the spindle structure can be mathematically coupled with an end mill which has arbitrary dimensions and materials. The model is compared against the previous approach and shown to have an improved accuracy in the experiments carried out with various size end mills. The experimentally proven method allows automated calibrations of spindle integrated force system whenever a tool change occurs.

5.1 RECEPTANCE COUPLING OF AN END MILL WITH THE SPINDLE ASSEMBLY

The cutting forces are monitored by the sensors integrated to the spindle housing as shown in Figure 5.1. The objective of the receptance coupling method is to identify the transfer function $\Phi_{31}(s) = F_3(s)/F_1(s)$ where $F_1(s)$ is the cutting force applied at the tool tip and $F_3(s)$ is the measured force by the sensor integrated to the spindle. It is necessary to identify the FRF (H_{31}) of the structure between points *1* (i.e., at the tip of the tool) and *3* (i.e., the spindle integrated sensor location). Since the force is felt via a spring constant of the sensor which can be easily calibrated using static tests, the transfer function (Φ_{31}) can be obtained as $H_{31}(s) = x_3(s)/F_1(s) \rightarrow k_s H_{31}(s) = \Phi_{31}(s)$. The structure is divided into *Substructure A* representing the end mill, and *Substructure B* representing the remaining spindle-tool holder assembly, see Figure 5.1.

Similar to receptance coupling proposed by Schmitz et al. [Schmitz 00], the structural dynamic model of the end mill at its two free ends, i.e. points *1* and *2*, can be analytically modeled using continuous beam formulation or Finite Element techniques. The direct and cross frequency responses of the spindle assembly at tool joint (*2*) and sensor location (*3*) can be identified using modal impact tests. The receptance coupling method enables the two substructures to be joined so that the experimental evaluation of Frequency Response Function of the force sensor system is avoided whenever end mill change occurs. Consider the FRFs of end mill (*A*) at two free ends to be (*1, 2*):

$$\begin{Bmatrix} X_1 \\ X_{A,2} \end{Bmatrix} = \begin{bmatrix} H_{A,11} & H_{A,12} \\ H_{A,21} & H_{A,22} \end{bmatrix} \begin{Bmatrix} F_1 \\ F_{A,2} \end{Bmatrix} \tag{5.1}$$

where X_1, and $X_{A,2}$ represent displacement vectors with both translational and angular displacements as components, and F_1 and $F_{A,2}$ represent force vectors which contain both force and moment applied on the structure at points *1* and *2*, respectively. $H_{A,ij}$ vectors are FRFs between points *i* and *j*.

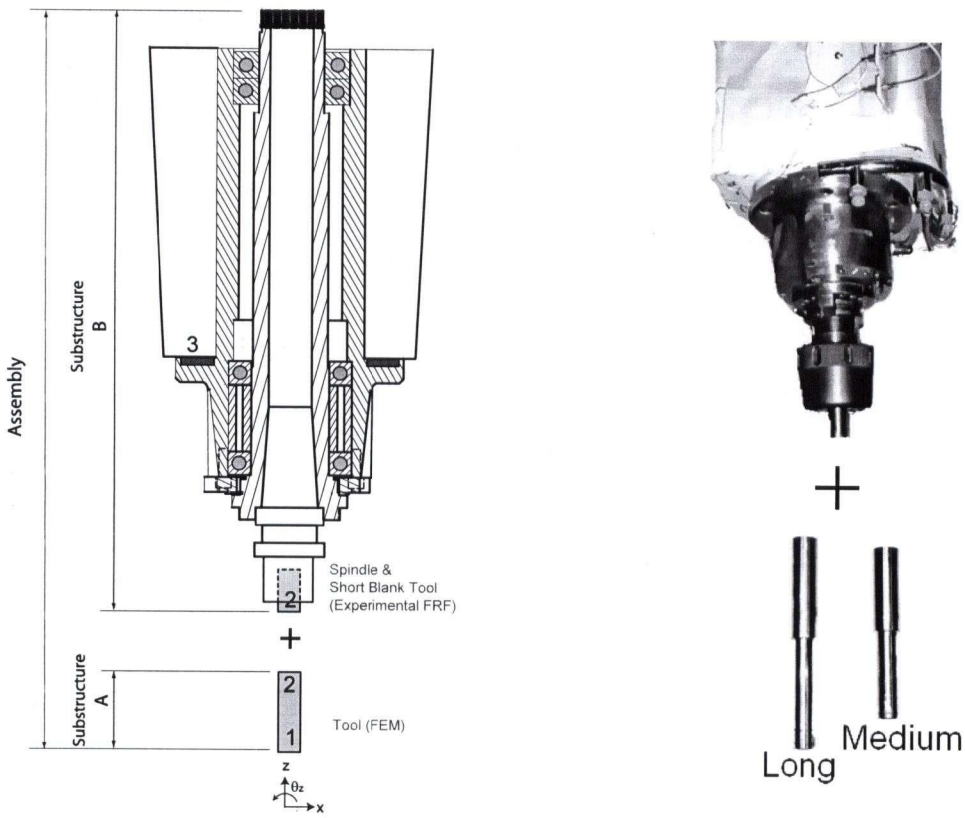

(a) Schematic (b) Pictorial

Figure 5.1 Spindle / Tool Holder and Tool Substructures

Similarly, the FRFs of the spindle structure (*B*) at its free end (*2*) and a location at the spindle integrated force sensors (*3*) are:

$$\begin{Bmatrix} X_{B,2} \\ X_3 \end{Bmatrix} = \begin{bmatrix} H_{B,22} & H_{B,23} \\ H_{B,32} & H_{B,33} \end{bmatrix} \begin{Bmatrix} F_{B,2} \\ F_3 \end{Bmatrix} \tag{5.2}$$

The equilibrium and compatibility conditions at the tool-spindle joint (*2*) are:

$$F_2 = F_{A,2} + F_{B,2}$$
$$X_2 = X_{A,2} = X_{B,2} \tag{5.3}$$

which are used in coupling the spindle (B) with the free-free model of the end mill (A). By considering the compatibility (Eq. 5.3) in the FRFs (Eqs. 5.1 and 2),

$$X_2 = H_{B,22}F_{B,2} + H_{B,23}F_3 = H_{A,21}F_1 + H_{A,22}F_{A,2} \leftarrow F_{A,2} = (F_2 - F_{B,2})$$
$$F_{B,2} = (H_{A,22} + H_{B,22})^{-1}(H_{A,21}F_1 + H_{A,22}F_2 - H_{B,23}F_3) \tag{5.4}$$

Letting $H_2 = (H_{A,22}+H_{B,22})$, the displacements X_1, X_2, and X_3 can be expressed as functions of FRFs and applied forces F_1, F_2, and F_3 as follows:

$$\begin{aligned}
X_1 &= H_{A,11}F_1 + H_{A,12}(F_2 - F_{B,2}) = H_{A,11}F_1 + H_{A,12}F_2 - H_{A,12}F_{B,2} \\
&= H_{A,11}F_1 + H_{A,12}F_2 - H_{A,12}H_2^{-1}(H_{A,21}F_1 + H_{A,22}F_2 - H_{B,23}F_3) \\
&= (H_{A,11} - H_{A,12}H_2^{-1}H_{A,21})F_1 + (H_{A,12} - H_{A,12}H_2^{-1}H_{A,22})F_2 + H_{A,12}H_2^{-1}H_{B23}F_3 \\
X_2 &= H_{A,21}F_1 + H_{A,22}(F_2 - F_{B,2}) \\
&= H_{A,21}F_1 + H_{A,22}F_2 - H_{A,22}H_2^{-1}(H_{A,21}F_1 + H_{A,22}F_2 - F_{B,23}F_3) \\
&= (H_{A,21} - H_{A,22}H_2^{-1}H_{A,21})F_1 + (H_{A,22} - H_{A,22}H_2^{-1}H_{A,22})F_2 + H_{A,22}H_2^{-1}H_{B,23}F_3 \\
X_3 &= H_{B,32}F_{B,2} + H_{A,33}F_3 \\
&= H_{B,32}H_2^{-1}(H_{A,21}F_1 + H_{A,22}F_2 - H_{B,23}F_3) + H_{A,33}F_3 \\
&= H_{B,32}H_2^{-1}H_{A,21}F_1 + H_{B,32}H_2^{-1}H_{A,22}F_2 + (H_{A,33} - H_{B,32}H_2^{-1}H_{B,23})F_3
\end{aligned} \tag{5.5}$$

The equations can be rearranged in a matrix form as follows:

$$\begin{Bmatrix} X_1 \\ X_2 \\ X_3 \end{Bmatrix} = \begin{bmatrix} (H_{A,11} - H_{A,12}H_2^{-1}H_{A,21}) & (H_{A,12} - H_{A,12}H_2^{-1}H_{A,22}) & H_{A,12}H_2^{-1}H_{B,23} \\ (H_{A,21} - H_{A,22}H_2^{-1}H_{A,21}) & (H_{A,22} - H_{A,22}H_2^{-1}H_{A,22}) & H_{A,22}H_2^{-1}H_{B,23} \\ H_{B,32}H_2^{-1}H_{A,21} & H_{B,32}H_2^{-1}H_{A,22} & (H_{A,33} - H_{B,32}H_2^{-1}H_{B,23}) \end{bmatrix} \begin{Bmatrix} F_1 \\ F_2 \\ F_3 \end{Bmatrix} \tag{5.6}$$

Considering the assembly of the linear tool ($H_{A,12} = H_{A,21}^T$) to the spindle, $H_{A,22}$, $H_{A,21}$ of the free-free end mill can be modeled using a Finite Element model of the beam and cross ($H_{B,32}$), and the direct FRF ($H_{B,22}$) at the joint must either be measured experimentally and/or deduced from the indirect measurement and application of inverse receptance coupling, as described in the following section.

Schmitz et al. [Schmitz 00] measured translational degree of freedom responses at the joint and adjusted the rotational displacement effects of the spindle at the flexible joint until the trials agreed with the measured values of the FRF of a complete assembly. This study presents a method that allows the direct identification of the joint FRFs with both translational and rotational degrees of freedom responses. By substituting $H_2 = (H_{A,22}+H_{B,22})$ into Eq. 5.6, the following direct and cross receptances at the tool tip are obtained:

$$\left.\begin{aligned} \frac{X_1}{F_1} &= H_{A,11} - H_{A,12}(H_{A,22}+H_{B,22})^{-1}H_{A,21} \\ \frac{X_1}{F_2} &= H_{A,12} - H_{A,12}(H_{A,22}+H_{B,22})^{-1}H_{A,22} \end{aligned}\right\} \tag{5.7}$$

Each FRF now contains both translation and rotational displacement elements; hence Eq. 5.7 at the free end of the tool can be expanded as;

$$\begin{aligned} \begin{Bmatrix} x_1 \\ \theta_1 \end{Bmatrix} &= \begin{bmatrix} h_{11,ff} & h_{11,fM} \\ h_{11,Mf} & h_{11,MM} \end{bmatrix} \begin{Bmatrix} f_1 \\ M_1 \end{Bmatrix} \rightarrow \quad \{X_1\} = [H_{11}]\{F_1\} \\ \begin{Bmatrix} x_1 \\ \theta_1 \end{Bmatrix} &= \begin{bmatrix} h_{12,ff} & h_{12,fM} \\ h_{12,Mf} & h_{12,MM} \end{bmatrix} \begin{Bmatrix} f_2 \\ M_2 \end{Bmatrix} \rightarrow \quad \{X_1\} = [H_{12}]\{F_2\} \end{aligned} \tag{5.8}$$

where each element in the matrix (h_{ij}) must be evaluated from the receptance coupling expression (Eq. 5.7) by including both translational (x) and rotational (θ) displacements due to forces and moments. By substituting Eq. 5.8 into Eq. 5.7, the direct and cross FRFs at the tool tip, which include both the translational and rotational degrees of freedom, can be shown as;

$$[H_{11}] = \begin{bmatrix} h_{A11,ff} & h_{A11,fM} \\ h_{A11,Mf} & h_{A11,MM} \end{bmatrix} - \begin{bmatrix} h_{A12,ff} & h_{A12,fM} \\ h_{A12,Mf} & h_{A12,MM} \end{bmatrix} [H_2]^{-1} \begin{bmatrix} h_{A21,ff} & h_{A21,fM} \\ h_{A21,Mf} & h_{A21,MM} \end{bmatrix} \tag{5.9}$$

$$[H_{12}]=\begin{bmatrix} h_{A12,ff} & h_{A12,fM} \\ h_{A12,Mf} & h_{A12,MM} \end{bmatrix}-\begin{bmatrix} h_{A12,ff} & h_{A12,fM} \\ h_{A12,Mf} & h_{A12,MM} \end{bmatrix}[H_2]^{-1}\begin{bmatrix} h_{A22,ff} & h_{A22,fM} \\ h_{A22,Mf} & h_{A22,MM} \end{bmatrix}$$

where

$$[H_2]^{-1}=\left\{\begin{bmatrix} h_{A22,ff} & h_{A22,fM} \\ h_{A22,Mf} & h_{A22,MM} \end{bmatrix}+\begin{bmatrix} h_{B22,ff} & h_{B22,fM} \\ h_{B22,Mf} & h_{B22,MM} \end{bmatrix}\right\}^{-1}$$

$$=\begin{bmatrix} h_{2,ff} & h_{2,fM} \\ h_{2,Mf} & h_{2,MM} \end{bmatrix}^{-1}=\frac{1}{h_{2,Mf}^2-h_{2,MM}h_{2,ff}}\begin{bmatrix} -h_{2,MM} & h_{2,fM} \\ h_{2,Mf} & -h_{2,ff} \end{bmatrix}$$

where $h_{2,ij} = (h_{A22,ij}+h_{B22,ij})$ for each element ($i,j \rightarrow f, M$) in the matrix. Furthermore, $h_{2,Mf}$ and $h_{2,fM}^T$ are equal due to reciprocity. Substituting $[H_2]^{-1}$ into Eq. 5.9 leads to:

$$[H_{11}]=\begin{bmatrix} h_{A11,ff} & h_{A11,fM} \\ h_{A11,Mf} & h_{A11,MM} \end{bmatrix}-$$
$$\frac{1}{h_{2,Mf}^2-h_{2,MM}h_{2,ff}}\begin{bmatrix} h_{A12,ff} & h_{A12,fM} \\ h_{A12,Mf} & h_{A12,MM} \end{bmatrix}\begin{bmatrix} -h_{2,MM} & h_{2,fM} \\ h_{2,Mf} & -h_{2,ff} \end{bmatrix}\begin{bmatrix} h_{A21,ff} & h_{A21,fM} \\ h_{A21,Mf} & h_{A21,MM} \end{bmatrix}$$

$$[H_{12}]=\begin{bmatrix} h_{A12,ff} & h_{A12,fM} \\ h_{A12,Mf} & h_{A12,MM} \end{bmatrix}-$$
$$\frac{1}{h_{2,Mf}^2-h_{2,MM}h_{2,ff}}\begin{bmatrix} h_{A12,ff} & h_{A12,fM} \\ h_{A12,Mf} & h_{A12,MM} \end{bmatrix}\begin{bmatrix} -h_{2,MM} & h_{2,fM} \\ h_{2,Mf} & -h_{2,ff} \end{bmatrix}\begin{bmatrix} h_{A22,ff} & h_{A22,fM} \\ h_{A22,Mf} & h_{A22,MM} \end{bmatrix}$$

The first elements in the matrices $[H_{11}]$ and $[H_{12}]$ are:

$$H_{11}(1,1)=\frac{x_1}{f_1}=h_{A11,ff}+\frac{1}{h_{2,Mf}^2-h_{2,MM}h_{2,ff}}[h_{A21,MF}(-h_{2,Mf}h_{A12,ff}+h_{A12,Mf}h_{2,ff})$$
$$+h_{A21,ff}(-h_{2,Mf}h_{A12,Mf}+h_{2,MM}h_{A12,ff})] \tag{5.10}$$

$$H_{12}(1,1)=\frac{x_1}{f_2}=h_{A12,ff}+\frac{1}{h_{2,Mf}^2-h_{2,MM}h_{2,ff}}[h_{A22,MF}(-h_{2,Mf}h_{A12,ff}+h_{A12,Mf}h_{2,ff})$$
$$+h_{A22,ff}(-h_{2,Mf}h_{A12,Mf}+h_{2,MM}h_{A12,ff})] \tag{5.11}$$

The FRFs of the free-free end mill can be evaluated with the analytical method (see Appendix B) or the Finite Element model of the beam, thus the elements (h_{A11}, h_{A12}, h_{A21}, h_{A22}) in *Substructure A* can be evaluated using a predetermined damping ratio (i.e., $\zeta =$

0.01) for the tool material (i.e., carbide). The FRF values at the joint ($h_{2,Mf}$, $h_{2,ff}$, $h_{2,MM}$) are required. The direct transfer function $h_{2,ff} = (h_{A,22,ff} + h_{B22,ff})$ can be evaluated by measuring the spindle with a short blank at point *2* ($h_{B22,ff}$) and $h_{A22,ff}$ is obtained from the free-free beam model. The remaining two ($h_{2,Mf}$, $h_{2,MM}$) reflect the rotational degree of freedom of the assembly, and it is difficult to experimentally measure directly at the joint. We need to apply both force and moment at the joint (*2*) for the experimental evaluation of the joint properties, which is not a practical exercise on the production floor. Instead, a practical methodology based on the two sets of equations (Eqs. 5.10 and 5.11), which have common FRF terms, are proposed. Eqs. 5.10 and 5.11 can be rewritten as:

$$\begin{aligned} u &= a + \frac{f(-\beta b + ek) + c(-\beta e + \delta b)}{\beta^2 - \delta k} \\ v &= b + \frac{g(-\beta b + ek) + d(-\beta e + \delta b)}{\beta^2 - \delta k} \end{aligned} \tag{5.12}$$

where

$$\begin{aligned} &H_{11}(1,1) = u,\ H_{12}(1,1) = v \\ &h_{A11,ff} = a,\ h_{A12,ff} = b,\ h_{A21,ff} = c,\ h_{A22,ff} = d \\ &h_{A12,Mf} = e,\ h_{A21,Mf} = f,\ h_{A22,Mf} = g,\ h_{2,ff} = k \\ &h_{2,Mf} = \beta, h_{2,MM} = \delta \end{aligned}$$

The equations are reduced to the following form:

$$(\beta^2 - \delta k)(u - a) - f(-\beta b + ek) - c(-\beta e + \delta b) = 0 \tag{5.13}$$

$$(\beta^2 - \delta k)(v - b) - g(-\beta b + ek) - d(-\beta e + \delta b) = 0 \tag{5.14}$$

Two unknowns in above Eqs. 5.13 and 14 are β and δ. Through the utilization of the symbolic non-linear analytical toolbox [Matlab], the unknowns are expressed as:

$$\beta = (-kug + kfv + kag - kfb + fdb - cbg)/(ad - ud - cb + cv) \tag{5.15}$$

$$\delta = \frac{1}{(ab-ud-cb+cv)^2}[kf^2v^2 + (2kagf + bf^2d\text{-}2kugf\text{-}ec^2g + defc\text{-}2bkf^2\text{-}bfcg)v\text{-}d^2efu$$
$$+ d^2efa + g^2ka^2\text{-}decga + decgu + g^2ku^2 + bdgfa\text{-}2g^2kua + bec^2g\text{-}bdgfu\text{-}bdefc + 2bkugf$$
$$+ b^2kf^2\text{-}2bkagf + bg^2cu + b^2fcg\text{-}b^2f^2d\text{-}bg^2ca]$$

Therefore, the rotational degrees of freedom FRFs, $h_{B22,Mf}$ and $h_{B22,MM}$ can be obtained as:

$$\begin{aligned} h_{B22,Mf} &= \beta - h_{A22,Mf} \\ h_{B22,MM} &= \delta - h_{A22,MM} \end{aligned} \tag{5.16}$$

It is proposed that one short and one long blank cylinder are used as calibration gauges. The short cylinder is used to identify the spindle - tool holder assembly dynamics ($h_{B,22,ff}$) and the long cylinder is used to identify the joint parameters ($h_{2,Mf}$, $h_{2,MM}$). Direct ($H_{11}(1,1) = x_1/f_1$) and cross ($H_{12}(1,1) = x_1/f_2$) transfer functions of the system with a long cylinder can be measured by attaching the accelerometer at point (*1*), and applying impact tests at both points *1* and *2*. Since $H_{11}(1,1)$ and $H_{12}(1,1)$ are now available, the two unknown FRF parameters ($h_{2,Mf}$, $h_{2,MM}$) can be extracted directly from Eqs. 5.15 and 16, and stored as constant properties of the spindle-tool holder assembly. After keeping the spindle-tool holder FRF parameters ($h_{2,Mf}$, $h_{2,ff}$, $h_{2,MM}$) in a constant database and the FRF (h_{A11}, h_{A12}, h_{A21}, h_{A22}) of a free - free end mill of any geometry identified with the FE analysis, one can evaluate the FRF of a tool-spindle assembly (x_1/f_1) using Eq. 5.10.

5.2 COUPLING OF FORCE SENSOR AND SPINDLE-TOOL STRUCTURE ASSEMBLY

For the dynamic compensation of cutting forces, the force/force transfer function between the tool and sensor ($\Phi_{31} = F_3/F_1$) is needed. The receptance coupling equation

from Eq. 5.6, element *(3,1)* is used to show the cross FRF from the tool tip to the force sensors:

$$H_{31} = \frac{x_3}{F_1} = H_{B,32}(H_{A,22} + H_{B,22})^{-1} H_{A,21}$$

$$\begin{bmatrix} H_{31,ff} & H_{31,fM} \\ H_{31,Mf} & H_{31,MM} \end{bmatrix} = \begin{bmatrix} H_{B32,ff} & H_{B32,Mf} \\ H_{B32,fM} & H_{B32,MM} \end{bmatrix} \left(\begin{bmatrix} H_{A22,ff} & H_{A22,Mf} \\ H_{A22,fM} & H_{A22,MM} \end{bmatrix} + \begin{bmatrix} H_{B22,ff} & H_{B22,Mf} \\ H_{B22,fM} & H_{B22,MM} \end{bmatrix} \right)^{-1} \begin{bmatrix} H_{a21,ff} & H_{A21,Mf} \\ H_{A21,fM} & H_{A21,MM} \end{bmatrix} \tag{5.17}$$

The FRFs of the tool ($H_{A,22}, H_{A,21}$) are evaluated from the Finite Element model of the Timoshenko beam (i.e. the end mill). The comparison of the FRFs between the analytical and the FE methods show no difference when the uniform beams are used. However, the analytical beam analysis is difficult when the tool does not have a uniform diameter. The FRFs of the joint at the spindle end can be obtained through the experimental measurements for $h_{B22,ff}$ and the RDOF FRFs ($h_{B22,Mf}$, $h_{B22,MM}$) can be obtained through the utilization of the algorithm shown in Eqs. 5.15 and 5.17. The cross FRF ($H_{B,32}$) is required for the overall coupling. Since the structure will have the same eigenvalues, regardless of force/force or displacement/force measurements, it can be assumed that the force is transmitted to the sensor via a spring, k_s, as;

$$\Phi_{32} = \frac{F_3}{F_2} = \frac{x_3}{F_2} \times k_s = H_{B32,ff} \times k_s \tag{5.18}$$

where k_s is the scaling factor representing the spring constant of the sensor. Therefore, the receptance ($H_{B32,ff} = x_3 / F_2$) between the spindle end (*2*) and the spindle sensor location (*3*), as well as the FRF of the force transmission ($\Phi_{32} = F_3 / F_2$) are measured by impact modal tests, see Figure 5.2.

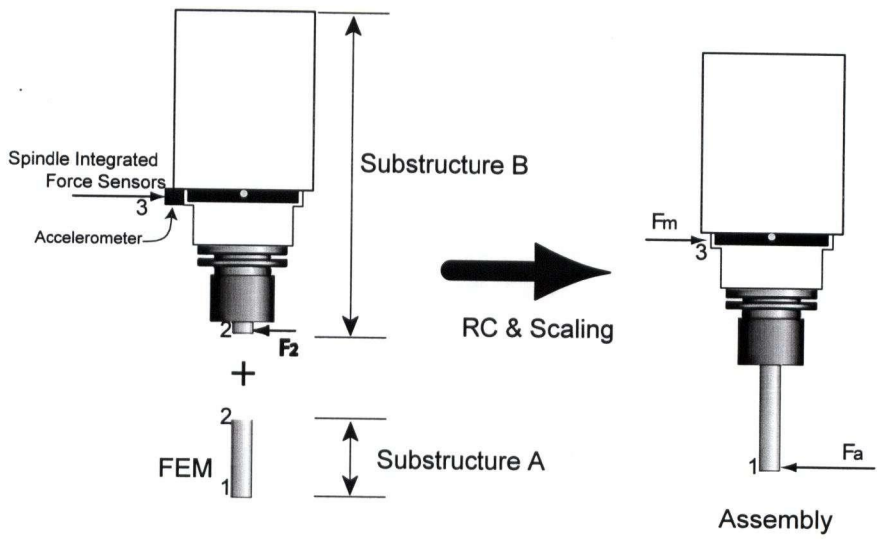

Figure 5.2. Coupling of force/force cross transfer function with an arbitrary end mill

The sensor spring constant (k_s) is identified by evaluating the ratio $k_s = \Phi_{32} / H_{B32,ff}$ using a least square method, which leads to $k_s = 3.13 \times 10^8 [N/m]$ for the spindle assembly with the mechanical chuck as shown in Figure 5.3. The prediction accuracy would have been better if it was possible to load and measure the spindle exactly at the sensor locations. However, the sensors are buried in the assembly. The discrepancies between the displacement/force and scaled force/force FRFs are mainly due to nonlinearities in the spindle structure and noise in the measurements.

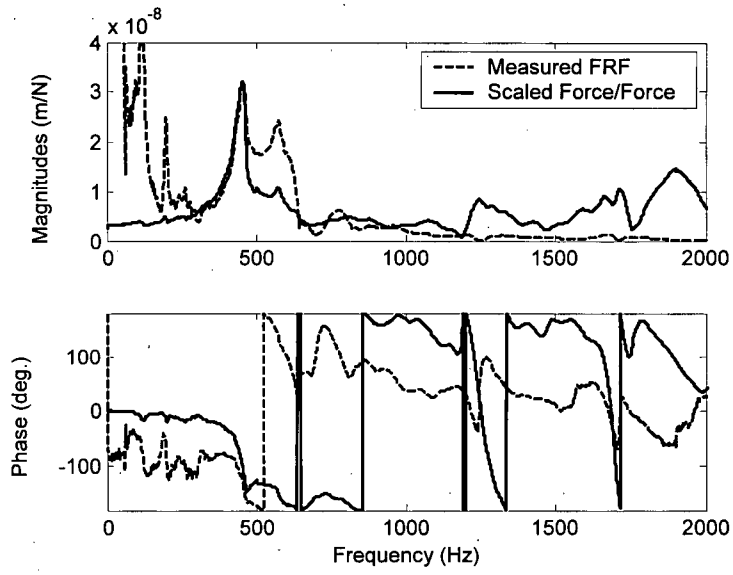

Figure 5.3. Cross transfer functions ($H_{B,32}$) measured from experimental analysis using the accelerometer and scaled from force/force transfer function

When we assume that the cross RDOF FRFs for $H_{B,32}$ (i.e., $h_{B32,Mf}$, $h_{B32,fM}$) are very close to zero, Eq. 5.17 (1,1) becomes as:

$$H_{31,ff} \approx -h_{B32,ff} \frac{\left(h_{2,MM} h_{A21,ff} - h_{2,Mf} h_{A21,Mf}\right)}{\left(-h_{2,ff} h_{2,MM} + h_{2,Mf}{}^{2}\right)} \tag{5.19}$$

In summary, the transfer function between the force applied at the tool tip (F_1) and the force measured at the spindle integrated force sensor (F_3) is evaluated by;

$$\Phi_{31}(s) = \frac{F_3}{F_1} = k_s H_{31,ff}(s) \tag{5.20}$$

where $H_{31,ff}$ can be evaluated from Eq. 5.19 by substituting measured and analytically obtained FRFs. The procedure is repeated in both feed and normal directions of the spindle in order to reconstruct the cutting forces in the plane of cut.

5.3 EXPERIMENTAL RESULTS

The proposed system is experimentally evaluated on the three axis vertical machining center. The force sensors are integrated to the spindle as shown in Figure 5.1. Three carbide-cylindrical blanks are used to identify the spindle and joint dynamic properties, see Figure 5.4. The density and the modulus of the carbide blanks, which are used as end mill materials, are 14,450 kg/m^3 and 5.8e11 N/m^2, respectively. The blanks are pushed 20 mm inside the collet of the mechanical chuck in all cases. The proposed method is verified in milling experiments conducted with a four fluted carbide end mill with the mechanical chuck. A short blank cylinder with 19.05 mm diameter is inserted in the chuck through the collet.

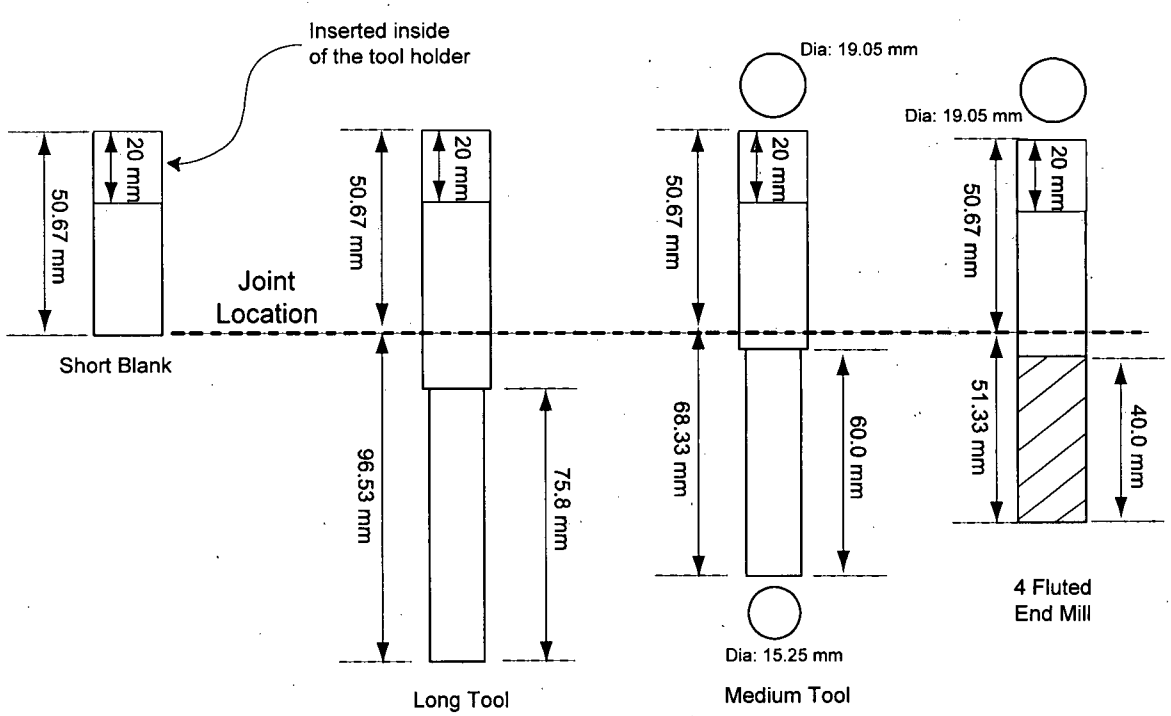

Figure 5.4. The cylindrical blanks and the Four fluted end mill used in identifying the spindle-tool holder joint dynamics.

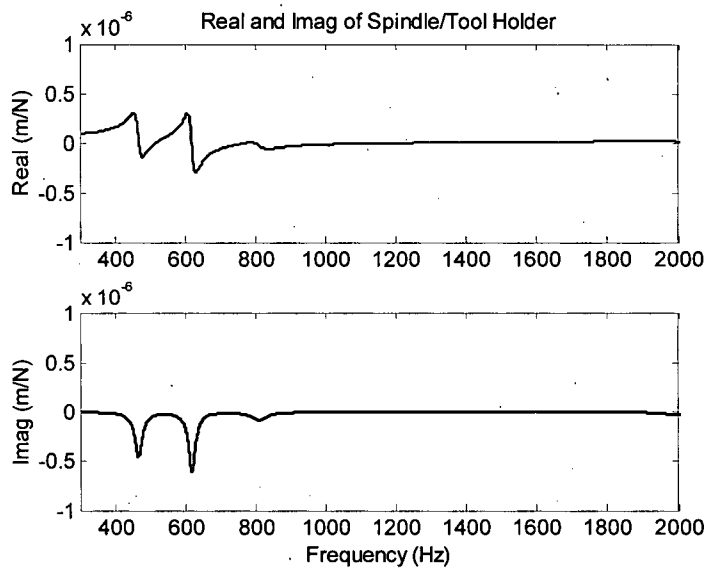

(a) FRF of Spindle / Tool Holder measured with impact tests.

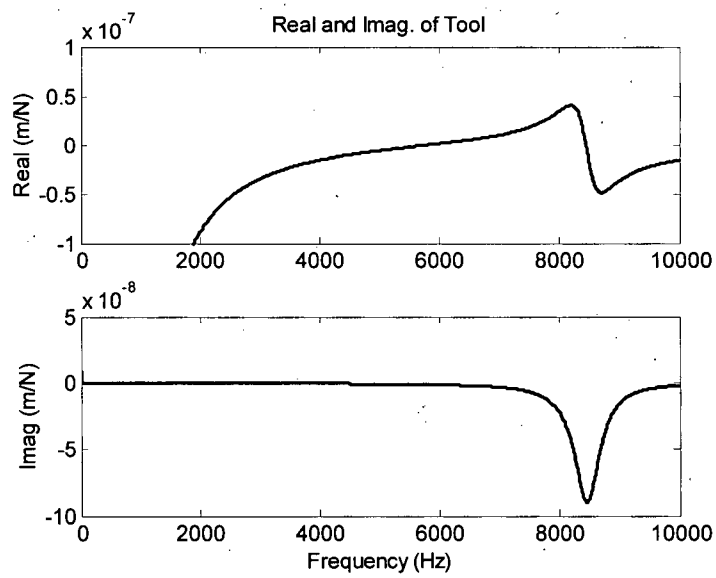

(b) FRF of the long blank identified with Finite Element method.

Figure 5.5. Frequency responses of Spindle / Tool holder and long blank.

Impact tests are applied at the short blank's end to obtain the FRFs of the spindle system ($h_{B22,ff}$, Eq. 5.9). Figure 5.5(a) shows the translational part of this response. The spindle system has three dominant modes at 465, 617 and 812 Hz, respectively. Figure 5.5(b) shows the FE-based free-free response of the long tool substructure modeled using Timoshenko beam elements as depicted in Figure 5.6. We have also used Bernoulli-Euler beam elements, and the differences between FRFs obtained using the two beam elements are negligible since the first non-rigid body mode of the tool occurs at approximately 8400 Hz. From the FE analysis, translational and rotational frequency responses of each tool at its two ends are obtained by applying forces and moments at the two ends and calculating nodal and rotational displacements. The damping ratio used for the FE beam analysis is 1% which is based on several impact tests. The tool model should be in free-free condition because the rigid modes of the tool play a significant role in the coupling of substructures.

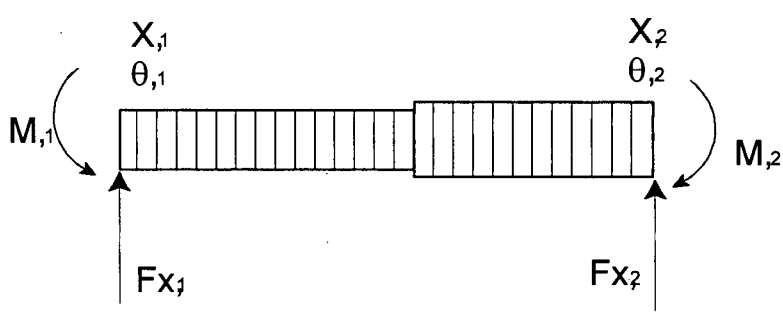

Figure 5.6. Finite Element Analysis of the Tool

Figure 5.7 shows the comparison between the experimental and predicted receptance coupling results at the tool tip based on the first element (H_{11}) of Eq. 5.9 without the RDOF FRFs (i.e., $h_{B22,Mf}$ and $h_{B22,MM}$ are zero) for the spindle with the long length blank. The first three dominant modes occur very close to the modes of the

spindle system without tool, which show that these modes are clearly contributed by the spindle. The fourth mode for the long blank is at 1015 Hz, which is due to the interaction between the tool and the spindle system. The prediction is inaccurate in Figure 5.7, and some modes, which are due to rotational joint dynamics (i.e. 1015 Hz), are not even visible when RDOF FRFs are neglected. In this study, first, the rotational DOF FRFs (i.e., $h_{B22,Mf}$ and $h_{B22,MM}$) are acquired by making a second impact test applied to the medium length blank inserted to the spindle using Eqs. 5.15 and 16, and the obtained RDOF FRFs are depicted in Figure 5.8. The receptance coupling result at the tool tip with the consideration of the obtained RDOF FRFs is shown in Figure 5.9 for the spindle with the long length blank. The prediction accuracy is excellent for the first, and quite acceptable for the second mode.

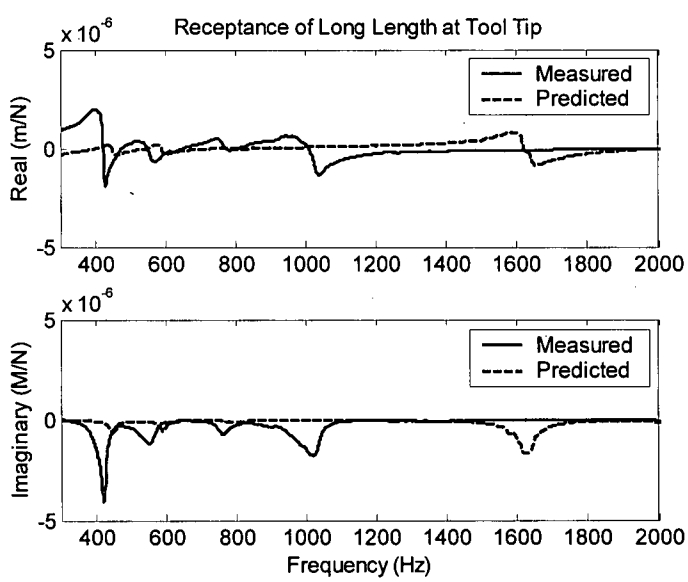

Figure 5.7. Predicted and measured FRF of the long blank attached to the spindle when the rotational dynamics are neglected.

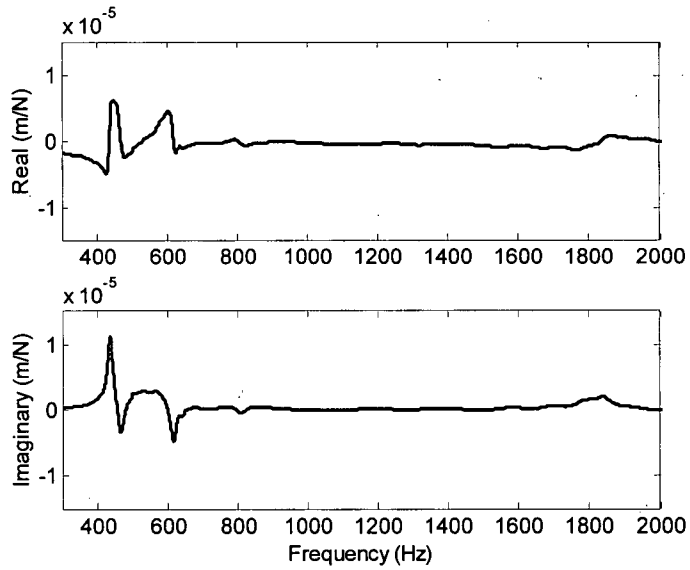

(a) RDOF FRF ($h_{B22,Mf}$)

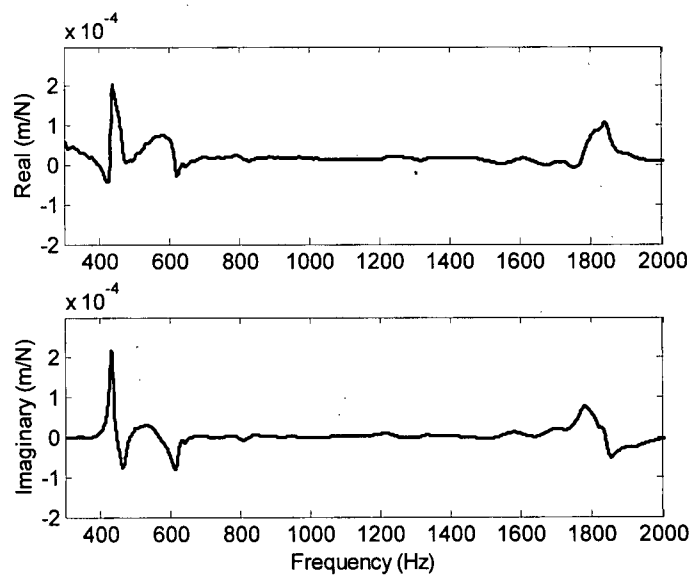

(b) RDOF FRF ($h_{B22,MM}$)

Figure 5.8. Identified Rotational FRFs at the free end of the short blank attached to the spindle.

Based on the observations from Figures 5.7 and 5.8, the magnitude of the translational FRF is of order of 10^{-6}, while the magnitudes for the translational/rotational FRFs ($h_{B22,Mf}$ and $h_{B22,fM}$) and for the rotational FRF ($h_{B22,MM}$) are of orders 10^{-5} and 10^{-4}, respectively. This observation helps us to understand that the RDOF responses have the largest contribution to the flexibility of the assembled structure, and their inclusion in the coupling analysis is crucial in predicting the FRF of the spindle-tool assembly accurately.

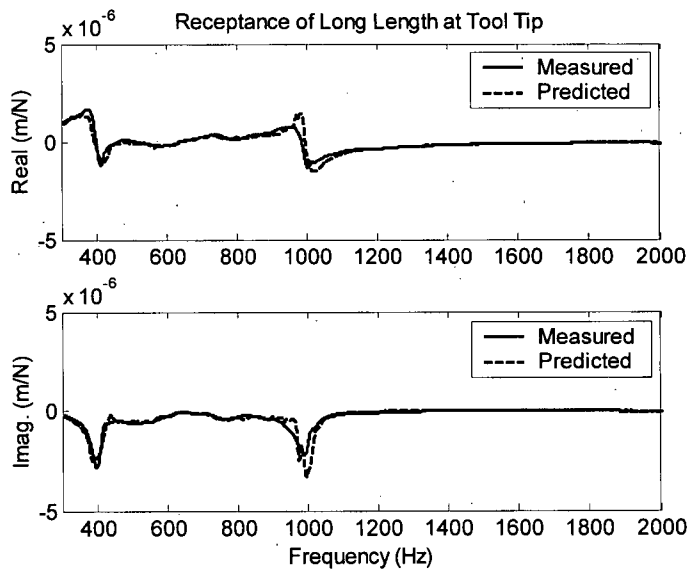

Figure 5.9. Predicted and measured FRF of the long blank attached to the spindle when the rotational dynamics are considered.

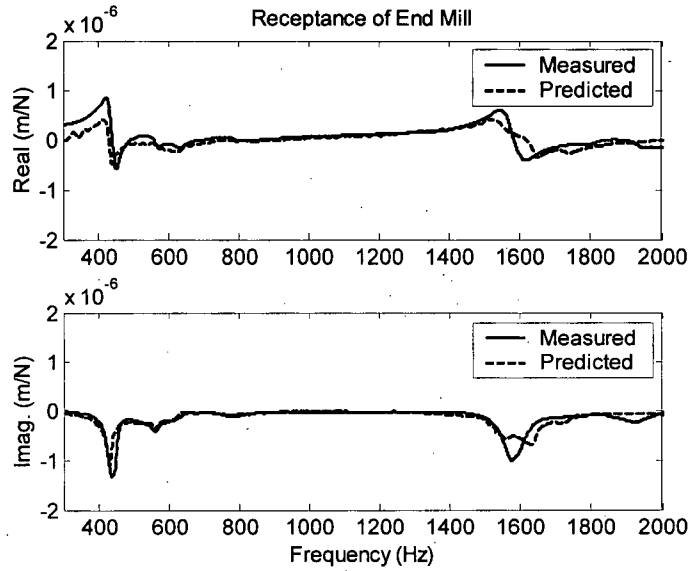

Figure 5.10 Comparison between Measured and Predicted (RC) FRFs for four fluted end mill with RDOF FRFs acquired from the medium tool

A four fluted carbide end mill with 19.05 mm diameter and 82 mm stick out from the collet is tested on a vertical machining center. The fluted section of the end mill (i.e., 40 mm) is considered to be 80 % of the total diameter [Kops 90] in the Finite Element model. The measured and predicted FRF of the end mill attached to the spindle is shown in Figure 5.10. The prediction accuracy is good for the first mode (465 Hz), and quite acceptable for the second dominant mode around 1600 Hz.

CASE STUDY 1: DIFFERENT MACHINE

The Receptance Coupling method is also tried on the different machine (i.e., Sajo Knee Type Milling Machine). The medium length tool is used to recalculate the RDOF response for the Sajo milling machine. Then, the FRF of the long length tool is predicted as illustrated in Figure 5.11. The comparison between the predicted and the measured

values illustrates a good agreement with each other. Thus, the Receptance Coupling method can be applied for different machine tools.

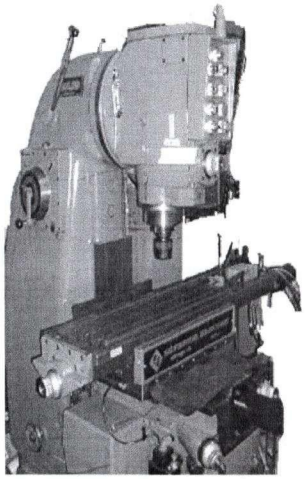

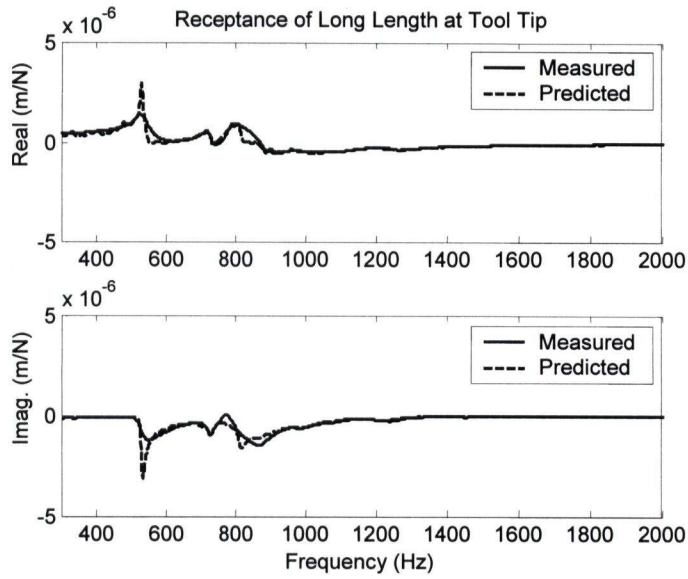

Figure 5.11 Comparison between Measured and Predicted (RC) FRFs for Sajo VMC with Long length tool with RDOF FRFs acquired from the medium tool

CASE STUDY 2: DIFFERENT DIAMETER TOOLS

In this case study, the effects of different diameter tools on the RC are investigated.

First, the different diameter effects on the FRFs for the short tools are examined (i.e., dynamics of the spindle and tool holder). The FRF is measured with the shorter stick out length (i.e., 15 mm instead of 30.87 mm) of the small tool for ¾", and 1" diameters (i.e., to predict spindle/tool holder dynamics). The obtained FRFs for the small cylinder exhibit very similar translational FRFs as shown in Figure 5.12. Therefore, diameters of the small blank cylinders do not significantly affect the FRFs because the mass of the tool is insignificant compared with the rest of the spindle structure.

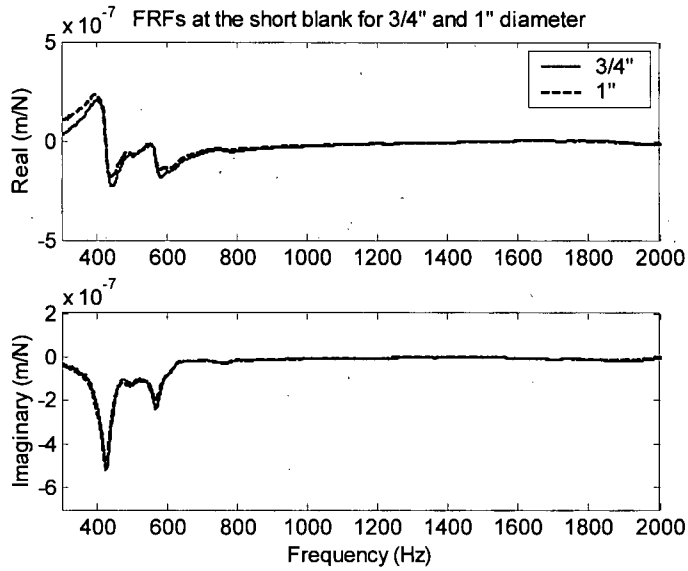

Figure 5.12 Comparison of the FRFs at the short blank using different diameter cylinders mounted on the spindle

Second, the RDOF response from ¾" (19.05 mm) diameter tool is used to couple the ½" (12.7 mm) and 1" (25.4 mm) tools. The small tool FRF (i.e., spindle dynamics, $h_{B22,ff}$) using ¾" diameter instead of responses from ½" and 1" tools is also utilized to prove the first hypothesis (i.e., independency of diameters for the short blank). Both the tools are made from the same carbide materials as other tools. Figure 5.12 (a) depicts the FRF prediction through the Receptance Coupling of 1" (25.4 mm) diameter tool with the stick out length of 128.9 mm. The experimental FRF versus the Receptance Coupled FRF show a very good match even when the RDOF response from the ¾" tool is used. Similarly, Figure 5.12 (b) illustrates the FRF prediction of the Receptance Coupled response using the ½" (12.7 mm) diameter tool with the stick out length of 128.9 mm. The comparison between the experimental and predicted responses shows a comparatively good match except at 630 Hz mode. This discrepancy may have come from measurement errors especially due to high frequency residual modes. Thus, the

RDOF response can be used for other diameter tools with cautions especially for coupling with small diameter tools.

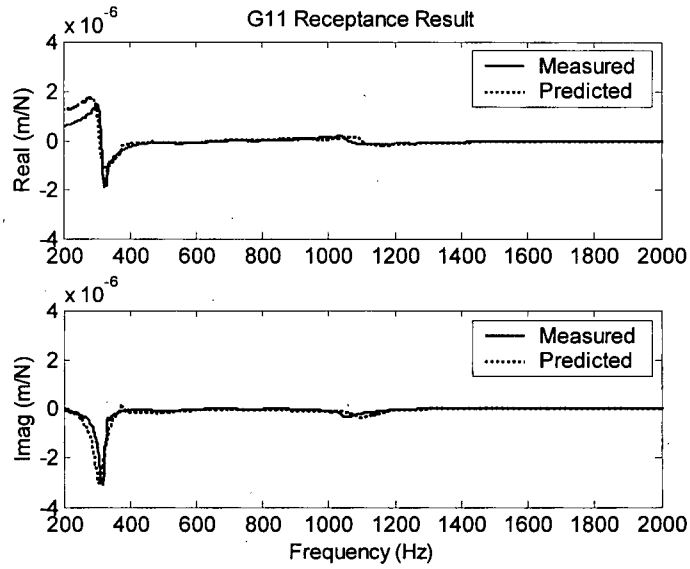

(a) Uniform 25.4 mm (1") Diameter Tool (stick out length is 128.9 mm)

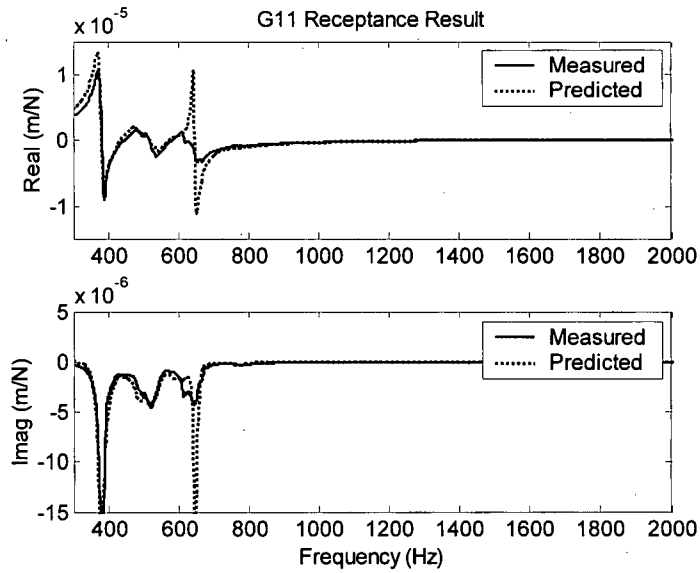

(b) Uniform 12.7 mm (0.5") Diameter Tool (stick out length is 128.9 mm)

Figure 5.13 Receptance Coupling using the RDOF response obtained from 19.05 mm diameter tool

FORCE / FORCE DYNAMICS COUPLING

The coupling of the tool and the spindle dynamics for force/force FRFs are depicted in Figure 5.14 using the four fluted end mill which is mounted on the mechanical chuck. The assembled receptances are first acquired, and then the scaling factor is applied to the receptances to get the force/force FRFs (see Eq. 5.20). The effective diameter (80 % of the total diameter) is used for the fluted section of the end mill. The predicted FRFs show very good matches between the experimental results, especially below 1200 Hz. Therefore, the assumption that cross RDOF FRFs for $H_{B,32}$ (i.e., $h_{B32,Mf}$, $h_{B32,fM}$) are very close to zero is legitimate because acquiring the cross RDOF response is exceptionally difficult. When these RDOF FRFs for the spindle part are accessible the accuracy can be further improved.

The predicted cross transfer function is fitted by a modal curve fitting technique, which leads to the following:

$$\Phi_{31}(s) = \frac{F_3(s)}{F_1(s)} = \sum_{k=1}^{3} \frac{\alpha_k^{-1} \cdot \omega_{n,k}^{2}}{s^2 + 2\xi_k \omega_{n,k} s + \omega_{n,k}^{2}} \tag{5.21}$$

where k is the number of modes, F_3 is the measured force from the spindle integrated force sensor and F_1 is the applied force at the tool tip. The fitted modal parameters in X direction are identified as:

Mode	ω_n	ζ	α
1	*432 Hz*	*0.048*	*0.9311*
2	*579 Hz*	*0.045*	*-3.393*
3	*1272 Hz*	*0.021*	*4.840*

Based on the estimated transfer function, an exemplar dynamic compensation is carried out at 7000 rev/min (see Appendix C).

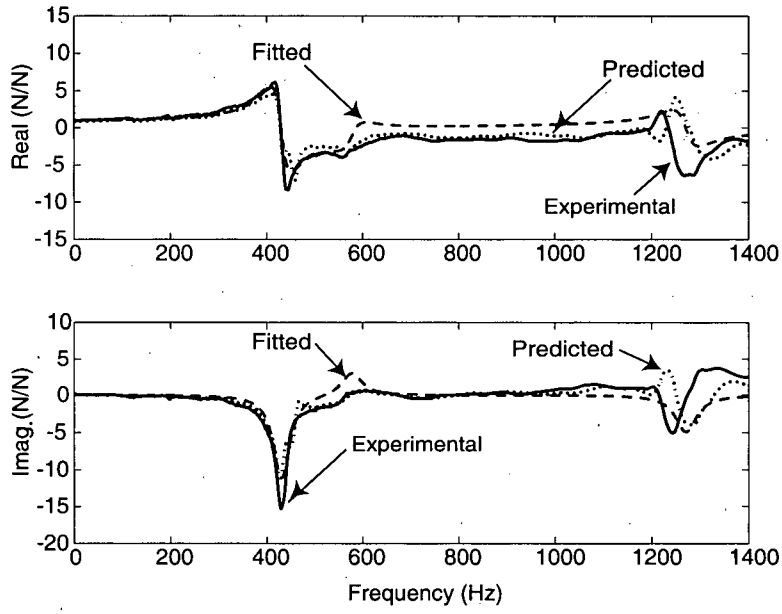

Figure 5.14. Coupling of Spindle and the End mill for force/force FRF and fitted FRF *(Experimental: impact hammer test response, Predicted: Receptance Coupled dynamics, Fitted: modal fitting of Predicted dynamics)*

5.4 DISCUSSIONS ON THE FLEXIBLE JOINT ANALYSIS

The initial attempt to use the flexible joint to couple the spindle and the tool substructures as outlined by many researchers [Schmitz 02, Tsai 88, Wang 90, Ren 95] did not lead to accurate identification. The connection between two structures such as joints is very difficult to model using an analytical approach. The intention of the joint identification is to minimize the difference between the measured assembled FRFs with the predicted or simulated FRFs through the identified joints. One of the major difficulties with the identification is various errors in the measurements which significantly affects the joint identification processes as well as the receptance coupling methods. We have assumed that two springs as shown in Figure 5.15 are the flexible

joint. In this flexible joint approach, the RDOF FRFs are assumed to be negligible because the flexible springs would offset the RDOF FRFs.

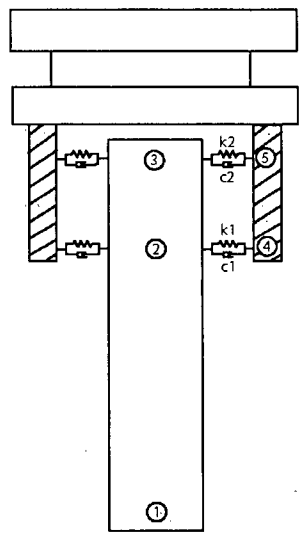

Figure 5.15 Coupling with flexible joint model (Collet and Tool)

For the model considered in Figure 5.15, the coupling equation is:

$$G_{11} = H_{11} - \{H_{12} \quad H_{13}\} \left(\begin{bmatrix} H_{22} & H_{23} \\ H_{32} & H_{33} \end{bmatrix} + \begin{bmatrix} H_{44} & H_{45} \\ H_{54} & H_{55} \end{bmatrix} + \begin{bmatrix} \dfrac{1}{k_1 + j\omega C_1} & \dfrac{1}{k_3 + j\omega C_3} \\ \dfrac{1}{k_3 + j\omega C_3} & \dfrac{1}{k_2 + j\omega C_2} \end{bmatrix} \right)^{-1} \begin{Bmatrix} H_{21} \\ H_{31} \end{Bmatrix} \tag{5.22}$$

The non-linear optimization algorithm by the Minimum Squared Error function (MSE) is applied to acquire the unknown spring and damping coefficients. However, some of the identified joint parameters are negative and may not have the physical representations. The difficulties with the non-linear optimization are that without the proper initial values, the optimization may converge at local minima instead of the global minima. The method may be beneficial since the RDOF response may not be needed and the tool

holder – tool dynamics can be used. However, the difficulties outweigh the benefits for our case because of the challenges associated with the joint parameters.

5.5 CONCLUSION

The receptance coupling technique is proposed to predict the dynamics of the end mill attached to the machine tool spindle. The machine-tool spindle assembly dynamics are measured using a short (30 mm stick out) blank inserted to the tool holder. The FRF of a free – free end mill is identified using the FE beam model. The rotational dynamics of the end mill – spindle assembly are extracted mathematically from the direct and cross FRF measurements applied to a medium length (70 mm stick out) blank attached to the spindle. The proposed method eliminates repetitive impact hammer tests of each tool attached to the spindle-tool holder system. The dynamics of the spindle and the joint are measured once and stored in a process planning database. RDOF FRFs between two substructures which are affected by the bending are very important for the receptance coupling. In this study, a new method is presented in determining the Rotational DOF FRFs from the two translational FRF measurements. The transfer function of the overall system is predicted by coupling the receptances of the analytically modeled end mill and the experimentally measured spindle structure. The coupled receptance measurements are then scaled with the spring constant to acquire the desired force/force cross transfer. Further study is needed to suppress measurement noise in order to accurately acquire the RDOF FRFs and needed to investigate the non-linearity effects on FRF measurements due to non-linearity of bearings on the spindle. The dynamic compensation of the spindle

integrated forces can be performed by obtaining the transfer function FRFs from the force sensors and applied at the tool tip with any arbitrary tool geometry.

CHAPTER 6.

DYNAMIC COMPENSATION OF CUTTING FORCES

The cutting forces are measured from the sensors embedded in the spindle housing, which has three dominant structural modes influencing the measurements. The modes distort the cutting forces and therefore, the compensation of the structure modes is vital for reconstructing cutting forces at high rotational speeds. Based on the experimentally obtained transfer function in X direction, an exemplar cutting compensation is performed using the disturbance Kalman Filter to acquire the estimated actual force at the tool tip from the force measured at the Spindle-Integrated sensors and vibrations measured at the accelerometer. Then, the compensation is extended to all three directions (i.e., feed, normal, and axial directions) using the disturbance Kalman Filter approach. The alternative force measurement from the non-contact capacitance type displacement sensor is also examined. The displacement signal is interpreted as the force signal through the calibration factor and the bandwidth of the displacement sensor is increased using the disturbance Kalman Filter. The force sensing and the proposed dynamic compensation method are experimentally verified. One of the significant features of this dynamic compensation method compared with others is that the method considers the system and measurement noise to optimally acquire the accurate cutting forces at the tool tip.

6.1 DISTURBANCE KALMAN FILTER COMPENSATION USING THE IDENTIFIED TRANSFER FUNCTION MODEL OF THE SPINDLE-INTEGRATED SENSORS

The objective of dynamic compensation of the spindle force sensor system is to reduce the influence of the three structural dynamic modes which distort the cutting force measurements. The Kistler table dynamometer (Kistler 9255B) set up is used as a reference force sensing system. The disturbance Kalman Filter is used to reconstruct the force signals where the estimator acts similarly to an inverse filter [Weihrich 78, Pritschow 99]. Prior to performing the compensation, unbalanced forces F_u, which may be caused by dynamic unbalance of the spindle system, are preprocessed by subtracting the air cutting forces from the measured forces at the Spindle-Integrated Force Sensors using the spindle encoder as a synchronization clock. Furthermore, the transfer function parameters of the system (Eqs. 4.6-4.8) are updated as a function of the spindle speed because the bearing stiffness may change at high spindle speeds. The experimental modal analyses are performed to acquire the FRFs with respect to the spindle rotational speeds from 1000 rpm to 12,000 rpm. Based on the observation, the first two modes are almost insensitive to the spindle speeds whereas the third modal frequency decreases by up to 12 % at 12,000 rpm due to centrifugal effects resulting from the bending of the spindle shaft. The details of the measured unbalanced force and changing dynamics due to the spindle rotations can be found in Appendix D. The thermal growth of the particular spindle is not a concern, since the air cutting forces do not change even after running the machine for a period of more than an hour (see Section 3.5). However, some

spindles may experience severe thermal growths when they are not cooled properly. The thermal growth increases the bearing preloads which shifts modal frequencies.

The transfer functions given in Eqs. 4.6 - 4.8 are mapped into the following state space form;

$$\begin{aligned} \dot{x} &= A_s x + B_s u \\ z &= C_s x \end{aligned} \tag{6.1}$$

where x is the state vector, $u = F_a$ is the input or the actual force applied to the tool, and $z = \{F_m \;\; Acc.\}^T$ is the measurement vector containing the measured cutting force from the spindle force sensor and the acceleration from the accelerometer, respectively. The aim of the Kalman Filter is to reconstruct the actual force (F_a) applied at the tool. Since the natural frequencies and damping ratios are the same for both the force and acceleration transfer functions, (i.e., poles of both Eqs. 4.7 and 4.8 are the same), the system matrix A_s is common. The measurement matrix C_s has two rows obtained from the zeros of the two transfer functions (Eqs. 4.7 and 4.8). The resulting state space equations representing the spindle dynamics can be expressed as follows [Dutton 97];

$$\begin{bmatrix} x_1 \\ x_2 \\ x_3 \\ x_4 \\ x_5 \\ x_6 \end{bmatrix} = \begin{bmatrix} -a_1 & -a_2 & -a_3 & -a_4 & -a_5 & -a_6 \\ 1 & 0 & 0 & 0 & 0 & 0 \\ 0 & 1 & 0 & 0 & 0 & 0 \\ 0 & 0 & 1 & 0 & 0 & 0 \\ 0 & 0 & 0 & 1 & 0 & 0 \\ 0 & 0 & 0 & 0 & 1 & 0 \end{bmatrix} \begin{bmatrix} x_1 \\ x_2 \\ x_3 \\ x_4 \\ x_5 \\ x_6 \end{bmatrix} + \begin{bmatrix} 1 \\ 0 \\ 0 \\ 0 \\ 0 \\ 0 \end{bmatrix} F_a$$

$$\begin{bmatrix} F_m \\ Acc. \end{bmatrix} = \begin{bmatrix} b_0 & b_1 & b_2 & b_3 & b_4 & b_5 \\ c_0 & c_1 & c_2 & c_3 & c_4 & c_5 \end{bmatrix} \begin{bmatrix} x_1 \\ x_2 \\ x_3 \\ x_4 \\ x_5 \\ x_6 \end{bmatrix} \tag{6.2}$$

where the system polynomial parameters are given in Eqs. 4.7 and 4.8. The matrices A_s and C_s contain both very large and very small numbers which result in poorly conditioned matrices with respect to the inversion of matrices and eigenvalues analysis. Consequently, the system matrices are transformed into an equivalent system (i.e., $x_n = Tx$) by applying the transformation matrix T as follows;

$$\begin{aligned} \dot{x}_n &= A_n x_n + B_n u \\ z &= C_n x_n \end{aligned} \tag{6.3}$$

$$A_n = TA_sT^{-1},\ B_n = TB_s / \lambda,\quad C_n = \lambda C_s T^{-1}$$

where λ is the scalar factor and T is the similarity transformation matrix. λ is determined to be 1 for the force transfer function and 0.5 for the acceleration transfer function. The similarity transformation matrix, T, for the sensor system is found based on the algorithm in [Anderson 99] to be:

$$T = diag([64\ \ 1.048e6\ \ 8.589e9\ \ 3.518e13\ \ 1.441e17\ \ 2.95e20]) \tag{6.4}$$

The identified equivalent state matrices are:

$$A_n = \begin{bmatrix} -752 & -4220.9 & -250.55 & -2504.8 & -150.4 & -1690 \\ 16384 & 0 & 0 & 0 & 0 & 0 \\ 0 & 8192 & 0 & 0 & 0 & 0 \\ 0 & 0 & 4096 & 0 & 0 & 0 \\ 0 & 0 & 0 & 4096 & 0 & 0 \\ 0 & 0 & 0 & 0 & 2048 & 0 \end{bmatrix}$$

$$B_n = [64 \quad 0 \quad 0 \quad 0 \quad 0 \quad 0]^T$$

$$C_n = \begin{bmatrix} 0 & 20.432 & 1.1567 & 22.791 & 2.6111 & 46.14 \\ 0 & 5.671 & 0.323 & 5.997 & 0.355 & 5.521 \end{bmatrix}$$

Furthermore, the observability matrix, W, is found to be full rank, which guarantees the observability of the state space model of the system.

$$W^T = [C_n^T \quad A_n^T C_n^T \quad \cdots \quad (A_n^{n-1}) C_n^T] \tag{6.5}$$

MODEL EXPANSION

The modeled spindle system dynamics can be expanded to include the input force (F_a) as one of the unknown states. If a sampling frequency is quite high relative to a tooth passing frequency, the input forces can be treated to be piecewise constant so that the derivative of the input is only a function of process noise. If a sampling frequency is low, a more general scheme can be used so that the input cutting forces (F_a) at the tool tip consist of the harmonic component, denoted by 'ac' and the dc (static) component, denoted by 'dc' as shown below:

$$F_a = F_{a\_dc} + F_{a\_ac} \tag{6.6}$$

The dc component of the cutting force is constant, which would make the derivative of the dc input as a function of the dc process noise, w_{dc}, only:

$$\dot{F}_{a\_dc} = 0F_{a\_dc} + w_{dc} \tag{6.7}$$

Whereas, the dynamics of the ac component of the cutting force is assumed to be a harmonic function at the tooth passing frequency, which is represented as a cosine function with the periodic disturbance, w_{ac}. The Laplace domain representation of the harmonic part of the force is expressed as;

$$\frac{\hat{F}_{a\_ac}(t)}{w_{ac}(t)} = \cos\omega_T t \overset{Laplace}{\Longrightarrow} \frac{\hat{F}_{a\_ac}(s)}{w_{ac}(s)} = \frac{s}{s^2 + \omega_T^{\ 2}} \tag{6.8}$$

where ω_T is the tooth passing frequency which can be defined as the number of revolutions per second multiplied by the number of teeth on the cutter. The state space equivalent of Eq. 6.8 is:

$$\begin{aligned} \dot{x}_F &= A_F x_F + G_F w_{ac} \\ \hat{F}_{a\_ac} &= C_F x_F \end{aligned} \tag{6.9}$$

where

$$A_F = \begin{bmatrix} 0 & -\omega_T^2 \\ 1 & 0 \end{bmatrix};\ G_F = \begin{bmatrix} 1 \\ 0 \end{bmatrix};\ C_F = \begin{bmatrix} 1 & 0 \end{bmatrix};\ x_F = \begin{bmatrix} x_{F1} \\ x_{F2} \end{bmatrix} \tag{6.10}$$

By substituting Eqs. 6.6 and 6.9 into Eq. 6.3, the overall state space equation then becomes:

$$\begin{aligned} \dot{x}_n &= A_n x_n + B_n\left(F_{a\_dc} + F_{a\_ac}\right) = A_n x_n + B_n\left(F_{a\_dc} + C_F x_F\right) \\ z &= C_n x \end{aligned} \tag{6.11}$$

The actual cutting force applied on the tool can be considered as one of the unknown states by expanding Eq. 6.11:

$$\begin{aligned} \dot{x}_{e(9\times1)} &= A_{e(9\times9)} x_{e(9\times1)} + \Gamma_{(9\times1)} w \\ z_{(2\times1)} &= C_{e(2\times9)} x_{e(9\times1)} + v_{(2\times1)} \end{aligned} \tag{6.12}$$

where w is the system disturbance and v is the measurement noise. The expanded state vector is depicted as:

$$x_{e(9\times1)} = [x_{n(1\times6)} \; F_{a\_dc(1\times1)} \; x_{F(1\times2)}]^T, u_e = [0] \tag{6.13}$$

The expanded state space model in Eq. 6.12 can be re-written as;

$$\begin{bmatrix} \dot{x}_{n(6\times1)} \\ \dot{F}_{a\_dc(1\times1)} \\ \dot{x}_{F(2\times1)} \end{bmatrix} = \begin{bmatrix} A_{n(6\times6)} & B_{n(6\times1)} & B_n C_{F(6\times2)} \\ 0_{(1\times6)} & 0_{(1\times1)} & 0_{(1\times2)} \\ 0_{(2\times6)} & 0_{(2\times1)} & A_{F(2\times2)} \end{bmatrix} \begin{bmatrix} x_{n(6\times1)} \\ F_{a\_dc(1\times1)} \\ x_{F(2\times1)} \end{bmatrix} + \begin{bmatrix} 0_{(6\times1)} \\ \theta_{dc(1\times1)} \\ \theta_{ac(2\times1)} \end{bmatrix} w \tag{6.14}$$

$$z_{(2\times1)} = \begin{bmatrix} C_{n(2\times6)} & 0_{(2\times1)} & 0_{(2\times2)} \end{bmatrix} \begin{bmatrix} x_{n(6\times1)} \\ F_{a\_dc(1\times1)} \\ x_{F(2\times1)} \end{bmatrix}$$

where θ_{dc} and θ_{ac} are the ratio between w_{dc} and w_{ac} with respect to w. The expanded state vector can be estimated through the expanded disturbance Kalman Filter of the Spindle-Integrated Force Sensor system which can be shown as:

$$\begin{aligned} \dot{\hat{x}}_e &= A_e \hat{x}_e + K(z - \hat{z}) = A_e \hat{x}_e + K(z - C_e \hat{x}_e) \\ &= (A_e - KC_e)\hat{x}_e + K z \\ \hat{z}_o &= C_o \hat{x}_e = \hat{F}_a, \quad where\ C_o = [0 \;\; 1 \;\; C_F] \end{aligned} \tag{6.15}$$

where K is the continuous Kalman Filter gain. Figure 6.1 depicts the expanded Kalman Filter configuration.

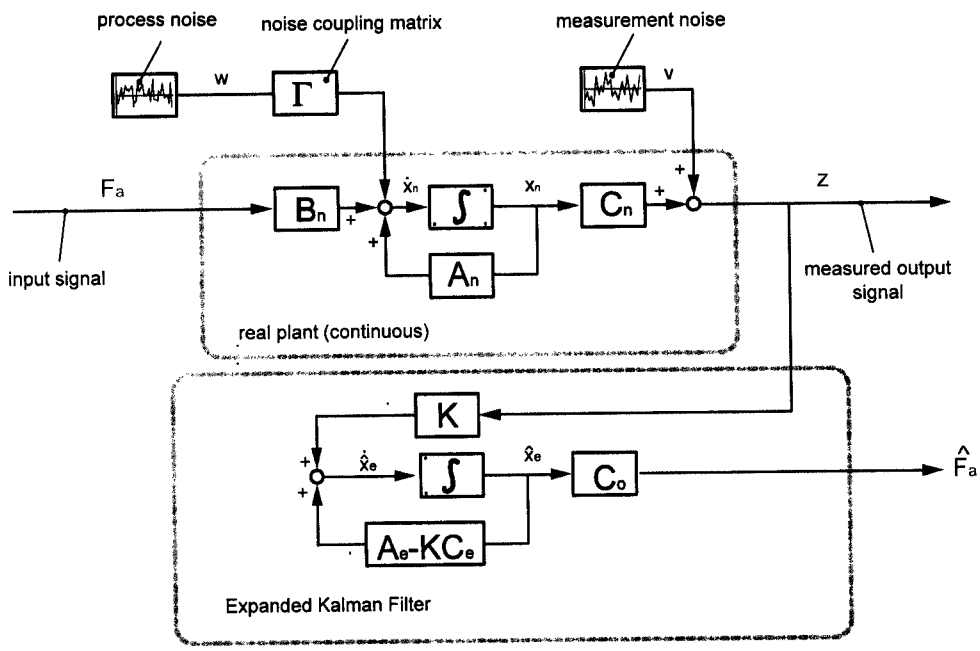

Figure 6.1 Schematic of the Expanded Disturbance Kalman Filter

In order to determine the Kalman Filter transfer functions, the state space equation in Eq. 6.15 can be written as the following:

$$\begin{aligned}\hat{F}_a &= \frac{C_0 adj[sI-(A_e-KC_e)]}{\det[sI-(A_e-KC_e)]}\begin{bmatrix}K_{(9\times1,1)} & K_{(9\times1,2)}\end{bmatrix}^T\begin{bmatrix}F_m\\ Acc.\end{bmatrix}\\ &= \begin{bmatrix}G_{\hat{F}_a/F_m} & G_{\hat{F}_a/\ddot{x}}\end{bmatrix}\begin{bmatrix}F_m\\ Acc.\end{bmatrix}\end{aligned} \tag{6.16}$$

where $G_{\hat{F}_a/F_m}$ and $G_{\hat{F}_a/\ddot{x}}$ are the Kalman Filter transfer functions due to the measured force and the acceleration, respectively.

The actual force can be estimated using the Kalman Filter approach by discretizing the state space Eq. 6.15. The discrete equivalent of the estimated state vector, $\hat{x}_e$, can be expressed as:

$$\hat{x}_e(k+1) = \exp\{(A_e - KC_e)t_d\}\hat{x}_e(k) + [\int_0^{t_d} \exp\{(A_e - KC_e)\tau\} K\, d\tau\ ]\ z(k)$$
$$\hat{F}_a(k+1) = C_o\, \hat{x}_e \tag{6.17}$$

where the discrete sampling time, t_d, is 50 microseconds in this application.

KALMAN FILTER DERIVATION

The Kalman Filter gain is identified by minimizing the state estimation error covariance, $P = E[\tilde{x}_e\ \ \tilde{x}_e^T]$, from the actual and estimated models, where the estimated error is $\tilde{x}_e = x_e - \hat{x}_e$. A linear differential equation for the state estimation error $\tilde{x}_e = x_e - \hat{x}_e$ can be derived as:

$$\tilde{x}_e = x_e - \hat{x}_e \xrightarrow{d/dt} \dot{\tilde{x}}_e = \dot{x}_e - \dot{\hat{x}}_e \tag{6.18}$$

Substituting $\dot{x}_e$ from Eq. 6.12 and $\dot{\hat{x}}_e$ from Eq. 6.15 into Eq. 6.18 would yield the following equation:

$$\begin{aligned}\dot{\tilde{x}}_e &= A_e x_e + \Gamma w - [(A_e - KC_e)\hat{x}_e + Kz] \\ &= A_e x_e + \Gamma w - [(A_e - KC_e)\hat{x}_e + K(C_e x_e + v)] \\ &= (A_e - KC_e)\tilde{x}_e + \Gamma w - Kv\end{aligned} \tag{6.19}$$

Another linear differential equation for the state estimation error covariance matrix P can be attained as:

$$P = E\{\tilde{x}_e \cdot \tilde{x}_e^T\} \xrightarrow{d/dt} \dot{P} = E\{\dot{\tilde{x}}_e \cdot \tilde{x}_e^T\} + E\{\tilde{x}_e \cdot \dot{\tilde{x}}_e^T\} \tag{6.20}$$

Substituting $\dot{\tilde{x}}_e$ from Eq. 6.19 into Eq. 6.20 would yield;

$$\dot{P} = (A_e - KC_e)P + P(A_e - KC_e)^T + \Gamma P_{wx} + P_{xw}\Gamma^T + KP_{vx} + P_{xv}K^T \tag{6.21}$$

where $P_{wx} = E\{w \cdot \tilde{x}_e^T\}$, $P_{xw} = E\{\tilde{x}_e \cdot w^T\}$, $P_{vx} = E\{v \cdot \tilde{x}_e^T\}$, and $P_{xv} = E\{\tilde{x}_e \cdot v^T\}$.

For white noise signals, the last four terms in Eq. 6.21 can be represented as:

$$\Gamma P_{wx} + P_{xw}\Gamma^T = \Gamma Q \Gamma^T$$
$$KP_{vx} + P_{xv}K^T = KRK^T \tag{6.22}$$

The proof for Eq. 6.22 can be illustrated in the following [Mendel 95]. For the discrete time equivalent state space equivalent of the system matrix can be depicted as:

$$\Phi(t + \Delta t, t) \approx I + A_o(t)\Delta t + \cdots \tag{6.22a}$$

where $A_0 = (A_e - KC_e)$. If we integrate Eq. 6.19,

$$\tilde{x}(t) = \Phi(t, t_0)\tilde{x}(t_0) + \int_{t_0}^{t} \Phi(t,\tau)\Gamma(\tau)w(\tau)d\tau + \int_{t_0}^{t} \Phi(t,\tau)K(\tau)v(\tau)d\tau \tag{6.22b}$$

If we take the expected value respect $\tilde{x}$ and w^T, the above equation becomes as:

$$E\{\tilde{x}(t)w^T(t)\} = \Phi(t,t_0)E\{\tilde{x}(t_0)w^T(t)\} + \int_{t_0}^{t} \Phi(t,\tau)\Gamma(\tau)E\{w(\tau)w^T(t)\}d\tau \tag{6.22c}$$

Then, the first term becomes zero because $\tilde{x}$ (t) and w^T (t) are independent and w^T (t) has zero mean; hence:

$$E\{\tilde{x}(t)w^T(t)\} = \int_{t_0}^{t} \Phi(t,\tau)\Gamma(\tau)Q(\tau)d\tau = \Phi(t,t)\Gamma(t)Q(t)\int_{t_0}^{t} \delta(t-\tau)d\tau = \frac{\Gamma(t)Q(t)}{2} \tag{6.22d}$$

where $\int_{t_0}^{t} \delta(t-\tau)d\tau = \lim_{\varepsilon \to 0} \int_{t_0}^{t} \delta_\varepsilon(t-\tau)d\tau = \int_{t-\varepsilon}^{t} \frac{1}{2\varepsilon}d\tau = \frac{1}{2}$ and $\Phi(t,t) \approx I$. Furthermore,

$E\{w(t)\tilde{x}^T(t)\} = [E\{\tilde{x}(t)w^T(t)\}]^T = Q(t)\Gamma^T(t)/2$.

Thus, the first equality for Eq. 6.22 can be shown as:

$$\Gamma(t)E\{w(t)\tilde{x}^T(t)\} + E\{\tilde{x}(t)w^T(t)\}\Gamma^T(t) = \Gamma(t)Q(t)\Gamma^T(t)$$
$$\Gamma(t)\frac{Q(t)\Gamma^T(t)}{2} + \frac{\Gamma(t)Q(t)}{2}\Gamma^T(t) = \Gamma(t)Q(t)\Gamma^T(t) \tag{6.22e}$$

The similar approach can be used to equate the second equality for Eq. 6.22 by taking the expected value between $\tilde{x}$ (t) and v^T (t).

The covariance of the system noise and measurement noise are $Q = E[w\ w^T]$ and $R = E[v\ v^T]$, respectively. By substituting Eq. 6.22 into Eq. 6.21, we obtain the following form:

$$\dot{P} = A_e P + P A_e^{\ T} - K C_e P - P C_e^{\ T} K^T + \Gamma Q \Gamma^T + K R K^T \tag{6.23}$$

Optimum state estimates are obtained if the error covariance matrix $P = E\{\tilde{x}_e \cdot \tilde{x}_e^{\ T}\}$ is minimum. The following simple relationship can be observed;

$$\tilde{x}_e^{\ T} \cdot \tilde{x}_e = \mathrm{tr}\{\tilde{x}_e \cdot \tilde{x}_e^{\ T}\} \tag{6.24}$$

where $\tilde{x}_e$ is the vector. Thus, the calculation of the expected value and the trace can be exchanged as:

$$E\{\tilde{x}_e \cdot \tilde{x}_e^{\ T}\} = \mathrm{tr}\{\ P(K)\ \} \tag{6.25}$$

A minimum $\tilde{x}_e$ exists if the following necessary condition is fulfilled:

$$\frac{\partial}{\partial K} tr\{\dot{P}\} = 0 \tag{6.26}$$

The following identifies can be used.

$$\begin{aligned} &\left(P C_e^{\ T} K^T\right)^T = K C_e P \\ &Tr\left(P C_e^{\ T} K^T\right) = Tr(K C_e P) \\ &\frac{\partial}{\partial K} tr\{K R K^T\} = 2KR \\ &\frac{\partial}{\partial K} tr\{K C_e P\} = P C_e^{\ T} \end{aligned} \tag{6.27}$$

Deriving Eq. 6.26 and substituting it for $\dot{P}$ from Eq. 6.23 yields the optimal Kalman Filter gain matrix K_{opt} as a function of P. The Kalman Filter gain is obtained from the covariance matrix Eq. 6.23 as:

$$\frac{\partial}{\partial K} tr\{\dot{P}\} = -2 P C_e^{\ T} + 2KR = 0 \tag{6.28}$$

$$K_{opt} = PC_e^{\ T}R^{-1}$$

Substituting Eq. 6.27 into Eq. 6.23 would make the differential equation for the covariance matrix P as;

$$\begin{aligned}\dot{P}(t\,|\,t) &= A_e(t)P(t\,|\,t) + P(t\,|\,t)A_e^T(t) \\ &\quad + \Gamma(t)Q(t)\Gamma^T(t) - P(t\,|\,t)C_e^T(t)R^{-1}C_e(t)P(t\,|\,t)\end{aligned} \tag{6.29}$$

The above equation is known as the Riccati equation. In this study, the measurement and the system covariance are assumed to be uncorrelated with each other (i.e., $E[w\,v^T] = 0$).

SOLVING ERROR COVARIANCE MATRIX FOR STEADY STATE CONDITION

The plant is assumed to be time invariant and stationary which must approach to zero for a stable ($A_e - KC_e$) observer. Then the derivative of the error covariance approaches zero (i.e., $\dot{P}(t\,|\,t) \rightarrow 0$) and the error covariance matrix is denoted as $\overline{P}$. Likewise, the steady state Kalman Filter gain can also be denoted as $\overline{K}$. Therefore, Eq. 6.28 can be rewritten as the following steady state equation:

$$0 = \dot{P} = A_e\overline{P} + \overline{P}A_e^{\ T} + \Gamma Q\Gamma^T - \overline{P}C_e^{\ T}R^{-1}C_e\overline{P} \tag{6.30}$$

The only unknown in the above equation is the steady state covariance matrix, $\overline{P}$, and we can solve it through the eigenvector [Potter 66] or the Schur decomposition approaches. The eigenvector approach to solve the error covariance matrix is illustrated in the following. The Riccati equation, Eq. 6.29 can be expressed as:

$$[-P \quad I]\begin{bmatrix} A_e^{\ T} & -C_e^{\ T}R^{-1}C_e \\ -\Gamma Q\Gamma^T & -A_e \end{bmatrix}\begin{bmatrix} I \\ P \end{bmatrix} = [-P \quad I]H\begin{bmatrix} I \\ P \end{bmatrix} = 0 \tag{6.29a}$$

where H is known as Hamiltonian matrix, and can be formulated as the eigenvector form as shown:

$$H = \begin{bmatrix} A_e^T & -C_e^T R^{-1} C_e \\ -\Gamma Q \Gamma^T & -A_e \end{bmatrix} = V \begin{bmatrix} \Lambda_a & 0 \\ 0 & \Lambda_b \end{bmatrix} V^{-1} \tag{6.29b}$$

where V is the real eigenvectors $V = \begin{bmatrix} V_{11} & V_{12} \\ V_{21} & V_{22} \end{bmatrix}$ and $\Lambda = diag(\lambda_1, \cdots \lambda_n)$ is eigenvalues with block diagonal matrices with real and complex eigenvalue $(a + jb)$ appearing as $\lambda = \begin{bmatrix} a & b \\ -b & a \end{bmatrix}$. Furthermore, λ is equal to Λ_a and conjugate of $-\lambda$ is equal to Λ_b with the inverse order. The eigen-vectors and values for Eq. 6.29b can be obtained by utilizing Matlab^{TM}'s *reig* command. The following form of P ensures;

$$[-P \quad I] V \begin{bmatrix} \Lambda_a & 0 \\ 0 & \Lambda_b \end{bmatrix} V^{-1} \begin{bmatrix} I \\ P \end{bmatrix} = 0 \text{ so that}$$

$$[-P \quad I] \begin{bmatrix} V_{11} & V_{12} \\ V_{21} & V_{22} \end{bmatrix} = [0 \quad C] \text{ and } \begin{bmatrix} V_{11} & V_{12} \\ V_{21} & V_{22} \end{bmatrix}^{-1} \begin{bmatrix} P \\ I \end{bmatrix} = \begin{bmatrix} C \\ 0 \end{bmatrix} \tag{6.29c}$$

where C is non-zero component. Thus, the desired error covariance matrix can be acquired as:

$$P = V_{21} V_{11}^{-1} \tag{6.29d}$$

For non-steady state cases, the error covariance can be solved based on algorithms presented in the references [Brown 97, Mendel 95].

The measurement noise covariance matrix, R, is determined from the electrical noise which is defined as the average electrical RMS reading when the machine is stationary and the average differences in air cutting force fluctuations. The system disturbance covariance matrix, Q, is tuned to accommodate the compensations. The

measurement, the system noise covariance, and the system noise vector, Γ, used in the piecewise constant analysis are:

$$R=\begin{bmatrix}100 & 0\\ 0 & 100\end{bmatrix};\ Q=\begin{bmatrix}1e9 & 0\\ 0 & 1e9\end{bmatrix};\ \Gamma=\begin{bmatrix}0 & 0 & 0 & 0 & 0 & 0 & 1\end{bmatrix} \tag{6.31}$$

When the input is assumed to contain both dc and harmonic components, the measurement and the system error covariance matrices, and the system noise vector are found to be:

$$R=\begin{bmatrix}100 & 0\\ 0 & 100\end{bmatrix};\ Q=\begin{bmatrix}1e7 & 0\\ 0 & 5e7\end{bmatrix};\ \Gamma=\begin{bmatrix}0 & 0 & 0 & 0 & 0 & 0 & 0.6 & 0.8 & 0\end{bmatrix}^T \tag{6.32}$$

For the piecewise constant input, the error covariance matrix P and the Kalman Filter gain of the state space system using Eq. 6.27, which minimizes the error covariance matrix P, are:

$$P=\begin{bmatrix}0.1753 & 0.0066 & -0.0529 & -0.0051 & 0.0022 & 0.0001 & 0.0722\\ 0.0066 & 0.0255 & 0.0002 & -0.0086 & -0.0001 & 0.0001 & 0.0283\\ -0.0529 & 0.0002 & 0.0183 & 0.0011 & -0.0009 & -0.0000 & 0.0295\\ -0.0051 & -0.0086 & 0.0011 & 0.0035 & 0.0000 & -0.0000 & 0.0164\\ 0.0022 & -0.0001 & -0.0009 & 0.0000 & 0.0000 & 0.0000 & 0.0009\\ 0.0001 & 0.0001 & -0.0000 & -0.0000 & 0.0000 & 0.0000 & -0.0000\\ 0.0722 & 0.0283 & 0.0295 & 0.0164 & 0.0009 & -0.0000 & 8.3817\end{bmatrix}\times 1e5 \tag{6.33}$$

$$K=\begin{bmatrix}-0.0074 & 0.0379 & 0.0894 & 0.1122 & 0.1168 & 0.0475 & 4.3377\\ -0.0043 & 0.0150 & 0.0369 & 0.0510 & 0.0157 & -0.0164 & 1.0884\end{bmatrix}^T\times 1000$$

The Kalman Filter gain (Eq. 6.32) for the dc and harmonic input has different gain values depending on the specific tooth passing frequencies because the error covariance matrix is a function of A_e as shown in Eq. 6.12 which is affected by the tooth passing frequency.

The Kalman Filter gain, K, is kept time invariant for the modeled Spindle-Integrated Force Sensor system. The actual force applied at the tool tip is evaluated from

the spindle sensors and vibration sensors by applying a discrete time domain recursive filter Eq.6.17 at each sampling instant where the measurements from acceleration (*Acc.*) and Spindle-Integrated force (F_m) sensors are collected.

EXPERIMENTAL VERIFICATION

For the piecewise constant input, the Kalman Filter transfer function between the estimated actual force at the tool tip, $\hat{F}_a$, and measured force at the spindle housing, F_m, can be obtained using Eq. 6.16 to be:

$$G_{\hat{F}_a/F_m} = \frac{\hat{F}_a}{F_m} = \frac{4338s^6 + 3.312e6s^5 + 3.001e11s^4 + 1.457e14s^3 + 5.977e18s^2 + 1.445e21s + 3.383e25}{s^7 + 6185s^6 + 8.8e7s^5 + 3.772e11s^4 + 2.204e15s^3 + 6.786e18s^2 + 1.606e22s + 3.538e25} \quad (6.34)$$

Likewise for the piecewise constant input, the Kalman Filter transfer function between the estimated actual force at the tool tip, $\hat{F}_a$, and the measured acceleration, *Acc.*, is

$$G_{\hat{F}_a/\ddot{x}} = \frac{\hat{F}_a}{Acc.} = \frac{1088s^6 + 1.089e6s^5 + 7.516e10s^4 + 6.231e13s^3 + 1.496e18s^2 + 7.8e20s + 8.491e24}{s^7 + 6185s^6 + 8.8e7s^5 + 3.772e11s^4 + 2.204e15s^3 + 6.786e18s^2 + 1.606e22s + 3.538e25} \quad (6.35)$$

The modeled Frequency Response Function (FRF) of the uncompensated force sensor system (Eq. 4.7, $\Phi(s) = F_m / F_a$), the FRF of the Kalman Filter for force (Eq. 6.16, $G_{\hat{F}_a/F_m}(s) = \hat{F}_a / F_m$), and the FRF of the compensated system ($\Phi(s) \times G_{\hat{F}_a/F_m}$) are illustrated in Figure 6.2(a). Similarly the FRF of the uncompensated acceleration system (Eq. 4.8 $\Phi_a(s) = Acc. / F_a$), the FRF of the Kalman Filter for acceleration (Eq. 6.16, $G_{\hat{F}_a/\ddot{x}}(s) = \hat{F}_a / Acc.$), and the FRF of the compensated system ($\Phi_a(s) \times G_{\hat{F}_a/\ddot{x}}$) are illustrated in Figure 6.2 (b).

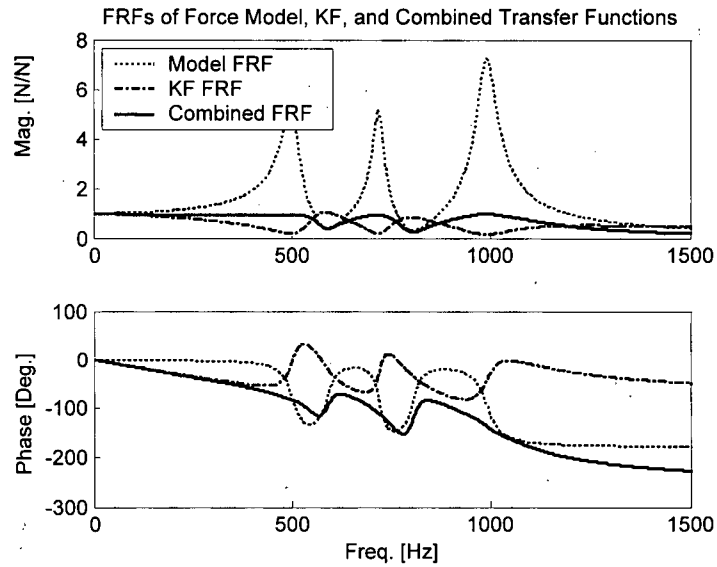

(a) The force model ($\Phi(s) = F_m / F_a$), the Kalman Filter ($G_{\hat{F}_a / F_m}(s) = \hat{F}_a / F_m$), and the cascaded ($\Phi(s) \times G_{\hat{F}_a / F_m}(s)$) FRFs.

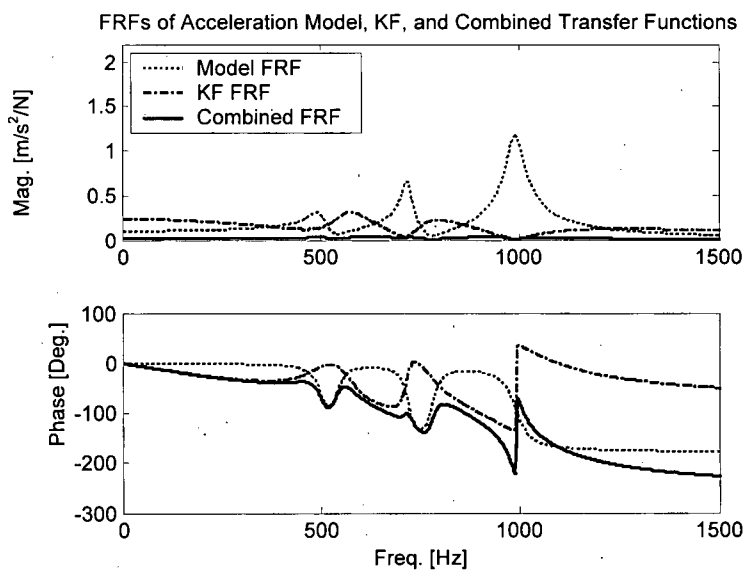

(b) The acceleration model ($\Phi_a(s) = Acc. / F_a$), the Kalman Filter ($G_{\hat{F}_a / \ddot{x}}(s) = \hat{F}_a / Acc.$), and the cascaded ($\Phi_a(s) \times G_{\hat{F}_a / \ddot{x}}(s)$) FRFs.

Figure 6.2 Comparison of the FRFs between the measured model, the piecewise constant Kalman Filter, and compensated Spindle-Integrated force sensing system

Although the cascaded transfer function (i.e., $G(s) \times G_{\hat{F}_a / F_m}(s)$) between the measured and the Kalman Filter FRFs does not have a perfect unity gain at the regions of modal frequencies as shown in Figure 6.2 (a), the amplifications of force measurements at these regions are significantly reduced with the Kalman Filter.

For the case of the dc and harmonic input, the FRFs of the Kalman Filter vary with respect to the tooth passing frequencies, ω_T. Generally, the combined Kalman Filter and the model FRFs have similar trends, with the piecewise constant case as the following exception: the magnitude at low frequency regions is not constant at one. An example of the FRFs at 9000 rpm is shown in Figure 6.3 and its corresponding transfer functions are shown below. The Kalman Filter transfer function between the estimated actual force at the tool tip, $\hat{F}_a$, and the measured force at the spindle housing, F_m, at 9000 rev/min spindle speed is:

$$G_{\hat{F}_a / F_m} = \frac{\hat{F}_a}{F_m} = \frac{\begin{array}{r} 480s^8 - 2.45e6s^7 + 4.11e10s^6 - 1.71e14s^5 + 1.26e18s^4 \\ -3.37e21s^3 + 1.67e25s^2 - 1.85e28s + 7.88e31 \end{array}}{\begin{array}{r} s^9 + 2351s^8 + 9.38e7s^7 + 1.66e11s^6 + 3.03e15s^5 + 3.87e18s^4 \\ +4.01e22s^3 + 3.35e25s^2 + 1.80e29s + 8.16e31 \end{array}} \tag{6.36}$$

Similarly, the Kalman Filter transfer function between the estimated actual force at the tool tip, $\hat{F}_a$, and the measured acceleration at the spindle housing, *Acc.*, at 9000 rev/min spindle speed is:

$$G_{\hat{F}_a / \ddot{x}} = \frac{\hat{F}_a}{Acc.} = \frac{\begin{array}{r} 170.9\,s^8 - 5.40e5\,s^7 + 1.35e10\,s^6 - 3.98e13\,s^5 + 3.58e17\,s^4 \\ -8.27e20\,s^3 + 3.97e24\,s^2 - 4.76e27\,s + 1.62e3 \end{array}}{\begin{array}{r} s^9 + 2351s^8 + 9.38e7\,s^7 + 1.66e11\,s^6 + 3.03e15\,s^5 + 3.87e18\,s^4 \\ +4.01e22\,s^3 + 3.35e25\,s^2 + 1.80e29\,s + 8.16e3 \end{array}} \tag{6.37}$$

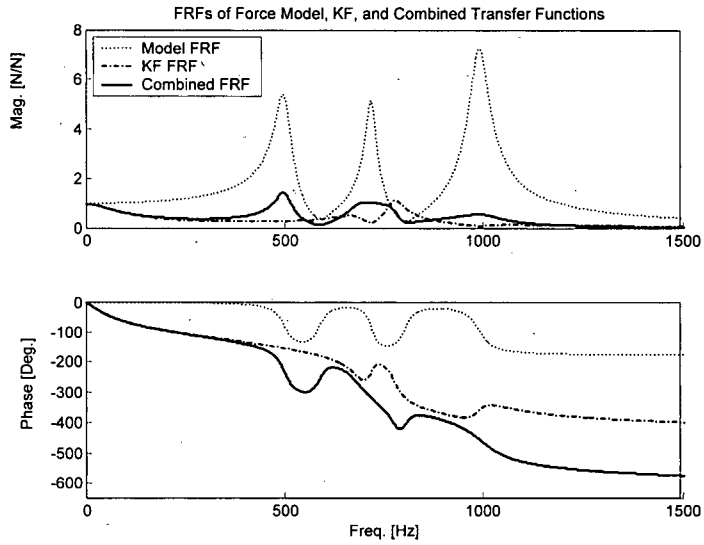

(a) The force model ($\Phi(s) = F_m / F_a$), the Kalman Filter ($G_{\hat{F}_a / F_m}(s) = \hat{F}_a / F_m$), and the cascaded ($\Phi(s) \times G_{\hat{F}_a / F_m}(s)$) FRFs.

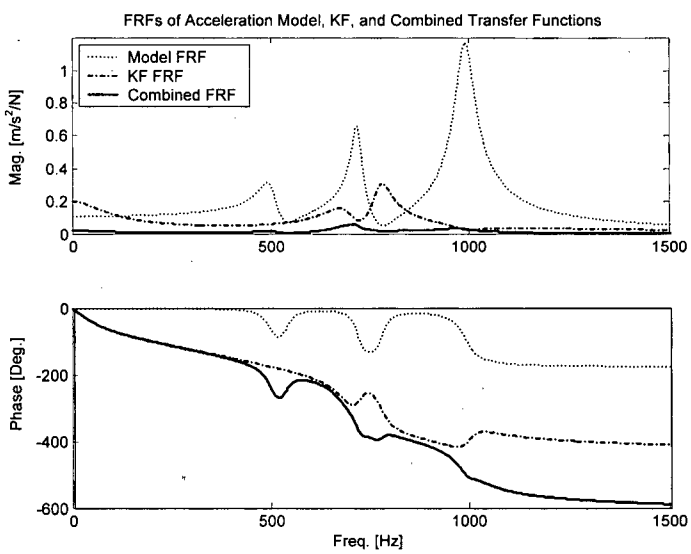

(b) The acceleration model ($\Phi_a(s) = Acc. / F_a$), the Kalman Filter ($G_{\hat{F}_a / \ddot{x}}(s) = \hat{F}_a / Acc.$), and the cascaded ($\Phi_a(s) \times G_{\hat{F}_a / \ddot{x}}(s)$) FRFs.

Figure 6.3 Comparison of the FRFs between the measured model, the dc and harmonic Kalman Filter, and the compensated Spindle-Integrated force sensing system at 9000 rpm.

Several cutting tests are performed at tooth passing frequencies ranging from 50 Hz to 1000 Hz. A five-fluted 19.05 mm cylindrical end mill clamped in the hydraulic tool holder is used to machine a block of aluminum Al7075-T6. The depth of cut is 1.5 mm, the feed rate is 0.1 mm/tooth, and the cutting condition is full immersion slot milling. Figure 6.4 to Figure 6.7 depict both the piecewise constant input cases in the top figures (a), and the dc and harmonic input cases in the bottom figures (b). The cutting forces measured from the spindle force sensor without compensation, the compensated forces with the proposed Kalman Filter, and the reference forces measured with the Kistler table dynamometer are presented in the figures. The cutting force measurements from the clamped table dynamometer are also distorted when the frequency contents of the forces are beyond 500 Hz. The reference forces are therefore collected from the Kistler table dynamometer at 1000 rev/min because there is no other means of collecting a reference force. The reference forces are assumed to be consistent up to speeds of 12000 rev/min.

The cutting test results for a spindle speed of 1000 rev/min or with a tooth passing frequency of 83.35 Hz are given in Figure 6.4. Since the tooth passing frequency and its first two harmonics are within the bandwidth of the spindle force sensor, the responses obtained from the uncompensated spindle sensor and the dynamometer are almost identical. Both the piecewise constant and the dc and harmonic Kalman Filters remove the noise from the measurements, and the frequency spectrum of all three force measuring systems are almost identical. The maximum amplitude of the cutting force is just under 100 N, and this measurement is used as a reliable reference force for high speed tests where the dynamometer fails to measure forces accurately due to its limited bandwidth. When the spindle speed is increased to 6000 rev/min, the tooth passing

frequency (500 Hz) coincides with the first natural frequency of the spindle sensor, leading to almost double the force amplitude. However, the Kalman Filter compensates the dynamic amplification due to the first mode, and brings the force to the level provided by the dynamometer, see Figure 6.5. At 9000 rev/min, where the tooth passing frequency is 750 Hz, which is very close to the second mode (719 Hz), the Kalman Filter still compensates the dynamic distortion and noise quite well, as shown in Figure 6.6. When the speed is increased to 12000 rev/min, the tooth passing frequency becomes 1000 Hz as shown in Figure 6.7. The Kalman Filter compensated forces experience difficulty here and attenuates the force measurements. Generally, the compensation with the dc and harmonic input show smoother compensation than just the piecewise constant input, but at the expense of having spindle speed dependent Kalman Filter gains. As long as the sampling frequency is about 10-15 times higher than the tooth passing frequency, the Kalman Filter with a piecewise constant force input seems to be sufficient in reconstructing the cutting forces.

The results agree with the Frequency Response Function of the compensated spindle force sensors with the Kalman Filter. The forces are attenuated slightly more around natural frequencies where the compensation is not trivial due to slight changes in the damping and magnitude of the actual spindle sensor system during machining. However, in general the compensated force sensor provided reliable measurements up to 1000 Hz. The compensation of the third mode at 990 Hz is found to be the poorest, not only due to the Kalman Filter design but also due to significant changes in the spindle's damping and frequency as the speed of the spindle change. Furthermore, we hypothesize that with the operation of the milling machine at very high speeds, the aluminum

workpiece would be softened due to heat generations caused by cutting operations which would decrease the magnitudes of cutting forces. The disturbance Kalman Filter effectively compensates the structural modes up to 1000 Hz. The comparison between the piecewise constant model and the dc and harmonic model shows almost no difference in the compensated forces except that the dc and harmonic model caused a large phase delay. In summary, the periodic milling forces can be modeled as a piecewise constant input to the Kalman Filter provided that the sampling frequency is high. The addition of ac components does not improve the performance of the Kalman Filter significantly while making it speed dependent, which is not practical.

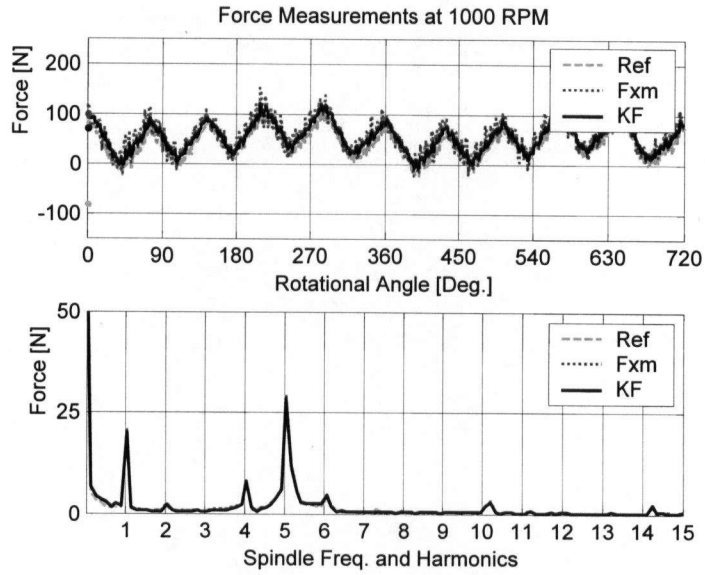

(a) DC Input

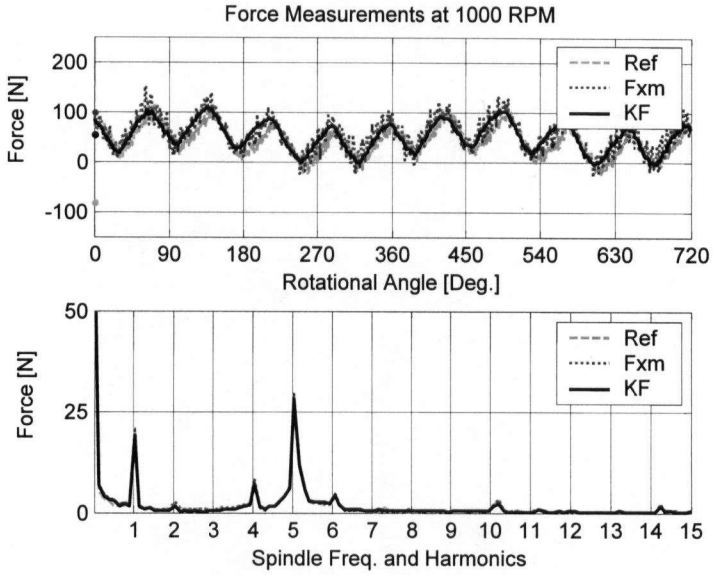

(b) DC and Harmonic Input

Figure 6.4. Five fluted cutting force measurements at 1,000 rpm in (a) DC and (b) DC and Harmonic inputs. *The top figure is shown in the time domain and the bottom figure is shown in the frequency (normalized with the spindle freq.) domain. Ref. denotes the reference cutting forces from the dynamometer at 1000 rpm, Fxm denotes the measured force from the Spindle-Integrated Force Sensor system, KF denotes the Kalman Filter compensated cutting forces.*

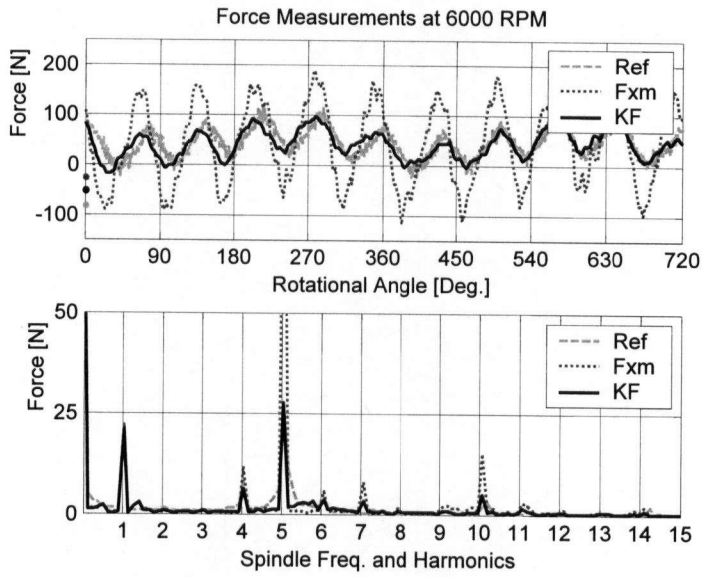

(a) DC Input

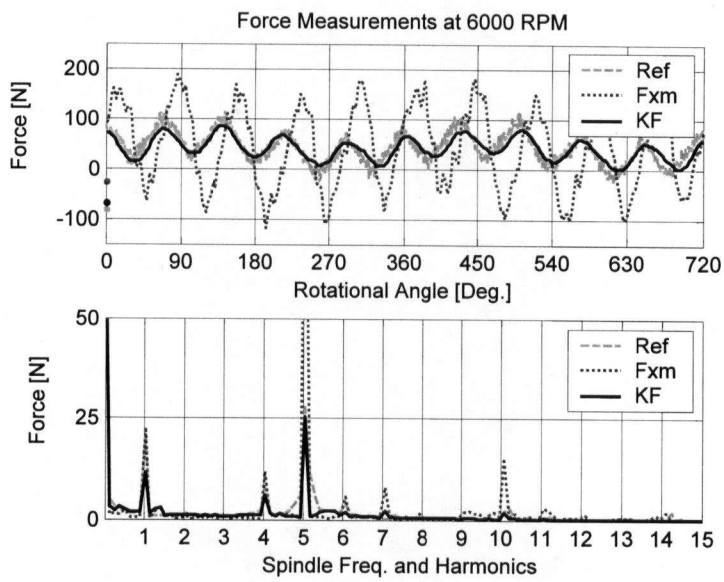

(b) DC and Harmonic Input

Figure 6.5. Five fluted cutting force measurements at 6,000 rpm in (a) DC and (b) DC and Harmonic inputs. *The top figure is shown in the time domain and the bottom figure is shown in the frequency (normalized with the spindle freq.) domain.*

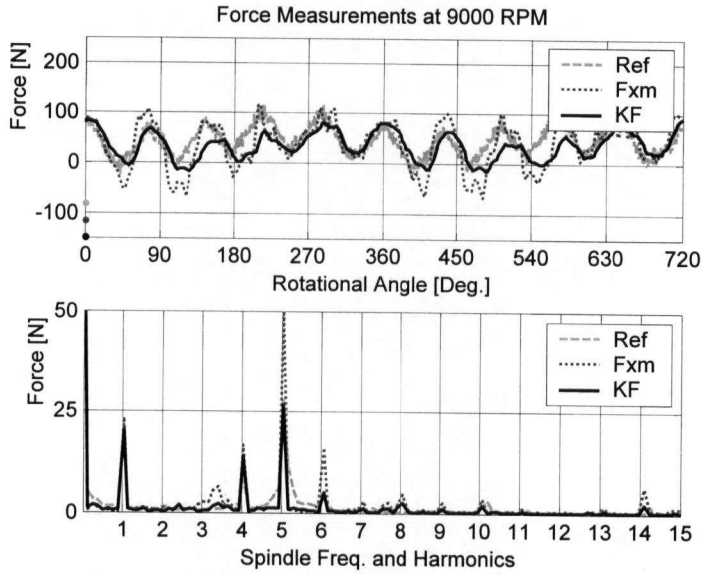

(a) DC Input

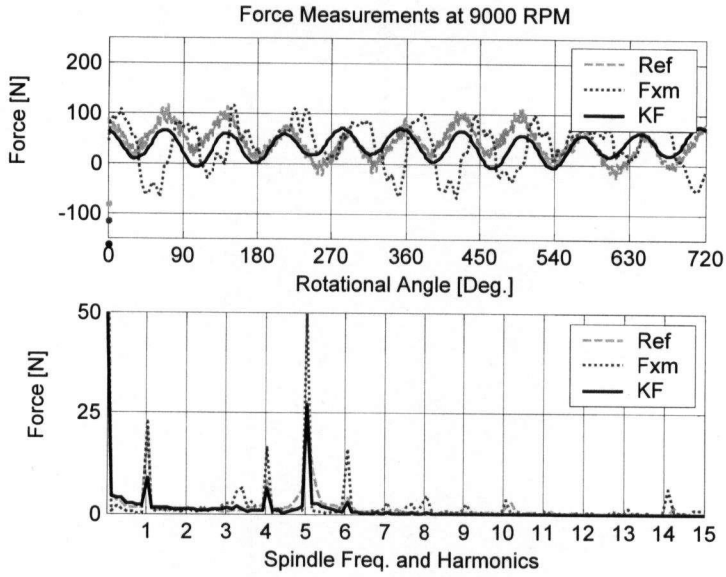

(b) DC and Harmonic Input

Figure 6.6. Five fluted cutting force measurements at 9,000 rpm in (a) DC and (b) DC and Harmonic inputs. *The top figure is shown in the time domain and the bottom figure is shown in the frequency (normalized with the spindle freq.) domain.*

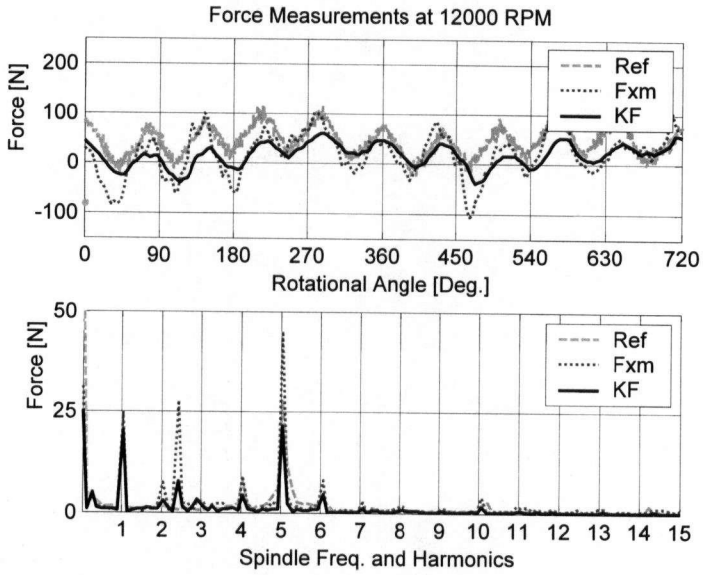

(a) DC Input

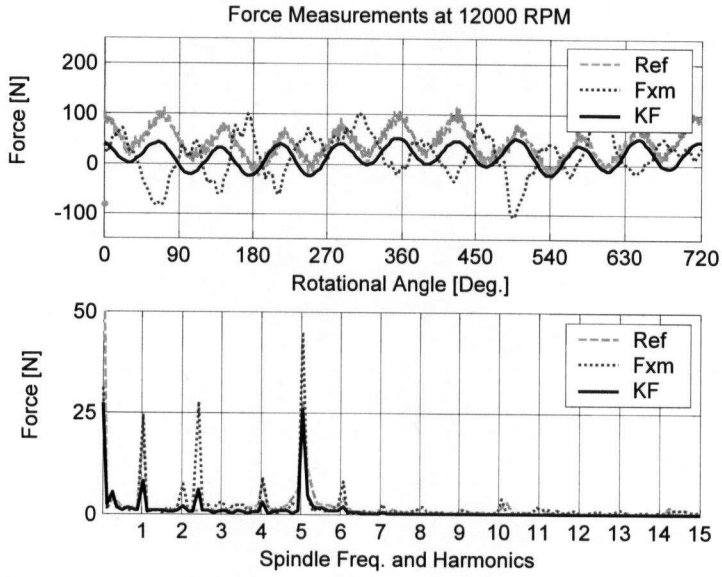

(b) DC and Harmonic Input

Figure 6.7. Five fluted cutting force measurements at 12,000 rpm in (a) DC and (b) DC and Harmonic inputs. *The top figure is shown in the time domain and the bottom figure is shown in the frequency (normalized with the spindle freq.) domain*

6.2 DISTURBANCE KALMAN FILTER COMPENSATION IN THREE DIRECTIONS

The disturbance Kalman Filter compensation method is extended to three directions based on the same procedure presented in the previous section. The compensation method is slightly modified since the addition of the accelerometer attached to the spindle did not further improve the applied cutting force estimations. Furthermore, the applied cutting forces are assumed to be piecewise constant since the addition of the ac component of the applied cutting force model deteriorated the phase response. Since the cutting forces in three directions are considered, the cross talk terms are used to compensate the structure modes, as depicted in Appendix E. However, the compensation with all the cross talk terms did not improve although the order, phase mis-synchronization, and the complexity of the filter increased significantly. Therefore, the transfer functions ($\Phi(s)$) between the force applied at the tool tip (F_a) and the Spindle-Integrated Force Sensor system (F_m) in three orthogonal directions (see Figure 6.8) are only used to compensate the cutting forces. The transfer function measurements indicate that the spindle sensor system can reliably measure milling forces that have harmonics less than 300 Hz, 500 Hz, and 150 Hz in X, Y, and Z directions, respectively. The reconstruction of cutting forces in the feed, normal, and axial directions are successfully performed with the disturbance Kalman Filter.

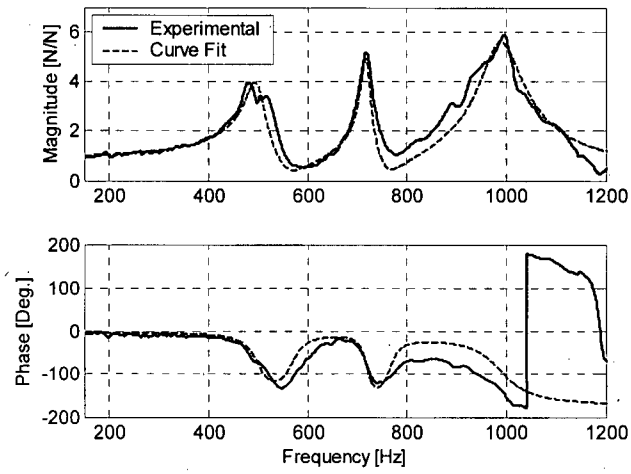

(a) Φ_{xx}

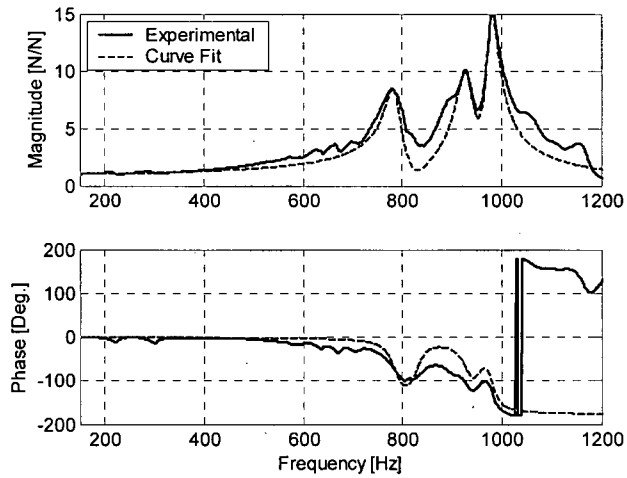

(b) Φ_{yy}

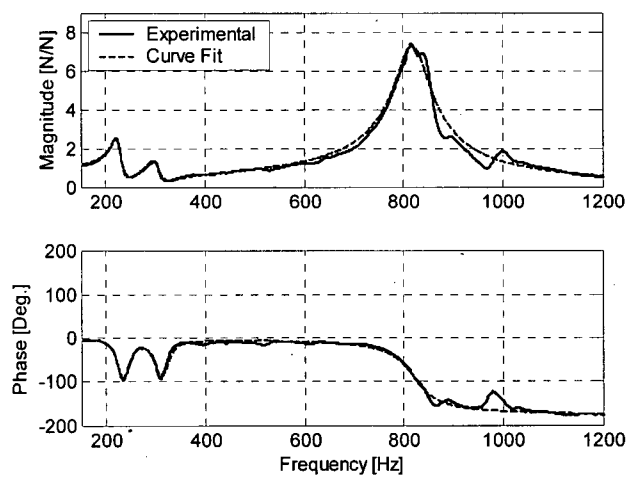

(c) Φ_{zz}

Figure 6.8. (a) Transfer Function $\Phi_{xx}(\omega) = F_{xm}(\omega) / F_{xa}(\omega)$, (b) Transfer Function $\Phi_{yy}(\omega) = F_{ym}(\omega) / F_{ya}(\omega)$, and (c) Transfer Function $\Phi_{zz}(\omega) = F_{zm}(\omega) / F_{za}(\omega)$

The experimentally measured transfer function is identified by a modal curve fitting technique as;

$$\Phi_{qq}(s) = \frac{F_{qm}(s)}{F_{qa}(s)} = \sum_{k=1}^{k} \frac{\alpha_{qk}^{-1} \cdot \omega_{qn,k}^{2}}{s^2 + 2\xi_{qk}\omega_{qn,k}s + \omega_{qn,k}^{2}}; \quad q \in x, y, z \tag{6.38}$$

where k is the number of modes, F_{qm} is the measured force from the Spindle-Integrated Force Sensor, and F_{qa} is the applied force at the tool tip. The modal parameters in three directions are given in Table 6.1. The measured and curve fitted transfer functions are in good agreement as shown in Figure 6.8. The modal equations (Eq. 6.37) can be expanded into polynomial forms as;

$$\Phi_{qq}(s) = \frac{F_{qm}(s)}{F_{qa}(s)} = \frac{b_{q1}s^4 + b_{q2}s^3 + b_{q3}s^2 + b_{q4}s + b_{q5}}{s^6 + a_{q1}s^5 + a_{q2}s^4 + a_{q3}s^3 + a_{q4}s^2 + a_{q5}s + a_{q6}}; \quad q \in x, y, z \tag{6.39}$$

where the parameters are depicted in Table 6.2. The cross talk transfer functions have also been measured and found to reflect the same magnitudes as measured in the static case, see Chapter 4.

Table 6.1. Modal Parameters obtained by Curve Fitting the Transfer functions

q	k	ω_n (Hz)	ξ	α
x	1	500	0.044	*3.091*
	2	719	0.015	*7.407*
	3	990	0.045	*1.993*
y	1	785	0.021	*3.064*
	2	930	0.020	2.922
	3	980	0.013	2.86
z	1	224	0.048	4.924
	2	300	0.044	10.40
	3	820	0.045	1.517

Table 6.2. Polynomial Coefficients obtained based on the Transfer functions

i	b_{xi}	a_{xi}	b_{yi}	a_{yi}	b_{zi}	a_{zi}
1	2.536e7	967.2	3.288e7	603.1	1.824e7	767.6
2	1.242e10	6.924e7	1.331e10	9.651e7	5.732e9	3.224e7
3	9.117e14	3.967e10	2.076e15	3.898e10	1.191e14	1.14e10
4	2.32e17	1.378e15	4.215e17	3.052e15	1.819e16	1.549e14
5	7.484e21	3.811e17	3.207e22	6.187e17	1.791e20	2.484e16
6	-	7.794e21	-	3.149e22	-	1.868e20

The transfer functions given in Eq. 6.38 are mapped individually for each axis into the following state space form;

$$\begin{aligned} \dot{x} &= A_s x + B_s u \\ z &= C_s x \end{aligned} \tag{6.1'}$$

where x is the state vector, $u = F_a \in \{F_{xa}, F_{ya}, F_{za}\}$ is the input or the actual force applied to the tool, and $z = F_m \in \{F_{xm}, F_{ym}, F_{zm}\}$ is the measured cutting force from the spindle force sensor. Since the inclusion of the cross talk did not improve the force estimation noticeably, the Kalman Filter is applied on each force direction independently. The state space equations representing the spindle dynamics can be expressed as;

$$\begin{bmatrix} \dot{x}_1 \\ \dot{x}_2 \\ \dot{x}_3 \\ \dot{x}_4 \\ \dot{x}_5 \\ \dot{x}_6 \end{bmatrix} = \begin{bmatrix} -a_1 & -a_2 & -a_3 & -a_4 & -a_5 & -a_6 \\ 1 & 0 & 0 & 0 & 0 & 0 \\ 0 & 1 & 0 & 0 & 0 & 0 \\ 0 & 0 & 1 & 0 & 0 & 0 \\ 0 & 0 & 0 & 1 & 0 & 0 \\ 0 & 0 & 0 & 0 & 1 & 0 \end{bmatrix} \begin{bmatrix} x_1 \\ x_2 \\ x_3 \\ x_4 \\ x_5 \\ x_6 \end{bmatrix} + \begin{bmatrix} 1 \\ 0 \\ 0 \\ 0 \\ 0 \\ 0 \end{bmatrix} F_a$$

$$[F_m] = [0 \quad b_1 \quad b_2 \quad b_3 \quad b_4 \quad b_5] \begin{bmatrix} x_1 \\ x_2 \\ x_3 \\ x_4 \\ x_5 \\ x_6 \end{bmatrix} \tag{6.40}$$

where the system's polynomial parameters are given in Table 6.2. The system matrices are transformed into an equivalent system (i.e., $x_n = Tx$) by applying the transformation matrix, T, as;

$$\begin{aligned} \dot{x}_n &= A_n x_n + B_n u \\ z &= C_n x_n \end{aligned} \tag{6.3'}$$

where

$$A_n = T A_s T^{-1},\ B_n = T B_s,\quad C_n = C_s T^{-1}$$

where T is the similarity transformation matrix. The similarity transformation matrix, T, for the sensor system in each direction is found to be:

$$T_{xx} = diag([6.40e1\ 1.05e6\ 8.59e9\ 3.52e13\ 1.44e17\ 2.95e20])$$

$$T_{yy} = diag([1.28e2\ 2.10e6\ 1.72e10\ 1.41e14\ 5.76e17\ 1.18e21])$$

$$T_{zz} = diag([6.40e1\ 5.24e5\ 2.15e9\ 8.80e12\ 9.01e15\ 9.22e18])$$

The identified equivalent state matrix in X direction is;

$$A_{xn} = \begin{bmatrix} -967.2 & -4226 & -295.6 & -2507 & -169.2 & -1690 \\ 16384 & 0 & 0 & 0 & 0 & 0 \\ 0 & 8192 & 0 & 0 & 0 & 0 \\ 0 & 0 & 4096 & 0 & 0 & 0 \\ 0 & 0 & 0 & 4096 & 0 & 0 \\ 0 & 0 & 0 & 0 & 2048 & 0 \end{bmatrix}$$

$$B_{xn} = [64\ \ 0\ \ 0\ \ 0\ \ 0\ \ 0]^T$$

$$C_{xn} = [0\ \ 24.19\ \ 1.446\ \ 25.91\ \ 1.61\ \ 25.36].$$

and in Y direction;

$$A_{yn} = \begin{bmatrix} -603.1 & -5890 & -290.4 & -2775 & -137.4 & -3415 \\ 16384 & 0 & 0 & 0 & 0 & 0 \\ 0 & 8192 & 0 & 0 & 0 & 0 \\ 0 & 0 & 4096 & 0 & 0 & 0 \\ 0 & 0 & 0 & 4096 & 0 & 0 \\ 0 & 0 & 0 & 0 & 2048 & 0 \end{bmatrix}$$

$$B_{yn} = [128\ \ 0\ \ 0\ \ 0\ \ 0\ \ 0]^T$$

$$C_{yn} = [0 \quad 15.68 \quad 0.7746 \quad 14.75 \quad 0.7312 \quad 27.16]$$

and in Z direction:

$$A_{zn} = \begin{bmatrix} -767.6 & -3936 & -339.8 & -1127 & -176.5 & -1296 \\ 8192 & 0 & 0 & 0 & 0 & 0 \\ 0 & 4096 & 0 & 0 & 0 & 0 \\ 0 & 0 & 4096 & 0 & 0 & 0 \\ 0 & 0 & 0 & 1024 & 0 & 0 \\ 0 & 0 & 0 & 0 & 1024 & 0 \end{bmatrix}$$

$$B_{zn} = [64 \quad 0 \quad 0 \quad 0 \quad 0 \quad 0]^T$$

$$C_{zn} = [0 \quad 34.79 \quad 2.669 \quad 13.54 \quad 2.02 \quad 19.41]$$

DISTURBANCE MODEL EXPANSION

The input forces are assumed to be piecewise constant so that the derivative of the input is only the function of process noise, w:

$$\dot{F}_a = 0F_a + w \tag{6.7'}$$

The actual cutting force applied on the tool can be considered as one of the unknown states by expanding Eq. 6.12 as;

$$\begin{aligned} \dot{x}_{e(7\times1)} &= A_{e(7\times7)}x_{e(7\times1)} + \Gamma_{(7\times1)}w_{(1\times1)} \\ z_{(1\times1)} &= C_{e(1\times7)}x_{e(7\times1)} + v_{(1\times1)} \end{aligned} \tag{6.41}$$

where Γ is the system noise vector, and v is measurement noise. The expanded state space (denoted by 'e') model is given in Eq. 6.40, which can be re-written as:

$$\begin{aligned} \begin{bmatrix} \dot{x}_{n(6\times1)} \\ \dot{F}_{a(1\times1)} \end{bmatrix} &= \begin{bmatrix} A_{n(6\times6)} & B_{n(6\times1)} \\ 0_{(1\times6)} & 0_{(1\times1)} \end{bmatrix} \begin{bmatrix} x_{n(6\times1)} \\ F_{a(1\times1)} \end{bmatrix} + \Gamma_{(7\times1)}w_{(1\times1)} \\ z_{(1\times1)} &= \begin{bmatrix} C_{n(1\times6)} & 0_{(1\times1)} \end{bmatrix} \begin{bmatrix} x_{n(6\times1)} \\ F_{a(1\times1)} \end{bmatrix} + v_{(1\times1)} \end{aligned} \tag{6.42}$$

The state vector can be estimated through the expanded disturbance Kalman Filter of the Spindle-Integrated Force Sensor system as:

$$\begin{aligned}\dot{\hat{x}}_e &= A_e\,\hat{x}_e + K(z-\hat{z}) = A_e\,\hat{x}_e + K(z - C_e\,\hat{x}_e)\\ &= (A_e - KC_e)\hat{x}_e + K\,z\end{aligned} \tag{6.15'}$$

$$\hat{z}_o = C_o\,\hat{x}_e = \hat{F}_a, \quad \text{where } C_o = [0_{(1\times 6)}\ 1]$$

where K is the continuous Kalman Filter gain. The transfer function of the Kalman Filter can be derived from the above equation as;

$$\begin{aligned}\hat{F}_a &= \left\{\frac{C_0 adj[sI-(A_e-KC_e)]}{\det[sI-(A_e-KC_e)]}K\right\}F_m\\ &= G_{\hat{F}_a/F_m}F_m\end{aligned} \tag{6.43}$$

For this case the measurement noise covariance, R, the system noise covariance, Q, and the system noise vector, Γ, are:

$$\begin{aligned}&R_{xx} = [32.58];\ Q_{xx} = [1e9];\ \Gamma_{xx} = [0_{(1\times 6)}\quad 1]^T\\ &R_{yy} = [36.67];\ Q_{yy} = [1e9];\ \Gamma_{yy} = [0_{(1\times 6)}\quad 1]^T\\ &R_{zz} = [55.84];\ Q_{zz} = [1e7];\ \Gamma_{zz} = [0_{(1\times 6)}\quad 1]^T\end{aligned} \tag{6.44}$$

The corresponding error covariance matrices in each direction are:

$$P_{xx} = \begin{bmatrix} 0.0079 & 0.0001 & -0.0471 & 0.0000 & 0.0377 & 0.0000 & 0.0096\\ 0.0001 & 0.0948 & 0.0006 & -0.1503 & 0.0003 & 0.0642 & 0.0370\\ -0.0471 & 0.0006 & 0.3019 & 0.0004 & -0.2556 & 0.0002 & 0.0453\\ 0.0000 & -0.1503 & 0.0004 & 0.2562 & 0.0002 & -0.1172 & 0.0328\\ 0.0377 & 0.0003 & -0.2556 & 0.0002 & 0.2349 & 0.0001 & 0.0343\\ 0.0000 & 0.0642 & 0.0002 & -0.1172 & 0.0001 & 0.0591 & -0.0024\\ 0.0096 & 0.0370 & 0.0453 & 0.0328 & 0.0343 & -0.0024 & 3.7728 \end{bmatrix} \times 1e5$$

$$P_{yy} = \begin{bmatrix} 0.0349 & 0.0003 & -0.1383 & -0.0009 & 0.1397 & 0.0003 & 0.0060\\ 0.0003 & 0.2783 & 0.0011 & -0.5600 & -0.0009 & 0.1441 & 0.0161\\ -0.1383 & 0.0011 & 0.5589 & 0.0003 & -0.5748 & -0.0003 & -0.0082\\ -0.0009 & -0.5600 & 0.0003 & 1.1504 & 0.0003 & -0.3020 & -0.0118\\ 0.1397 & -0.0009 & -0.5748 & 0.0003 & 0.6033 & 0.0002 & 0.0134\\ 0.0003 & 0.1441 & -0.0003 & -0.3020 & 0.0002 & 0.0810 & 0.0041\\ 0.0060 & 0.0161 & -0.0082 & -0.0118 & 0.0134 & 0.0041 & 0.3480 \end{bmatrix} \times 1e6$$

$$P_{zz} = \begin{bmatrix} 0.0007 & 0.0000 & -0.0049 & -0.0000 & 0.0064 & 0.0001 & 0.0008 \\ 0.0000 & 0.0098 & 0.0000 & -0.0510 & -0.0001 & 0.0188 & -0.0025 \\ -0.0049 & 0.0000 & 0.0511 & 0.0000 & -0.0759 & -0.0004 & -0.0045 \\ -0.0000 & -0.0510 & 0.0000 & 0.3028 & 0.0007 & -0.1221 & 0.0364 \\ 0.0064 & -0.0001 & -0.0759 & 0.0007 & 0.1243 & 0.0018 & 0.0585 \\ 0.0001 & 0.0188 & -0.0004 & -0.1221 & 0.0018 & 0.0586 & 0.0954 \\ 0.0008 & -0.0025 & -0.0045 & 0.0364 & 0.0585 & 0.0954 & 2.5699 \end{bmatrix} \times 1e4$$

The Kalman Filter gains using Eq. 6.27 for each axis of the sensor which minimizes the error covariance matrix, P, are:

$$K_{xx} = [-1.20e1\ 8.67e1\ 1.68e2\ 1.03e2\ 7.45e1\ 3.89e1\ 5.54e3]^T$$

$$K_{yy} = [-1.79e2\ 5.14e2\ 6.87e2\ -3.52e2\ -2.53e2\ 1.43e2\ 5.22e3]^T \qquad (6.45)$$

$$K_{zz} = [1.42E\text{-}1\ 2.63\ -4.38\ -7.85\ 1.58e1\ 2.54e1\ 4.23e2]^T$$

The actual force applied at the tool tip is evaluated from the spindle sensor by applying discrete time domain recursive filter Eq. 6.17 at each sampling instant, where the measurements from the Spindle-Integrated force (F_m) sensors in X, Y, and Z directions are collected.

EXPERIMENTAL VERIFICATION

The modeled Frequency Response Function (FRF) of the uncompensated force sensor system (Eq. 6.38, $\Phi(s) = F_m / F_a$), the FRF of the Kalman Filter for force (Eq. 6.42, $G_{\hat{F}a/Fm}(s) = \hat{F}_a / F_m$), and the FRF of the compensated system ($\Phi \times G_{\hat{F}a/Fm}$) are illustrated in Figure 6.9 for three force measurement directions. The cascaded response in X direction shows that the system does not have a perfect unity gain at the regions of modal frequencies, as shown in Figure 6.9 (a); however, the amplifications of force measurements at these regions are significantly reduced with the Kalman Filter. The compensated response in Y direction shows an almost perfect unity gain and the

magnitude drops at high frequency regions. There are two low and one strong high frequency modes (224, 300, and 820 Hz) in Z direction. The cutting forces in Z direction are always dominated by a static (dc) component, and harmonic (ac) components have low amplitudes in milling [Altintas 00]. The Kalman Filter has been designed to attenuate *ac* components which are dominated by the structural modes. The compensation strategy creates phase delays in all directions. Although a phase compensation technique is tried on the filters, the result is an increased computation complexity without significant gains in monitoring cutting forces where the correct magnitude is more important than the delay. Even in adaptive control of cutting forces, the feed cannot be changed in less than 0.03 seconds due to the large inertia of the table and low bandwidth of the feed drives. Hence, the delay does not cause any inconvenience in monitoring the forces.

The Kalman Filter transfer function between the estimated actual force at the tool tip, $\hat{F}_a$, and the measured force at the spindle housing, F_m, can be obtained in three directions using Eq. 6.42 as:

$$Gxx_{\hat{F}_a/F_m} = \frac{5540s^6 + 5.358e6s^5 + 3.835e11s^4 + 2.197e14s^3 + 7.635e18s^2 + 2.111e21s + 4.317e25}{s^7 + 7076s^6 + 9.38e7s^5 + 4.272e11s^4 + 2.36e15s^3 + 7.753e18s^2 + 1.693e22s + 4.146e25}$$

$$Gyy_{\hat{F}_a/F_m} = \frac{5222s^6 + 3.149e6s^5 + 5.039e11s^4 + 2.035e14s^3 + 1.593e19s^2 + 3.231e21s + 1.645e26}{s^7 + 7708s^6 + 1.26e8s^5 + 6.713e11s^4 + 4.918e15s^3 + 1.878e19s^2 + 6.047e22s + 1.675e26} \tag{6.46}$$

$$Gzz_{\hat{F}_a/F_m} = \frac{423.1s^6 + 3.248e5s^5 + 1.364e10s^4 + 4.824e12s^3 + 6.555e16s^2 + 1.051e19s + 7.906e22}{s^7 + 1265s^6 + 3.275e7s^5 + 2.548e10s^4 + 1.62e14s^3 + 9.007e16s^2 + 2.024e20s + 7.577e22}$$

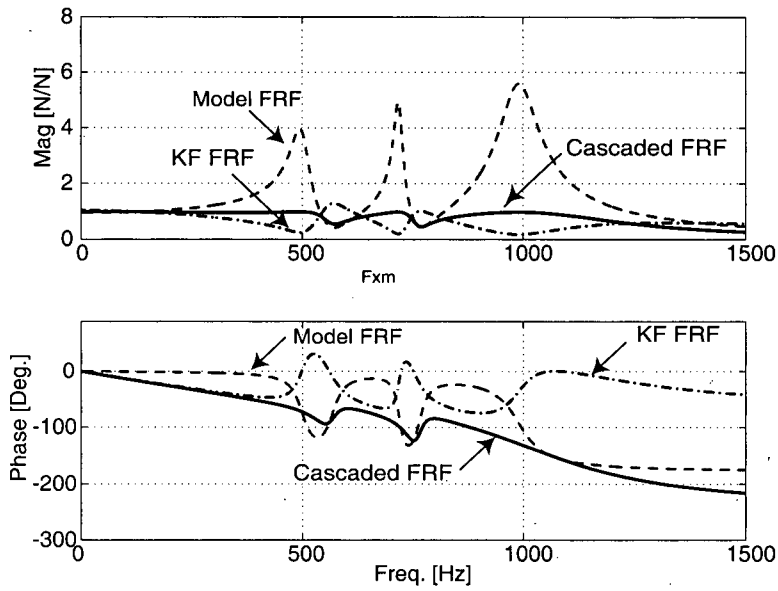

(a) The model ($G(s) = F_m / F_a$), the Kalman Filter ($G_{\hat{F}_a / F_m}(s) = \hat{F}_a / F_m$), and the cascaded ($G(s) \times G_{\hat{F}_a / F_m}(s)$) FRFs in X direction.

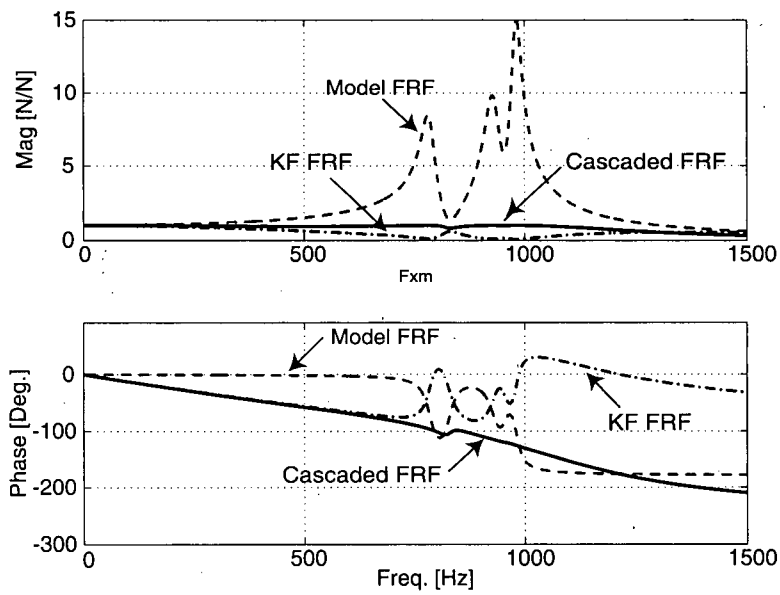

(b) The model ($G(s) = F_m / F_a$), the Kalman Filter ($G_{\hat{F}_a / F_m}(s) = \hat{F}_a / F_m$), and the cascaded ($G(s) \times G_{\hat{F}_a / F_m}(s)$) FRFs in Y direction.

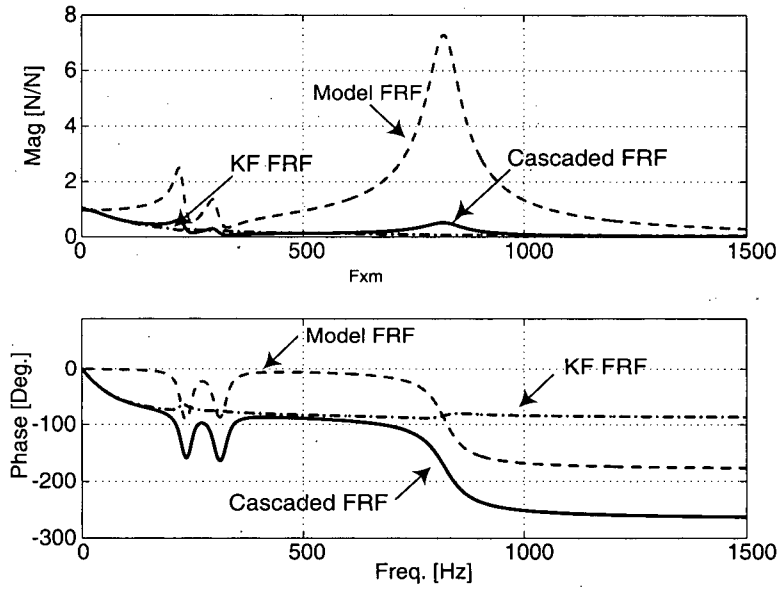

(c) The model ($G(s) = F_m / F_a$), the Kalman Filter ($G_{\hat{F}_a / F_m}(s) = \hat{F}_a / F_m$), and the cascaded ($G(s) \times G_{\hat{F}_a / F_m}(s)$) FRFs in Z direction.

Figure 6.9 FRFs of the measured, the Kalman Filter, and the compensated Spindle-Integrated force sensing system

The cutting tests are performed with spindle speeds ranging from 1000 rev/min to 12,000 rev/min where the axial depth of cut is 2 mm and the cutting condition is slotting. The cutting test results for a spindle speed of 1000 rev/min, or with the tooth passing frequency of 83.35 Hz are given in Figure 6.10. The reference cutting force in Z direction has very few *ac* components. When the spindle speed is increased to 6000 rev/min, the tooth passing frequency (500 Hz) coincides with the first natural frequency in X axis of the spindle sensor. The force amplitude measured from the spindle sensors increased by three times. However, the Kalman Filter compensates the dynamic amplification due to the first mode, and brings the force to the level provided by the dynamometer, see Figure 6.11 (a). The cutting forces in Y direction are slightly amplified due to the modes in Y

direction, see Figure 6.11 (b). The small *ac* component in the Z direction leads to distortion of the cutting forces by the low frequency modes of the spindle structure. The Kalman Filter compensates them significantly as shown in Figure 6.11 (c). At 9000 rev/min the tooth passing frequency is 750 Hz which is beyond the two modes in Z direction, but very close to the second mode (719 Hz) in X, and the first mode (785 Hz) in Y axes. Particularly, the measured forces are severely amplified in Y direction. The compensated force measurements are still in good agreement with the reference forces in all three directions, as shown in Figure 6.12. When the speed is increased to 12000 rev/min, the tooth passing frequency becomes 1000 Hz as illustrated in Figure 6.13. The measured cutting forces from the spindle sensors are distorted by modes in all three directions. However, the compensated cutting forces are still in a reasonable agreement with the reference forces.

The disturbance Kalman Filter with the direct transfer functions successfully compensates the modes in all three directions. The exclusion of the accelerometer did not deteriorate the compensation, and the piecewise constant assumption satisfies the compensated results.

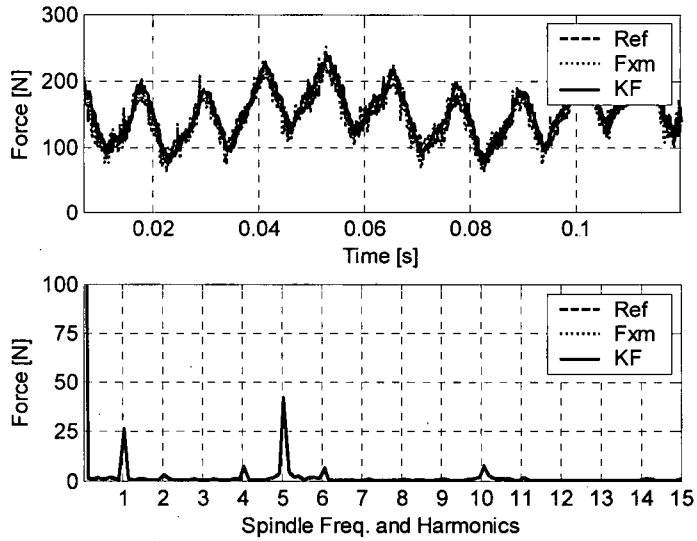

(a) X direction

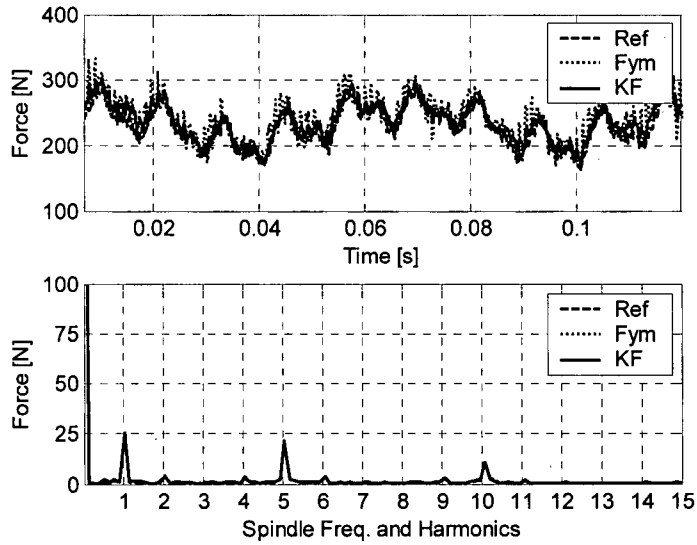

(b) Y direction

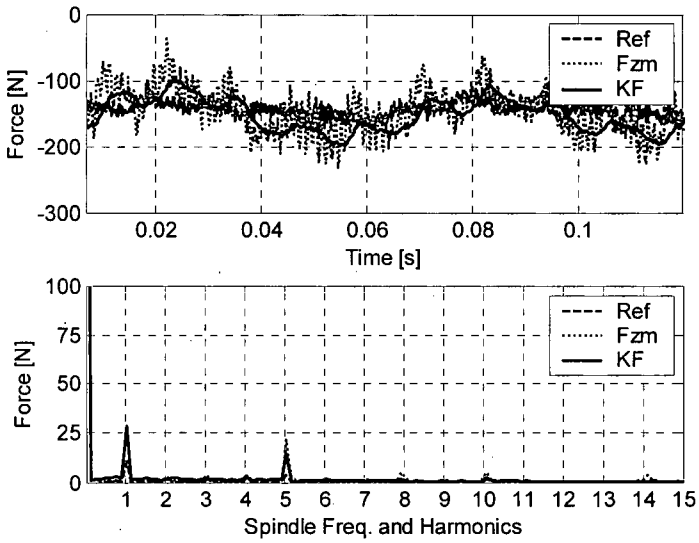

(c) Z direction

Figure 6.10 Five fluted cutting force measurements at 1000 rpm in (a) X, (b) Y, and (c) Z directions. The figures are shown in the time and frequency (normalized with the spindle freq.) domains. The spindle frequency at 1000 rpm corresponds to 16.7 Hz. *('Ref.' denotes the reference cutting forces from the dynamometer at 1000 rpm, 'Fm' denotes the measured force from the Spindle-Integrated Force Sensor system, and 'KF' denotes the Kalman Filter compensated cutting forces)*

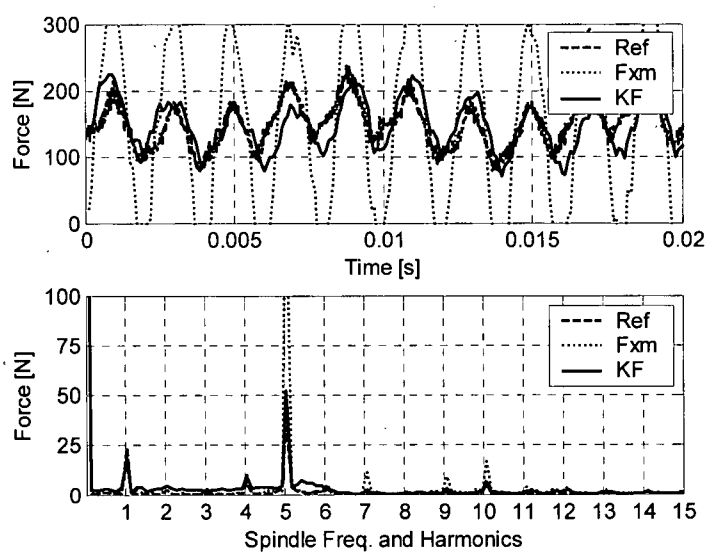

(a) X direction

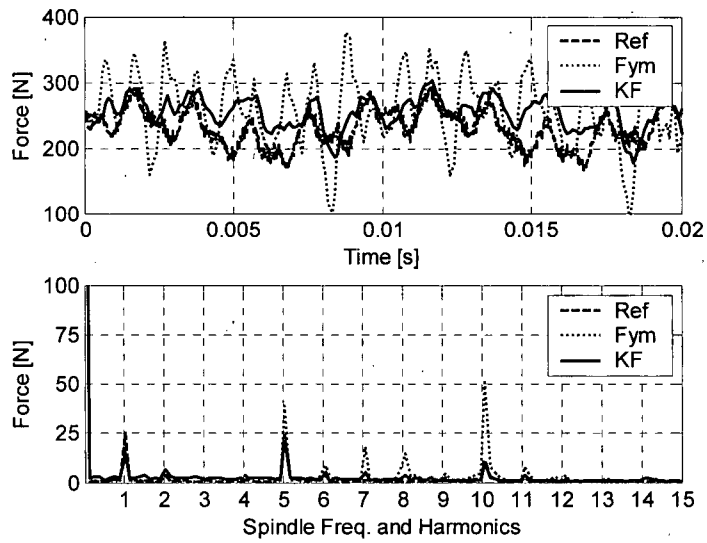

(b) Y direction

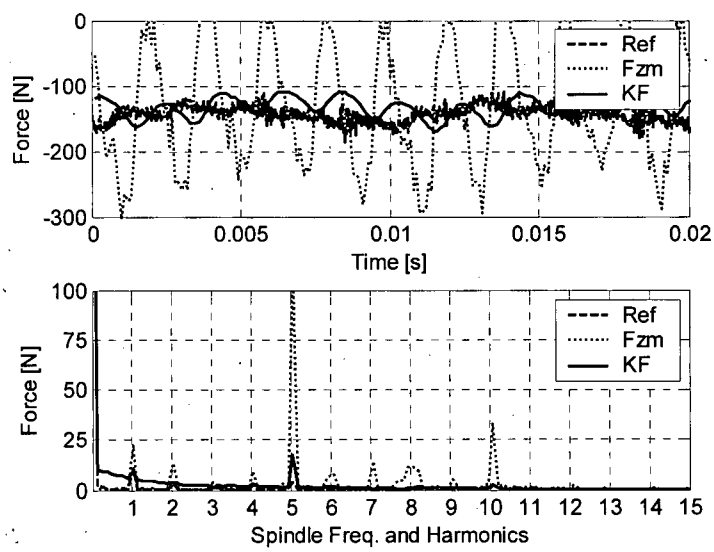

(c) Z direction

Figure 6.11 Five fluted cutting force measurements at 6000 rpm in (a) X, (b) Y, and (c) Z directions. *The figures are shown in the time and frequency (normalized with the spindle freq.) domains. The spindle frequency at 6000 rpm corresponds to 100 Hz.*

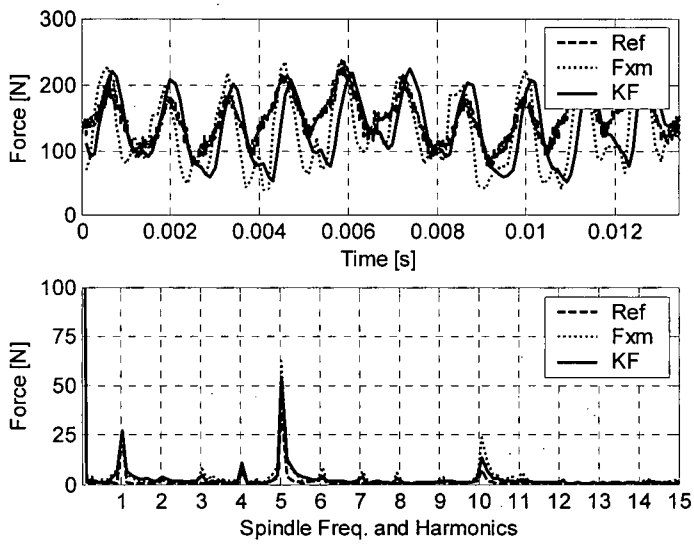

(a) X direction

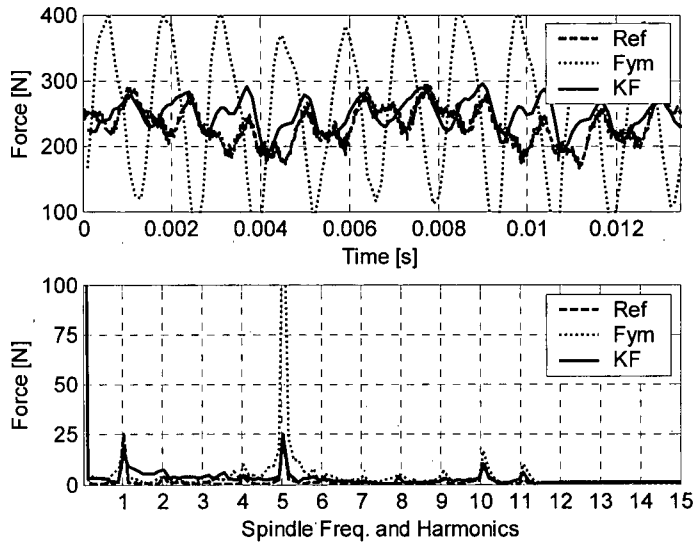

(b) Y direction

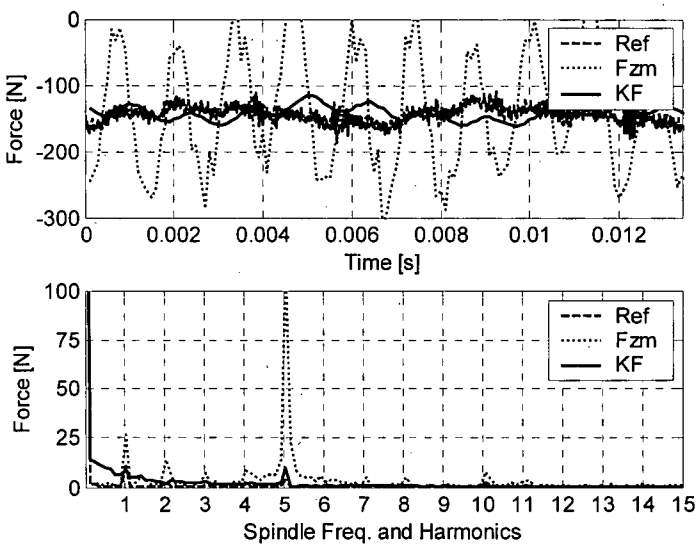

(c) Z direction

Figure 6.12 Five fluted cutting force measurements at 9000 rpm in (a) X, (b) Y, and (c) Z directions. *The figures are shown in the time and frequency (normalized with the spindle freq.) domains. The spindle frequency at 9000 rpm corresponds to 150 Hz.*

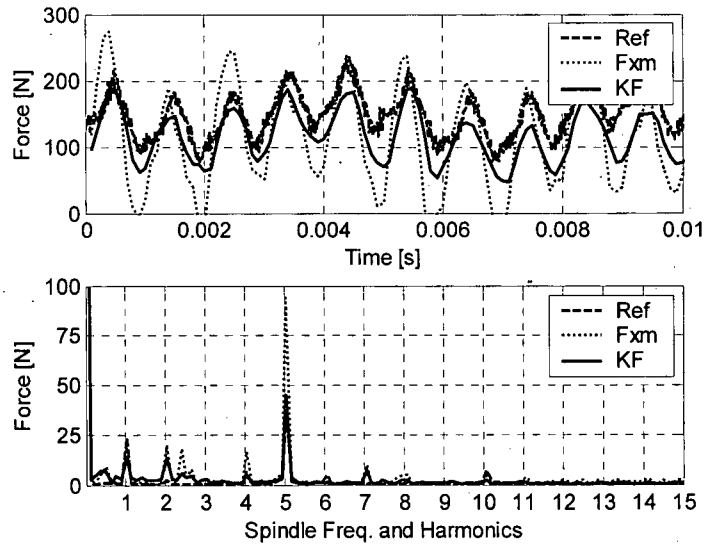

(a) X direction

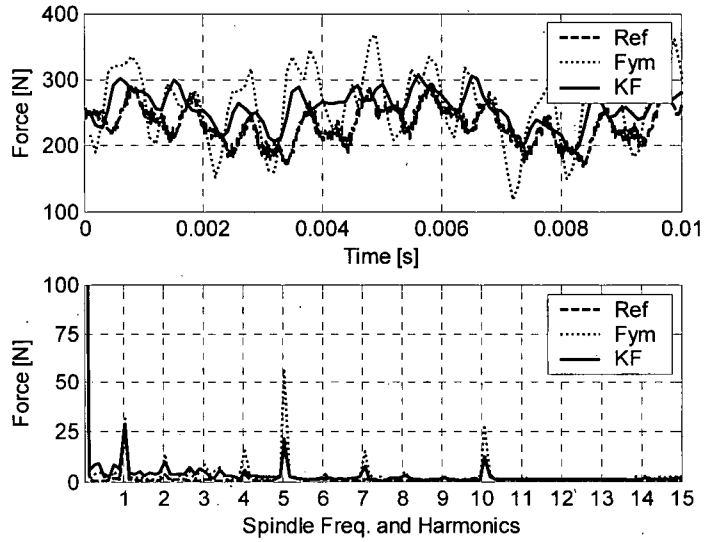

(b) Y direction

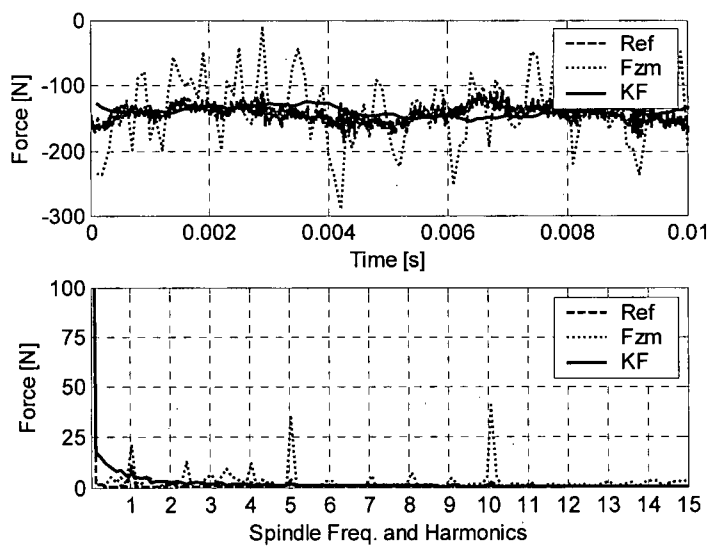

(c) Z direction

Figure 6.13 Five fluted cutting force measurements at 12000 rpm in (a) X, (b) Y, and (c) Z directions. *The figures are shown in the time and frequency (normalized with the spindle freq.) domains. The spindle frequency at 12000 rpm corresponds to 200 Hz.*

In addition to slot machining experiments, the system has been tested on a number of different configurations including low immersion milling where the forces have zero

values between the tooth impacts. The sample experimental results at 1000 and 6000 rev/min are shown in Figures 6.14 and 6.15 where the width of cut is only 3 mm, and the tooth engagement is very short to test highly dynamic cases. The axial depth of cut is 2 mm. Figure 6.14 depicts the cutting forces at 1000 rev/min where the reference forces and the compensated forces are almost identical. Moreover, it can be seen that the Kalman Filter effectively compensates unwanted dynamics in X and Y directions at 6000 rev/min which corresponds to the tooth passing frequency of 500 Hz as shown in Fig. 5.22. However, the test is a severe case with strong harmonics beyond the 1000 Hz range of the Kalman Filter. Therefore the second harmonics of the tooth passing frequency components (i.e., beyond 1000 Hz) are not effectively compensated due to the bandwidth of the compensation scheme.

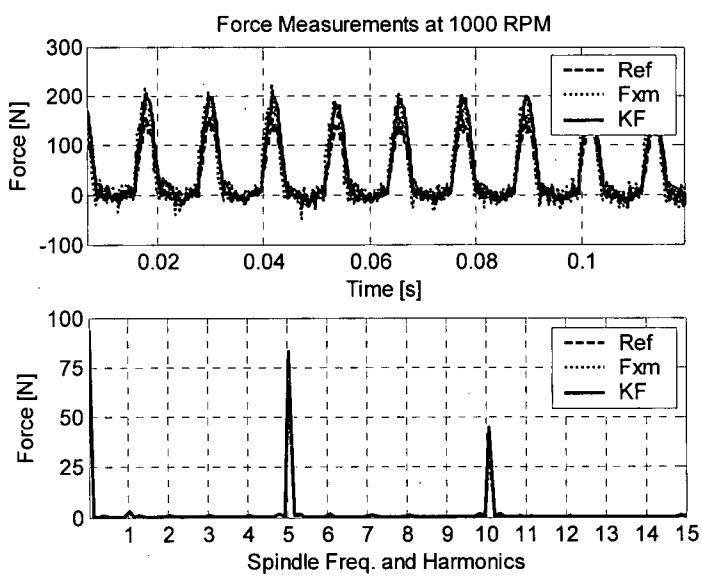

(a) X direction

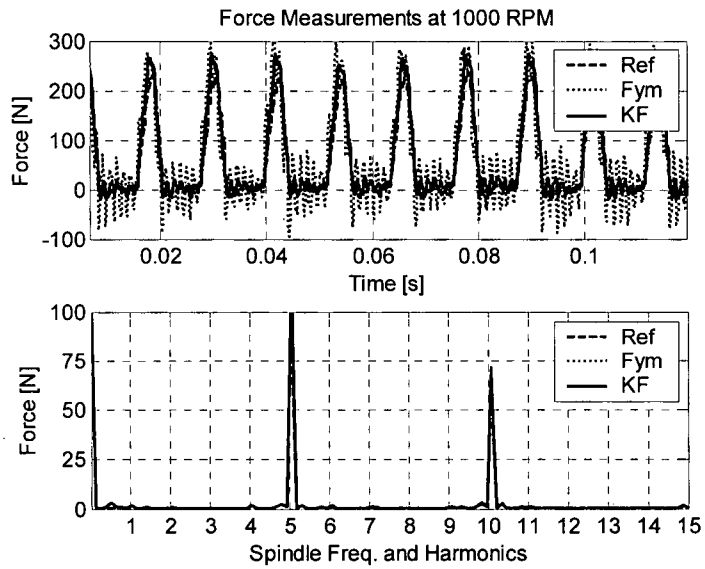

(b) Y direction

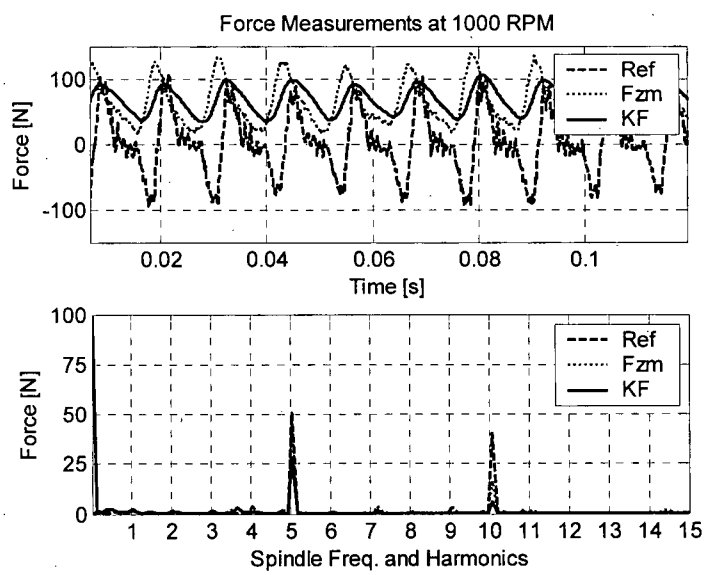

(c) Z direction

Figure 6.14 Five fluted cutting force measurements at 1000 rpm in (a) X, (b) Y, and (c) Z directions. The figures are shown in the time and frequency (normalized with the spindle freq.) domains. The spindle frequency at 1000 rpm corresponds to 16.7 Hz. *('Ref.' denotes the reference cutting forces from the dynamometer at 1000 rpm, 'Fm' denotes the measured force from the Spindle-Integrated Force Sensor system, and 'KF' denotes the Kalman Filter compensated cutting forces).*

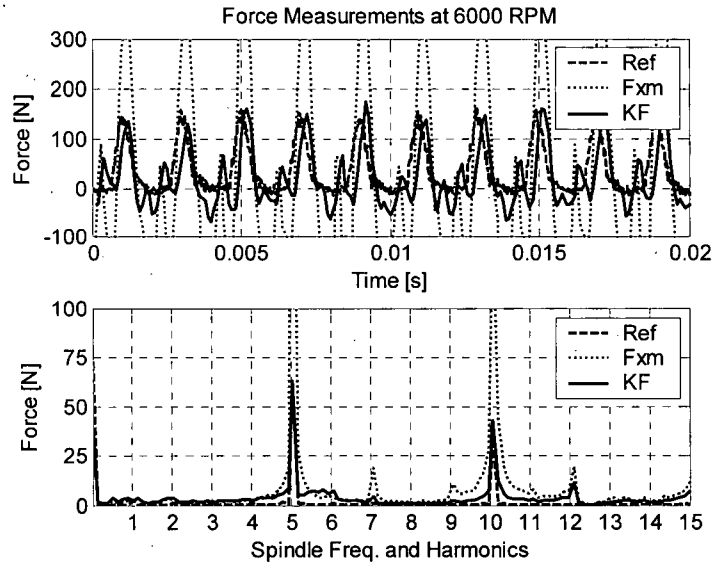

(a) X direction

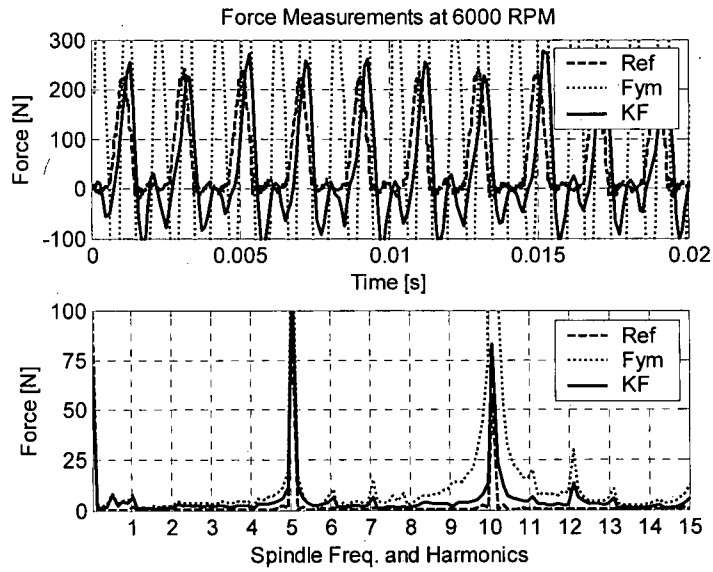

(b) Y direction

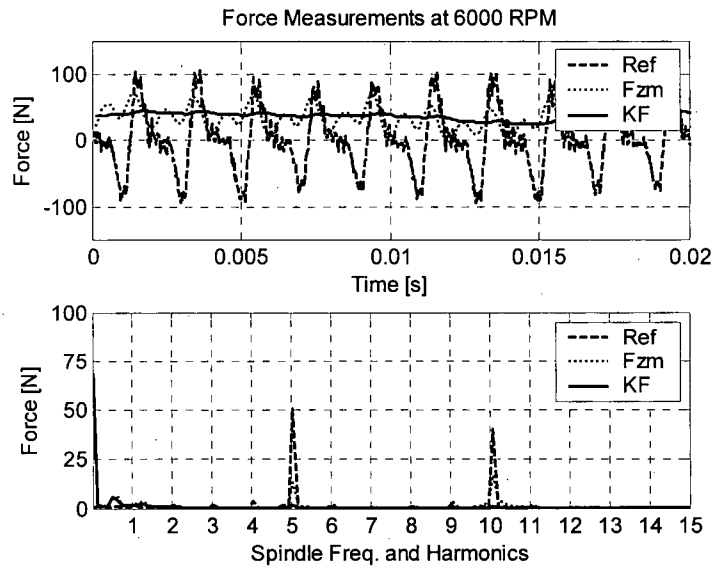

(c) Z direction

Figure 6.15 Five fluted cutting force measurements at 6000 rpm in (a) X, (b) Y, (c) Z directions. *The figures are shown in the time and frequency (normalized with the spindle freq.) domains. The spindle frequency at 6000 rpm corresponds to 100 Hz.*

6.3 CUTTING FORCE MEASUREMENT USING THE CAPACITANCE DISPLACEMENT SENSOR

The measurement of spindle shaft displacements is investigated as an alternative method to the Spindle-Integrated Force Sensors to measure cutting forces. The capacitance displacement probe is mounted on the outside of the spindle housing through the mounting bracket. The capacitance measurement system is insensitive to overload and is not subject to wear because the sensors are not in contact with the spindle. The displacement sensor measures the distance to the target object (i.e., spindle shaft flange) over the spot size. The sensor measures variations in the electrical field as a voltage signal. However, changes in the electrical field may not always be caused by a variation in the size of the gap between the sensor head and the spindle flange. Since the electric field of the capacitive sensor reacts to air humidity or dirt on the target surface, slight variations may occur if the environment is not properly controlled. One of the challenges associated with the force measurements using capacitance displacement probes is that the eccentricity of the spindle and vibrations between the bracket and probe hinder measurements. Furthermore, the displacement sensors are more prone to thermal growth which changes the overall transfer function as well as the calibration factor. Similar to the SIFS system when the cutting force frequency contents are beyond the natural modes of the spindle structure, the vibrations distort the displacement signals. To compensate the effects of the spindle dynamics, the same disturbance Kalman Filter compensation procedure in Section 6.2 is used to recover the cutting force signals from the distorted displacement measurements obtained from the capacitance probe.

The tool is loaded statically, and the static deflection is measured from the capacitance probe, which leads to the calibration of the sensing system. The displacement sensor is statically calibrated in X direction of the machine to measure the cutting forces by applying a gradually increasing load on the tool tip while measuring both reference force and displacement, as shown in Figure 4.6. Displacement over force yields the static compliance G_s of the spindle system, where the static stiffness K_s is the inverse value:

$$G_s = \frac{\delta}{F} = \frac{1}{K_S} = 0.02\ [\mu m/N],\ K_s = 50\ N/\mu m \tag{6.47}$$

The spindle structure is excited on the tool tip by applying a short impact with an instrumented force hammer. The displacements are measured with the Spindle-Integrated capacitance sensor. Both the impact force and displacement response of the spindle structure are recorded synchronously and processed to obtain the transfer function of the sensing system. The displacement transfer function (Φ_d) is scaled with the static stiffness K_s as shown in Eq. 6.47:

$$\Phi_d = \frac{\delta\ [m]}{F\ [N]} \times K_s[N/m] = \frac{\delta_F\ [N]}{F\ [N]} \tag{6.48}$$

The static and dynamic cross talks are found to be negligible for the displacement sensor. Therefore in this study, the cutting force in X direction measured from the capacitance sensor is used as an example case, and it can be extended to Y and Z directions using the identical procedure.

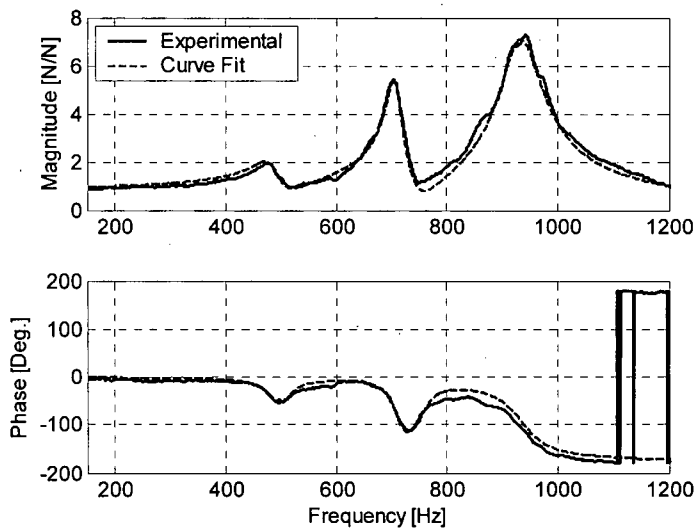

Figure 6.16 Transfer Function $\Phi_d(\omega) = \delta_F(\omega) / F_a(\omega)$ in X direction

The transfer functions ($\Phi_d(s)$) between the force applied at the tool tip (F_a) and the calibrated displacement (δ_F) in X direction are shown in Figure 6.16 where the output measurements are transformed into Newton. The first major resonance peak is at approximately 486 Hz and the second mode is at 708 Hz, and these modes originate from the bending of the spindle and the tool holder at the tapered interface. The third peak is at 934 Hz, which is due to the tool holder assembly bending at the CAT 40 (7/24) spindle taper interface.

The displacement sensor also records cutting forces caused by spindle run out. Prior to the compensation, the spindle run out is compensated by subtracting the air cutting measurements from the cutting forces where the spindle encoder is used as a synchronization clock. During the air cutting measurements, the tool needs to be engaged onto the workpiece without cutting the material to preload the spindle shaft. When the preload is not applied during the air cutting, the dc components of the force from the displacement sensor cannot be measured properly. This may be due to the slight variation of the tool holder and the taper (7/24) interface, which causes slight tilting of

the tool holder without touching the interface. Similar to the Spindle-Integrated Force Sensor system, the transfer function parameters of the system are updated as a function of the spindle speed (see Appendix D).

The experimentally measured transfer function is identified by a modal curve fitting technique as;

$$\Phi_d(s) = \frac{\delta_F(s)}{F_a(s)} = \sum_{k=1}^{3} \frac{\alpha_k^{-1} \cdot \omega_{n,k}^{2}}{s^2 + 2\xi_k \omega_{n,k} s + \omega_{n,k}^{2}} \tag{6.49}$$

where k is the number of modes, δ_F is the measured force from the Spindle-Integrated force sensor, and F_a is the applied force at the tool tip. The modal parameters in three directions are given in Table 6.3. The modal equation (Eq. 6.48) is expanded into polynomial forms as:

$$\begin{aligned}\Phi(s) = \frac{\delta_F(s)}{F_a(s)} &= \frac{b_0 s^5 + b_1 s^4 + b_2 s^3 + b_3 s^2 + b_4 s + b_5}{s^6 + a_1 s^5 + a_2 s^4 + a_3 s^3 + a_4 s^2 + a_5 s + a_6} \\ &= \frac{2.55\text{e}7 s^4 + 1.43\text{e}10 s^3 + 8.39\text{e}14 s^2 + 2.43\text{e}17 s + 5.89\text{e}21}{s^6 + 989 s^5 + 6.39\text{e}7 s^4 + 3.94\text{e}10 s^3 + 1.19\text{e}15 s^2 + 3.62\text{e}17 s + 6.35\text{e}21}\end{aligned} \tag{6.50}$$

Table 6.3 Modal Parameters obtained by Curve Fitting the Transfer functions at the stationary spindle speed

k	ω_n (Hz)	ξ	α
1	486	0.050	*6.00*
2	708	0.022	*4.58*
3	934	0.041	*1.71*

DYNAMIC COMPENSATION

The same dynamic compensation procedure is used in Section 6.2. The transfer functions given in Eq. 6.48 are mapped individually for each axis into the following state space form;

$$\begin{aligned} \dot{x} &= A_s x + B_s u \\ z &= C_s x \end{aligned} \tag{6.1'}$$

where x is the state vector, $u = F_a$ is the input or the actual force applied to the tool, and $z = \delta_F$ is the measured cutting force from the displacement sensor. The Kalman Filter is designed to reconstruct the actual force (F_a) applied at the tool.

$$\begin{bmatrix} \dot{x}_1 \\ \dot{x}_2 \\ \dot{x}_3 \\ \dot{x}_4 \\ \dot{x}_5 \\ \dot{x}_6 \end{bmatrix} = \begin{bmatrix} -a_1 & -a_2 & -a_3 & -a_4 & -a_5 & -a_6 \\ 1 & 0 & 0 & 0 & 0 & 0 \\ 0 & 1 & 0 & 0 & 0 & 0 \\ 0 & 0 & 1 & 0 & 0 & 0 \\ 0 & 0 & 0 & 1 & 0 & 0 \\ 0 & 0 & 0 & 0 & 1 & 0 \end{bmatrix} \begin{bmatrix} x_1 \\ x_2 \\ x_3 \\ x_4 \\ x_5 \\ x_6 \end{bmatrix} + \begin{bmatrix} 1 \\ 0 \\ 0 \\ 0 \\ 0 \\ 0 \end{bmatrix} F_a$$

$$[\delta_F] = [0 \quad b_1 \quad b_2 \quad b_3 \quad b_4 \quad b_5] \begin{bmatrix} x_1 \\ x_2 \\ x_3 \\ x_4 \\ x_5 \\ x_6 \end{bmatrix} \tag{6.51}$$

where the system polynomial parameters are given in Eq. 6.49. The system matrices are transformed into an equivalent system (i.e., $x_n = Tx$) by applying the transformation matrix T. The similarity transformation matrix, T, for the sensor system is found to be:

$$T = diag([6.40e1 \ 1.05e6 \ 6.59e9 \ 3.52e13 \ 6.20e16 \ 1.48e20]) \tag{6.52}$$

The identified equivalent state matrix in X direction is:

$$A_n = \begin{bmatrix} -989 & -3898 & -293.7 & -2170 & -321.3 & -2756 \\ 16384 & 0 & 0 & 0 & 0 & 0 \\ 0 & 8192 & 0 & 0 & 0 & 0 \\ 0 & 0 & 4096 & 0 & 0 & 0 \\ 0 & 0 & 0 & 4096 & 0 & 0 \\ 0 & 0 & 0 & 0 & 2048 & 0 \end{bmatrix}$$

$$B_n = [64 \quad 0 \quad 0 \quad 0 \quad 0 \quad 0]^T$$

$$C_n = [0 \quad 24.38 \quad 1.67 \quad 23.84 \quad 3.372 \quad 39.88]$$

DISTURBANCE MODEL EXPANSION

The actual cutting force applied on the tool can be considered as one of the unknown states. The expanded state vector is depicted as:

$$x_{e(7\times1)} = \left[x_n^T{}_{(1\times6)} \quad F_a^T{}_{(1\times1)}\right]^T,\ u_e = [0] \tag{6.53}$$

For the dynamic compensation using the capacitance probe, the measurement, system noise covariance, and the system noise vector, Γ, are:

$$R = [56.59];\ Q = [1e9];\ \Gamma = \left[0_{(1\times6)} \quad 1\right]^T \tag{6.54}$$

The Kalman Filter gains for each axis of the sensor that minimize the error covariance matrix, P, are:

$$K = [\,-0.0192 \quad 0.0787 \quad 0.1889 \quad 0.1055 \quad 0.0089 \quad 0.0095 \quad 4.2034]^T x1e3 \tag{6.55}$$

The Kalman Filter transfer function between the estimated actual force at the tool tip, $\hat{F}_a$, and measured force at the displacement sensor, δ_F, can be obtained as:

$$\begin{aligned}\hat{F}_a &= \left\{\frac{C_0 adj[sI-(A_e-KC_e)]}{\det[sI-(A_e-KC_e)]}K\right\}\delta_F \\ &= G_{\hat{F}_a/\delta_F}\delta_F\end{aligned} \tag{6.56}$$

with the following parameters:

$$G_{\hat{F}_a/\delta_F} = \frac{203s^6 + 4.157e6s^5 + 2.684e11s^4 + 1.657e14s^3 + 5.015e18s^2 + 1.521e21s + 2.671e25}{s^7 + 6144s^6 + 8.224e7s^5 + 3.308e11s^4 + 1.843e15s^3 + 5.317e18s^2 + 1.14e22s + 2.474e25} \tag{6.57}$$

The modeled Frequency Response Function (FRF) of the uncompensated force sensor system (Eq. 6.48, $\Phi_d(s) = \delta_F / F_a$), the FRF of the Kalman Filter for force (Eq. 6.56, $G_{\hat{F}_a/\delta_F}(s) = \hat{F}_a / \delta_F$), and the FRF of the compensated system ($\Phi_d \times G_{\hat{F}_a/\delta_F}$) are illustrated in Figure 6.17. Similar to the force sensor compensation, the cascaded response in X direction shows that the system does not have a perfect unity gain at the

regions of modal frequencies, especially at anti-mode locations. However, the amplifications of the force measurements at these regions are significantly reduced with the Kalman Filter. The compensation strategy creates phase delays of 90 degrees at 500 Hz.

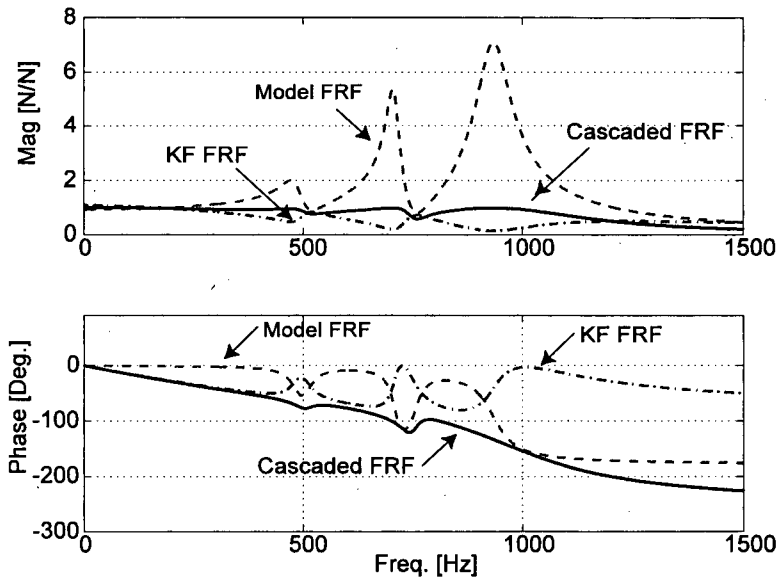

Figure 6.17 FRF of the measured, the Kalman Filter, and the Compensated Indirect force sensing system in X direction

EXPERIMENTAL VERIFICATION

Identical cutting conditions as the compensation of forces for the SIFS (i.e., depth of cut of 2 mm, slotting) are used for the displacement sensor case. The cutting test results for a spindle speed of 1000 rev/min, or with the tooth passing frequency of 83.35 Hz, are given in Figure 6.18. The bandwidth of the sensor (i.e., 350 Hz) is large enough to capture the first two harmonics of the force measurements. Therefore, the

displacement sensor effectively measures cutting forces (see the spectrum contents at the tooth passing frequency).

When the spindle speed is increased to 6000 rev/min, the tooth passing frequency (500 Hz) becomes extremely close to the first mode (486 Hz). Therefore, the dynamics of the first mode distort the displacement measurements. The Kalman Filter effectively compensates the distortions at the tooth passing frequency and its harmonics, and brings the force to the level provided by the dynamometer, see Figure 6.19.

At 9000 rev/min, the tooth passing frequency is 750 Hz, which is very close to the second mode (708 Hz). The compensated force measurements are still in good agreement with the reference forces in all three directions, as shown in Figure 6.20.

When the speed is increased to 12000 rev/min, the tooth passing frequency becomes 1000 Hz. The third mode of the structure dynamics has the highest magnitude, which is very close to the tooth passing frequency. Therefore, the forces measured from the Spindle-Integrated sensors are severely amplified due to the dynamics, as shown in Figure 6.21, where displacement sensor force signals are twice the measured reference force. The Kalman Filter successfully compensates the distorted signals to match the reference force very closely.

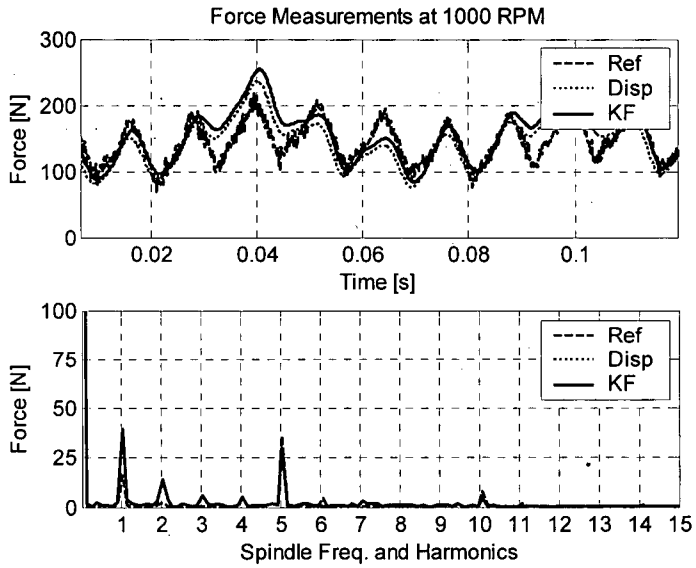

Figure 6.18 Five-fluted cutting force measurements at 1000 rpm. The figures are shown in the time and frequency (normalized with the spindle freq.) domains. The spindle frequency at 1000 rpm corresponds to 16.7 Hz. *('Ref.' denotes the reference cutting forces from the dynamometer at 1000 rpm, 'Disp' denotes the measured force from the displacement sensor system, and 'KF' denotes the Kalman Filter compensated cutting force).*

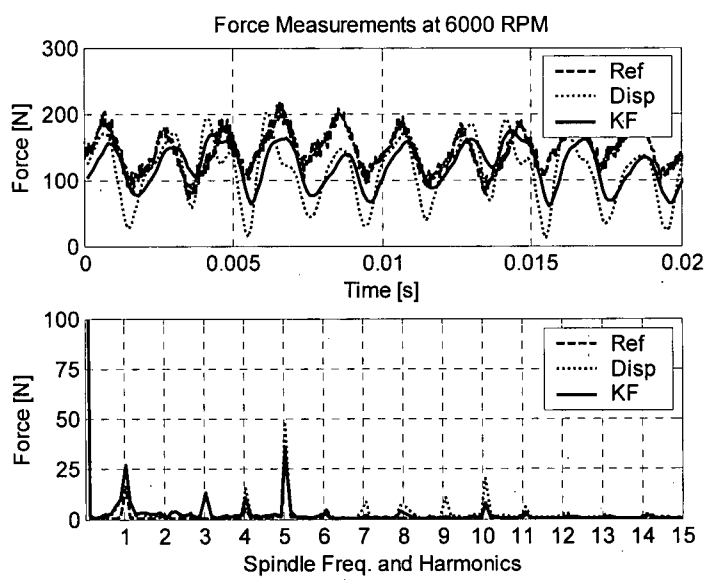

Figure 6.19 Five-fluted cutting force measurements at 6000 rpm. The spindle frequency at 6000 rpm corresponds to 100 Hz.

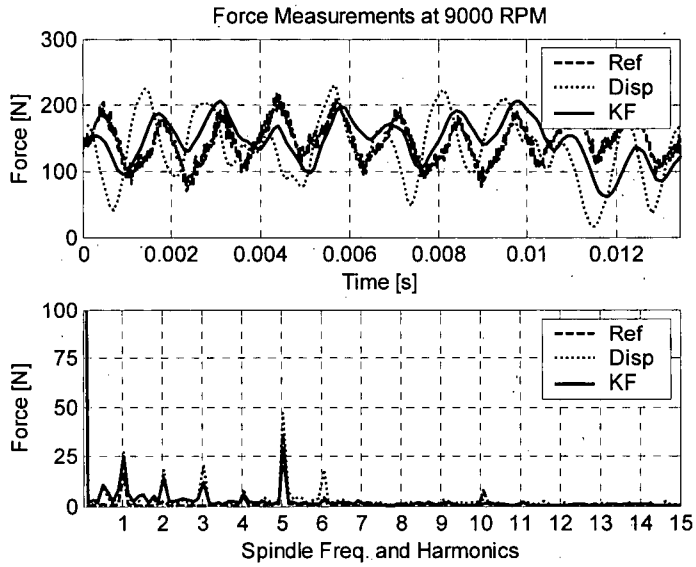

Figure 6.20 Five-fluted cutting force measurements at 9000 rpm. The spindle frequency at 9000 rpm corresponds to 150 Hz.

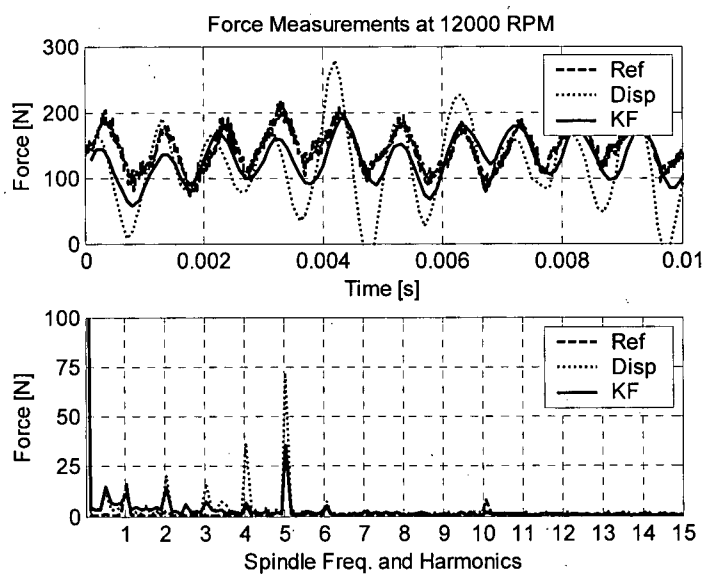

Figure 6.21 Five-fluted cutting force measurements at 12000 rpm. The spindle frequency at 12000 rpm corresponds to 200 Hz.

6.4 CONCLUSION

The Spindle-Integrated Force Sensor and the capacitance displacement sensor systems present a viable solution to measure cutting forces in production machines. However, once the spindle sensors are mounted on the spindle that is away from the tool tip, the spindle dynamics affect the force measurements at the integrated sensors. Thus, the compensation of these spindle dynamics is paramount to acquire the accurate cutting forces at high speeds. The identification of the spindle dynamics is carried out using the experimental modal analysis. Based on the identified model of the spindle dynamics, the disturbance Kalman Filter method is used to compensate the dynamics. The cutting tests indicate that the bandwidth of the compensated system is significantly increased while compensating the influences of the modes of the spindle structure from 350 Hz to 1000 Hz. The comparison between the SIFS and the capacitance displacement sensor systems indicates that the capacitance sensor is more susceptible to temperature fluctuation and that constant preloads are required to remove any movement of the tool holder inside of the taper 7/24 interface.

CHAPTER 7.

APPLICATIONS OF THE SPINDLE INTEGRATED FORCE SENSOR SYSTEM

In this chapter, applications of the Spindle Integrated Force Sensors are examined where the cutting forces are reconstructed using the disturbance Kalman Filter. The first application of the spindle sensors deals with the on-line Adaptive Control with Constraint (ACC) through the use of the Generalized Predictive Control (GPC) scheme. The GPC allows inclusion of future transient changes in cutting forces to control the feed rate of the CNC system to maintain the desired resultant cutting force. The proposed control scheme is implemented using the Open Architecture Real-Time Operating System (ORTS) based on a Digital Signal Processing (DSP) board. The second application of the sensors is the chatter detection. The chatter is caused by self-excited vibrations due to the interactions between the tool and the workpiece dynamics. Chatter vibration leads to accelerated tool wear and eventually to tool failures. The filtered cutting forces are analyzed in the frequency domain to detect the unstable cutting conditions (i.e., chatter) based on the predetermined chatter thresholds. The third application is tool breakage detection by estimating the residues of the cutting process using the first order Auto Regressive (AR) filter. If the residues of the process violate the threshold limits, the tool is assumed to be broken. The experiments are performed to verify the usability of the spindle integrated sensors.

7.1 ADAPTIVE CONTROL WITH CONSTRAINT (ACC)

In traditional CNC systems, the machining parameters are selected for the worst case cutting condition scenario according to handbooks or experience of operators to avoid machine failures. Therefore, productivity of machining processes suffers because CNC machines cannot fully utilize their peak performances. To improve the productivity and accuracy of milling operations, the adaptive control can be used to provide optimal machining parameters by adapting to the changes in cutting conditions such as depth and width of cuts. Several researchers have used Adaptive Control with Constraint to maximize cutting processes by maintaining cutting forces at desired amplitudes [Tlusty 77, Lauderbaugh 85, Liu 01, Altintas 00, Altintas 94]. In this study, the Adaptive Control with Constraint (ACC) based on the GPC algorithm presented by Altintas [Altintas 00] is utilized to adjust feed rates of the XY table of the milling machine to keep the peak resultant force at a desired level to avoid excessive forces. Similarly, the maximum force normal to the finished surface can be constrained so that the static tool deflection is kept within the tolerance. The cutting forces obtained from the spindle integrated sensors with the disturbance Kalman Filter are used to match the reference force.

7.1.1 MACHINING PROCESS IN THE ADAPTIVE CONTROL

Machining process mainly consists of the CNC feed drive dynamics and the cutting process dynamics. Figure 7.1 depicts the overall CNC schematics where the input of the machining process plant is feed rate (f_c) and the output is the resultant force applied at the tool tip. The force applied at the tool tip (F_a) is measured from the Spindle Integrated Force Sensor (SIFS) system with the disturbance Kalman Filter compensation

scheme. Run out component of cutting forces cause fluctuations in the cutting forces which would send similar fluctuating feed signals to the low bandwidth machine tool drives. This is not desirable and many researchers have used the peak force at each spindle revolution to minimize the oscillatory behaviour of the controller [Altintas 00].

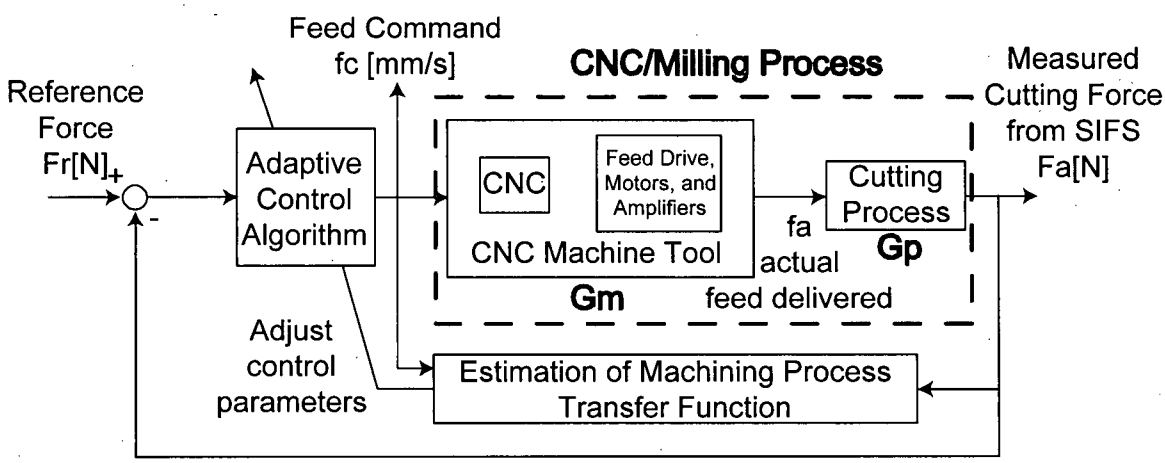

Figure 7.1 Block diagram of a general adaptive control system in machining [Altintas 00]

The CNC and feed drive system can be approximated to be [Altintas 96, Spence 91]:

$$G_m(z) = \frac{f_a(z)}{f_c(z)} = \frac{\left(g_0 + g_1 z^{-1} + g_2 z^{-2}\right)}{1 - h_1 z^{-1}} \tag{7.1}$$

where f_a and f_c are the actual output and command input values of feed speed [mm/s]. Depending on the feed rate and spindle speed change, the servo transfer function parameters g_0, g_1, g_2, and h_1 will vary. In any case, h_1 must be less than one to be stable.

For the cutting process, the maximum cutting force normal to the machined surface acts approximately at the tool ends and the dimensional error left on the part due to the end mill's flexibility can be expressed by [Altintas 96]:

$$\delta_y(k) = \frac{F_a(j)}{k_t} \tag{7.2}$$

where $F_a(j)$ is the maximum cutting force normal to the finished surface at period j, and k_t is the end mill's stiffness. The static tool deflection diagram is illustrated in Figure 7.2.

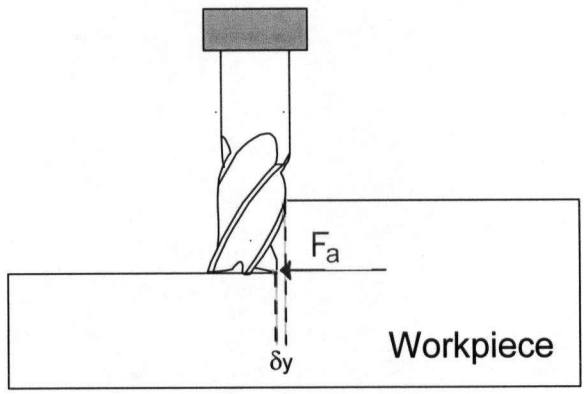

Figure 7.2 Static Tool Deflection

The maximum cutting force changes depending on the axial (b) depth of cut. The maximum cutting force can be expressed as:

$$F_a(k) = K_s b h_m(j) \tag{7.3}$$

where h_m is the maximum chip thickness, and K_s is the cutting coefficient. In this analysis, the edge forces are assumed to be negligible. The chip thickness is also affected by the deflection of the tools as shown in Figure 7.3.

$$h_m(k) = c(k-1) - \delta(k) + \delta(k-1) \tag{7.4}$$

where c is the feed rate [mm/tooth].

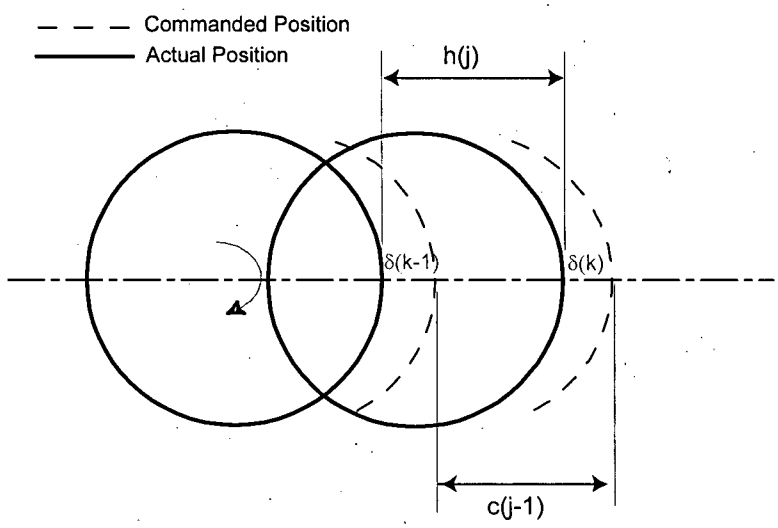

Figure 7.3 Chip Thickness of Milling Process

By combining above equations (7.2 – 7.4), the following equation can be obtained:

$$\frac{F_a(j)}{K_s b} = c(j-1) - \frac{F_a(j)}{k_t} + \frac{F_a(j-1)}{k_t} \tag{7.5}$$

where

$$c(j) \quad [mm/tooth] = f_a(j)[mm/\sec]/Mn \tag{7.6}$$

M is the number of flutes and n is the spindle rotational speed [rev/sec]. Rearranging Eq. 7.5 into the discrete transfer function of the cutting process can be represented as:

$$G_p(z) = \frac{F_a(j)}{f_a(j)} = \frac{\beta z^{-1}}{1 + \alpha z^{-1}} \tag{7.7}$$

where

$$\mu = \frac{K_s a}{k_t};\ \alpha = \frac{-\mu}{1+\mu};\ \beta = \frac{k_t \mu}{Mn(1+\mu)} \tag{7.8}$$

By combining the feed drive dynamics and cutting dynamics, we can acquire the overall plant dynamics, G_c as;

$$G_c = G_m \times G_p = \frac{B(z)}{A(z)} = \frac{F_a(z)}{f_c(z)} = \frac{\left(g_0 + g_1 z^{-1} + g_2 z^{-2}\right)}{1 - h_1 z^{-1}} \frac{\beta z^{-1}}{1 + \alpha z^{-1}}$$
$$= \frac{z^{-1}\left(b_0 + b_1 z^{-1} + b_2 z^{-2}\right)}{1 + a_1 z^{-1} + a_2 z^{-2}} \tag{7.9}$$

where $b_0 = g_0 \times \beta$, $b_1 = g_1 \times \beta$, $b_2 = g_2 \times \beta$, $a_1 = (-h_1 + \alpha)$ and $a_2 = -h_1 \times \alpha$. The plant dynamics can be represented as the simple dynamic system, where the sampled input signal is the feed rate, f_c(t), and the output signal is the resultant cutting force at the tool tip, F_a(t);

$$A(q^{-1})F_a(t) = B(q^{-1})f_c(t) \tag{7.10}$$

where A and B are polynomials defined in backward shift operator (q^{-1}) as:

$$A(q^{-1}) = 1 + a_1 q^{-1} + a_2 q^{-n2}$$
$$B(q^{-1}) = b_0 q^{-1} + b_1 q^{-2} + b_2 q^{-3} \tag{7.11}$$

The time varying linear plant dynamics parameters in Eq. 7.11 are estimated based on the Recursive Least Square (RLS) algorithm. The detailed derivation of the RLS is depicted in Appendix F.

7.1.2 GENERALIZED PREDICTIVE CONTROL (GPC)

The Generalized Predictive Control (GPC) method [Clarke 88] uses a receding horizon prediction approach where the controller predicts the changes in the controlled variable that will occur in the future using present process knowledge and control. The prediction of the process well beyond the rise time gives the robustness which may lack in other control methods such as a pole placement approach. Figure 7.4 depicts the basic principle of the prediction control. The time scale is expressed in terms of sampling period with discrete sample j. The predictive controller output (f_c) is calculated as closely

as possible to the desired reference force, F_r, within the minimum horizon, N_1, and the maximum horizon, N_2. A quadratic cost function, which is indicative of the desired performance over the considered horizon, is solved through the optimization procedure. The quadratic cost function in the GPC is represented as:

$$J = E\left(\sum_{j=N_1}^{N_2} [F_a(t+j) - F_r(t+j)]^2 + \sum_{j=1}^{Nu} \rho[\Delta f_c(t+j-1)]^2 \right) \tag{7.12}$$

where $F_r(t+j)$ is a sequence of future set points, N_1 is the minimum prediction horizon, N_2 is the maximum prediction horizon, N_u is the control horizon, and ρ is a control weighting factor where higher ρ results in less active control. The design parameters of the GPC algorithm are N_1, N_2, N_u, and ρ to minimize the cost function. The GPC algorithm used in this study [Altintas 00] is described in Appendix G.

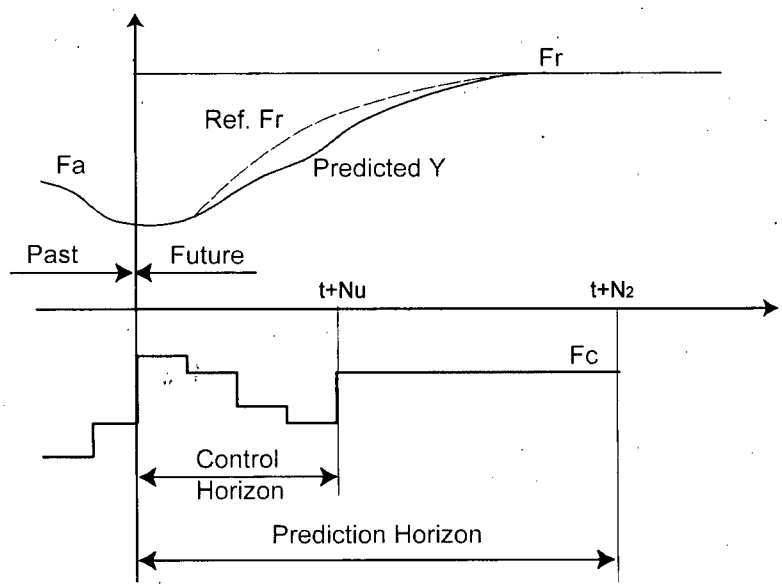

Figure 7.4 Basic Principle of Generalized Prediction Control Scheme

7.1.3 ADAPTIVE CONTROL IMPLEMENTATION WITH THE OPEN ARCHITECTURE SYSTEM

The Adaptive Control with Constraint (ACC) is performed with the vertical machining centre and the Open Architecture Real-Time Operating System (ORTS). The ORTS, developed in the Manufacturing Automation Laboratory, University of British Columbia, is a general purpose real-time operating system which runs on the DSP board (Spectrum Daytona Dual C6701 PCI) connected to a host PC (Windows NT). The cutting forces in the feed and normal directions from the Spindle Integrated Force Sensors are fed into the interface board of the ORTS. The output signal from the ORTS is connected to the CNC's feed over-ride potentiometer. The flow chart of the adaptive control process is illustrated in Figure 7.5. First, the nominal feed rate, the spindle speed, and the machine coordinates are entered through the CNC commands. In addition, the adaptive control parameters are selected through the ORTS script file. The desired resultant cutting force is set as 300 N. The sampling rate of the open architecture system is selected at 4000 Hz which is the maximum rate without deterioration of measured forces due to the limitation of the DSP board. To prevent large transient surge in the adaptive control, the desired force is incrementally increased (i.e., 4 steps). The maximum and minimum feed rates are selected as safety limits on the CNC feed drive. The script file of the adaptive control in the ORTS environment is depicted in Appendix H. The disturbance Kalman Filters in the feed and normal directions are used to compensate the unwanted structure dynamics as illustrated in Chapter 6. Furthermore, the compensated force signals are low pass filtered to remove unwanted noise.

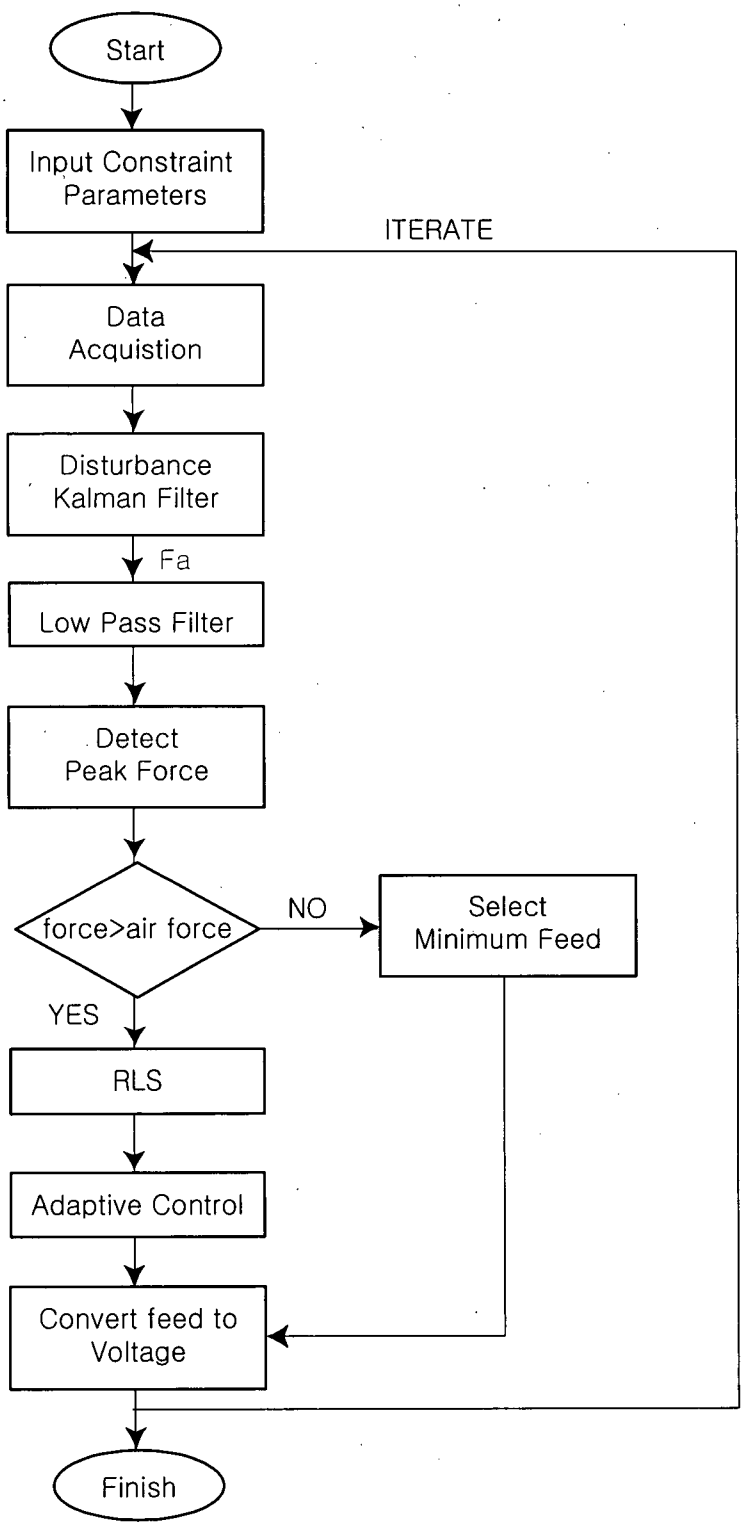

Figure 7.5 Flow Chart for the Adaptive Control with Constraint using the Forces measured from the Spindle Integrated Force Sensors

Then, the resultant force is determined by;

$$F(j) = \sqrt{F_x^{\,2}(j) + F_y^{\,2}(j)} \tag{7.13}$$

where F_x and F_y are the measured cutting forces in the feed and normal directions at the sampling interval of j. The axial forces are assumed to be negligible since the majority of forces in milling operations is in the feed and normal directions. Since the bandwidth of the CNC and the feed drive are less than 30 Hz, the adaptive control frequency is selected at 25 Hz. Therefore, the peak detection algorithm is used to determine the peak force at every 1.6 revolutions of the spindle rotation. This peak detection of the resultant force also minimizes run out effects which may cause fluctuation of control signals. The peak cutting force is then checked with the air cutting threshold to distinguish between cutting and non-cutting (i.e., air cutting) conditions. In this application, the air cutting threshold is set as 100 N. If the peak cutting force is below the air cutting threshold, the predetermined feed rate (i.e., minimum feed rate) is designed to operate the table without cutting. Conversely when the peak force is above the threshold, the plant parameters are estimated from the Recursive Least Square algorithm (see Appendix F). The initial RLS parameters are selected as 0.1, 0.001, 5 N, 1, and 0.01 for c_1, c_2, ε, λ, and initial θ, respectively. Consequently, the adaptive controller (i.e., GPC) determines the feed rate in [mm/min] by constraining the cutting force based on the reference force. The GPC parameters, N_1, N_2, N_u, and ρ are selected to be 1, 4, 1, and 0.2, respectively. The feed rate command is converted to the voltage signal which is then fed into the potentiometer of the feed rate controller in the CNC to adjust the feed rate of the XY table. The process iterates until the desired position is reached.

The three sets of tests are performed using the five fluted end mill at 1000, 3000, and 6000 rev/min to examine the adaptive controller with the forces measured from the spindle integrated sensors. The cutting profile is shown in Figure 7.6 where the depth of cut varies from 0 mm to 2 mm which are chatter free conditions using the Aluminum 7050. In order to filter high frequency noise, the cutoff frequencies of low pass filters are used as 300, 500, and 1000 Hz for 1000, 3000, and 6000 rev/min, respectively. Table 7.1 depicts the adaptive control parameters for the machining tests, ORTS, GPC, and RLS.

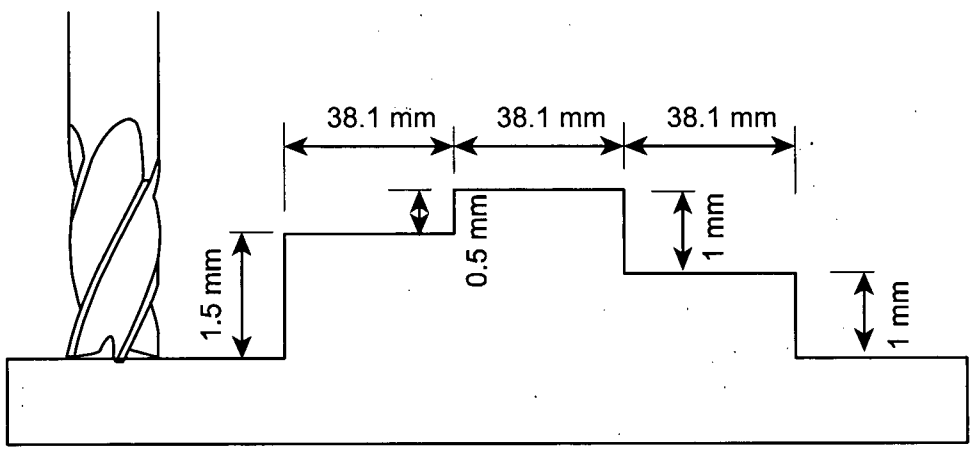

Figure 7.6 Cutting Profile

At 1000 rev/min, the resultant force and the feed rate are depicted in Figure 7.7 where the reference cutting force, F_r, is selected as 300 N. There is 25 % overshoot of the force at the first transient when the tool enters the workpiece. The resultant cutting force is generally in good agreement with the reference force. Figure 7.8 depicts the RLS parameter adaptations where the plant parameters change with respect to the different workpiece geometry.

In Figure 7.9, the same reference force is used to control the feed rate at 3000 rev/min. The maximum feed rate is chosen as 1500 mm/min. The measured resultant peak force generally follows the reference force except at the last portion of the cut where the depth of cut is 1 mm. This phenomenon is caused by the RLS algorithm which may not be fast enough to converge (see Figure 7.10).

At 6000 rev/min, the tooth passing frequency is 500 Hz coinciding with the first mode of the spindle (see Figure 7.11). Therefore, the disturbance Kalman Filter compensation of the unwanted dynamics is essential. The adaptively controlled force is closely matched with the reference force at 300 N with some deviations. These deviations mainly come from the small bandwidth (25 Hz) of the adaptive control scheme.

For all three cases, the feed rate suddenly surges when the tool partially exits the workpiece. During this instance, the cutting force is beyond the air cutting constraint (i.e., 100 N) and the controller tries to ramp up the feed rate to match the reference force. To prevent these phenomena, a more sophisticated algorithm may be needed to minimize the sudden surge of the feed rate when the tool exits the workpiece.

Table 7.1 ACC Experiment Parameters

Machine Operating parameters

Speed	1000 rev/min	3000 rev/min	6000 rev/min
No. of Flutes	5	5	5
Sampling Rate	2500 Hz	2500 Hz	2500 Hz
Adaptive Control Frequency	25 Hz	25 Hz	25 Hz
Low Pass Filter Cutoff Frequency	200 Hz	500 Hz	800 Hz

ORTS parameters

Speed	1000 rev/min	3000 rev/min	6000 rev/min
Reference Force	300 N	300 N	300 N
Maximum Feed rate	1000 mm/min	1500 mm/min	3000 mm/min
No. of steps to Reference Force	4	4	4
Minimum Feed rate	100 mm/min	500 mm/min	1000 mm/min
Air Cutting Threshold	100 N	100 N	100 N

GPC parameters

N_1	1
N_2	4
Nu	1
ρ	0.2

RLS parameters

c_1	0.1
c_2	0.001
$\bar{a}$	1
λ	1
ε	5 N
$\theta^T{}_{init} = [a_1, a_2, b_0, b_1, b_2]$	$[0.01 \quad 0.01 \quad 0.01 \quad 0.01 \quad 0.01]$

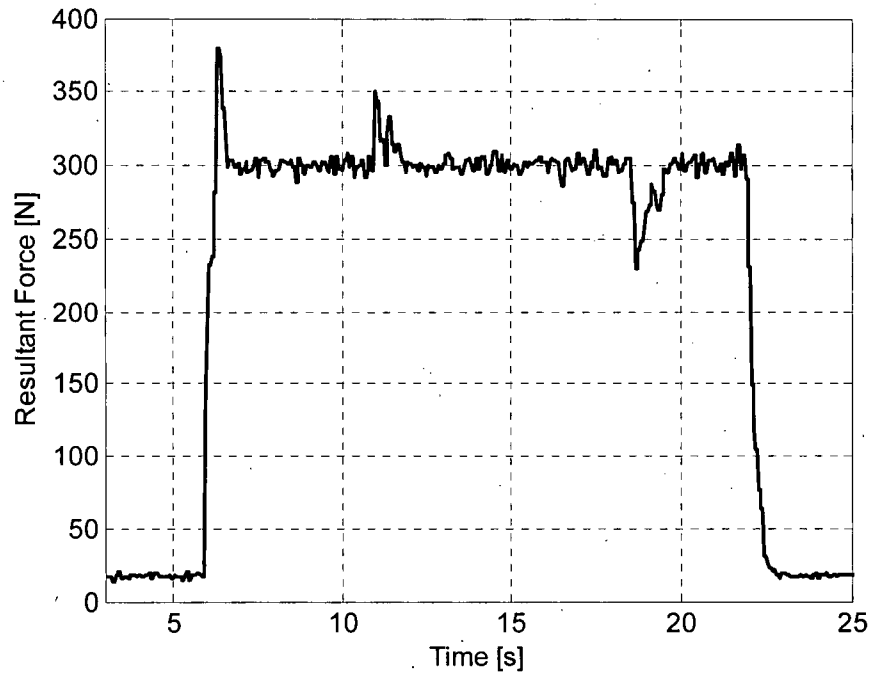

(a) Resultant force

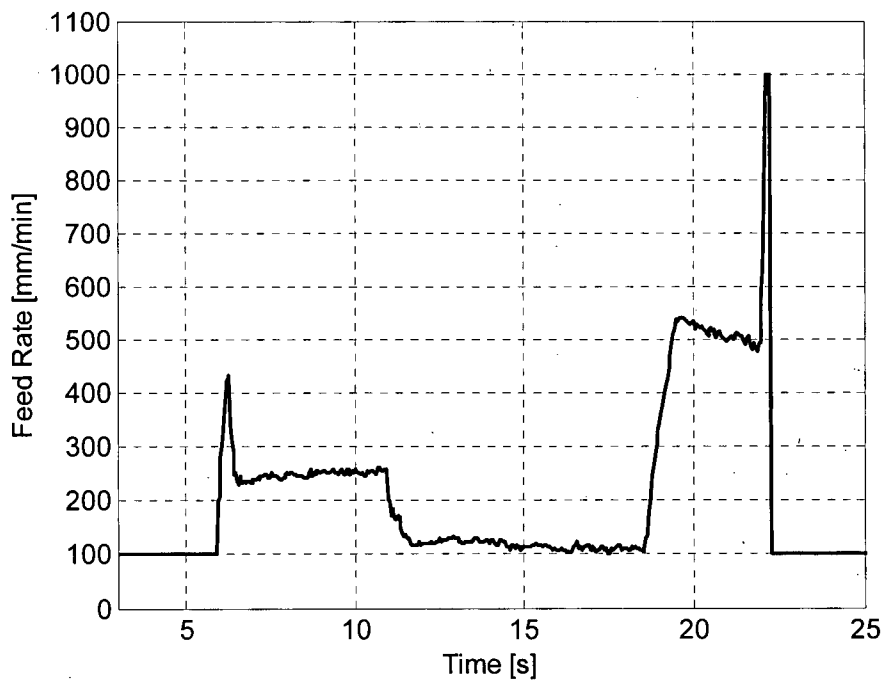

(b) Feed Rate

Figure 7.7 Adaptive Controlled Resultant Cutting Force at 1000 rpm where the reference force is at 300 N

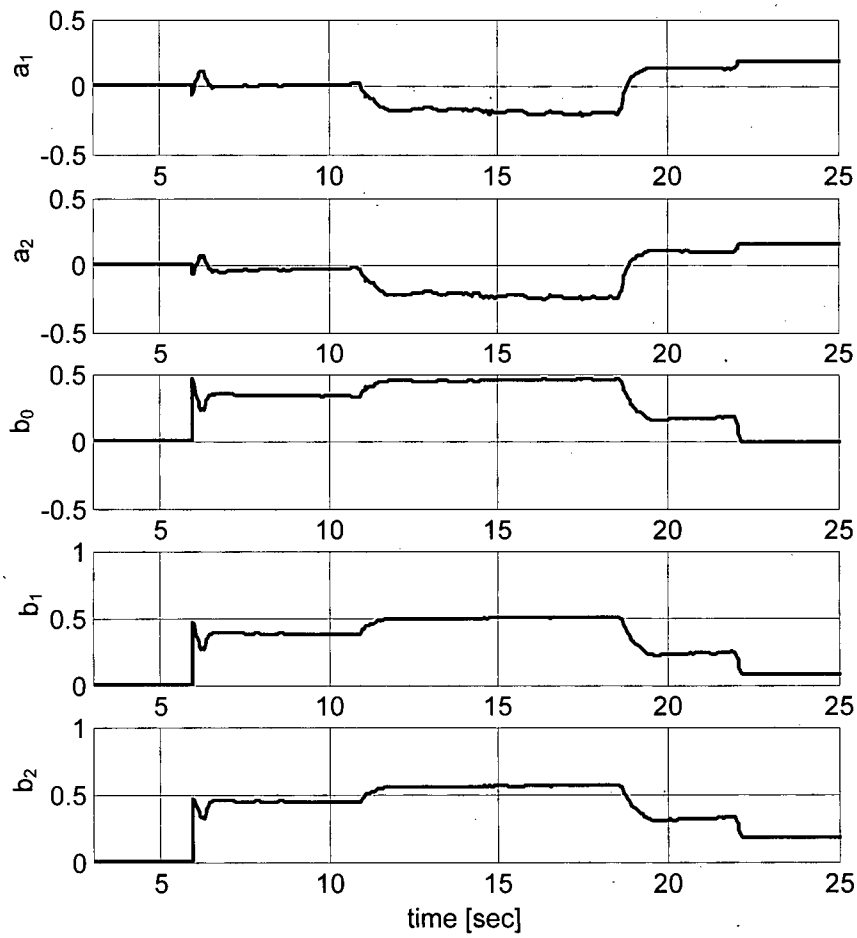

Figure 7.8 Recursive Least Square Parameter adaptations at 1000 rpm

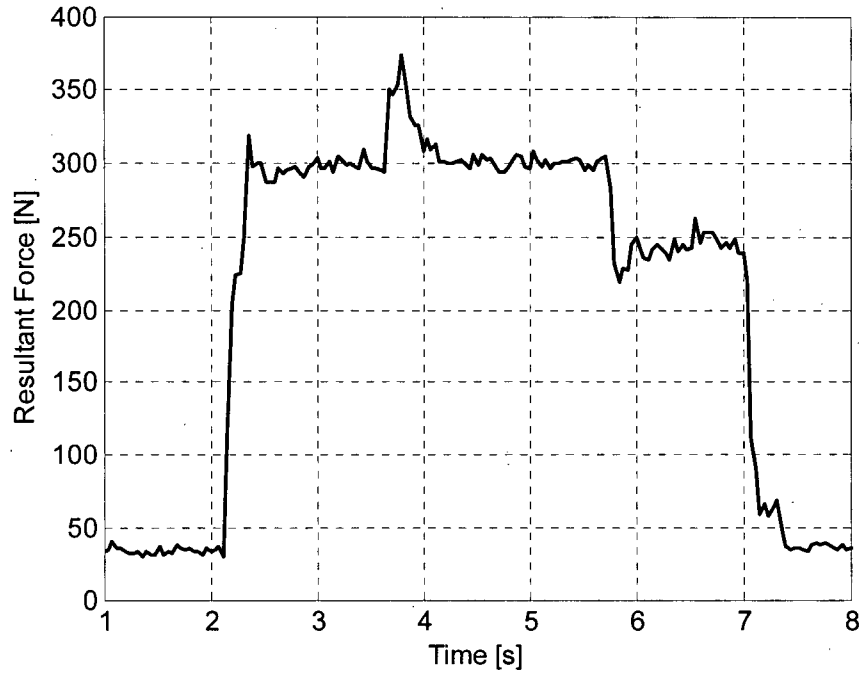

(a) Resultant Force

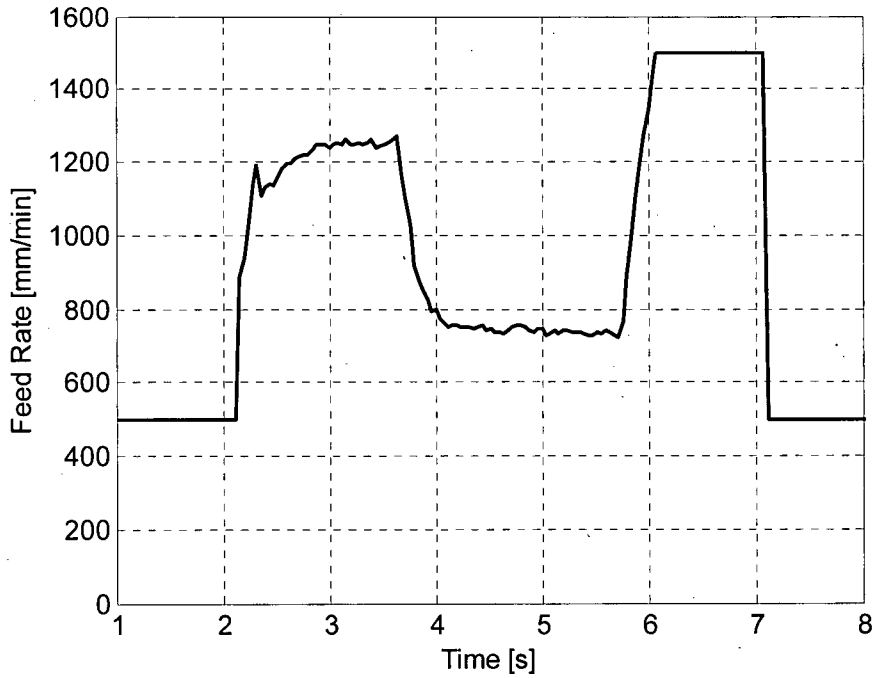

(b) Feed rate

Figure 7.9 Adaptive Controlled Resultant Cutting Force at 3000 rpm where the reference force is at 300 N

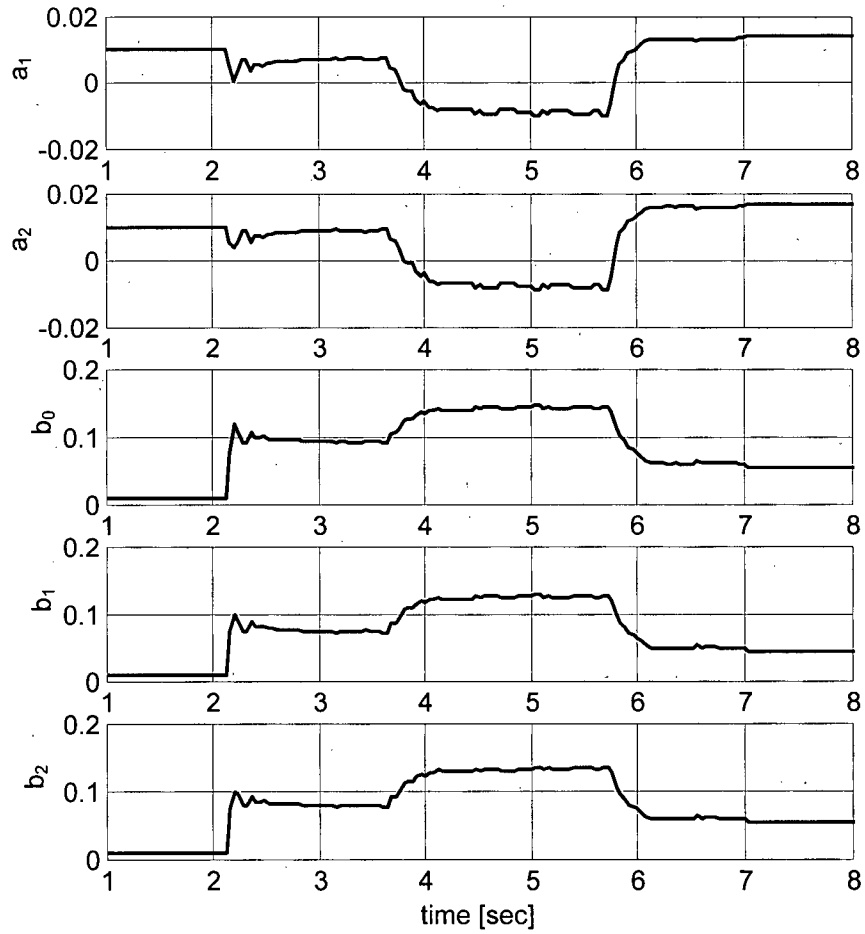

Figure 7.10 Recursive Least Square Parameter adaptations at 3000 rpm

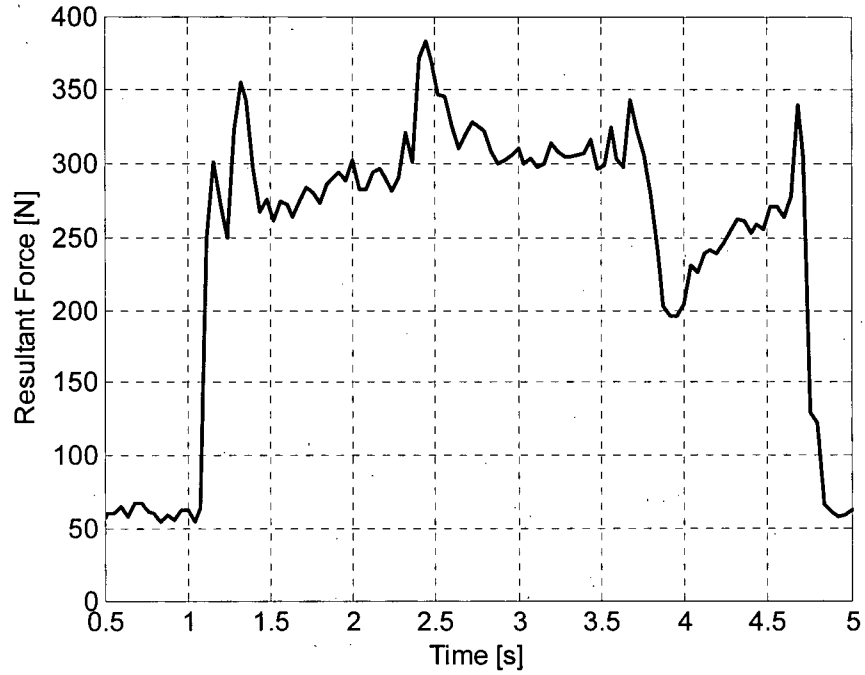

(a) Resultant Force

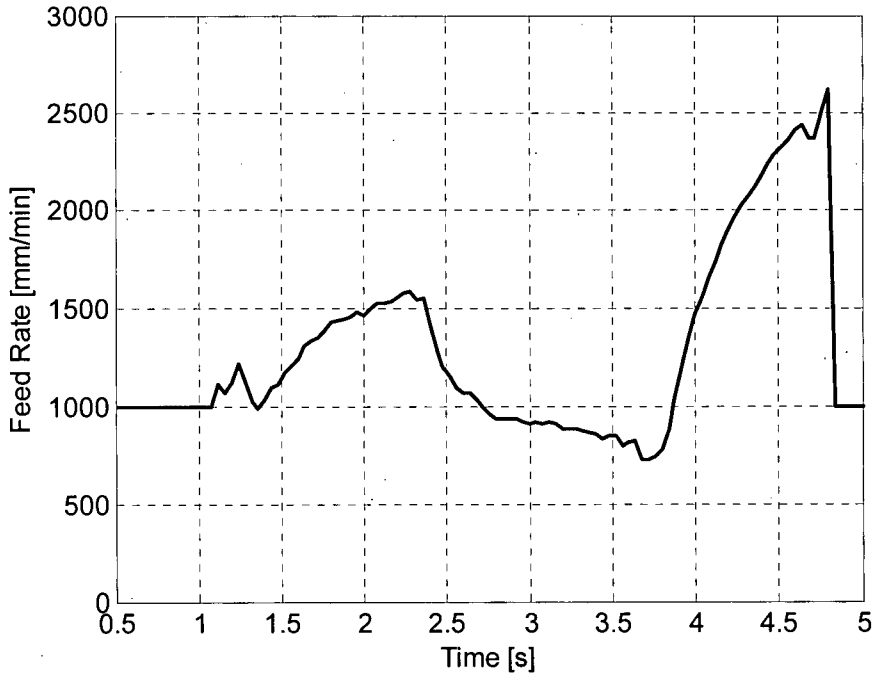

(b) Feed rate

Figure 7.11 Adaptive Controlled Resultant Cutting Force at 6000 rpm where the reference force is at 300 N

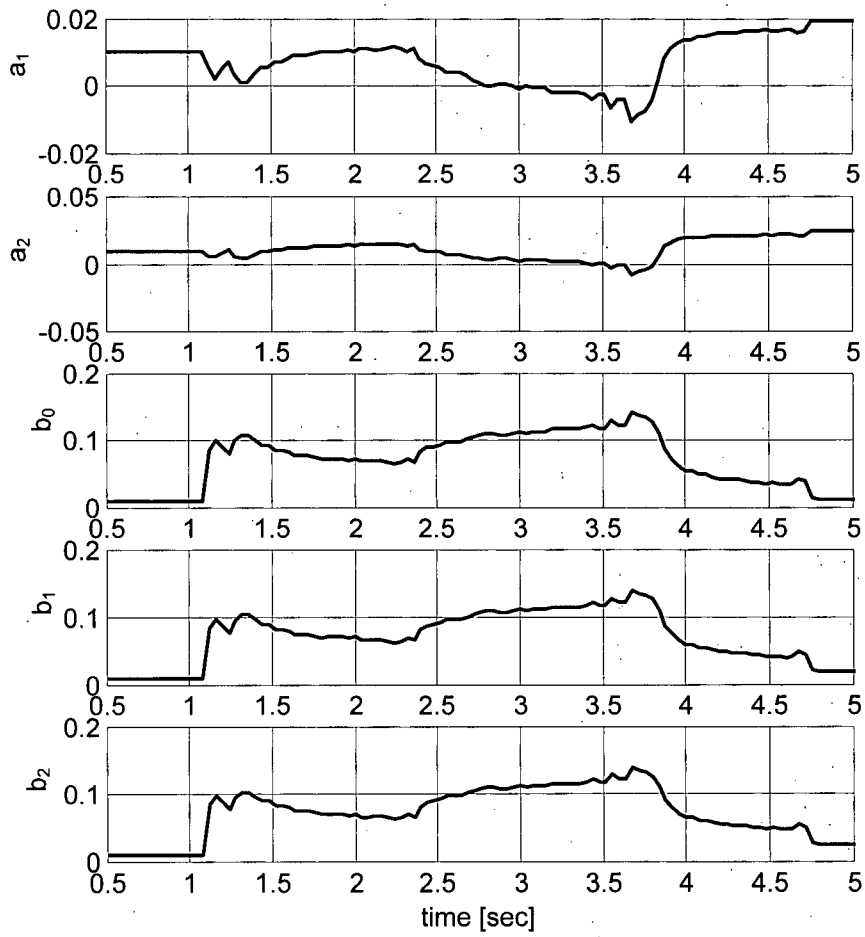

Figure 7.12 Recursive Least Square Parameter adaptations at 6000 rpm

7.2 CHATTER VIBRATION DETECTION

The detection and minimization of chatter vibrations in milling operations are paramount to achieve accuracy and productivity. The theory of chatter in metal cutting has been established since 1950's by Tobias [Tobias 65] and Tlusty [Tlusty 67, 86]. According to the literature, the primary cause of chatter for most of the machining conditions is the regeneration effect. Chatter stabilities have been commonly expressed by stability lobe diagrams, which plot the boundary that separates stable and unstable machining in the form of axial depth of cut limits versus spindle speeds for a specific radial width of cut and a workpiece-cutting tool combination. Unlike the time domain chatter stability solutions presented by others, Altintas and Budak [Altintas 95, Budak 95] solved chatter stability lobes using the analytical frequency domain prediction where the dynamic milling process was modeled by considering the Fourier series expansion of the time varying milling coefficients.

The on-line detection and suppression of chatter vibrations are proposed by Smith [Smith 89] and Tarng [Tarng 94] by matching the tooth passing frequency with the on-line detected chatter frequency. This would provide the highest stability lobe but does not provide the chatter free depth of cut. Alternatively, Weck [Weck 75] proposed to suppress the chatter by automatically reducing the axial depth of cut. Although the latter procedure reduces the productivity, it always suppresses chatter vibrations and is especially applicable for the low speed applications. In this study, the analytical stability lobes are obtained based on the work of Altintas and Budak [Altintas 00]. The cutting forces measured from the Spindle Integrated Force Sensors are used to determine the

chatter free conditions by examining the frequency domain components of the force spectrum at a particular rotational speed.

7.2.1 CHATTER DETECTION IMPLEMENTATION

In order to obtain the chatter stability lobes, information about the workpiece material, the radial width of cut, the number of flutes on the end mill, and the spindle dynamics are needed. The workpiece used in the experiment is Aluminum 7075 where the cutting constants are K_t = 752 MPa, and K_r = 0.3. The four fluted milling cutter is used to simulate the stability lobes. The experimentally obtained transfer functions in X and Y directions are depicted as:

$$\Phi(s) = \frac{x(s)}{F_a(s)} = \sum_{j=1}^{n} \frac{k_j^{-1}\omega_{n,j}^{2}}{s^2 + 2\zeta_j\omega_{n,j}s + \omega_{n,j}^{2}} \tag{7.14}$$

where j is the number of modes, x is the displacement at the tool tip and F_a is the applied force at the tool tip. The modal parameters in X direction are identified as:

ω_{n1}	493 Hz	ζ_1	0.0555	k_1	8.21e7 N/m
ω_{n2}	706 Hz	ζ_2	0.0254	k_2	8.32e7 N/m
ω_{n3}	897 Hz	ζ_3	0.0636	k_3	3.96e7 N/m

The modal parameters in Y direction are identified as:

ω_{n1}	750 Hz	ζ_1	0.0354	k_1	7.86e7 N/m
ω_{n2}	962 Hz	ζ_2	0.0408	k_2	4.80e7 N/m

Based on the modal parameters and cutting conditions, the stability lobes for slotting operations are simulated (see Figure 7.13). The critical chatter free depth of cut, a_{lim} is

3.2 mm. Below this depth, the machine would operate in the chatter free condition at any rotational speed.

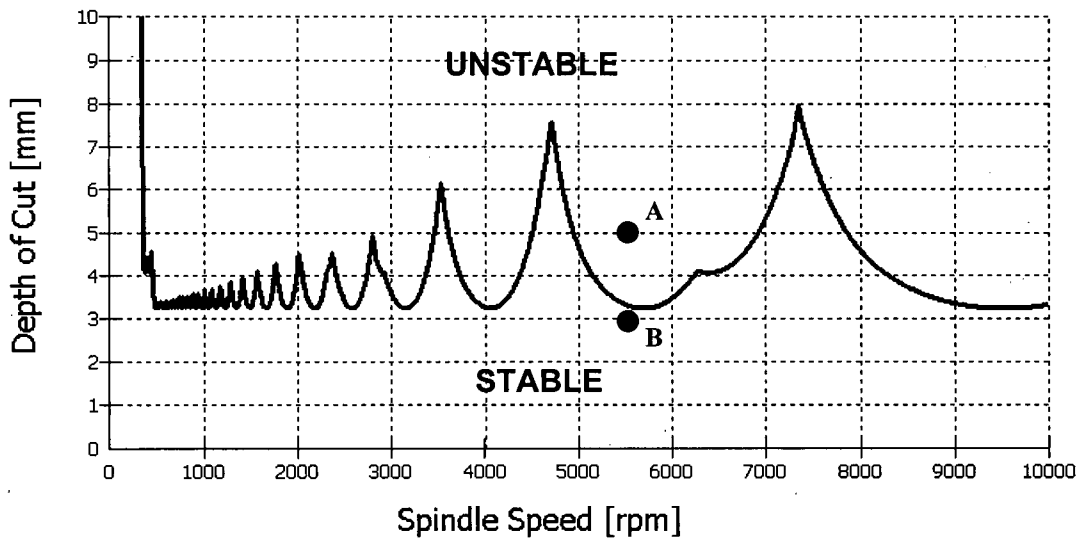

Figure 7.13 Stability Lobes for the 4 fluted end mill with Slotting – A: 5560 rpm at 5 mm depth of cut, B: 5560 rpm at 3 mm depth of cut

Two experiments are performed with the rotational spindle speed of 5560 rev/min at 5 and 3 mm depth of cut to detect chatter vibrations. The measured cutting forces from the spindle integrated sensors are compensated using the Kalman Filter. Figure 7.14 depicts the resultant cutting force with 5 mm depth of cut at 5560 rev/min. The tooth passing frequency of the cutting operation is 371 Hz. Clearly, the frequency domain components of the resultant milling force are severely amplified at the chatter frequency (i.e., 880 Hz). Figure 7.15 illustrates the frequency domain components of the resultant cutting forces during the stable cutting process where the depth of cut is 3 mm. During the chatter vibration, the cutting force magnitudes are amplified by ten times compared with the chatter free operation. The chatter threshold is selected to be 100 N which is

well above the maximum amplitude of the chatter free cutting condition. When the frequency component of the resultant cutting force violates the chatter threshold limit, the on-line monitoring algorithm activates to reduce the depth of cut to minimize chatter vibrations.

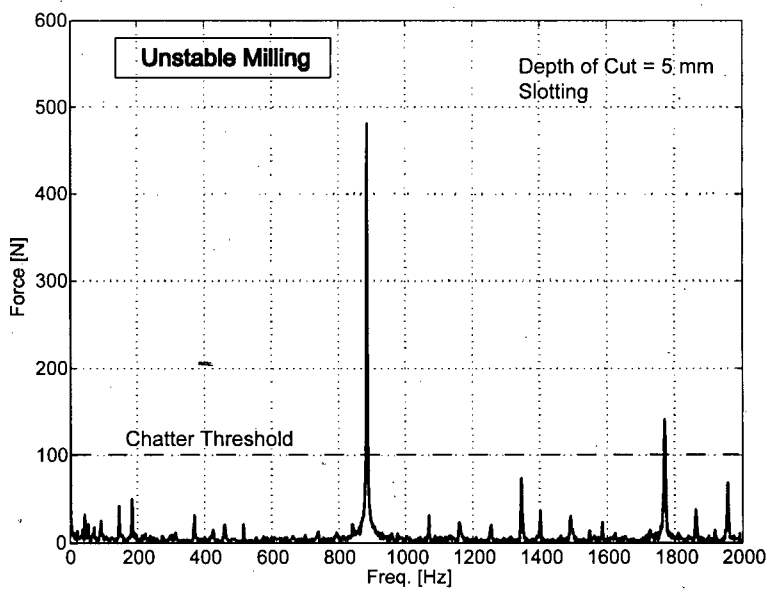

Figure 7.14 Forces during Unstable machining in Frequency domain at 5560 rpm

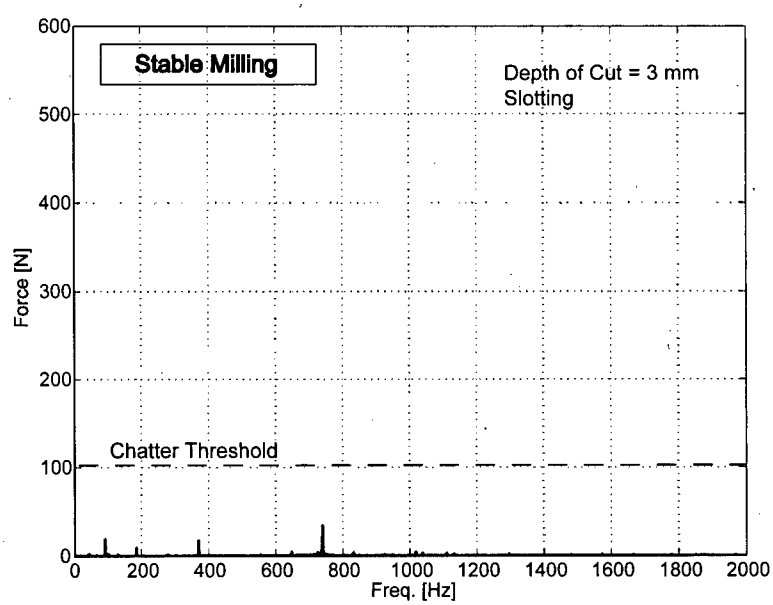

Figure 7.15 Forces during Stable machining in Frequency domain at 5560 rpm

7.3 TOOL BREAKAGE DETECTION

Accurate and quick tool breakage detection could prevent catastrophic failures in milling operations. In this study, the tool breakage detection in the NC milling processes is presented by examining the cutting forces measured from the Spindle Integrated Force Sensors. Several researchers have investigated the tool breakage detection in milling operations. Matsushima et al. [Matsushima 82] applied 28th order Auto-Regressive filters to detect tool breakage using the spindle motor current. The same approach has been used by Lan et al. [Lan 86] using the 15th order auto-regressive (AR) filters by monitoring the cutting forces in milling. The biggest problems associated with the high order filters are that they require large computation time windows and they cannot effectively distinguish tool breakages during the stable cutting transients such as holes, entry and exit of the workpiece, feed rate change, and change in depth or width of cuts. Altintas [Altintas 88] proposed the first order AR filter to detect the tool breakage with two residual indexes. The underlying principle behind this approach is that the residuals, which are the difference between the measured and predicted forces based on the AR filter, keep the large magnitudes when the tool breakage occurs.

7.3.1 TOOL BREAKAGE DETECTION IMPLEMENTATION

The tool breakage detections are experimentally performed by measuring cutting forces with a good cutter and a broken four fluted end mill where one of the flutes is damaged. To investigate the cutting transients, the workpiece is machined with the cutter in full immersion slotting with the hole in the middle as shown in Figure 7.16. The cutting forces are reconstructed using the disturbance Kalman Filter where the forces are

measured from the Spindle Integrated Force Sensors. The machining conditions such as the spindle speed, the depth of cut, and the feed rate are selected as 1000 rev/min, 1 mm, and 0.1 mm/tooth, respectively.

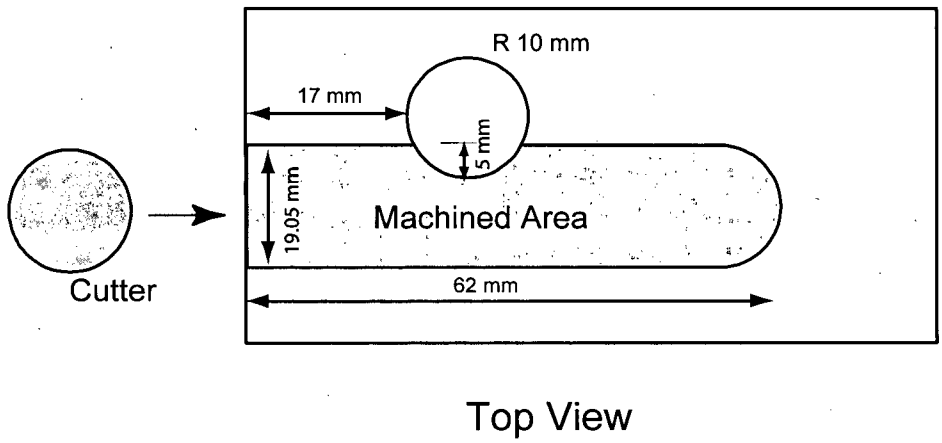

Figure 7.16 Tool Breakage Detection Test Workpiece (Aluminum 7050) with the 20 mm diameter hole

According to Altintas [Altintas 00], the first order AR process is sufficient to model the cutting process since the cutting forces are functions of tooth passing and/or spindle frequencies with their harmonics. Thus, the synchronization of cutting force measurements with the tooth passing frequency and the spindle encoder enables us to detect tool breakage. The average cutting forces per tooth period (m) is measured by:

$$F_a(m) = \frac{\sum_{i=1}^{P} \sqrt{F_x(i)^2 + F_y(i)^2}}{P} \tag{7.15}$$

where P is the number of force samples collected at tooth period, m. The average resultant cutting forces for every tooth period are shown in Figure 7.17 for both the good and the broken tool. Clearly, the average cutting force magnitudes of the broken tool are

significantly higher (80 % higher) than that of the good tool. Since the broken flute cannot remove the workpiece, the flute next to the broken one has to remove the additional workpiece material. This would cause rapid increases in cutting force magnitudes.

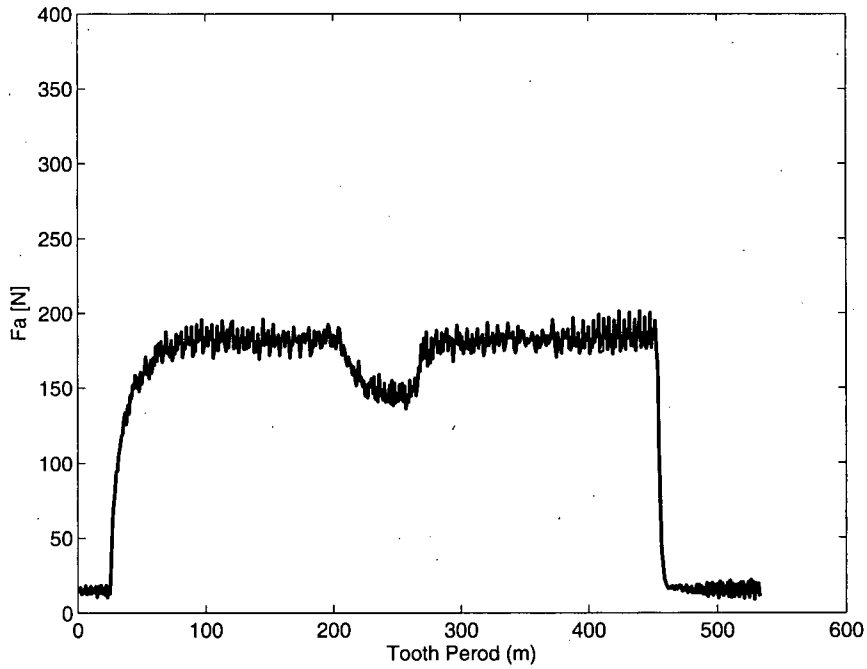

(a) Good Tool

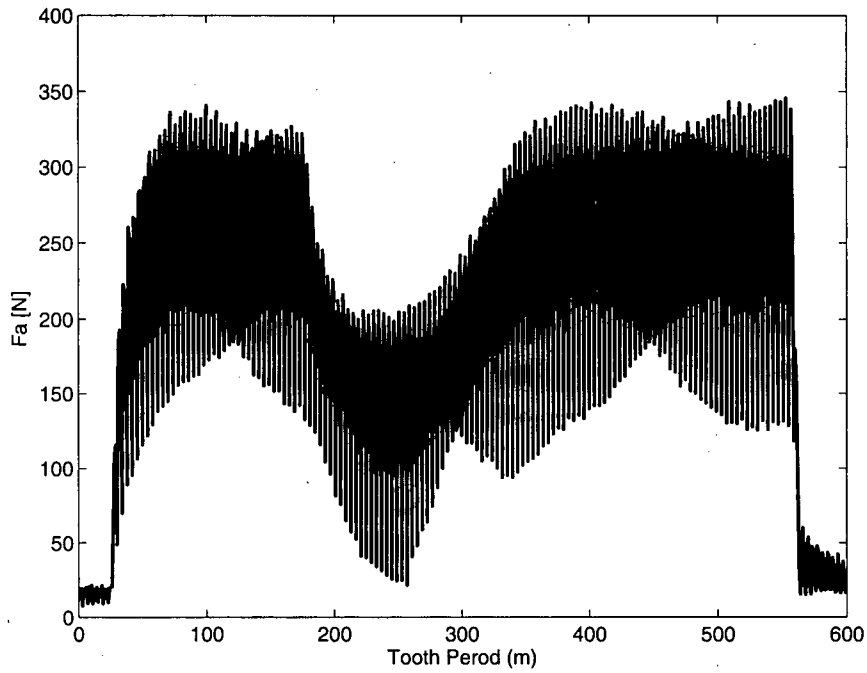

(b) Broken Tool

Figure 7.17 Average Resultant Cutting Force at every tooth period

Two indexes are used in the tool breakage detection algorithm [Altintas 00] to overcome the difficulties associated with the large run out. The first index is the residue of the cutter process obtained by recursively estimating the first order AR filter to remove slow varying dc trends caused by the changes in the workpiece geometry.

$$\varepsilon_1(m) = (1 - \hat{\phi}_1 z^{-1})\Delta F_a(m) \tag{7.16}$$

where $\hat{\phi}_1$ is estimated from measuments $\Delta F_a(m)$ using the Recursive Least Square (RLS) algorithm and the difference in average cutting forces is:

$$\Delta F_a(m) = F_a(m) - F_a(m-1) = (1 - z^{-1})F_a(m) \tag{7.17}$$

The difference in average cutting forces is used to determine the sudden changes in the cutting process. However, the first residual index may not be enough to detect the tool breakage if the run outs on the cutter teeth are not the same. Therefore, the secondary

monitoring index is derived by removing the run out of each tooth by comparing the average force at each revolution. The second residual index is shown as:

$$\varepsilon_2(m) = (1 - \hat{\phi}_2 z^{-1})\Delta^N F_a(m) \tag{7.18}$$

where

$$\Delta^N F_a(m) = F_a(m) - F_a(m - N) \tag{7.19}$$

where $\hat{\phi}_2$ is estimated from measuments and N is the number of teeth. The distinction between the two indexes is that the first index uses the difference in the resultant cutting force between one tooth interval and the second index uses the one spindle period (i.e., N = 4 flutes). The two first order AR filters are recursively estimated in parallel using the Recursive Least Square method outlined in Appendix F with the following parameters in Table 7.2.

Table 7.2 RLS parameters for the tool breakage detection

c_1	0.1
c_2	0.001
$\bar{a}$	1
λ	0.99
ε	5 N
$\theta^T{}_{init} = \hat{\phi}_1 = \hat{\phi}_2$	[0.1]
P_{init}	10

The two index residuals contain the influence of run outs on the cutter but not the cutting transients which are filtered by the algorithm. If the residue indexes are within the specified thresholds, the cutter is assumed to be in a good condition. The thresholds are selected by scaling the maximum residuals by user defined scaling factors, α_1 and α_2.

$$Limit_1 = \alpha_1 \max(\varepsilon_1),\ Limit_2 = \alpha_2 \max(\varepsilon_2) \tag{7.20}$$

The tool breakage occurs if the residues exceed both the threshold limits, Limit 1 and Limit 2.

The first residue index (ε_1) is estimated based on Eq. 7.16 which is shown in Figure 7.18 with the good (a) and broken (b) tools. In parallel, the second residue index (ε_2) is estimated based on Eq. 7.19 which is shown in Figure 7.18. Intuitively, the threshold Limits 1 and 2 are set as 100 N which corresponds to α_1 and α_2 as 2 and 1.25, respectively. The first residue index (ε_1) concisely distinguishes the differences between the good and the broken tools. Furthermore, the residue from the broken tool violates the threshold limit. Similarly, the second residue index (ε_2) shows similar behaviours between the good and the broken tools. The residues from the broken tool infringe the threshold level. Therefore, tool failure is detected since both residues exceed the thresholds at the tooth period (m = 30) for the broken tool.

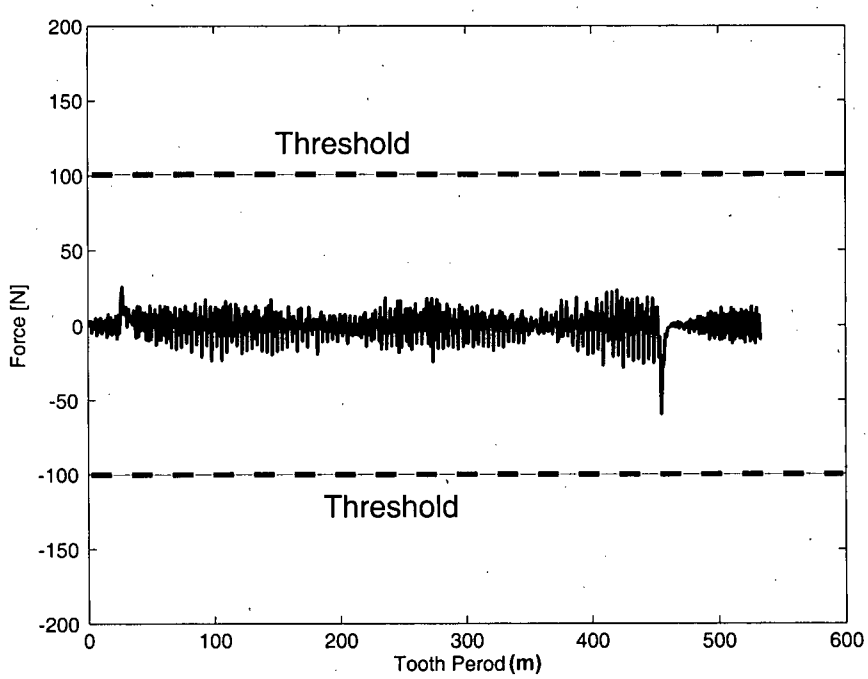

(a) Good Tool

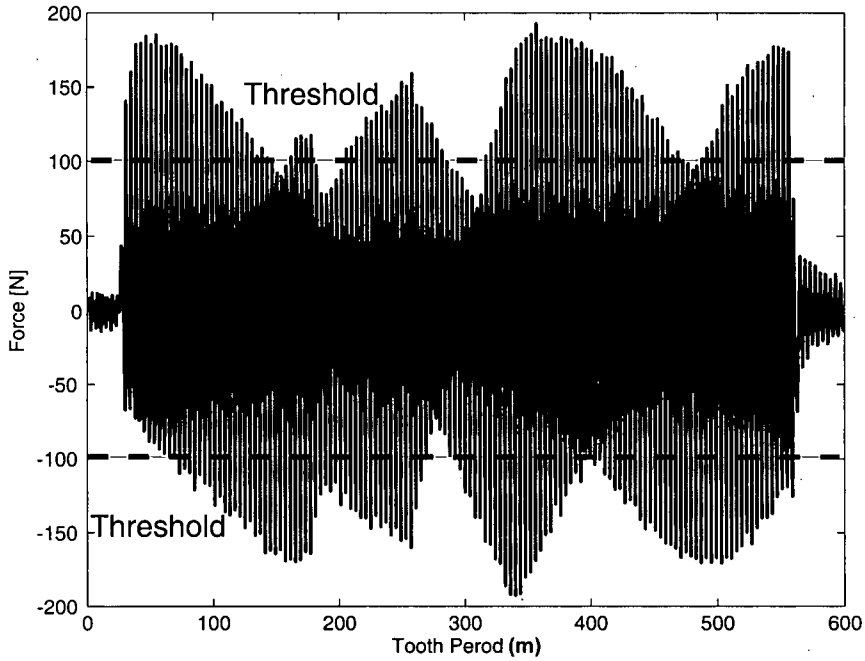

(b) Broken Tool

Figure 7.18 Tool Breakage Detection Index (ε_1)

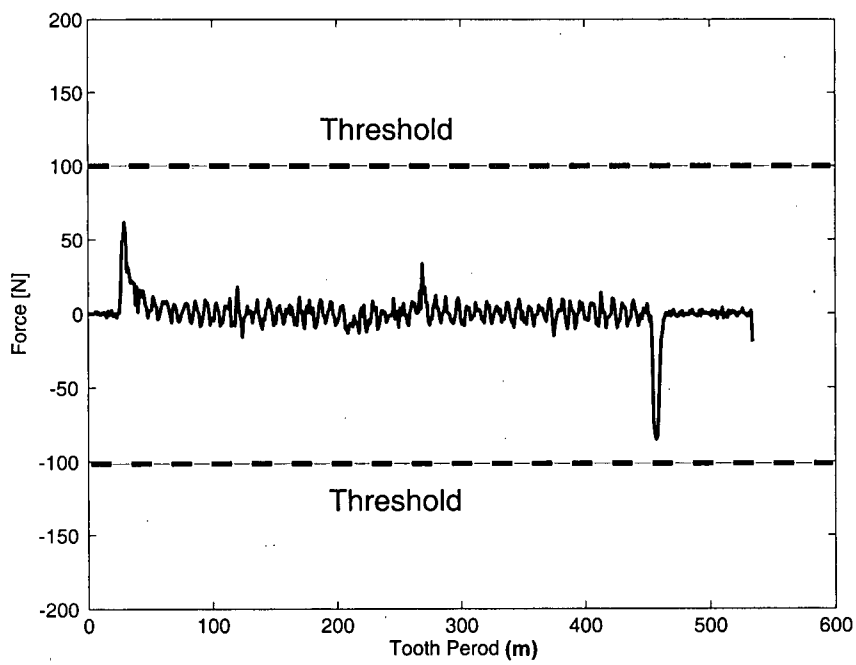

(a) Good Tool

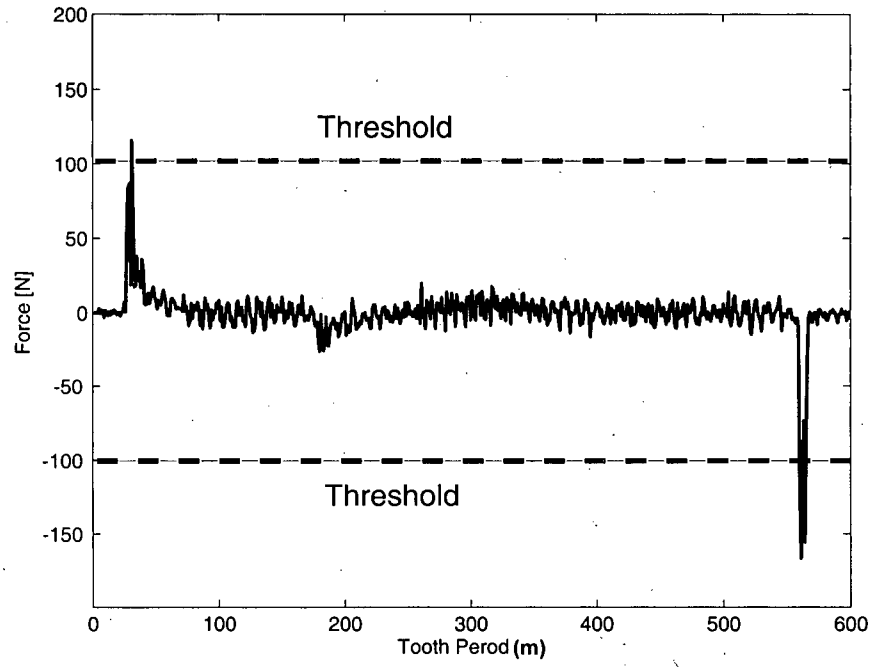

(b) Broken Tool

Figure 7.19 Tool Breakage Detection Index (ε_2)

7.4 CONCLUSION

The Spindle Integrated Force Sensors system can be used in wide areas of machine tools monitoring. The three applications are presented in this chapter including the Adaptive Control with Constraint (ACC), the chatter detection, and the tool breakage detection. The accurate cutting force measurements are critical in all these monitoring applications. The reconstruction of cutting forces using the disturbance Kalman Filter effectively provides the high bandwidth sensor requirements. The Adaptive Control with Constraint provides effective means of increasing the machining productivity through adjustments of feed rates by constraining cutting forces. The GPC scheme is used to consider the future and present events. The RLS algorithm estimates the changing dynamics during machining. The experiments are performed through the open

architecture system which enables the control of the feed rates depending on the desired reference force. The detection of chatter vibration in machining operation is important to maintain quality surface finishes. The cutting forces measured from the spindle sensors provide the sufficient information as to whether the cutting operations are stable or not. Furthermore, the tool breakage detection is performed using a good and a damaged tool. The two residual indices are examined to determine the tool breakage when the residual indices exceed the threshold limits. The experiments verify the successful monitoring strategies using the spindle integrated sensors.

CHAPTER 8.

SUMMARY AND FUTURE WORK

8.1 SUMMARY

A Spindle Integrated Force Sensor (SIFS) system is conceptually designed and implemented in this thesis. Piezo-electric force sensors are installed between the spindle housing and flange with preloads. The shear and axial forces are transmitted through the kinematic chain of tool, tool holder, spindle shaft, angular contact bearings, flange, sensors, and housing. The actual force applied on the tool tip has to pass through the kinematic chain where each component has structural dynamic flexibility. Depending on the frequency contents of the cutting forces, the structural dynamics of the spindle assembly distorts the transmitted cutting forces along the kinematic path. This thesis presents signal processing methods which improve the accuracy and frequency bandwidth of the overall spindle integrated force measuring system. The fundamental challenges and corresponding contributions are summarized as follows:

a. An existing spindle is instrumented with force and displacement sensors. While the force sensors slightly reduced the dynamic stiffness of the spindle, they are shown to be less sensitive to thermal growth and spindle run-out than the non-contact displacement sensor.

b. The structural dynamics model of the spindle is developed. It is shown that the main flexibilities which affect the force transmission from the tool to the sensors are the tool holder, spindle shaft, and housing connections. They have natural modes within 1000 Hz, which is typical for most machine tools. The identification of the structural

dynamics of the system showed that the force sensors are not affected by the thermal expansion of the spindle shaft when the heat is localized at the bearings. The influence of the speed on the dynamic model of the spindle – sensor assembly was negligible at low speeds (i.e. under 5000 rev/min), but the natural modes shift slightly at higher speeds. When the sensor is used for finish machining where the cutting forces have amplitudes under 100 N, the influence of the speed must be considered in the dynamic model.

c. The bandwidth of the proposed spindle integrated force sensors is found to be 350 Hz, which is already close to the bandwidth of table dynamometers used as research instruments in the laboratories. A disturbance Kalman Filter is developed in expanding the bandwidth of the sensors from 350 Hz to 1000 Hz. The identified transfer function between the force at the tool tip and the force measured at the sensor is converted into state space equations where the force at the tool tip is considered to be an unknown input. The Kalman Filter's gain is identified off line by using the variances of measurement and disturbance noises. The measurement noise is identified from air cutting tests and electrical noise, and the disturbance noise is tuned with trials. The Kalman Filter is designed to be time invariant, hence it is identified only once for the sensor assembly. The proposed Kalman Filter effectively removed the dynamic distortions of periodic milling forces caused by three structural modes up to 1000 Hz. The performance of the Kalman Filter is proven with cutting tests up to 12000 rev/min where the frequency content of the cutting forces reach 1000 Hz.

d. As an alternative to spindle integrated force sensors, a non-contact capacitive type displacement probe is integrated to the spindle housing. The same Kalman Filter approach is applied successfully on the displacement sensor based force measurement system. However, the transfer function between the force applied at the tool tip and displacement measurement is shown to be sensitive to thermal expansion of the spindle and spindle run-out. Hence, the displacement sensor based force measuring methods require additional filtering and identification of the transfer function as a function of time which is not as robust and practical as the Spindle Integrated Force Sensor system.

e. When the tool is replaced by an end mill having a different dimension, the transfer function of the sensor system changes which requires time consuming re-measurement and identification of the system dynamics. The thesis contributes a new method which allows mathematical assembly of a spindle with the known dynamics and analytically predicted dynamics of the tool. The receptance coupling of the spindle and arbitrary tool structures require identification of tool – holder joint dynamics which include both translational and rotational degrees of freedom. A new method, which leads to identification of rotational degrees of freedom at the tool-holder joint, is developed and experimentally proven. The proposed receptance coupling technique allows the use of force sensors with the Kalman Filter without having to identify the system at each tool change.

f. The proposed force sensing system has numerous applications in monitoring and control of machining operations during production. The sensor is demonstrated to work effectively in adaptive control of milling operations where the force is kept at

desired levels along the tool path. Adaptive Generalized Predictive Control is used in controlling the forces. The presence of chatter is detected by monitoring the power spectrum of cutting forces measured by the spindle integrated force sensor during machining tests. As an example for tool condition monitoring, the sensor signals are adaptively filtered with an adaptive autoregressive filter which allows the detection of tool breakage. The tool breakage detecting algorithm is shown to be independent of changes in the workpiece geometry during machining tests.

8.2 FUTURE WORK

Although a novel force measurement system is developed in the thesis, its practicality can be improved by further research in the following directions.

The dynamics of the spindle change with different tool holders. The proposed receptance coupling technique for end mills can be extended to include tool holder-spindle taper interfaces.

The spindle speed influences the gyroscopic and centrifugal forces, which lead to changes in the contact angle of the bearings. Since the contact angles are directly related to the bearing stiffness, the transfer function of the spindle integrated sensors become speed dependent. The mathematical modeling of the transfer function as a function of spindle speed may eliminate the tuning of the Kalman Filter for each spindle speed range. However, the system transfer function becomes nonlinear which requires the investigation of a speed dependent Kalman Filter design.

The structural dynamics of the machine tool may vary along the tool path depending on the kinematic configuration of its drives. In particular, five axis machine tools and parallel kinematic machine tools have varying transfer functions within their working space. The accuracy and practicality of the proposed sensor system can be greatly improved if the transfer function of the sensors system can be modeled as a function of machine tool kinematics and position.

In addition, the transfer function of the system may change as a function of temperature distribution in the machine tool elements. The spindle can be equipped with thermo-couples, and the transfer function of the sensor system and the Kalman Filter can be adaptively updated as a function of temperature measurements.

BIBLIOGRAPHY

Abele, E., "Online Process Monitoring vs. Offline Chatter Prediction", *Proc. IMECE'03*, 2003.

Altintas, Y. Budak, E., "Analytical Prediction of Stability Lobes in Milling", *Annals of CIRP*, 44, 357-362, 1995.

Altintas, Y., "Direct Adaptive Control of End Milling Process", *Int. J. Mach. Tools and Manufact.*, 34 (4), 461-472, 1994.

Altintas, Y., "Manufacturing Automation: Metal Cutting Mechanics, Machine Tool Vibrations, and CNC Design", *Cambridge University Press*, 2000.

Altintas, Y., "Prediction of cutting forces and tool breakage in milling from feed drive current measurements", *ASME J. of Eng. of Ind.*, 114, 386-392, 1992.

Altintas, Y., "Analytical Prediction of Three Dimensional Chatter Stability in Milling", *Proceedings of JSME*, 44, 717-723, 2001.

Altintas, Y., Munasinghe, W.K., "Modular CNC design for Intelligent Machining, Part 2: Modular Integration of Sensor based Milling Process Monitoring and Control Tasks", *J. of Manuf. Sci. and Eng.*, 118, 514-521, 1996.

Altintas, Y., Yellowley, I., "The process detection of tool failure in milling using cutting force models", *ASME J. of Eng. for Industry*, 111, 149-157, 1989.

Altintas, Y., Yellowley, I., Tlusty, J., "Detection of Tool breakage in milling", *ASME, WAM Miami,* PED-18, 41-48, 1985.

Altintas, Y., "In Process Detection of Tool Breakage using Time Series Monitoring of Cutting Forces", *Int. J. Mach. Tools and Manufact.*, 28, 157-172, 1988.

Anderson, E., Bai, Z., "LAPACK User's Guide", *Third Edition, SIAM*, Philadelphia, 1999.

Aoyama, H., Inasaki, I., Suda, I., Ohzeki, H., "Prediction of tool wear and tool failure in milling by utilizing magnetostrictive torque sensor", *Proc. of the NAMRC XXVI Conference*, Atlanta, GA, USA, 1998.

Astrom, K.J., Wittenmark, B., "Adaptive Control", *Addison Wesley*, New York, 1994.

Avitabile, P., "Twenty Years of Structural Dynamic Modification", *Proc. of 20th IMAC*, Los Angeles, USA, 356-372, 2002.

Bimschas, K., "Verbesserung der Werkstückqualität durch Simulation des Bearbeitungsprozesses", Dissertation, *Technische Hochschule Darmstadt*, 1994.

Blevins, R., "Formulas for Natural frequency and Mode shape", *Van Nostrand Reinhold* Co., NY, 1979.

Brown, R.G., "Introduction to Random Signals and Applied Kalman Filtering", *John Wiley and Sons*, New York, 1997.

Bryne, G., "Tool Condition Monitoring – the Status of Research and Industry Application", *Annals of CIRP*, 44, 541-567, 1995.

Budak, E., Altintas, Y., "Analytical Prediction of chatter stability in milling", *Proc. ASME Dynamics and Controls Division*, 57, 545-556, 1995.

Camponmanes, M., "Dynamics of Milling Flexible Structures", *Ma.Sc. Thesis*, UBC, 1998.

Chen, W.-H. and Cherng, J.-S., "Modal Synthesis Via Combined Experimental and Finite Element Techniques with Consideration of Rotational Effects", *Journal of Sound and Vibration*, 103, 1-11, 1985.

Choi, D., Kwon, W.T., Chu, C.N., "Real time monitoring of tool fracture in turning using sensor fusion", *Int. J. of A. Mfg. Tech.*, 15 (5) 305-310, 1999.

Choudhury, S.K., Rath, S., "In-process tool wear estimation in milling using cutting force model", *J. of Mat. Proc. Tech.*, 99(1-3), 113-119, 2000.

Chung, Y.L., Spiewak, S.A., "A Model of High Performance Dynamometer", *J. of Eng. for Ind.*, 116, 279-288, 1994.

Chung, Y.L., Spiewak, S.A., "Model based adaptive compensation of dynamic characteristics of in-process sensors", *Ph.D Dissertation*, University of Wisconsin, 1993.

Clark, R., Saunders, W., Gibbs, G., "Adaptive Structures: Dynamics and Control", *John Wiley*, 1998.

Clarke, D.W., "Application of Generalized Predictive Control to Industrial Processes", *IEEE, Control System Magazine*, 49-55, 1988.

Constantinides, N., Bennett, S., "An investigation of methods for on line estimation of tool wear", *Int. J. or Mach. Tool and Mfg.*, 27 (2), 225-237, 1987.

Craig, R.R., "Structural Dynamics, An introduction to Computer Methods", *John Wiley and Sons*, 1981.

CutPro, www.malinc.com

Dimarogonas, A., "Vibration for Engineers", Prentice Hall, New Jersey, 1996.

Dimla, D.E. Snr, "Tool wear monitoring using cutting force measurements", *15th NCMR, University of Bath*, 33-37, 1999.

Dimla, D.E. Snr., "Sensor Signals for tool wear monitoring in metal cutting operations – a review of methods", *Int. J. Mech. Sci., 40*, 1073-1098, 2000.

Dorfeld, D.A., "Monitoring of ultraprecision machining processes", *8th Int. Machine Tool Eng. Conf (IMEC)*, Osaka, 1998.

Dornfeld, D.A., "Neural network sensor fusion for tool conditioning monitoring", *Anals of CIRP*, 39 (1), 101-105, 1990.

Durate, M.L.M., Ewins, D.J., "Rotational Degrees of Freedom For Structural Coupling Analysis Via Finite Difference Technique with Residual Compensation", *Mechanical Systems and Signal Processing*, 14, 205-212, 2000.

Dutton, K., Thompson, S., Barraclough, B., "The Art of Control Engineering", *Addison-Wesley*, Harlow, England, 1997.

El-Wardany, T.I., Gao, D., Elbestawi, M.A., "Tool condition monitoring in drilling using vibration signature analysis", *Int. J. Mach. Tools Mfg.*, 36 (6), 687-711, 1996.

Ewins, D.J., "Modal Testing: Theory and Practice", *Research Studies Press Ltd.*, London, 1984.

Gautschi, G.H., "Cutting forces in machining and their routine measurement with multi-component piezo-electric force transducers", *Proc. 12th Int. Mach. Tool design and research*, 113-120, 1971.

Gurney, J.P., "A general analysis of two degree of freedom instability in machine tools", *Journal of Mechanical Engineering Science*, 4, 1962.

Harris, C. M., "Shock Vibration Handbook – Chap. 13 Vibration Measurement Equipment and Signal Analyzers", *McGraw Hill*, 1988.

Hazem, S., Mori, J., Tsutsumi, M., Ito, Y., "A New Modular Tooling Systems of Curvic Coupling Type", *Proc. 26th Machine Tool Design and Research Conf.*, 261-267, 1987.

Schlitt, H., "Systemtheorie fuer stochastische Prozesse – Statistische Grundlagen, Systemdynamik, Kalman-Filter", Springer Verlag, Germany, 1992.

Hou, M., Muller, P.C., "Design of Observers for Linear Systems with Unknown Inputs", *IEEE Trans. Auto. Control.*, 37 (6), 871-875, 1992.

Jacobs, T.P., "Characterization of the Machine tool spindle to tool holder connection", *Master's Thesis*, University of Charlotte, 1999.

Jeppsson, J., "Aerospace manufacturing: Making HSM work", *Manufact. Eng.*, 124 (3), 72-82, 2000.

Jetmundensen, B., Bielawa, R.L., and Flannelly, G., "Generalized Frequency Domain Substructures Synthesis", *Journal of American Helicopter Society*, 55-64, 1988.

Jin, W.L., Venuvinod, P.K., Wang, X., "An optical fibre sensor based cutting force measuring device", *Int. J. Mach. Tools Manufact.*, 35(6), 877-883, 1995.

Jorgensen, B.R., Shin, Y.C., "Dynamics of machine tool spindle/bearing systems under thermal growth", *DSC Vol 58, ASME*, 333-340, 1996.

Jorgensen, B.R., Shin, Y.C., "Robust modeling of high speed spindle dynamics", *MED Vol 2-1, MFg Science and Engineering*, 643-656, 1995.

Jun, M.B., Ozdoganlar, O.B., DeVor, R.E., "Evaluation of a spindle-based force sensor for monitoring and fault diagnosis of machining operations", *Int. J. Mech. Sci*, 42(6), 741-751, 2002.

Kang, M.C., Kim, J.S., Kim, J.H., "A Monitoring technique using a multi-sensor in high speed machining", *J. Materials Process. Tech.*, 113, 331-336, 2001.

Kim, T.Y., Kim, J., "Adaptive Cutting Force Control for a Machining Center by Using Indirect Cutting Force Measurements", *International Journal of Machine Tools and Manufacturing*, 36, 925-937, 1996.

Kistler, Rotating Cutting Force Dynamometer 9123C/9124B Manual, 1999.

Kline, W.A., De Vor, R.E., Lindberg, J.R., "The prediction of cutting force in end milling with Application to cornering cuts", *Int. J. Mech. Sci.*, 22 (1), 7-22, 1982.

Knight, W.A., Sadek, M.M., "The correction for dynamic errors in machine tool dynamometers", *Annals of the CIRP*, 19, 237-245, 1971.

Koenig, W., Kluft, W., Froehlich, R., "Automatische Werk-zeugbrucherkennung bei der Drehbearbeitung", *Industrie-Anzeiger*, 100 (28), pp. 62-63, 1978.

Kops, L., Vo, D.T., "Determination of the Equivalent Diameter of an End Mill based on its Compliance", *Annals of CIRP*, 39, 93-96, 1990.

Koren, Y., "Computer control of manufacturing systems", *McGraw Hill*, New York, 1983.

Koren, Y., Ulsoy, A.G., Danai, K., "Tool wear and breakage detection using a process model", *Ann. CIRP*, 35(1), 283-288, 1986.

Lan, M.S., Naerheim, Y., "In process detection of tool breakage in milling", *ASME J. of Eng. for Industry*, 108, 197-197.

Landers, R.G., Ulsoy, G., "Model-Based Machining Force Control", *Journal of Dynamic Systems, Measurement, and Control*, 122, 2000.

Lauderbaugh, L.K., "Process dynamics models for the control of end milling", *American Control Conference*, 4, 2563 -2567, 2000.

Lauderbaugh, L.K., Ulsoy, A.G., "Dynamic Modeling for Control of Milling Process", *ASME PED*, 18, 149-158, 1985.

Lister, P.M., "On line measurement of tool wear", *Ph.D. Thesis*, UMIST, Manchester, UK, 1993.

Liu, W., "Structural Dynamic Analysis and Testing of Coupled Structures", *PhD Thesis*, Imperial College of London, 2000.

Liu, Y., Cheng, T., Zuo, L, "Adaptive Control Constraint of Machining Processes", *Int. J. of Adv. Manufacturing Tech.*, 17 (10), 720-726, 2001.

Ljung, L., Glad, T., "Modeling of Dynamic Systems", *Prentice Hall*, 1994.

Ljung, L., Soderstrom, T., "Theory and Practice of Recursive Identification", *MIT Press*, 1987.

Matsubara, A., Kakino, Y., Ogawa, T., Nakagawa, H., Sato, T., "Monitoring of Cutting Forces in End-milling for Intelligent Machine Tools", *Proc. of the 5th Int'l Conf. on Progress of Machining Technology (ICPMT)*, 615, 2000.

Matsushima, K, Bertok, P., Sata, T., "In process detection of tool breakage by monitoring the spindle current of a machine tool", *ASME J. of Meas. and Control*, 145-154, 1982.

Mendel, J.M., "Lessons in Estimation Theory for Signal Processing, Communications, and Control", *Prentice-Hall*, NJ, 1995.

Merritt, H.E., "Theory of self excited machine tool chatter", *ASME Journal of Engineering for Industry*, 447-454, 1965.

Moriwaki, T., "Detection for Tool fracture by AE measurement", *Annals of the CIRP*, 29, 35-40, 1980.

NSK Bearing Manual, Toronto.

O'Reilly, J., "Observers for linear systems", *Academic Press*, 1983, London.

Oraby, S.E., Hayhurst, D.R., "Tool wear and force relationship in metal cutting", *Int. J. Mech. Sci*, 33(1), 125-138, 1991.

[a]Park, S.S., Altintas, Y., "Dynamic Compensation of Spindle Integrated Force Sensors with Kalman Filter", *ASME Transactions Journal of Dynamics Systems, Measurement, and Control*, Accepted, Sept. 2003.

[b]Park, S.S., Altintas, Y., M. Movahhedy "Receptance Coupling for End Mill", *Int. J. of Mach. Tool and Mfg.*, 43, 889-896, 2003.

Park, S.S., Altintas, Y., "Dynamic Compensation of Cutting Forces Measured From the Spindle Integrated Force Sensor System", *ASME IMECE2002 DSC Conference*, New Orleans, Nov. 2002.

[c]Park, S.S., Altintas, Y., "Identification of Spindle Integrated Force Sensor's Transfer Function for Modular End Mills", *ASME Transactions, Journal of Manufacturing Science and Engineering*, submitted, Jan. 2003.

Patel, R.V., "Minimal order inverses for linear systems with zero and arbitrary initial states", *Int. J. Control*, 30 (2), pp. 245-258, 1979.

Potter, J.E., "Matrix Quadratic Solutions", *SIAM J. Appl. Math*, 14, 496-501, 1996.

Pricket, P.W., Johns, C., "An overview of approaches to end milling tool monitoring", *Int. J. Mech. Sci,* 39, 105-122, 1999.

Pritschow, G., Bretschneider, J., Fritz, S., "Reconstruction of process forces within digital servodrive systems", *Production Engineering*, 4 (1), 73-78, 1999.

Ren, Y., Beards, C.F., "An iterative FRF Joint Identification Technique", *Proceedings of 11th IMAC conference*, Florida, USA, 1133-1139, 1993.

Ren, Y., Beards, C.F., "Identification of Joint Properties of Structure Using FRF Data", *Journal of Sound and Vibration*, 186, 567-58, 1995.

Ren, Y., Beards, C.F., "A generalized receptance coupling technique", *11th IMAC 1993*, Kissimmee, Florida, 1993.

Reuber, M., "Prozessueberwachung beim Schlichfraesen von Freiformflaechen", *Dissertation*, WZL, RWTH Aachen, Germany, Berichte aus der Produktionstechnik, Vol. 3, 2001.

Rivin, E.I., "Stiffness and Damping in Mechanical Design – Chapter 4: Contact (Joint) Stiffness and Damping", *Marcel Dekker Inc.*, NY., 1999.

Sampath, A., Vajpayee, S., "Tool health monitoring using acoustic emission", *Int. J. Prod. Res.,* 25 (5) 703-719, 1987.

Santro, I, Peric, N., Petrovic, I., "Comparison of the self-tuning generalized predictive controller and pole placement controller", *Electrotechnical Conference. MELECON 98.*, 9th Mediterranean , 1, 18-20, 1998.

Scheer, C., Hoffmann, P., "Spindle-integrated force sensors for monitoring drilling and milling processes", *9th Int. Conf. for Sensors*, May 18-20, Nunberg, Germany, 1999.

Schmitz, T.L., "Predicting High Speed Machining Dynamics by Substructure Analysis", *Annals of CIRP*, 49, 303-308, 2000.

Schmitz, T.L. Davies, M., Kennedy, M.D., "Tool Point Frequency Response Prediction for High-Speed Machining by RCSA", *Journal of Mfg. Science and Eng.*, 123, 700-707, 2002.

Schmitz, T.L., Donaldson, R., "Predicting High Speed Machining Dynamics by Substructure Analysis", *Ann. CIRP*, 49, 303-308, 2000.

Shirase, K., Altintas, Y., "Cutting force and dimensional surface error generation in peripheral milling with variable pitch helical end mills", *Int. J. of Machine Tools and Manufacture*, 36 (5), 567-584, 1996.

Skogestad, Sigurd, Postlethwaite, "Multivariable Feedback Control", *John Wiley and Sons*, West Sussex, England, 1996.

Smith, D.A., Smith, S., Tlusty, J., "High performance milling torque sensor", *J. Manuf. Sci. ASME*, 120 (3), pp. 504-51, 1998.

Smith, S., Tlusty, J., "Efficient simulation program for Chatter in Milling", *Annals of CIRP*, 42, 463-466, 1993.

Smith, S., Delio, T., "Sensor Based Control for Chatter free milling by Spindle Speed Selection", *ASME 1989 WAM*, 18, 107-114, 1989.

Spence, A.D., Altintas, Y, "CAD assisted adaptive control for milling", *ASME J. of Dyn. Syst., Meas. And Control*, 116, 61-69, 1991.

Spiewak, S.A., Di Corpo, J., "Adaptive Compensation of Dynamic Characteristics for In-Process Sensors", *ASME J. Eng., Industry*, 113, 198-206, 1991.

Stein, J.L., Park, Y., "Measurement Signal Selection and a Simultaneous State and Input Observer", *J. of Dyn. Sys., Meas., and Con.*, 110, 151-159, 1988.

Stein, J.L., Tu, J.F., "A state space model for monitoring thermally induced preload in antifriction spindle bearings of high speed machine tools", *ASME Journal of engineering for Industry,* 116, 372-386, 1994.

Suh, S.H., Cho, J.H., "Incorporation of Tool Deflection in Tool Path Computation", *J. of Manufacturing Systems*, 15 (3), 190-199, 1996.

Tanaka, Y., Naoya, I., "Accelerometer applications to tool dynamometers with improved dynamic response", *Annals of the CIRP*, 18, 353-359, 1970.

Tarn, J.H., Tomizuka, M., "On-line monitoring of tool and cutting conditions in milling", *ASME J. of Eng. For Industry*, 111, 206-212, 1989.

Tarng, Y.S., Hseih, Y.W., Hwang, S.T., "Sensing tool breakage in face milling with neural network", *Int. J. of Mach. Tools and Mfg.*, 34 (5) 625-631, 1994.

Tarng, Y.S., Lee, B.Y., "A sensor for the detection of tool breakage in NC milling", *J. of Mat. Proc. Technology*, 36, 259-272, 1993.

Tarng, Y.S., Li, T.C., "On line Monitoring and Suppression of Self-Excited Vibration in End Milling", *Mechanical Systems and Signal Processing*, 8 (5), 597-606, 1994.

Tlusty, J., Koenigsberger, F., "Machine Tool Structures", *Pergamon Press*, 1967.

Tlusty, J., "Dynamics of High Speed Milling", *ASME Journal of engineering for Industry*, 108, 59-67, 1986.

Tlusty, J., Andrews, G.C., "A Critical Review of Sensors for Unmanned Machining", *Annals of CIRP*, 32 (2), 563-572, 1983.

Tlusty, J., Elbestawi, M.A., "Analysis of Transients in an adaptive control servomechanism for Milling with constant Force", *ASME J. of Eng. for Industry*, 99 (3), 766-772, 1977.

Tlusty, J., Ismail, F., "Basic Nonlinearity in Machining chatter", *Annals of the CIRP*, 30, 21-25, 1981.

Tlusty, J., Jang, D.Y., Tarng, Y.S., "Measurements of milling force over a wide frequency range", *15th NAMRC*, 273-280, 1987.

Tlusty, J., Smith, S., "Forced vibration chatter, accuracy in high speed milling", *13th NAMRC*, 221-229, 1985.

Tobias, S.A., Fishwick, W., "A theory of regenerative chatter", *The engineer*, London, 1958.

Tobias, S.A., "Machine Tool Vibrations", *Blackie and Sons,* 1965.

Tonshoff, H.K., "Developments and Trends in Monitoring and Control of Machining Processes", *Annals of CIRP*, 37 (2), 611-622, 1988.

Tounsi, N., Otho, A., "Dynamic cutting force measuring", *Int. J. of Mach. Tool and Mfg*, 40, 1157-1170, 2000.

Tsai, J.S., Chou, Y.F., "The identification of dynamic characteristics of a single bolt joint", *J. of Sound and Vibration*, 124 (3), 487-502, 1988.

Tu, J., "Strain field analysis and sensor design for monitoring machine tool spindle bearing force", *Int. J. Mach. Tools Manufact.*, 36, 203-216, 1996.

Ulsoy, A.G., Koren, Y., "Applications of adaptive control to machine tool process control", *IEEE Control Systems Magazine*, 9 (4), June 1989.

Ulsoy, G., Koren, Y., "Control of Machining Processes", *J. of Dynamic Systems, Measurement, and Control*, 115, 301-308, 1993.

Wang, J.H., Horng, S.B., "Investigation of the Tool Holder System with a Taper Angle 7:24", *Int. J. of Machine Tools and Manufacture*, 34, 1163-1176, 1994.

Wang, J.H., Liou, C.M., "Identification of Parameters of Structural Joints by Use of Noise-Contaminated FRFs", *Journal of Sound and Vibration*, 142, 261-27, 1990.

Warde, F.P., Lacey, S.J., Poon, S.Y., "Dynamic and static characteristics of a wide speed range machine tool spindle", *Precision engineering*, 5 (4), 175-183, 1983.

Weck, M., Verhaag, E., Gather, M., "Adaptive Control for Face-Milling Operations with Strategies for Avoiding Chatter-Vibrations and for Automatic Cut Distribution", *Annals of the CIRP*, 24, 1975.

Weihrich, G.,"Drehzahlregelung von Gleichstromantrieben unter Verwendung eines Zustands- und Störgrößenbeobachters", *Regelungstechnik*, 26, 349-380, 1978.

Yan, D., El-ardany, T.I., Elbestawi, M.A., "A multi-sensor strategy for tool failure detection in milling", *Int. J. Mach. Tool. And Mfg.*, 35 (3) 383-398, 1995.

Yang, M.Y., Choi, J.G., "A Tool Deflection Compensation System for End Milling Accuracy Improvement", *ASME J. of Manufact. Sci. Eng.*, 120, 222-229, 1998.

Yuan, J.X., Wu, X.M., "Identification of Joint Structural Parameters of Machine Tool by DDS and FEM", *Journal of Engineering for Industry*, 107, 64-69, 1985.

Yushimura, M., "Computer Aided Design Improvement of Machine Tool Structure Incorporating Joint Dynamics Data", *Annals of CIRP*, 28, 241-246, 1979.

APPENDIX A.

UNKNOWN INPUT ANALYSIS (UIA) TO ESTIMATE THE APPLIED CUTTING FORCE

The objective of the dynamic compensation is to gain the accurate estimation of the applied cutting force at the tool tip. We treat the unknown input as the desired applied cutting force as shown in Figure 4.8. The unknown input and the state estimation is performed based on the reduced order transformations. In his recent paper, Hou [Hou 92] presented a design for reduced order observers for continuous time linear systems with unknown inputs. He proposed to decompose the state equation of the system into two subsystems where the first subsystem is independent on the unknown input and the second subsystem is dependent on the unknown input. To overcome the difficulties associated with estimating the derivatives in the continuous time domain, the discrete Unknown Input Analysis (UIA) is used in this study. The model used in the UIA is obtained from the physical model, which is described in Section 4.22, to formulate the state space equation (Eq. 4.28). Once the continuous time state space equation is formulated, the equation is transformed to the discrete time by using Tustin approximation;

$$s \approx \frac{2}{T_s}\frac{z-1}{z+1} \tag{A1}$$

where the discrete sampling time, T_s, is 0.1 milliseconds in this application.

The equivalent discrete time LTI state space system can be depicted as;

$$\begin{aligned} x(k+1) &= A_d x(k) + B_d u(k) \\ z(k) &= C_d x(k) \end{aligned} \tag{A2}$$

where x is the state vector, A_d is the system matrix, B_d is the input vector, C_d is the output vector obtained from the physical model, $u = F_a$ is the input or the actual force applied to the tool, and $z = \{F_m\}^T$ is the measured cutting force from the spindle force sensor and vibrations. When we examine the state space equation, the size of z is $m \times 1$, the size of x is $n \times 1$, and the size of u is $q \times 1$. For our case, m, n, and q are 1, 6, and 1, respectively. The analysis tries to reduce the order in the input vector by performing the transformation in the input vector, B_d. For the reduced order design, Eq. A2 can be expressed as:

$$\begin{aligned} z &= \begin{bmatrix} C_{d1} & C_{d2} \end{bmatrix} \begin{bmatrix} x_1 \\ x_2 \end{bmatrix}, \quad \begin{aligned} x_1 &\in R^{n-q} \\ x_2 &\in R^{q} \end{aligned} \\ &= C_{d1} x_1 + C_{d2} x_2 \end{aligned} \tag{A3}$$

For the reduced order design, we perform an equivalence transformation (i.e., $x = T\bar{x}$). The transformation matrix, T, can be assumed to be

$$\begin{aligned} T &= \begin{bmatrix} N & B_d \end{bmatrix}; \quad T^{-1} = \begin{bmatrix} J \\ M \end{bmatrix} \\ T^{-1}T = I &= \begin{bmatrix} JN & JB_d \\ KN & MB_d \end{bmatrix} = \begin{bmatrix} I_{n-q} & 0 \\ 0 & I_q \end{bmatrix} \end{aligned} \tag{A4}$$

where N is an arbitrary $n \times (n\text{-}q)$ matrix. The transformation matrix, T, needs to be invertible and for simplicity, we have chosen the transformation matrix as:

$$T = \begin{bmatrix} I_{n-q} & B_d \\ [0] & \end{bmatrix} \tag{A5}$$

The transformed state space equation based on Eq. A2 is shown as;

$$\begin{aligned} \bar{x}(k+1) &= \bar{A}_d \bar{x}(k) + \bar{B}_d u(k) \\ y(k) &= \bar{C}_d \bar{x}(k) \end{aligned} \tag{A6}$$

where

$$\begin{aligned} &\bar{A}_d = T^{-1} A_d T,\ \bar{B}_d = T^{-1} B_d = \begin{bmatrix} 0 & MB_d \end{bmatrix}^T = \begin{bmatrix} 0 & I_q \end{bmatrix}^T, \\ &\bar{C}_d = C_d T = \begin{bmatrix} C_d N & C_d B_d \end{bmatrix} \end{aligned} \tag{A7}$$

Then, Eq. A6 can be expanded as:

$$\begin{bmatrix} \bar{x}_1(k+1) \\ \bar{x}_2(k+1) \end{bmatrix} = \begin{bmatrix} \bar{A}_{11} & \bar{A}_{12} \\ \bar{A}_{21} & \bar{A}_{22} \end{bmatrix} \begin{bmatrix} \bar{x}_1(k) \\ \bar{x}_2(k) \end{bmatrix} + \begin{bmatrix} 0 \\ I_q \end{bmatrix} u(k) \tag{A8}$$

$$y(k) = \begin{bmatrix} C_d N & C_d B_d \end{bmatrix} \begin{bmatrix} \bar{x}_1(k) \\ \bar{x}_2(k) \end{bmatrix} \tag{A9}$$

Since, Eq. A8 shows that the differential equation corresponding to the state sub-vector $\bar{x}_2$ is directly involved in the unknown input u, we simply drop this part. The above equations then become:

$$\bar{x}_1(k+1) = \bar{A}_{11} \bar{x}_1(k) + \bar{A}_{12} \bar{x}_2(k) \tag{A10}$$

$$y(k) = \begin{bmatrix} C_d N & C_d B_d \end{bmatrix} \begin{bmatrix} \bar{x}_1(k) \\ \bar{x}_2(k) \end{bmatrix} \tag{A11}$$

If $C_d B_d$ is a full column rank matrix, then there exists a non-singular matrix F.

$$F = \begin{bmatrix} C_d B_d & Q_u \end{bmatrix} = \begin{bmatrix} C_d B_d & C_d B_d(2) \\ & C_d B_d(1) \end{bmatrix}; \tag{A12}$$

$$F^{-1} = \begin{bmatrix} U_1 \\ U_2 \end{bmatrix} \tag{A13}$$

where $Q_u \in \Re^{m \times (m-q)}, U_1 \in \Re^{q \times m}, U_2 \in \Re^{(m-q) \times m}$. The matrix F is defined by putting vector Q_u as switching the rows of $C_d B_d$ vector. This ensures that the matrix F is non-singular. Pre-multiplying both sides of Eqs. A10 and A11 with inverse of F would make:

$$\begin{bmatrix} U_1 \\ U_2 \end{bmatrix} y = \begin{bmatrix} U_1 \\ U_2 \end{bmatrix} \begin{bmatrix} C_d N & C_d B_d \end{bmatrix} \begin{bmatrix} \bar{x}_1 \\ \bar{x}_2 \end{bmatrix}$$
$$= \begin{bmatrix} U_1 C_d N & U_1 C_d B_d \\ U_2 C_d N & U_2 C_d B_d \end{bmatrix} \begin{bmatrix} \bar{x}_1 \\ \bar{x}_2 \end{bmatrix} = \begin{bmatrix} U_1 C_d N & I_q \\ U_2 C_d N & 0 \end{bmatrix} \begin{bmatrix} \bar{x}_1 \\ \bar{x}_2 \end{bmatrix} \tag{A14}$$

The above equation is expanded as:

$$U_1 y = U_1 C_d N \bar{x}_1 + \bar{x}_2 \tag{A15}$$
$$U_2 y = U_2 C_d N \bar{x}_1 \tag{A16}$$

Eq. A15 can be rearranged as:

$$\bar{x}_2 = U_1 y - U_1 C_d N \bar{x}_1 \tag{A17}$$

Eq. A17 can be substituted into Eqs. A10 and A11 as;

$$\bar{x}_1(k+1) = \bar{A}_{11}\bar{x}_1(k) + \bar{A}_{12}(U_1 y(k) - U_1 C_d N \bar{x}_1(k))$$
$$= (\bar{A}_{11} - \bar{A}_{12} U_1 C_d N)\bar{x}_1(k) + \bar{A}_{12} U_1 y(k) \tag{A18}$$
$$\bar{y}_2(k) = U_2 C_d N \bar{x}_1(k) \tag{A19}$$

where $\bar{y}_2(k) = U_2 y(k)$. Eqs. A18 and A19 can be used to derive the gain matrix, K, using a Kalman filter (or Ackerman's formula). The discrete Kalman filter gain is obtained by solving the Ricatti equation [Brown 97, Mendel 95]. The measurement and system noise covariance, and the input vector are chosen as:

$$R = 1;\ Q = \begin{bmatrix} 1e7 & 0 \\ 0 & 1e8 \end{bmatrix} \times \tau_s;\ \ \Gamma = \begin{bmatrix} 1 & 1 & 1 & 1 & 1 \end{bmatrix}^T \times \tau_s \tag{A20}$$

The Kalman Filter model then becomes as;

$$\hat{\bar{x}}_1(k+1) = (A_0 - KC_0)\hat{\bar{x}}_1(k) + B_0 y(k) \tag{A21}$$

where

$$A_0 = \bar{A}_{11} - \bar{A}_{12} U_1 C_d N$$
$$B_0 = K U_2 + \bar{A}_{12} U_1 \tag{A22}$$
$$C_0 = U_2 C_d N$$

The unknown input u can be explicitly shown from Eqs. A10 and A11 and we can substitute $\bar{x}_2(k+1)$ and $\bar{x}_2(k)$ from Eq. A17 and $\bar{x}_1(k+1)$ from Eq. A21 to form;

$$u(k) = \bar{x}_2(k+1) - \bar{A}_{21}\bar{x}_1(k) - \bar{A}_{22}\bar{x}_2(k) \tag{A23}$$

and estimated unknown input becomes as

$$\begin{aligned}
\hat{u}(k) &= U_1 y(k+1) - U_1 C_d N\hat{\bar{x}}_1(k+1) - \bar{A}_{21}\hat{\bar{x}}_1(k) - \bar{A}_{22}(U_1 y(k) - U_1 C_d N\hat{\bar{x}}_1(k)) \\
&= U_1 y(k+1) - U_1 C_d N\{(A_0 - KC_0)\hat{\bar{x}}_1(k) + B_0 y(k)\} \\
&\qquad - \bar{A}_{21}\bar{x}_1(k) - \bar{A}_{22}(U_1 y(k) - U_1 C_d N\bar{x}_1(k)) \\
&= U_1 y(k+1) + \alpha_1 \hat{\bar{x}}_1(k) + \alpha_2 y(k) \\
&= \hat{F}_a(k)
\end{aligned} \tag{A24}$$

where

$$\begin{aligned}
\alpha_1 &= U_1 C_d NKU_2 C_d N + U_1 C_d N\bar{A}_{12} U_1 C_d N - U_1 C_d N\bar{A}_{11} - \bar{A}_{21} + \bar{A}_{22} U_1 C_d N \\
\alpha_2 &= -U_1 C_d NKU_2 - U_1 C_d N\bar{A}_{12} U_1 - \bar{A}_{22} U_1
\end{aligned} \tag{A25}$$

Thus, the estimated state vector $\hat{\bar{x}}_1(k)$ can be estimated from Eq. A21 and the unknown input can be estimated based on Eq. A24. The low pass filter using the 6th order Butterworth filter with the cutoff frequency of 1500 Hz was used to filter out any unwanted high frequency noise.

The cutting tests are performed from 1000 rpm to 12,000 rpm with a five fluted end mill. The Aluminum 7075 workpiece is slotted with the h of cut of 1.5 mm. Figures A1 to A4 depict the experimental results and the compensated applied forces. Even though the compensated values are very close to the reference table dynamometer, the method has several shortcomings. The biggest problem is coming up with good values of N and Q matrices. The matrices are chosen using an ad-Hoc approach. Furthermore, ensuring the full rank of $C_d B_d$ matrix is difficult. In addition, we were not able to get the same performance as the disturbance Kalman Filter (Chapter 6).

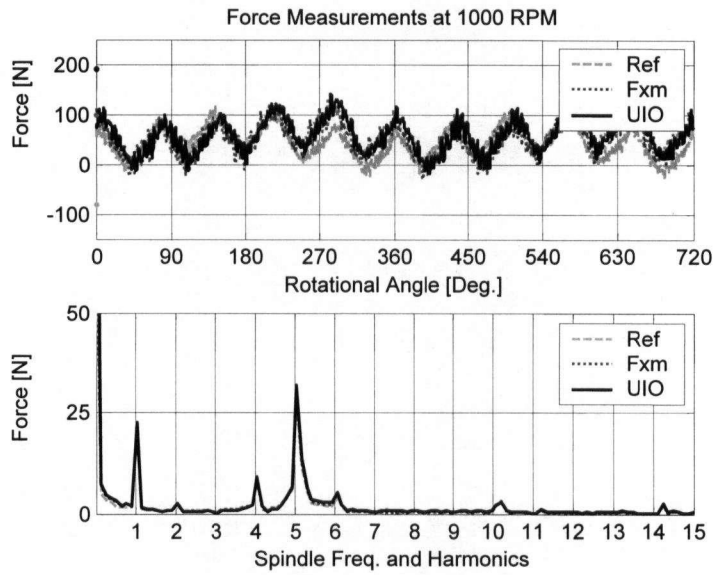

Figure A1. Five fluted cutting force measurements at 1,000 rpm with the piecewise constant input. *The top figure is shown in the time domain and the bottom figure is shown in the frequency (normalized with the spindle freq.) domain. Ref. denotes the reference cutting forces from the dynamometer at 1000 rpm, Fxm denotes the measured force from the spindle integrated force sensor system, UIO denotes the compensated cutting forces using the Reduced Order approach.*

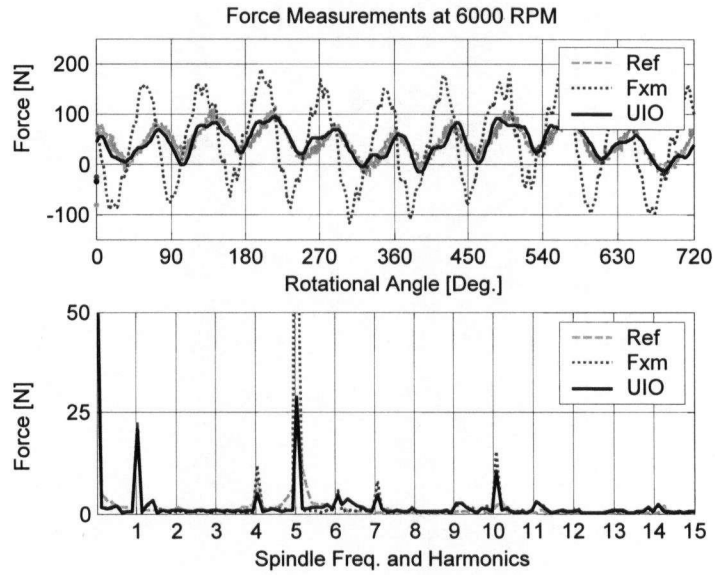

Figure A2. Five fluted cutting force measurements at 6,000 rpm with the piecewise constant input. *The top figure is shown in the time domain and the bottom figure is shown in the frequency (normalized with the spindle freq.) domain.*

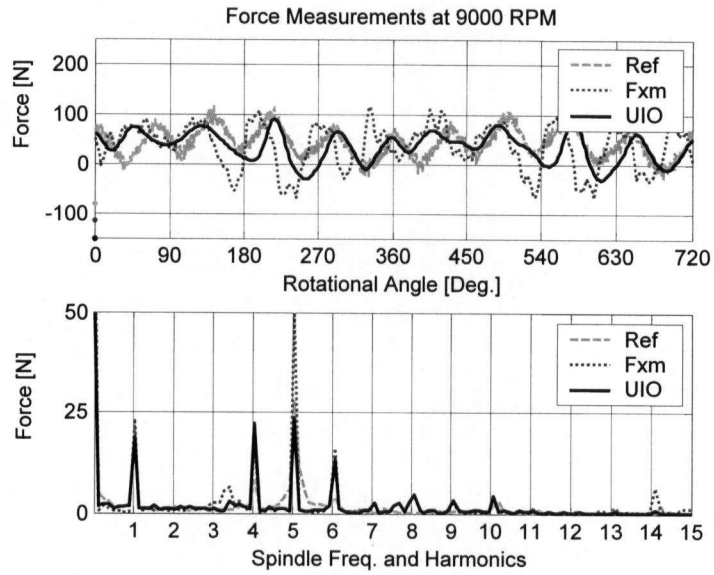

Figure A3. Five fluted cutting force measurements at 9,000 rpm with the piecewise constant input. *The top figure is shown in the time domain and the bottom figure is shown in the frequency (normalized with the spindle freq.) domain.*

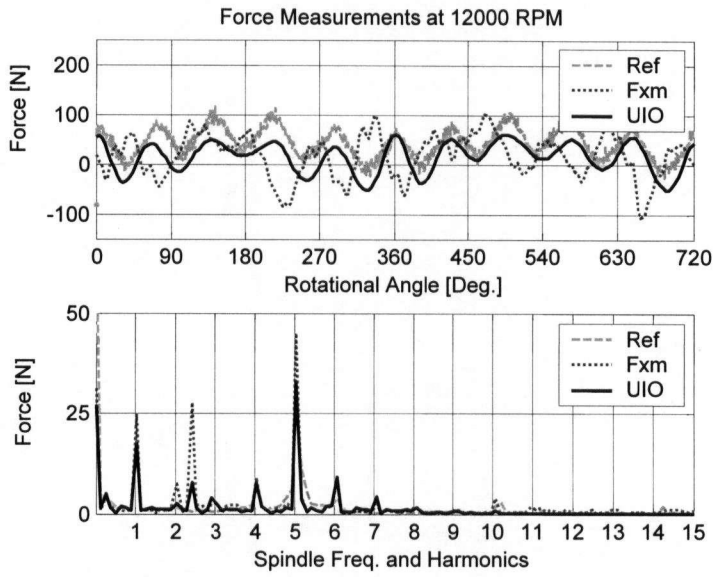

Figure A4. Five fluted cutting force measurements at 12,000 rpm with the piecewise constant input. *The top figure is shown in the time domain and the bottom figure is shown in the frequency (normalized with the spindle freq.) domain.*

APPENDIX B.

ANALYTICAL FREQUENCY RESPONSE FUNCTION DERIVATIONS OF BEAM MODELS

Alternative to the Finite Element method, the analytical analysis can be performed to obtain the FRFs of simple uniform beams [Blevins 79, Schmitz 00]. The analytical equations for FRFs contain both the rigid and non-rigid receptances. The rigid part (i.e., zero Hz component) consists of rigid modes with respect to translational and rotational modes. The non-rigid part (i.e., non zero Hz components) consists of sums of modal transfer functions. Free-free mode shapes of a beam can be depicted as;

$$\varphi_i(x) = \cosh\left(\frac{\lambda_i x}{L}\right) + \cos\left(\frac{\lambda_i x}{L}\right) - \sigma_i\left(\sinh\left(\frac{\lambda_i x}{L}\right) + \sin\left(\frac{\lambda_i x}{L}\right)\right) \tag{B1}$$

where $\sigma_i(x) = \dfrac{\cosh\lambda_i - \cos\lambda_i}{\sinh\lambda_i - \sin\lambda_i}$ and λ_i are found to be [Blevin 79]:

i	1	2	3	4	5	for i>5
λ_i	4.73004074	7.85320462	10.9956078	14.1371655	17.2787597	(2i + 1)/2

The natural frequencies and mass per area for the free-free beam would be:

$$\omega_n = \frac{\lambda_i^2}{L^2}\sqrt{\frac{EI}{\rho L}} \tag{B2}$$

where E is the modulus, I is the second moment of inertia, L is the length, and ρ is the density. Based on Eq. 5.8, the translational transfer functions, $H_{A,ff}$ can be shown as:

$$H_{A11,ff} = \frac{1}{ms^2} + \frac{3}{ms^2} + \sum_{i=1}^{\infty} \frac{\varphi_i(L)^2}{m(s^2 + 2\omega_n \zeta s + \omega_n{}^2)}$$

$$H_{A21,ff} = \frac{1}{ms^2} - \frac{3}{ms^2} + \sum_{i=1}^{\infty} \frac{\varphi_i(L)\varphi_i(0)}{m(s^2 + 2\omega_n \zeta s + \omega_n{}^2)} \tag{B3}$$

where $m = \rho L$. The RDOF transfer function, $H_{A,fM}$ is shown as:

$$H_{A11,fM} = \frac{-\sqrt{12}\sqrt{3}}{mLs^2} + \sum_{i=1}^{\infty} \frac{\dot{\varphi}_i(L)\varphi_i(L)}{m(s^2 + 2\omega_n \zeta s + \omega_n{}^2)}$$

$$H_{A21,fM} = \frac{\sqrt{12}\sqrt{3}}{mLs^2} + \sum_{i=1}^{\infty} \frac{\dot{\varphi}_i(0)\varphi_i(L)}{m(s^2 + 2\omega_n \zeta s + \omega_n{}^2)} \tag{B4}$$

Similarly, the RDOF transfer function, $H_{A,MM}$ can be obtained as:

$$H_{A11,MM} = \frac{12}{mLs^2} + \sum_{i=1}^{\infty} \frac{\dot{\varphi}_i(L)\dot{\varphi}_i(L)}{m(s^2 + 2\omega_n \zeta s + \omega_n{}^2)}$$

$$H_{A21,MM} = \frac{12}{mLs^2} + \sum_{i=1}^{\infty} \frac{\dot{\varphi}_i(0)\dot{\varphi}_i(L)}{m(s^2 + 2\omega_n \zeta s + \omega_n{}^2)} \tag{B5}$$

The above equations are used to simulate the FRFs of the tool. The first 20 modes are considered and the damping ratio is chosen as 1 % for carbide tools. The comparison of FRFs obtained from the FE and the analytical models for simple uniform beams show miniscule difference.

APPENDIX C.

DYNAMIC COMPENSATION USING THE RECEPTANCE COUPLED DYNAMICS

This section depicts an exemplar case study for the receptance coupled dynamics which can be used for the dynamic compensation. The predicted dynamics between the tool tip and the spindle integrated sensors are used in the feed direction compensation. The disturbance Kalman Filter compensation, which is outlined in Chapter 6, is performed. The modeled Frequency Response Function (FRF) of the uncompensated force sensor system ($\Phi_{31}(s) = F_3 / F_1$), FRF of the Kalman Filter for force ($G_{\hat{F}_1/F_3}(s) = \hat{F}_1 / F_3$), and FRF of the compensated system ($\Phi_{31}(s) \times G_{\hat{F}_1/F_3}(s)$) are illustrated in Figure C1. Sample cutting force tests are performed at 7000 rpm using the four-fluted end mill with the mechanical chuck. Figure C2 depicts the cutting forces measured from the spindle sensors and the compensated forces using the Kalman Filter. The reference cutting forces are also obtained from the table dynamometer. The spindle frequency and tooth passing frequency of a four fluted end mill at 7000 rpm are 117.67 Hz and 467.67 Hz, respectively. Since the first mode (432 Hz) of the spindle sensor dynamics is very close to the tooth passing frequency, the cutting forces measured from the spindle integrated sensors are severely distorted. However, the Kalman filter compensates the dynamic amplification due to the first mode, and brings the force to the level provided by the reference table dynamometer. The experiment demonstrates that the receptance coupled dynamics successfully provide the model for the compensation method.

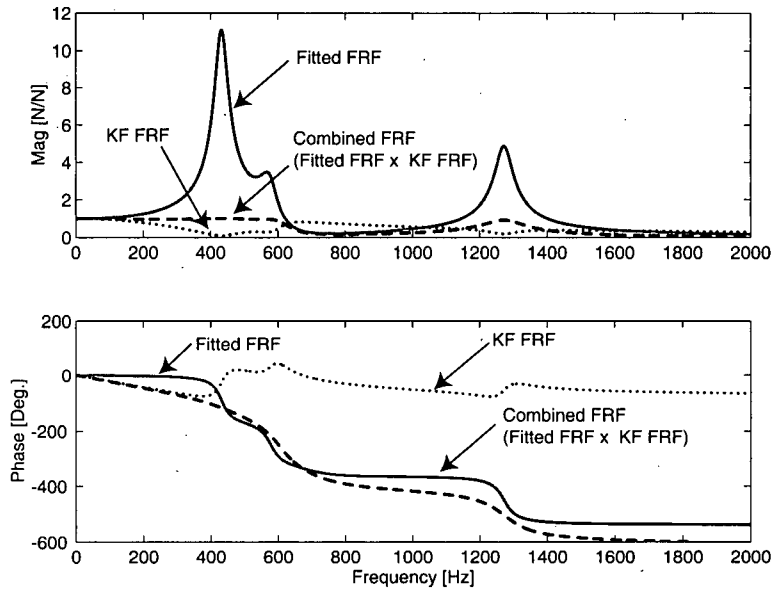

Figure C1. FRF of the measured, Kalman Filter and compensated spindle integrated force sensing system *(Fitted FRF: FRF identified using the RC; KF FRF: FRF of the Kalman Filter; Combined FRF: Cross product of Fitted FRF and KF FRF)*

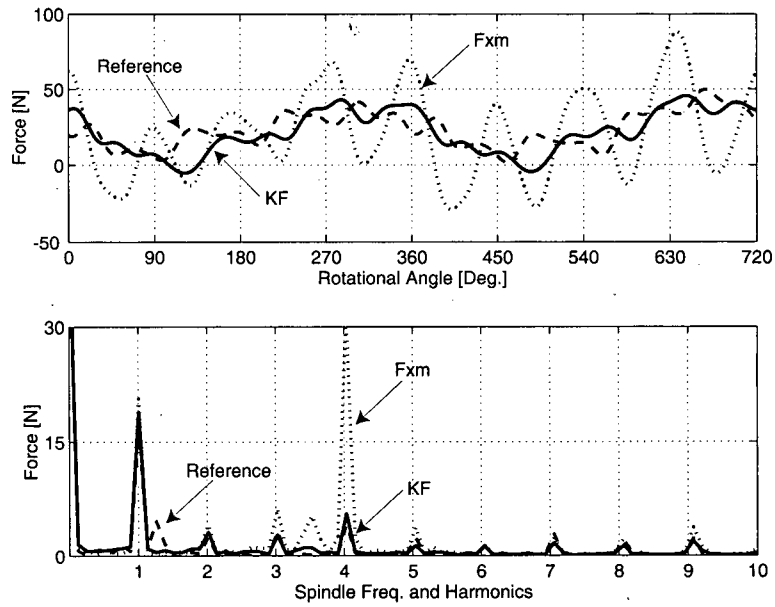

Figure C2. Five fluted cutting force measurements at 7000 rpm with piecewise constant input. *The spindle and tooth passing frequency at 7000 rpm corresponds to 117.67 Hz, and 467.67 Hz, respectively.*

APPENDIX D.

CHANGING DYNAMICS OF THE SPINDLE DUE TO THE SPINDLE SPEEDS

The spindle system is one of the most important parts of a metal cutting machine, and therefore understanding its dynamics directly affects the machine performance. The spindle bearing system serves to center and hold the cutting tool during machining process such as drilling, grinding, milling of the work piece under the effects of cutting forces. The spindle bearing system should be designed in such a way that it attains enough strength and stiffness as well as uniform balance to minimize deflections while rotating [Koenigsberger 64]. The spindle bearing undergoes a severe vibration due to external cutting force, regenerative chatter, and out of balance loads.

BEARING ANALYSIS

Angular contact ball bearings are still widely used in the industry instead of other bearings of high stiffness (i.e., roller bearings) mainly due to their thermal stability. As a rule of the thumb [NSK Bearing Manual], the first resonant frequency should be at least 200 Hz and the first resonant frequency should exceed the maximum spindle speed by at least 20%. In addition, the thermal effects should also be considered due to a high rotational speed. The thermal effects are critical because the damping and stiffness change.

Centrifugal forces and gyroscopic effects exist when the spindle rotates at high speeds. These effects, along with the increase in temperature, change the contact angle of the bearings which results in a decrease in stiffness. Centrifugal forces are dominant when the spindle speed is less than 10,000 rpm resulting in the enlargement of the normal forces on the outer ring of the bearing. Therefore, the contact angle decreases for the outer ring while the contact angle between the inner ring and the bearing increases. The change in the contact angle results in the additional centrifugal force (F_c) to balance the cutting forces as shown in Figure D1 [Abele 03] where F_n is the normal force at the contact locations. The dynamics of contact bearings are non-linear with functions of the amount of loads, unbalance, and temperature gradients. The increase in the speed also results in enlargement of the spindle shaft due to the temperature growth which then causes the dilation in the inner ring while the temperature of the outer ring remains constant. The enlargement of the inner ring partly compensates the centrifugal effects since the contact angle between the inner ring and the bearing decreases. Therefore, the increase in the speed decreases the bearing stiffness and these effects are more noticeable when the spindle speed increases beyond 10,000 rpm when also coupled with the gyroscopic moments.

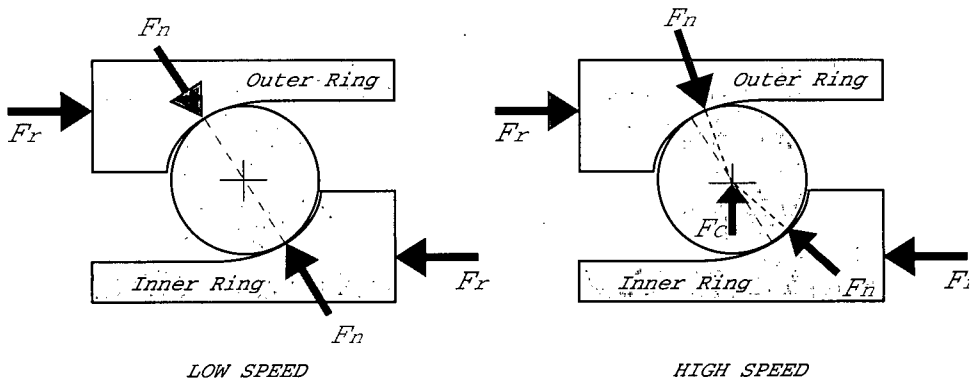

Figure D1. Bearing Dynamics depending on the spindle speed [Abele 03]

Empirical studies [Warde 83] have been carried out to determine the effects to predict the stiffness change. The empirical formula given by Warde for the static stiffness is;

$$k_a = 3.44e6 \times P_a^{1/3} N^{2/3} (\sin\beta)^{5/3} D^{1/3} \quad \text{[N/m]} \tag{D1}$$

$$k_r = 0.64 k_a \cot\beta \quad \text{[N/m]} \tag{D2}$$

where β is the contact angle, P_a is the preload, D is the ball diameter, and N is the number of balls. The bearing analysis is beyond the scope of this study. Further details can be found in [Harris 88]. More detailed research is needed to understand the effects of the preload and changes in the contact angle due to the temperature change.

EFFECTS OF SPINDLE SPEED ON THE DYNAMICS OF THE SPINDLE THROUGH ANALYSIS OF THE TRANSFER FUNCTIONS

The rotational speeds change the dynamics of the spindle. Experimental modal analyses are performed to acquire the FRFs with respect to the spindle rotational speeds. A deep groove ball bearing is used to measure the transfer functions at various rotational speeds. First, the ball bearing is tightly secured to the carbide shaft. While the spindle rotates, the outer ring of the bearing is secured with a piece of tape so that it will not rotate with the inner ring. The input source is the impact force hammer, which is applied at the outer ring of the bearing, and the output source is the laser sensor which measures the displacement of the outer ring of the bearing. Figure D2 illustrates the experimental setup.

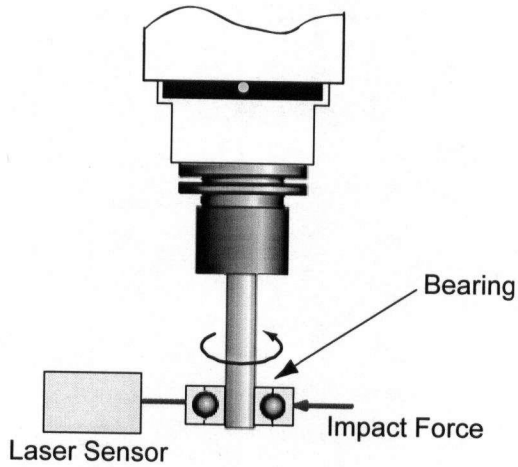

Figure D2. Experimental Modal Analysis Setup while the Spindle Rotates

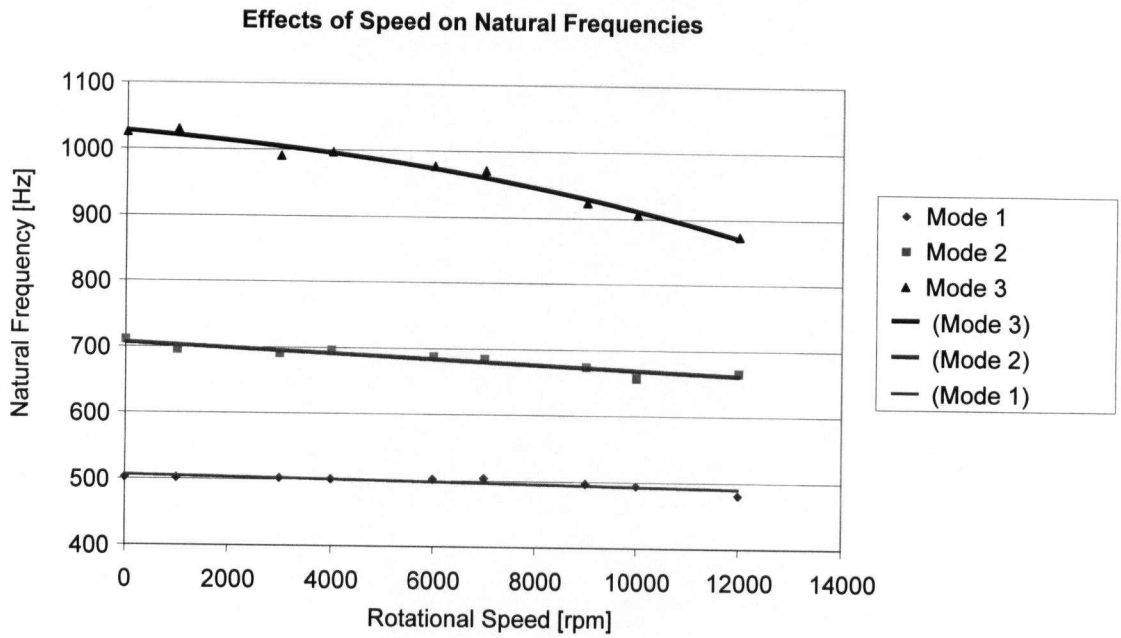

Figure D3. Natural frequencies vs. Rotational speeds

Figure D3 shows the effect of natural frequencies with respect to the rotational speeds. The rotational speeds of the spindle changed the spindle dynamics due to several reasons. The first and second mode did not drop significantly. In contrast, the last mode dropped about 12 %. This indicates that the last mode is more susceptible to the

centrifugal and gyroscopic effects. Furthermore, the damping ratio and the stiffness with respect to the rotational speeds are not very conclusive mainly due to the inadequate fittings. The increasing rotational speed results in the thermal growth of the spindle bearings. The thermal effect on bearing preloads significantly affects the stiffness and damping characteristics of the spindle structure. In addition, gyroscopic and centrifugal forces would hinder the critical speeds of the spindle and natural frequencies [Dimarogonas 96]. Thus, the investigation of the rotating spindle dynamics is important especially at high speeds. Even though the rotating dynamics produce significant effects, a relatively small number of studies has been performed on the modal analysis of the rotating spindle due to practical difficulties.

UNBLANCED FORCE COMPENSATION

Unbalanced rotating components of the spindle pose significant noise in the measurements especially at high rotating speeds. This disturbance noise is caused by the eccentricity (or unbalance) of the rotating spindle that exerts centrifugal forces. The equation below demonstrates the unbalance force where the right hand side of the equation is the centrifugal force acting on the unbalanced mass, m_o with respect to the distance of the unbalanced mass from the center, e, and the rotational speed of the spindle is denoted as ω_r.

$$M\ddot{x} + C\dot{x} + Kx = m_o e \omega_r^2 \sin \omega_r t \qquad \text{(D3)}$$

The unbalanced forces are square functions of the rotational speeds. For example, the comparison of unbalanced vibration occurring at 1000 rpm and 10,000 rpm would be 100 times.

These disturbances are distorting the estimation of the cutting forces because they appear as an additional force in the spindle integrated sensor within the same frequency range as the real cutting forces. Therefore, it is not possible to eliminate them by simple filtering. The appropriate way to compensate these disturbances is to subtract these unbalanced forces, F_u, from the measured forces, F_c.

$$F_m = F_c - F_u \tag{D4}$$

In order to compensate unwanted unbalanced forces, the 'air cutting' tests where the forces are measured without cutting the work piece at different spindle rotating speeds are performed. In order to synchronize the air cutting forces with the measured forces, the spindle position encoder has been utilized. Often, the air cutting force and the actual cutting force speeds vary. In these cases, the data are re-sampled to match between the two signals. Once the forces are synchronized for each revolution, the air cutting forces are subtracted from the measured forces to acquire eccentric compensated forces.

Figures D4 to D11 show the air cutting forces from the spindle integrated force sensors and the table dynamometer. The left side of the figures is in the time domain and the right side of the figures is in the frequency domain. The air cutting forces from the table dynamometer show that the eccentric forces are fluctuating approximately around +/- 5 N for up to 9000 rpm. Above 9000 rpm, the air cutting forces slightly increased. The air cutting forces from the force ring exhibit significant eccentric noise which escalated as the spindle speed increased. Especially at high speeds (i.e., 10000 and 12000 rpm), the disturbance would increase to +/- 80 N. Also, the frequency contents of the air cutting forces would occur at the spindle frequencies and the second harmonics. One thing to note is that during rotational speeds below 6000 rpm, a frequency content of the

second harmonic is higher than the spindle frequency. One hypothesis of this phenomenon would be that uneven temperature gradient may cause a shaft to bend. Even the structure bending modes would elevate the amplitudes of the second harmonics.

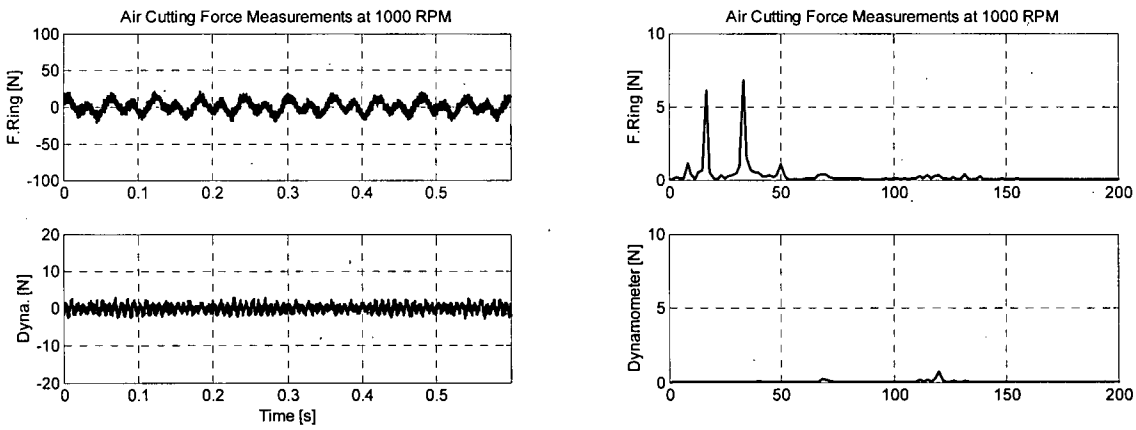

(a) Time Domain (b) Frequency Domain

Figure D4. Air Cutting force measurements at 1000 rpm at the spindle integrated force ring (top) and the table dynamometer (bottom) – *Spindle frequency of 16.67 Hz.*

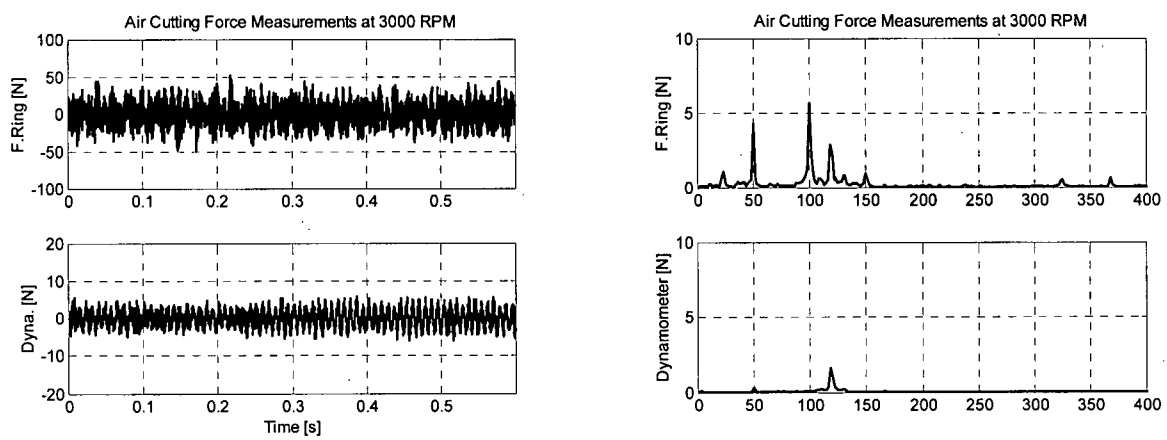

(a) Time Domain (b) Frequency Domain

Figure D5. Air Cutting force measurements at 3000 rpm at the spindle integrated force ring (top) and the table dynamometer (bottom) – *Spindle frequency of 50 Hz.*

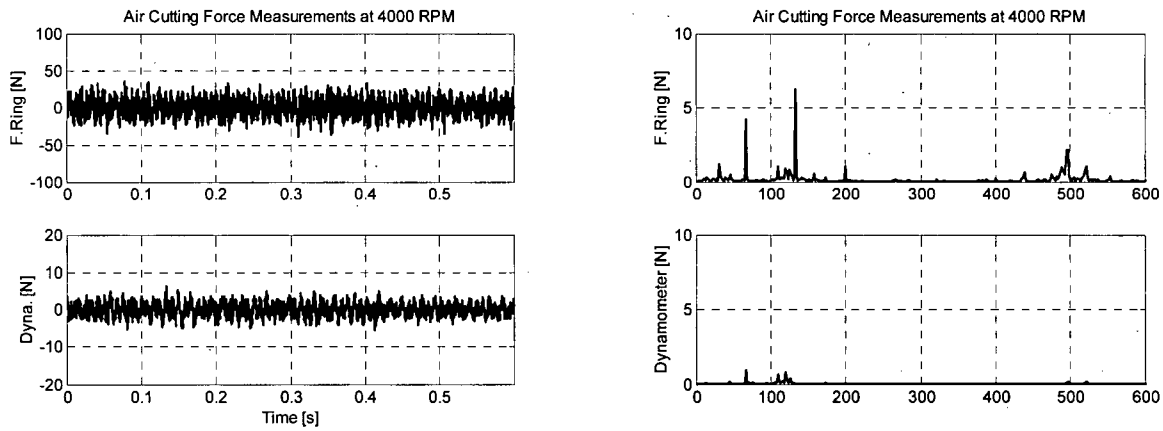

(a) Time Domain (b) Frequency Domain

Figure D6. Air Cutting force measurements at 4000 rpm at the spindle integrated force ring (top) and the table dynamometer (bottom) – *Spindle frequency of 66.67 Hz.*

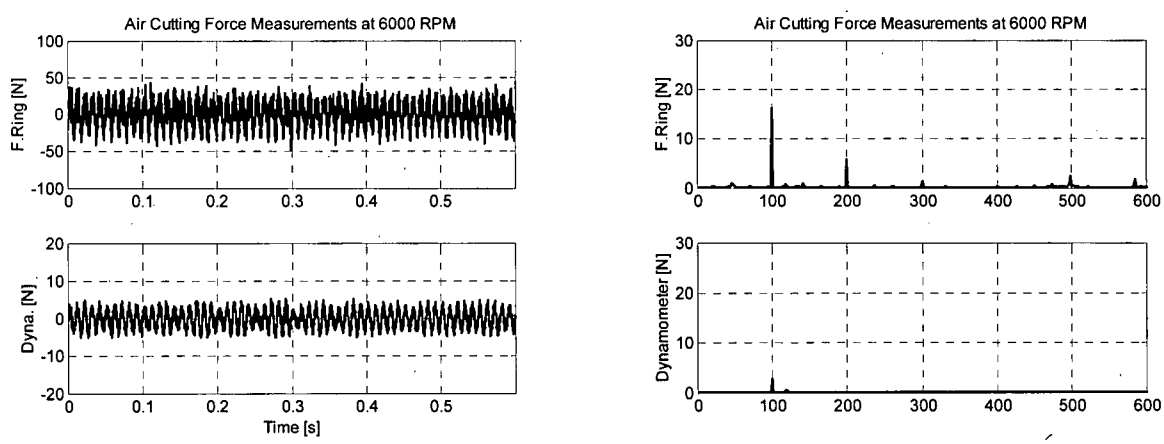

(a) Time Domain (b) Frequency Domain

Figure D7. Air Cutting force measurements at 6000 rpm at the spindle integrated force ring (top) and the table dynamometer (bottom) – *Spindle frequency of 100 Hz.*

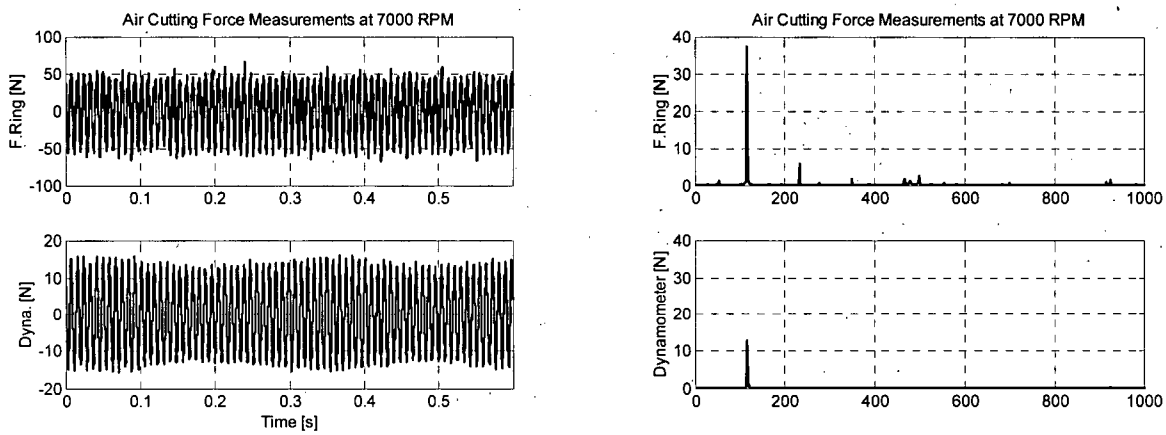

(a) Time Domain (b) Frequency Domain

Figure D8. Air Cutting force measurements at 7000 rpm at the spindle integrated force ring (top) and the table dynamometer (bottom) – *Spindle frequency of 116.67 Hz.*

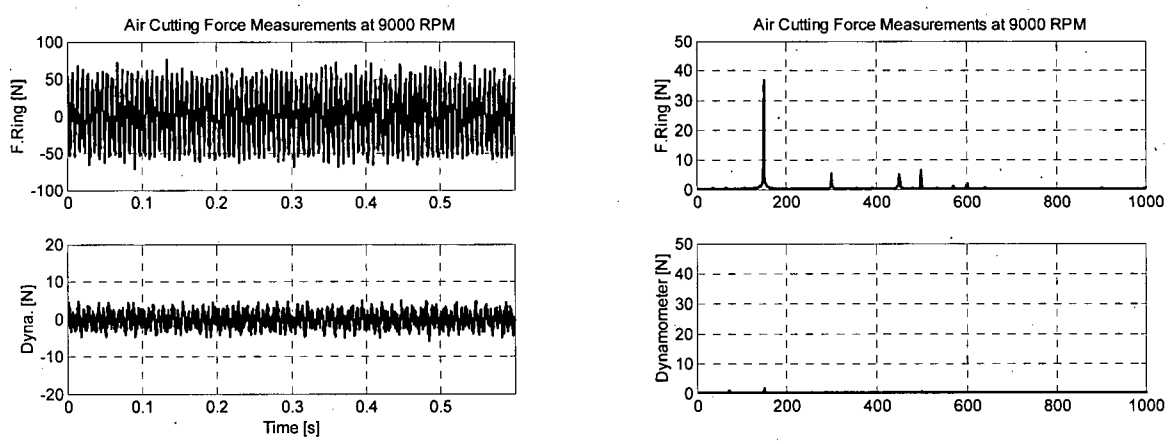

(a) Time Domain (b) Frequency Domain

Figure D9. Air Cutting force measurements at 9000 rpm at the spindle integrated force ring (top) and the table dynamometer (bottom) – *Spindle frequency of 150 Hz.*

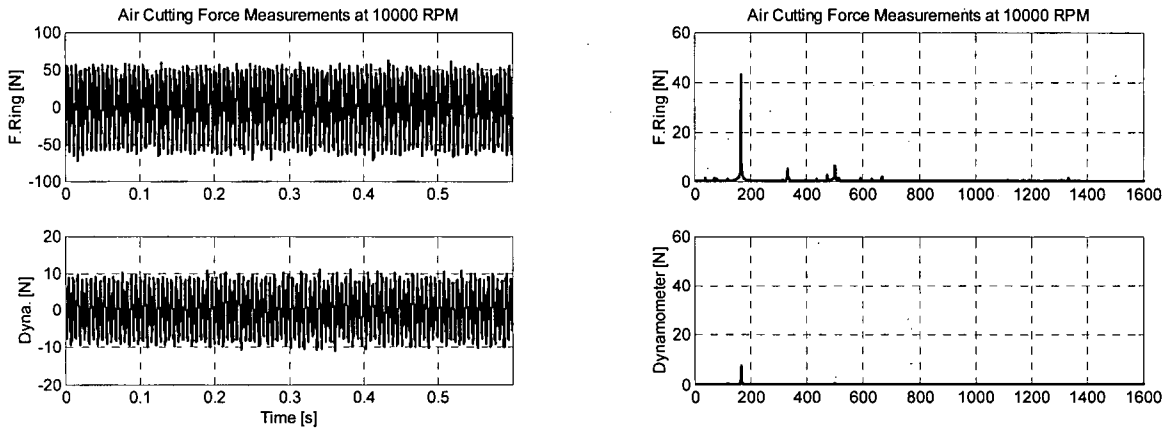

(a) Time Domain (b) Frequency Domain

Figure D10. Air Cutting force measurements at 10000 rpm at the spindle integrated force ring (top) and the table dynamometer (bottom) – *Spindle frequency of 166.67 Hz.*

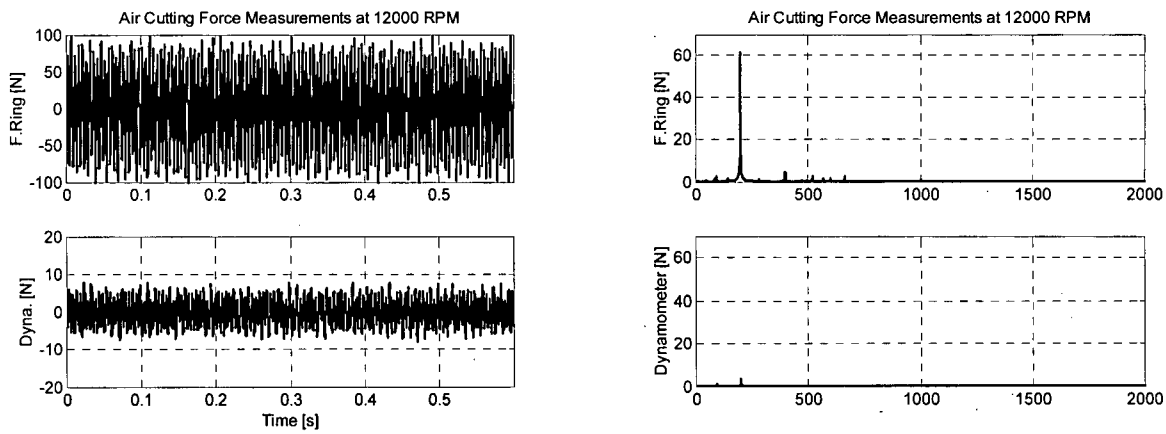

(a) Time Domain (b) Frequency Domain

Figure D11. Air Cutting force measurements at 12000 rpm at the spindle integrated force ring (top) and the table dynamometer (bottom) – *Spindle frequency of 200 Hz.*

APPENDIX E.

DISTURBANCE KALMAN FILTER COMPENSATION OF THREE DIRECTION CUTTING FORCES WITH THE CONSIDERATION OF THE CROSS TALKS

In this appendix, the disturbance Kalman Filter compensation with all cross talks and phase synchronization is examined. Even though we included all direct and cross transfer functions in the Kalman Filter design, the results did not improve compared to the Kalman Filter only with the direct transfer functions. The following results are obtained when the Kalman Filter is designed by considering all direct and cross transfer functions together. It can be seen that the compensated transfer functions are similar when only the direct transfer functions are considered. The phases between X and Y direction forces are almost identical, hence the force measurement is accurate regardless of the delay. Since the drives have only about 30 Hz and spindles only have about 5 Hz bandwidth, it is not important to capture the correct amplitude of the force with 1-2 ms delay, as long as the peaks are measured correctly with better than 80 % accuracy. (Tool run out, hard spots in the material, chip sticking and entangling affect the cutting force measurements even in laboratory dynamometers). The phase in Z direction is higher than in X and Y directions, whether the cross talks are included or not. The state vector size reaches 57 when all the cross transfer functions are included. The Kalman Filter parameters are shown below where R, Q, and Γ are the measurement, the system noise covariance, and the system noise matrix respectively;

$$R = diag[32.58 \quad 36.67 \quad 55.84];\ Q = diag[11e8 \quad 10e8 \quad 1e8];\ \Gamma = \begin{bmatrix} 0_{(1\times54)} & 1 & 0.4 & 0.6 \\ 0_{(1\times54)} & 0.4 & 1 & 0.4 \\ 0_{(1\times54)} & 0.6 & 0.4 & 1 \end{bmatrix}^T$$

where R is obtained from the measurements of electrical and air cutting disturbances, Q and Γ are obtained through the tuning. Reducing the order of the Kalman Filter would simplify the implementation while maintaining the same characteristics. Through the balanced truncation method [Skogestad 96], the order of the system has reduced from 57 states to 20 states.

PHASE SYNCHRONIZATION

The compensated force signals must be synchronized so that we combine the signals at the right instance. We attempted to synchronize the force measurements by synchronizing the phase shifts in direct and cross transfer functions. To achieve this, we converted the continuous Kalman Filter transfer functions into the discrete Kalman Filter transfer functions through a 'Tustin' approximation by equating 's' into 'z' domain. The modeled Frequency Response Function (FRF) of the uncompensated force sensor system ($\Phi = F_m / F_a$), the FRF of the Kalman Filter for force ($G_{\hat{F}a/Fm} = \hat{F}_a / F_m$), and the FRF of the compensated system ($\Phi \times G_{\hat{F}a/Fm}$) are illustrated in Fig. B1. We then identified the phase response of the cascaded system (i.e., $\Phi \times G_{\hat{F}a/Fm}$) and compared the direct transfer functions with the cross transfer function cases. The differences in phase are then converted into the number of sample delays, and the delay buffers are added to the faster responses to synchronize the response. This ensures that the compensated responses are correctly combined due to the direct and cross transfer functions. Based on Figures E1 to E5, we can conclude that the cross talk terms eliminate *ac* components of forces in Z

direction. However, the cutting forces in X direction, particularly at 6000 rpm, are not effectively compensated compared with the reference. To conclude, the inclusion of the cross talk terms complicates the compensation scheme and has positive effects in Z direction, but has adverse effects in X direction compared with the reference force. Overall, the design of the independent Kalman Filters using only direct transfer functions gives comparable results and the cross talk in Z direction can be reduced if the sensor contact surfaces are ground parallel to each other with better accuracy. Kistler, who sponsored this project by providing the sensors, warned us about this problem. They recommended us to install a 10 mm sensor ring which was going to be manufactured by them. However, the spindle housing did not have a 10 mm space to insert the ring due to bearings. Therefore, we had to take out the flange and Electro Discharge Machined the sensor holes but could not grind the faces of the cast housing and flange. It should have been done before the machine tool was assembled in the factory.

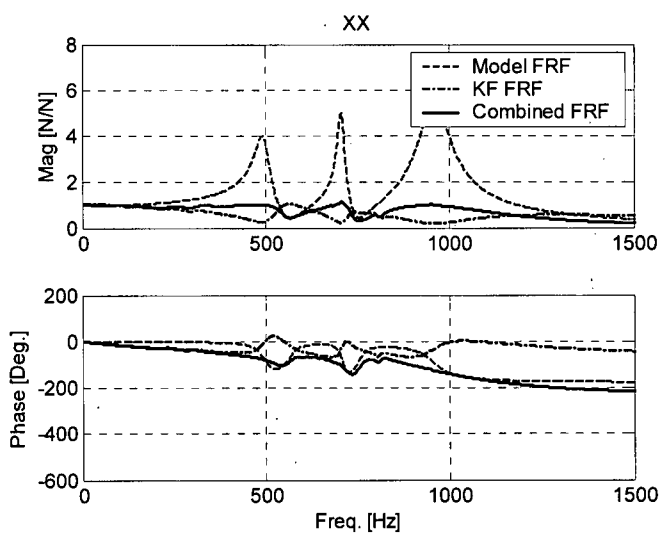

(a)

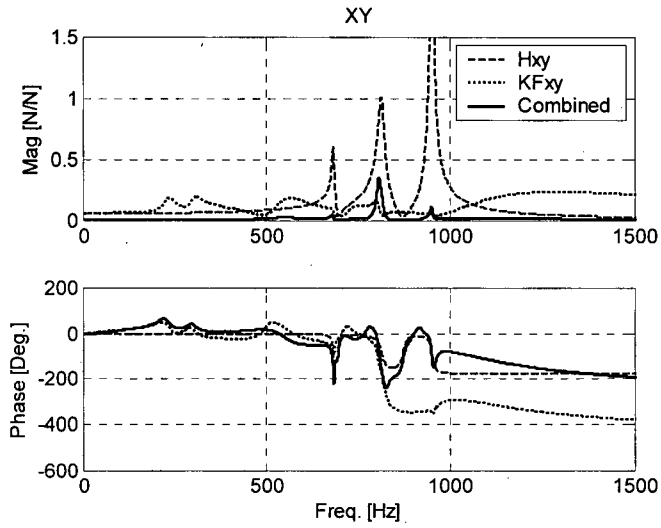
XY
Hxy
KFxy
Combined
Mag [N/N]
Phase [Deg.]
Freq. [Hz]

(b)

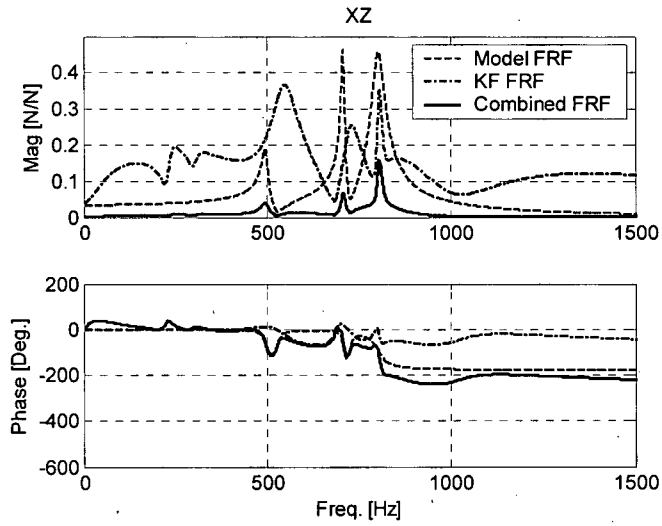
XZ
Model FRF
KF FRF
Combined FRF
Mag [N/N]
Phase [Deg.]
Freq. [Hz]

(c)

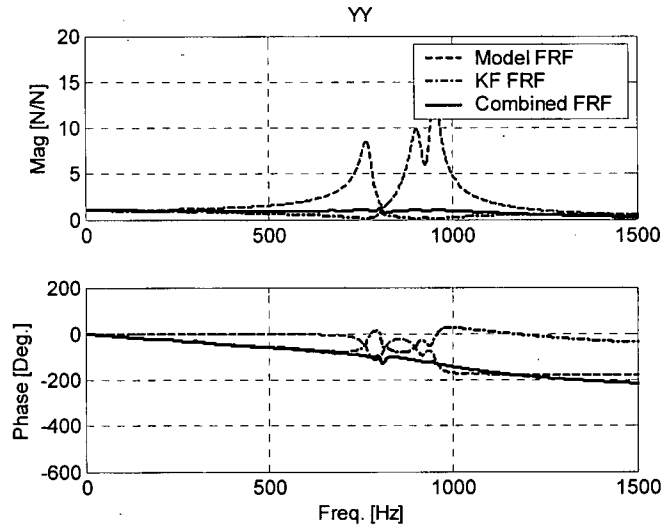
YY
Model FRF
KF FRF
Combined FRF
Mag [N/N]
Phase [Deg.]
Freq. [Hz]

(d)

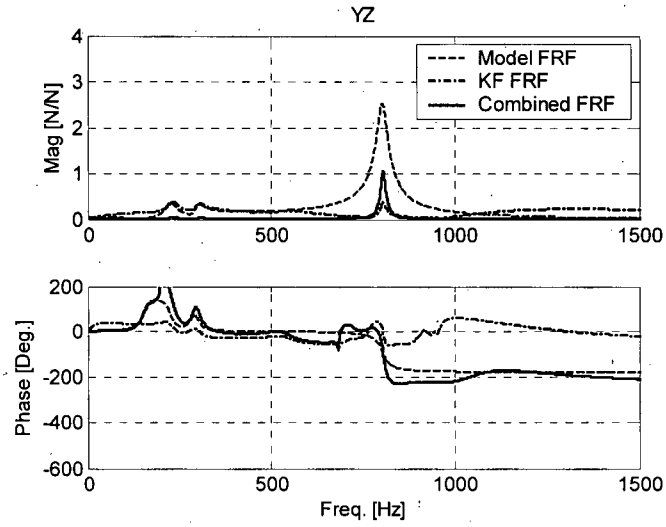

(e)

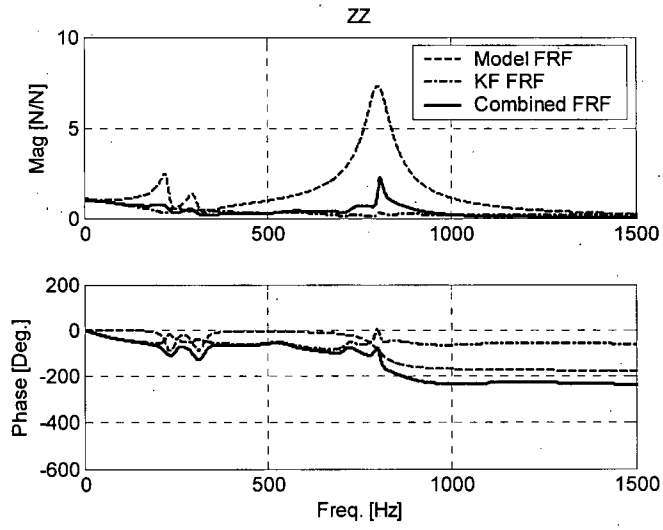

(f)

Figure E1. Model, KF, and Cascaded Transfer functions including direct and cross talks (a) Φ_{xx}, (b) Φ_{xy}, (c) Φ_{xz}, (d) Φ_{yy}, (e) Φ_{yz}, and (f) Φ_{zz}

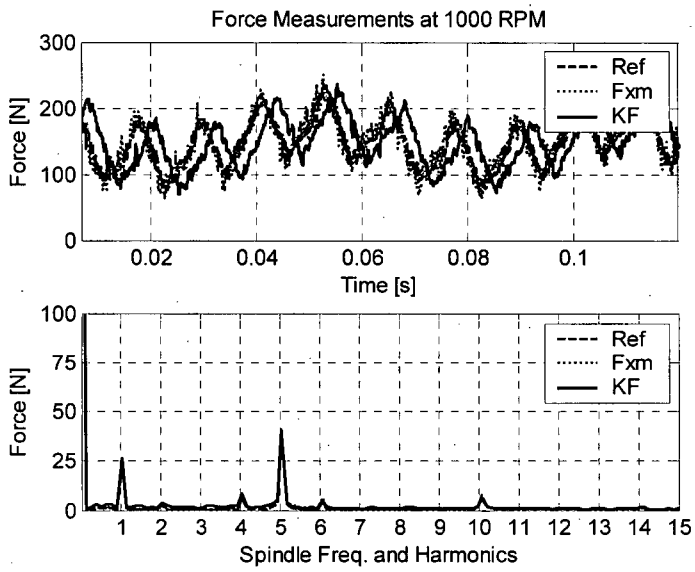

(a) X direction

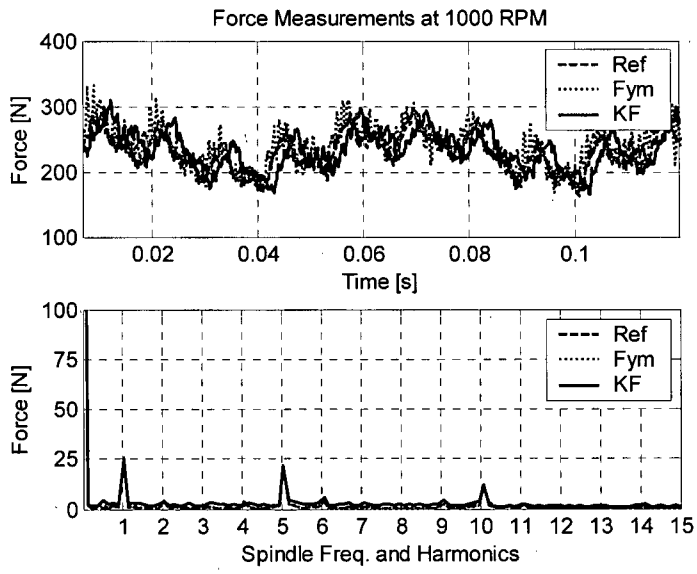

(b) Y direction

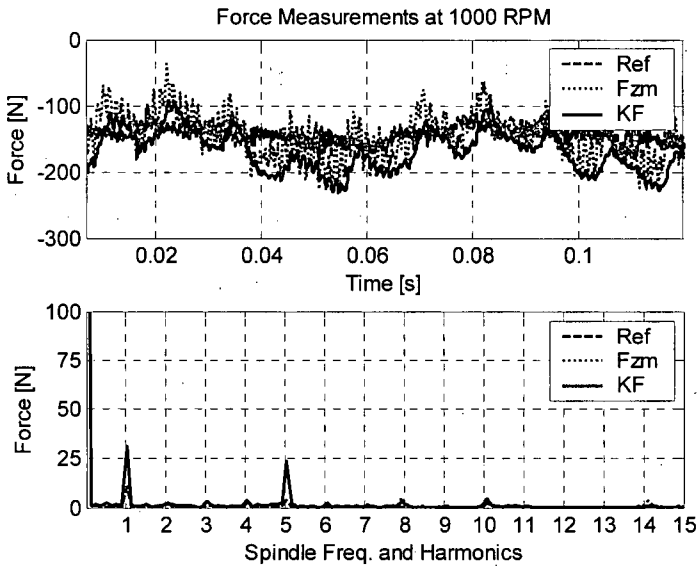

(c) Z direction

Figure E2. Five fluted cutting force measurements at 1000 rpm with (a) X, (b) Y, and (c) Z directions. *The figures are shown in the time and frequency (normalized with the spindle freq.) domains. The spindle frequency at 1000 rpm corresponds to 16.7 Hz. ('Ref.' denotes the reference cutting forces from the dynamometer at 1000 rpm, 'Fm' denotes the measured force from the spindle integrated force sensor system, and 'KF' denotes the Kalman Filter compensated cutting forces).*

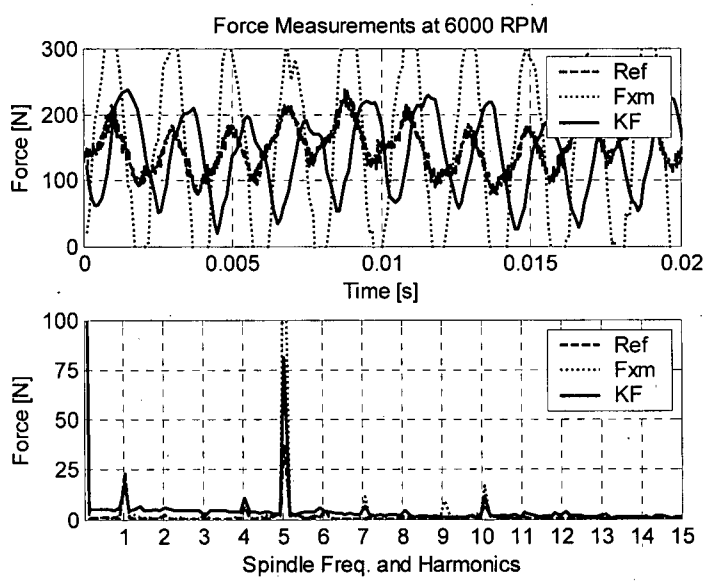

(a) X direction

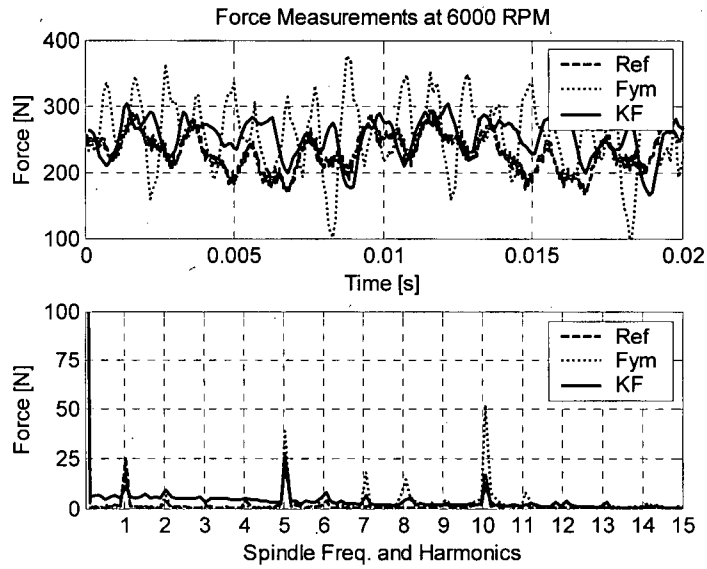

(b) Y direction

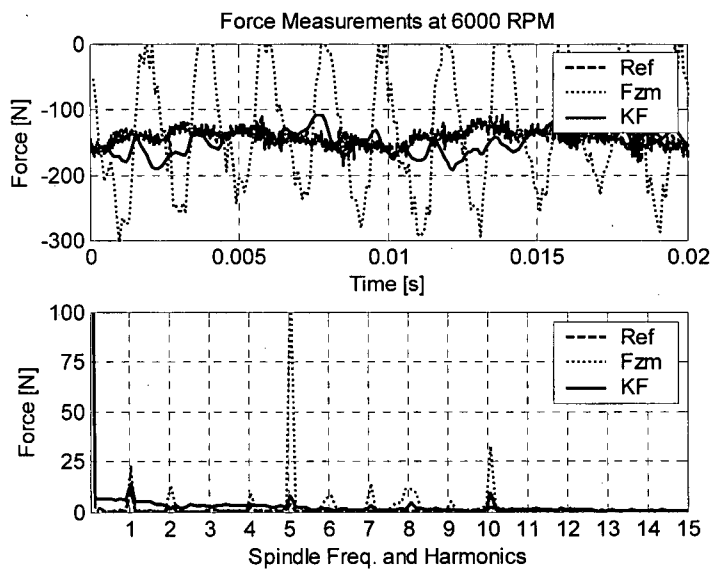

(c) Z direction

Figure E3. Five fluted cutting force measurements at 6000 rpm with (a) X, (b) Y, and (c) Z directions. *The figures are shown in the time and frequency (normalized with the spindle freq.) domains. The spindle frequency at 6000 rpm corresponds to 100 Hz.*

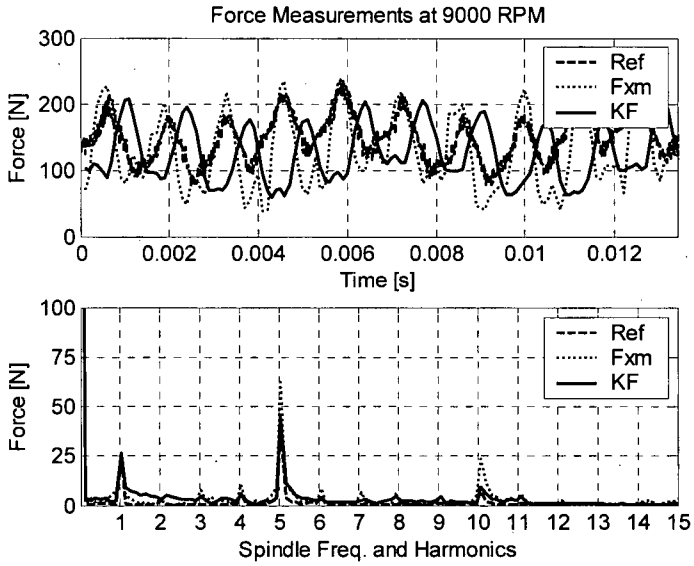

(a) X direction

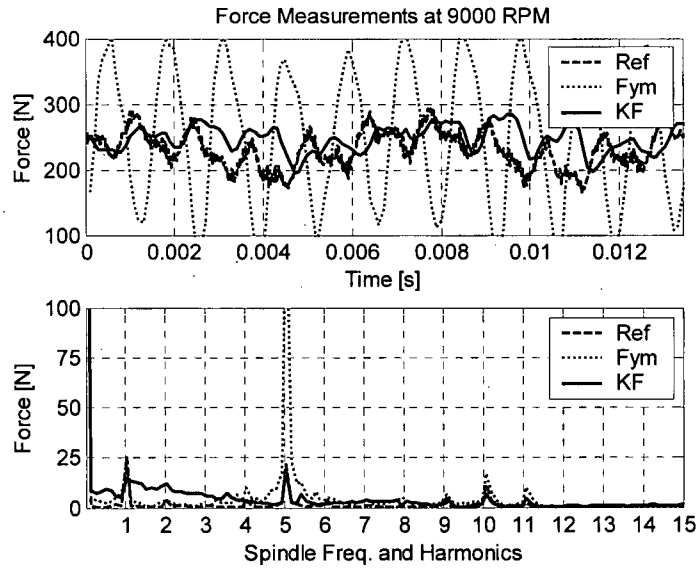

(b) Y direction

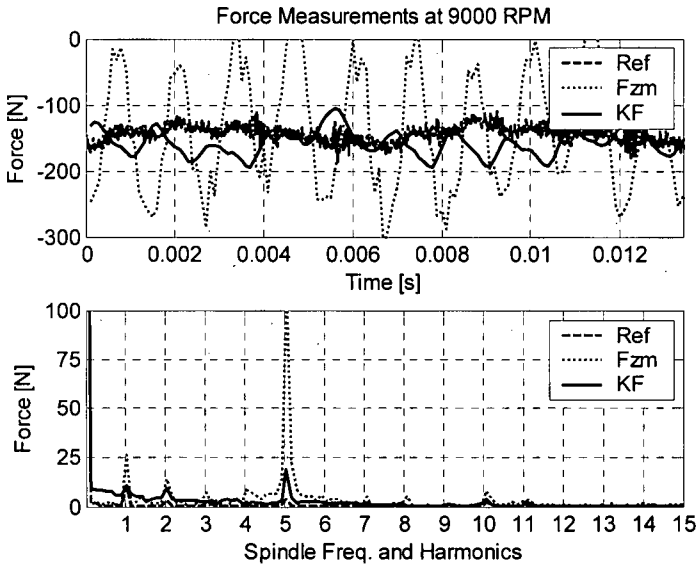

(c) Z direction

Figure E4. Five fluted cutting force measurements at 9000 rpm with (a) X, (b) Y, and (c) Z directions. *The figures are shown in the time and frequency (normalized with the spindle freq.) domains. The spindle frequency at 9000 rpm corresponds to 150 Hz.*

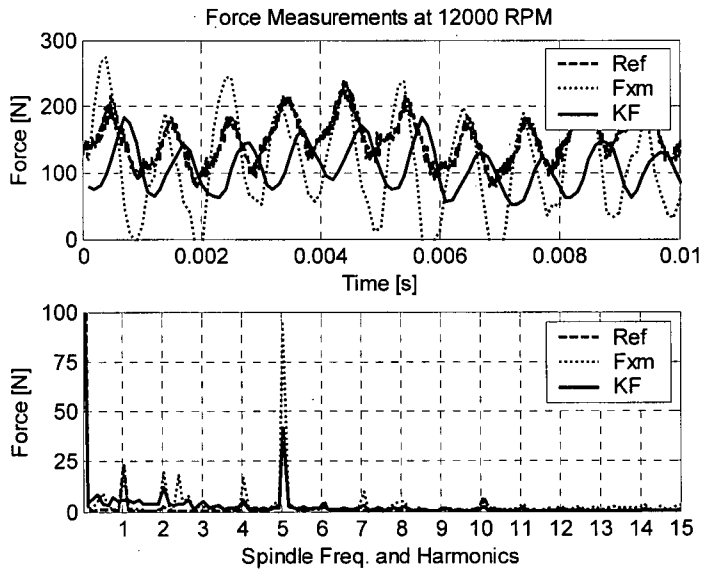

(a) X direction

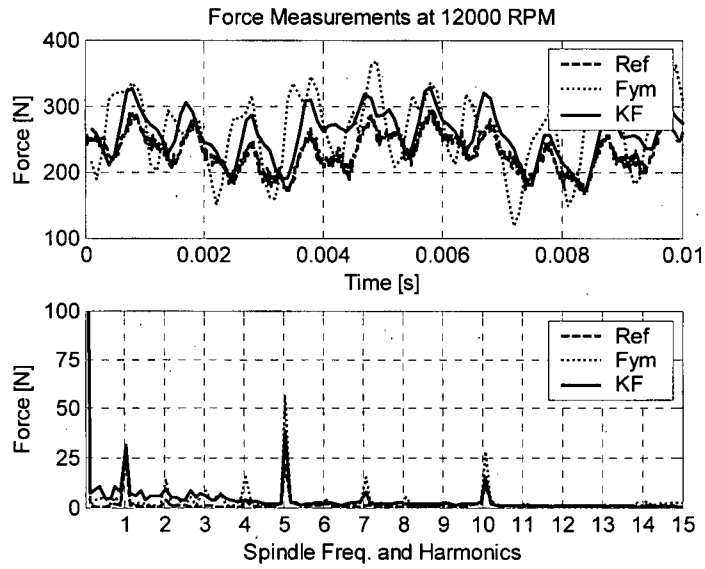

(b) Y direction

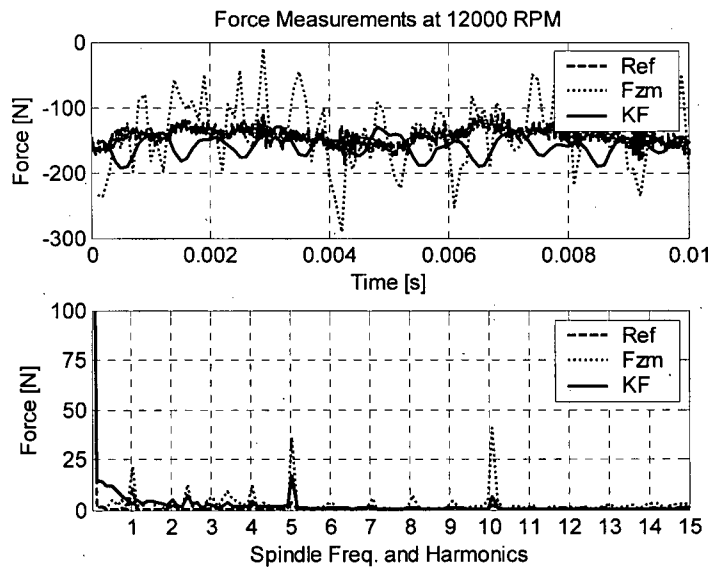

(c) Z direction

Figure E5. Five fluted cutting force measurements at 12000 rpm with (a) X, (b) Y, and (c) Z directions. *The figures are shown in the time and frequency (normalized with the spindle freq.) domains. The spindle frequency at 12000 rpm corresponds to 200 Hz.*

APPENDIX F.

SYSTEM IDENTIFICATION USING THE RECURSIVE LEAST SQUARE METHOD

The most common method to estimate a time varying linear process is through the Recursive Least Square (RLS) method [Ljung 87, Altitnas 00]. Consider a simple dynamic system where the sampled input signal is f_c(t) and output signal is F_a(t).

$$A(q^{-1})F_a(t) = B(q^{-1})f_c(t) \tag{F1}$$

where A and B are polynomials defined in backward shift operator (q^{-1})

$$\begin{aligned} A(q^{-1}) &= 1 + a_1 q^{-1} + a_2 q^{-n2} \\ B(q^{-1}) &= b_0 q^{-1} + b_1 q^{-2} + b_2 q^{-3} \end{aligned} \tag{F2}$$

The above equation can be rewritten in a concise form as:

$$F_a(t) = \theta^T \phi(t)$$

where

$$\theta^T = [a_1, a_2, b_0, b_1, b_2] \text{ and} \tag{F3}$$

$$\phi = [-F_a(t-1), -F_a(t-2), f_c(t-1), f_c(t-2), f_c(t-3),]$$

The parameter vector θ is estimated from measurements of input and output over N sampling time and by minimizing a cost function $J(\theta)$;

$$\begin{aligned} J(\theta) &= \sum_{k=1}^{N} e(t)^2 = (F_a - \phi\theta)^T (F_a - \phi\theta) \\ &= F_a{}^T F_a - F_a{}^T \phi\theta - \theta^T \phi^T F_a - \theta^T \phi^T \phi\theta \end{aligned} \tag{F4}$$

Minimizing the error by differentiating the cost function and equating to zero would yield the estimated parameter to be:

$$\theta = \left[\phi^T \phi\right]^{-1} \phi^T F_a \tag{F5}$$

It can be shown that [Ljung 87] the estimated parameter vector can be found in recursive manner at each sampling interval by:

$$\hat{\theta}(t) = \hat{\theta}(t-1) + a(t)K(t)\left(F_a(t) - \phi^T(t)\hat{\theta}(t-1)\right) \tag{F6}$$

$$K(t) = \frac{P(t-1)\phi(t)}{\lambda + \phi^T(t)P(t-1)\phi(t)} \tag{F7}$$

$$\overline{P}(t) = \frac{1}{\lambda}\left(\overline{P}(t-1) - a(t)K(t)\phi^T(t)P(t-1)\right) \tag{F8}$$

$$P(t) = c_1 \frac{\overline{P}(t)}{tr(\overline{P}(t))} + c_2 I \tag{F9}$$

$$a(t) = \begin{cases} 1 \; if \; \left|F_a(t) - \phi^T(t)\hat{\theta}(t-1)\right| \geq 2\delta \\ 0 \qquad\qquad otherwise \end{cases} \tag{F10}$$

where λ is the forgetting factor. c_1 and c_2 are greater than zero and δ is an estimate of the magnitude of the tolerable fluctuation of the output of the process or noise. The smaller value of λ, the faster the algorithm can track, but the estimate will vary even when the true parameters are time invariant. Furthermore, the small λ may also cause blow up of the covariance matrix, P, even in the absence of excitation.

APPENDIX G.

GENERALIZED PREDICTIVE CONTROL (GPC) ALGORITHM

Generalized Predictive Control (GPC) is proposed as a "general purpose" adaptive control method by Clarke et al. [Clarke 88]. The technique uses a receding horizon prediction approach where the controller predicts the changes in the controlled variable that will occur in the future using present process knowledge and control. Based on a model of the process, the controller predicts future process responses in terms of free and forced responses. The free response includes the effect of past and present inputs and assumes zero future control actions. Whereas the forced response considers the effect of future control actions as shown in Figure G1.

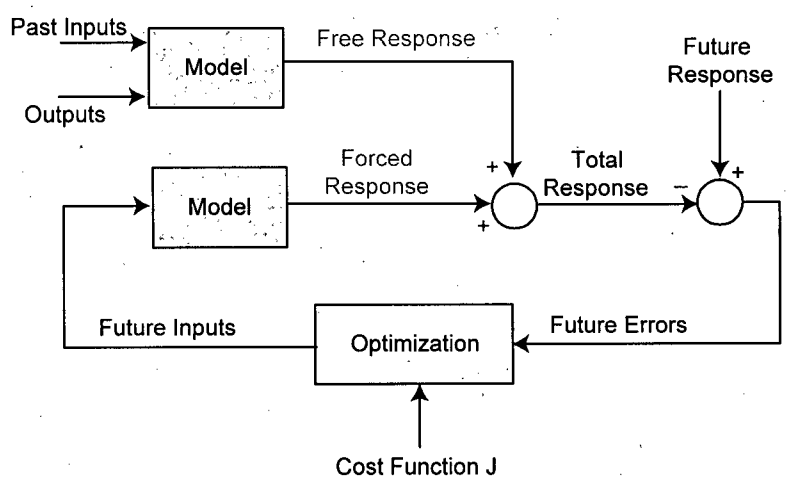

Figure G1. Basic Structure of Predictive Control

A quadratic cost function which is indicative of the desired performance over the horizon considered is solved through the optimization procedure:

$$J = E\left(\sum_{j=N_1}^{N_2} [F_a(t+j) - F_r(t+j)]^2 + \sum_{j=1}^{Nu} \rho[\Delta f_c(t+j-1)]^2 \right) \tag{G1}$$

where $F_r(t+j)$ is a sequence of future set points, N_1 is the minimum prediction horizon, N_2 is the maximum prediction horizon, N_u is the control horizon, and ρ is a control weighting factor where higher ρ results in less active control.

The minimization of J in Eq. G1 requires j-step ahead predictions of $y(t+j)$. Most often, a Controlled Auto Regressive Moving Average (CARIMA) model of the form below is used to describe the process:

$$A(q^{-1})F_a(t) = B(q^{-1})f_c(t-d) + Ce(t)/\Delta \tag{G2}$$

where $\Delta = (1 - q^{-1})$, $F_a(t)$ is output, $f_c(t)$ is input, d is delay, and $e(t)$ is disturbance. C and d are assumed to be one.

$$\begin{aligned} A(q^{-1}) &= 1 + a_1 q^{-1} + \cdots + a_{na} q^{-na} \\ B(q^{-1}) &= b_0 + b_1 q^{-1} + \cdots + b_{nb} q^{-nb} \end{aligned} \tag{G3}$$

We perform partial expansion of the delay term by considering the following Diophantine equation:

$$1 = A\Delta F_j(q^{-1}) + q^{-j} G_j(q^{-1}) \tag{G4}$$

where $deg\ F = j-1$, and $deg\ G = deg\ A = na$. The above equation can be expanded as:

$$\hat{F}_a(t+j \mid t) = G_j F_a(t) + BF_j \Delta f_c(t+j-d) \tag{G5}$$

The Δf_c term can explicitly contain future Δf_c terms by distinguishing the past through solving the following the Diophantine equation:

$$BF_j = E_j(q^{-1}) + q^{-j}\Gamma_j(q^{-1}) \tag{G6}$$

where *deg E=j-1*, and *deg Γ = nb-1*. The parameters, *G, E*, and *Γ* are recursively calculated. By inserting Eq. G6 into Eq. G5, the predicted output becomes as:

$$\begin{aligned} \hat{F}_a(t+j \mid t) &= \underbrace{G_j F_a(t) + \Gamma_j \Delta f_c(t-d)}_{Free\ \mathrm{Re}sponse} + \underbrace{E_j \Delta f_c(t+j-d)}_{Forced\ \mathrm{Re}sponse} \\ \hat{y} &= f + R\tilde{u} \end{aligned} \tag{G7}$$

The above equation can be rewritten as:

$$\hat{\mathbf{y}} = \mathbf{f} + \mathbf{R}\tilde{\mathbf{u}} \tag{G8}$$

where

$$\hat{\mathbf{y}} = \begin{bmatrix} \hat{F}_a(t+N_1) \\ \hat{F}_a(t+N_1+1) \\ \vdots \\ \hat{F}_a(t+N_2) \end{bmatrix}, \tilde{\mathbf{u}} = \begin{bmatrix} \Delta f_c(t) \\ \Delta f_c(t+1) \\ \vdots \\ \Delta f_c(t+N_u-1) \end{bmatrix}, \mathbf{f} = \begin{bmatrix} f_{N_1} \\ f_{N_1+1} \\ \vdots \\ f_{N_2} \end{bmatrix}$$

$$\mathbf{R} = \begin{bmatrix} E_{N_1,N_1} & E_{N_1-1,N_1} & \cdots & \cdots \\ E_{N_1+1,N_1+1} & E_{N_1,N_1+1} & \cdots & \cdots \\ \cdots & \cdots & \cdots & \cdots \\ E_{N_2,N_2} & E_{N_2-1,N_2} & \cdots & E_{N_2-Nu+1,N_2} \end{bmatrix}, \mathbf{y_m} = \begin{bmatrix} F_a(t+N_1) \\ F_a(t+N_1+1) \\ \vdots \\ F_a(t+N_2) \end{bmatrix} \tag{G9}$$

R is a *($N_2 - N_1 + 1$) x Nu* matrix which is also known as the dynamic matrix. The expected value of the cost function can be written as:

$$\begin{aligned} J &= E\left[(\mathbf{y}-\mathbf{y_m})^T(\mathbf{y}-\mathbf{y_m}) + \rho\tilde{\mathbf{u}}^T\tilde{\mathbf{u}}\right] \\ &= (\mathbf{R}\tilde{\mathbf{u}} + \mathbf{f} - \mathbf{y_m})^T(\mathbf{R}\tilde{\mathbf{u}} + \mathbf{f} - \mathbf{y_m}) + \rho\tilde{\mathbf{u}}^T\tilde{\mathbf{u}} \end{aligned} \tag{G10}$$

The minimization of the above equation (i.e., $\partial J / \partial u = 0$) will yield to the following:

$$\tilde{\mathbf{u}} = (\mathbf{R}^T\mathbf{R} + \rho I)^{-1}\mathbf{R}^T \tag{G11}$$

Only the first value of delta *u(t)* is applied from the array $\tilde{\mathbf{u}}$ resulting in the following simplification:

$$\Delta f_c(t) = r^T(\mathbf{y_m} - \mathbf{f}) = [1 \quad 0 \quad \cdots \quad 0] \cdot (\mathbf{R}^T\mathbf{R} + \rho I)^{-1}\mathbf{R}^T(\mathbf{y_m} - \mathbf{f}) \tag{G12}$$

By substituting Eqs. G27 and G29 into Eq. G12 yields the RST control in the form as shown in Figure G2.

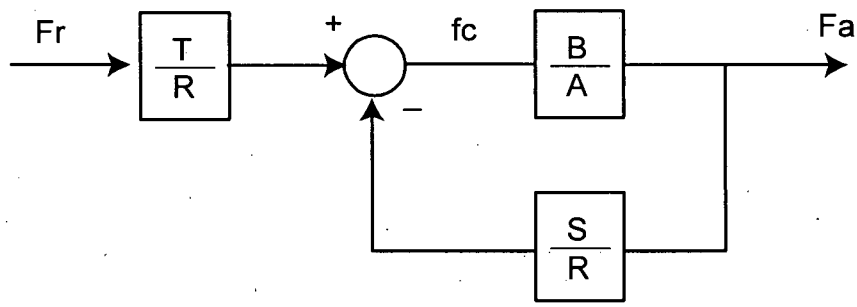

Figure G2. RST Control Scheme

$$R(q^{-1})f_c(t) = T(q^{-1})F_r(t) - S(q^{-1})F_a(t) \tag{G13}$$

where

$$R(q^{-1}) = \Delta\left[1 + r^T\begin{bmatrix}\Gamma_{N_1}\\ \vdots \\ \Gamma_{N_2}\end{bmatrix}q^{-d}\right],\ T(q^{-1}) = r^T\begin{bmatrix}q^{N_1}\\ \vdots \\ q^{N_2}\end{bmatrix},\ S(q^{-1}) = r^T\begin{bmatrix}G_{N_1}\\ \vdots \\ G_{N_2}\end{bmatrix} \tag{G14}$$

where *deg R = deg B, deg S = deg A, deg T =* N_2. Since the matrix R is $(N_2 - N_1 + 1)$ x *Nu*, when we choose *Nu* to be 1, R^TR matrix is always invertible or otherwise R^TR matrix needs to be positive semi-definite to be invertible when we choose N_u to be greater than 1.

APPENDIX H.

ORTS ADAPTIVE CONTROL SCRIPT FILE

The ORTS script file to run the adaptive control is depicted below:

```
/*****************************************************************************/
/* Adaptive Control Simon 03_Filter _ Adapted to ORTS Daytona16              */
/*      The adaptation is made on the estimated actual force at the tool tip. */
/* using 5 fluted cutter with Hydraulic chuck                                */
/* Cutting tests are performed on a FADAL VMC2216 Three Axis Machining Center */
/*                                                                           */
/* Assumed cutting conditions:                                               */
/* cutting conditions: Spindle Speed: 1000, 3000, 6000 [rpm]                 */
/* Adaptive control freq: 25 [Hz]                                            */
/*****************************************************************************/
DSP Daytona:
Link logData                                (dsp2pc,Node_A,buffered,1000,10);


FastCyclic control, Node_A, freq=4000:
{
    Link forceMeasurement(2),scaledForces(2),filteredForces(2), smoothedForces(2);
    Link peakForce(1), feedCommand(1), overrideVoltage(1), plantParameters(6);
    Link force1prev(1), force2prev(1), feed2prev(1), feed3prev(1);

    /* Read the measured force at the spindle housing */
    MFIO_ReadADC(1,2), output=(forceMeasurement);

    /* Scale the forces to be in Newton  */
    Gain(1000,1000), input=(forceMeasurement), output=(scaledForces);

    /* Filter the measured forces to estimate the actual forces at the tool tip */
    ControlFilter(
        2,                                                  // number of axis
  7,7,7,7,

// disturbance Kalman Filter polynomials at 4000 Hz
// in X direction
// Numerators
0.36219097210,
-0.69380873678,
0.91427383747,
-0.26802760099,
-0.38529114072,
0.91613107826,
-0.63191736995,
0.30496155841,

// Denominators
1.00000000000,
-2.93340450360,
5.39738449970,
-6.19642608136,
5.24773368662,
-2.99298109062,
1.19825989779,
-0.22259253074,

// in Y direction
// Numerators
0.31561274474,
-0.31069874319,
0.69143810488,
0.02211436256,
-0.02117166885,
0.68841319731,
-0.30079108663,
0.28525927745,
```

```
// Denominators
1.00000000000,
-1.96546142533,
3.87995498059,
-3.89740964256,
3.63696224226,
-1.97254437414,
0.91460935805,
-0.20094693501

        ), input=(scaledForces), output=(filteredForces);

    /*  Apply low pass filter to get rid of the measurement noise */
    FastFilter(Lowpass,4000,16,500), input=(filteredForces), output=(smoothedForces);

    /* Calculate the resultant force */
    PeakDetect(100,1), input=(smoothedForces), output=(peakForce);

    freq=1/160;                         // the PIMs beyond this point are executed at 25
[Hz]

    /* Adaptation process     */
    Adaptive(  300,                     // reference force                    [N]
               1000,                    // maximum feedrate                   [mm/min]
               4,                       // number of steps to reference force []
               .2,                      // lambda (feedrate fluctuation weight)      []
               500,                     // zero force feed                    [mm/min]
               100    ),                // air cutting force threshold                [N]
        input=(peakForce), output=(feedCommand, force1prev, force2prev, feed2prev,
feed3prev, plantParameters);


    /* Calculate the override Voltage to be sent to the Machine Tool       */
    FeedrateScale(     1000,            // commanded feedrate                 [mm/min]
                        0,              // minimum percentage feed override
                        137.7551,       // maximum percentage feed override
                        1.45,           // minimum feed override voltage
                        10.0),                // maximum feed override voltage
        input=(feedCommand), output=(overrideVoltage);

    /* Send override voltage to the machine tool     */
    MFIO_WriteDAC(1), input=(overrideVoltage);

    Log(1), input=(peakForce, feedCommand, overrideVoltage, plantParameters),
output=(logData);
}

PC:
priorityclass=normal;
SaveToDisk("AdaptiveControlSimon03.log"), input=(logData), priority=Highest;
```